Digital Rock: Understanding the mechanism of Enhanced Oil Recovery (EOR) Core Floods

Georgia Roussou

Emmanuel College

This dissertation is submitted for the degree of Doctor of Philosophy

June 2022

Magnetic Resonance Research Centre

Department of Chemical Engineering and Biotechnology

University of Cambridge

Preface

This dissertation is the result of my own work and includes nothing which is the outcome of work done in collaboration with others, except as declared in the Preface and specified in the text.

It is not substantially the same as any that I have submitted, or, is being concurrently submitted for a degree or diploma or other qualification at the University of Cambridge or any other University or similar institution, except as declared in the Preface and specified in the text. I further state that no substantial part of my dissertation has already been submitted, or, is being concurrently submitted for any such degree, diploma or other qualification at the University of Cambridge or any other University or similar institution except as declared in the Preface and specified in the text.

The research presented herein was conducted at the Magnetic Resonance Research Centre, Department of Chemical Engineering and Biotechnology, University of Cambridge between October 2017 and May 2022. This thesis does not contain more than 65,000 words and 150 figures, including references, tables and equations.

Georgia Roussou
May 2022

Acknowledgements

Firstly, I would like to thank my supervisor Prof. Lynn Gladden, for giving me the opportunity to study at the Magnetic Resonance Research Centre (MRRC), for her continued encouragement, guidance and support throughout the last few years, proofreading and editing this thesis. I would also like to thank Dr Andy Sederman and Dr Mick Mantle for their time, help and invaluable advice on a daily basis. For financial support, I gratefully acknowledge Shell and my family.

Thanks are also due to all those at the MRRC who have helped in this work. Particular thanks go to Dr Daan de Kort for his significant guidance throughout my first two years in making me an expert in spatially-resolved propagators, assisting me in the primary drainage measurements presented in Chapter 7 and helping me build the polymer core flooding system presented in Chapter 8. A special thanks also go to Dr Kaspars Karlsons who welcomed me into the Digital Rock group and shared his expertise in optimising the under-sampling scheme for better quality in the reconstructed images, a method used throughout my research. I would also like to particularly thank Sean Smith for useful discussions on the relaxation data expected for each rock, Amy Sparks for her insights into the measurements of diffusion, Dr Muhammad Asadullah Javed and Francesco Fraboni for sharing their knowledge and data on phase-contrast imaging used in Chapters 4 and 5.

In addition, I must thank several people at the Department of Chemical Engineering and Biotechnology for their help. I wish to thank Dr Simon Butler for conducting the rheometry measurements and providing the equipment for the production of the polymeric solution. Special thanks to Mark Scudder and Steven Guymer for helping me connect and set up the differential pressure transducer to the core flooding system. I am also indebted to several people at the Shell Technology Centre in Amsterdam (STCA) who prepared and sent over the rock core samples and who were willing to discuss the implications faced during polymer flooding. I am particularly grateful to Dr Matthias Appel for the many useful discussions and the new milestones that he was setting after our annual meetings. His continuous seeking for innovation helped me challenge myself and overcome my creativity limits.

Finally, I would like to thank my family and friends for their support throughout this time. To the many members of Emmanuel MCR, housemates and handball mates, for making me laugh, teaching a Greek person how to become vegetarian and creating fun memories. To my wonderful parent, Maria and Antonis for always being there for me, providing support and pushing me every time that I wanted to quit, especially during the COVID. To my mum who made sure that I had enough clothes and enough olive oil to sustain winter in the UK. To my dad who took a flight for the first time in his life to come and help me find again my enthusiasm and my passion for science and innovation. Lastly, I would like to thank my uncle, my aunt and my cousin Maria for helping me set up my write-up space and keeping me sane in this long process.

Abstract

Oil companies aim to increase their return on investment by extending the productive life of their existing oilfields. For that purpose, a better understanding of the physical phenomena which occur during waterflooding and enhanced oil recovery (EOR) is needed to optimise the oil recovery. In this thesis, Nuclear Magnetic Resonance (NMR) has been employed to detect fluid displacement at reservoir-representative velocities and dynamically monitor the oil and water behaviour during brine and polymer core flooding.

The first step for the analysis of the physical phenomena was the detection of velocities lower than 10 ft d^{-1} using Magnetic Resonance Imaging (MRI). For that reason, an optimisation toolbox, which uses the relaxation times and the diffusion coefficients of the porous system as input and derives the optimum experimental parameters for the MRI sequence, was developed. The novel MRI technique, also known as phase-contrast imaging, was initially tested in the ideal system of a bead pack having pore-scale resolution. Water velocities as low as 1 ft d^{-1} (3.5 μm s^{-1}) were detected for the first time. The acquisition of velocity maps in less than 1 h was achieved by taking advantage of the novel method for under-sampling of the k-space. The parameters of compressed-sensing reconstruction were optimised giving results of high quality. Combining the velocity maps with 3D spatially-resolved propagators without pore-scale resolution enabled the identification of the mechanisms of mechanical and diffusive mixing along the sample. Phase-contrast imaging and 3D spatially-resolved propagators were also employed for the detection of ultra-slow flows through one sandstone and three low-permeability carbonate core plugs. Interesting observations were derived for flow velocities below 15 ft d^{-1} in these complex pore structures.

After detecting ultra-slow flows through rocks, the research focused on the study of two-phase systems. A novel MRI sequence which enables the acquisition of 3D spatially-resolved propagators for the water and oil phase separately was developed and was tested in a bead pack and a carbonate rock. Then, oil was injected into a carbonate rock until the system reached reservoir-representative oil saturation. One-dimensional NMR spectra were used to monitor the saturation profiles, showing that water-wetting layers were distributed uniformly along the core. Brine was injected into the system simulating the process of waterflooding. The brine injection was monitored with chemically-selective images acquired in 16 min for each phase. The invasion percolation with cluster growth was identified as the main mechanism of oil displacement and 55.2% of the Original Oil In Place (OOIP) was removed. Then, brine injection was abruptly increased removing another 4.6% of OOIP trapped in the form of oil ganglia. The rest of the oil was trapped in unswept areas of the rock which could not be accessed by the abrupt increase in the brine injection. Xanthan gum polymer-EOR flood was employed to extract oil from these unswept areas. Comparison between the chemically-selective images and spatially-resolved propagators acquired before and after the polymer injection showed the diversion of the brine flow paths. This behaviour of the brine propagators was related to the

blocking of the pores and throats due to the deposition of polymeric molecules as mentioned in the literature. An extra 8.5% of OOIP was removed during the consecutive polymer and brine injections. Moreover, interesting insights into the different flow behaviour of the brine and the polymer were obtained by comparing the propagators of each phase obtained under the same conditions.

Table of Contents

Preface ..... **i**
Acknowledgements ..... **ii**
Abstract ..... **iii**
Abbreviations and Nonmeclature ..... **x**
Chapter 1 Introduction **1**
1.1 EOR: an Overview 1
1.2 Digital Rock (DR) Technology 1
1.3 Aims and Scope of This Thesis 3
1.4 Outline of Thesis Chapters 3
Chapter 2 Theoretical Background **5**
2.1 Principles of NMR 5
2.1.1 Nuclear Apin and Zeeman Effect 5
2.1.2 The Bloch Vector Model 6
2.1.3 Larmor Frequency 7
2.1.4 NMR Experiment 7
2.1.5 Relaxation Mechanisms 10
2.2 Basic Principles of MRI 14
2.2.1 Magnetic Field Gradients 14
2.2.2 k-Space 17
2.2.3 Nyquist Theorem 17
2.2.4 Resolution in MRI 18
2.2.5 k-Space Trajectories 19
2.2.6 RARE 19
2.2.7 SNR in NMR and MRI 21
2.3 Basic Principles of MRI in Translational Motion 21
2.3.1 Self-Diffusion 21
2.3.2 PFG-NMR for Studying Translational Motion 21
2.3.3 Conditional Probability, Echo Attenuation and Q-Space 23
2.3.4 Restricted Diffusion 23
2.3.5 Techniques for Measuring Restricted Diffusion in Porous Media 24
Chapter 3 Digital Image Processing **25**
3.1 Introduction 25
3.2 Under-Sampling in 3D RARE 26

3.2.1 Under-Sampling Patterns....26
3.2.2 k-Space Sampling Trajectories....27
3.3 Under-Sampling in 3D Propagators....28
3.4 Compressed Sensing Reconstructions....29
3.4.1 Optimisation of Image and Velocity Map Reconstruction Parameters....29
3.4.2 Optimisation of Propagator Reconstruction Parameters....31
3.5 Denoising Procedures....32
3.5.1 Distribution of Noise in MRI Images....32
3.5.2 Automatic Background Thresholding....33
3.5.3 Experimental Results of the Automatic Background Thresholding....33
3.5.4 Methods for Measuring SNR....35
3.6 Removal of Artefacts....37
Chapter 4 Ultra-Slow Flow in a Bead Pack....38
4.1 Introduction....38
4.2 Theoretical Background....39
4.2.1 Single-Phase Flow in Porous media....39
4.2.2 Flow MRI at Ultra-Slow Velocities....41
4.3 Materials and Methods....47
4.3.1 Materials....47
4.3.2 Methods....47
4.4 Results....53
4.4.1 Relaxation Measurements....53
4.4.2 Linear Relationship Between the Phase and the Gradients....53
4.4.3 Noise Analysis in Phase-Contrast Imaging....54
4.4.4 Velocity Maps from Phase-Contrast Imaging....56
4.4.5 Average Volumetric Velocity Profile from Phase-Contrast Imaging....59
4.4.6 Spatially-Resolved Propagator Measurements....59
4.4.7 Velocity Map and 3D Propagator of Same Resolution....61
4.5 Discussion....63
4.6 Conclusions....64
Chapter 5 Ultra-Slow Flow in Sedimentary Rocks....65
5.1 Introduction....65
5.2 Theoretical Background....66
5.2.1 NMR Techniques to Assess the Pore Throat Distribution in the Presence of Internal Gradients in Low-Permeability Rocks....66

5.2.2 Propagator Measurements in Sedimentary Rocks 66
5.3 Materials and Methods 67
5.3.1 Materials 67
5.3.2 Methods 67
5.4 Results 71
5.4.1 Validation of the Applied Techniques 71
5.4.2 Relaxation and Diffusion Measurements for all the Core Plugs 74
5.4.3 Noise Analysis in the Phase-Contrast Imaging for all the Core Plugs 78
5.4.4 Velocity Maps from Phase-Contrast Imaging and 3D Propagators 83
5.4.5 Flow Paths Formed from the Phase-Contrast Images 95
5.5 Discussion 96
5.6 Conclusion 98
Chapter 6 Two-Phase Flow in an Ideal and in a Rock-Porous System 99
6.1 Introduction 99
6.2 Methods for Achieving Chemical Selectivity 100
6.2.1 Chemically-Selective Pulse-Acquire Experiment 100
6.2.2 Chemically-Selective and Spatially-Resolved Spectra 100
6.2.3 Chemically-Selective RARE Images 101
6.2.4 Chemically-Selective and Spatially-Resolved Flow Propagators 102
6.3 Materials and Methods 103
6.3.1 Materials 103
6.3.2 Methods 105
6.4 Results and Discussion 109
6.4.1 Chemical Selectivity of the Pulse-Acquire Sequence in the Bead Pack 109
6.4.2 Chemical Selectivity in the 3D RARE Images of the Bead Pack 111
6.4.3 Chemically-Selective Propagators Following the APGSTE-RARE Sequence in the Bead Pack 113
6.4.4 Chemical Selectivity of the Pulse-Acquire Sequence in Estaillades 116
6.4.5 Chemical Selectivity in the 3D CS-RARE Images of the Estaillades 118
6.4.6 Chemically-Selective Propagators Following the APGSTE-RARE Sequence in the Estaillades 119
6.5 Conclusions 122
Chapter 7 Primary Drainage in Estaillades Carbonate Rock 124
7.1 Introduction 124
7.2 Theoretical Background 124

7.2.1 Definition of Primary Drainage 124
7.2.2 Techniques for Capillary Pressure Curves and Resistivity Index 125
7.2.3 Mechanisms of Immiscible Fluid Displacement 125
7.3 Materials and Methods 129
7.3.1 Material and Chemicals 129
7.3.2 Methods 130
7.4 NMR Data Processing 134
7.4.1 Methods for Measuring the Relative Saturations 134
7.4.2 Broadening of the Line Width and Deviation on the ppm Axis 134
7.4.3 Baseline Offset Error 135
7.4.4 Effect of Artefacts in the 'Integration' Method 136
7.4.5 Effect of Artefacts in the 'Line Shape' Method 138
7.4.6 Conclusions Driven by Comparing 'Integration' and 'Line shape' Methods 139
7.5 Results 140
7.6 Discussion 143
7.7 Conclusion 145
Chapter 8 Imbibition and Xanthan Gum Injection in the Estaillades Carbonate Rock 147
8.1 Introduction 147
8.2 Theoretical Background 148
8.2.1 Waterflooding and Oil Recovery 148
8.2.2 Pore-Filling Mechanisms in Imbibition 148
8.2.3 Displacement Patterns of Imbibition at Macro-Scale 149
8.2.4 Mechanical Behaviour of Polymers in EOR 151
8.2.5 Mechanisms of Oil Displacement in Polymer Flooding 152
8.3 Materials and Methods 153
8.3.1 Materials and Chemicals 153
8.3.2 EOR Polymer Concentration 153
8.3.3 Methods 156
8.4 Results 160
8.4.1 Dynamic Monitoring of the Imbibition 160
8.4.2 Removal of the Oil Ganglia 164
8.4.3 Dynamic Monitoring of Polymer and Brine Injections 164
8.4.4 Time-Dependence of the Recorded Pressure Drop 169

8.4.5 Comparing Propagator Data for Polymer and Brine Flow 170
8.4.6 Comparing Brine Propagators Before and After Polymer Injection 171
8.5 Discussion 172
8.6 Conclusions 173
Chapter 9 Summary of Conclusions and Future Work 175
9.1 Summary of Conclusions 175
9.2 Suggestions for Future Work 178
9.2.1 Systemic Study of Single-Phase Ultra-Slow Flow in Rocks 178
9.2.2 Dynamic Monitoring of Single-Phase Polymer Core Floods 178
9.2.3 Dynamic Monitoring of Multi-Phase Polymer Core Floods 178
References 180

Abbreviations and Nonmeclature

Abbreviations

Symbol	Definition
1D	One-Dimensional
2D	Two-Dimensional
3D	Three-Dimensional
APGSTE	Alternating Pulsed Gradient Stimulated Echo
CFS	Core Flooding System
CS	Compressed-Sensing
CSI	Chemical Shift Imaging
DI	Deionised (in context of laboratory purified deionised water)
DPR	Disproportionate Permeability Reduction
DR	Digital Rock
EOR	Enhanced Oil Recovery
FFT	Fast Fourier Transformation
FOV	Field-Of-View
FT	Fourier Transform
GCV	Generalized Cross Validation
HPAM	Hydrolysed Polyacrylamides
LBM	Lattice-Boltzmann Method
LSB	Low-Salinity Brine
LSSIM	Local Structural Similarity Index
LT	Long-Time regime
MAV	Motional Averaging regime
MIP	Mercury Intrusion Porosimetry
MR	Magnetic Resonance
MRI	Magnetic Resonance Imaging
MRRC	Magnetic Resonance Research Centre
NEMA	National Electrical Manufacturers Association
NMR	Nuclear Magnetic Resonance
NNLS	Non-Negative Least Squares
OOIP	Original Oil In Place
P.V.	Pore Volume
pdf	probability distribution function
PFG	Pulsed-Field Gradient
PGSE	Pulsed-Gradient Spin Echo
PP	Porous Plate technique
ppm	parts per million
PSF	Point Spread Function
PSNR	Peak Signal-to-Noise Ratio
PVT	Pressure-Volume-Temperature
r.f.	radio-frequency
RARE	Rapid Acquisition with Relaxation Enhancement
RCH	Rock Core Holder

RD	Recycle Delay
RI	Resistivity Index
ROI	Region-Of-Interest
SNR	Signal-to-Noise Ratio
SSIM	Structural Similarity Index
ST	Short-Time regime
STCA	Shell Technology Centre in Amsterdam
STP	Standard Temperature and Pressure conditions
SWPP	Short-Wait Porous Plate method
TPG	Threshold Pressure Gradient
WET	Water Suppression Enhanced Through $\boldsymbol{T_1}$ Effects
μCT	X-ray microcomputed tomography

Nomenclature

Romain Symbols	**Definition**
$[H]_{water}^{STP}$	concentration of hydrogen in pure water at STP
m_s	spin quantum number
IM_c	cut-off intensity value
A	original voxel intensity without the presence of noise
A_c	cross-sectional area
Ar_C	relative atomic mass of ^{13}C
Ar_H	relative atomic mass of ^{1}H
$\boldsymbol{B}_0$	static external magnetic field
$\boldsymbol{B}_1$	oscillating r.f. field
$C_1; C_2$	constants used for the calculation of SSIM
Ca	capillary number
$D_{//}$	the coefficient of the longitudinal (mechanical) dispersion
D_{app}	apparent diffusion coefficient
D_{eff}	effective diffusion coefficient
D_s	molecular self-diffusion coefficient
d_s	nominal diameter of the spheres
dS	signal element
dV	volume element in a sample
$E(\mathrm{q})$	amplitude of the echo attenuation
E_{diff}	echo attenuation from flow and diffusion
E_{relax}	echo attenuation coming from T_1 and T_2 relaxation
F	formation factor
f	frequency of the nucleus of interest
$\boldsymbol{f}_0$	Larmor frequency
f_s	frequency bandwidth of the signal
f_{TMS}	frequency of the nucleus of TMS
F_u	linear operator for the discrete 2D FT
$\mathrm{FOV}_{\mathrm{phase,freq}}$	FOV in the phase or the frequency encoding gradients
FOV_{prop}	FOV of the flow field
fun	fitting function to the intensity of the non-background voxels
g	PFG gradient pulse strength

g_r	gravitational acceleration
$\boldsymbol{G}$	gradient field
g_{eff}	amplitude of internal gradients
g_{factor}	percentage of the g_{max}
g_h	amplitude of a homospoil gradient
g_{max}	maximum gradient strength
G_{slice}	amplitude of the slice gradient
h	height
ħ	Plank's constant divided by 2π
$h(t)$	noiseless signal with time
h_0	free water level
$hist$	histogram function
$I(\boldsymbol{r})$	intensity of each voxel
I_0	zeroth-order Bessel modified function
I_o	integral of the oil peak
I_w	integral of the water peak
IM	measured voxel intensity
J	regularisation functional
k	absolute permeability
$\mathbf{k}$	**k**-space wave vector
K	scaling factor
k_B	Boltzmann constant
k_i	effective permeability of the phase i (i stands for displacing (D) and displaced (d) phase)
k_{max}	maximum sampled **k**-space coordinate
$\boldsymbol{k}_{phase1}$	phase1 dimension of phase encoding
$\boldsymbol{k}_{phase2}$	phase2 dimension of phase encoding
$\boldsymbol{k}_{read}$	read dimension of frequency encoding
k_{ri}	relative permeability of the phase i (i stands for displacing (D) and displaced (d) phase)
L	length of the sample
l_{char}	effective pore spacing or transport diameter
l_D	free-diffusion path
$\mathbf{L}_\mathrm{S}$	smoothing operator in Tikhonov regularisation
L_v	dispersivity length
$\mathbf{m}$	complex image (matrix)
m	array of **k**-space data along a chosen direction
$\boldsymbol{M}$	nuclear magnetic polarization
$m_{\boldsymbol{k}_0}$	index of the central point of the **k**-space
$\boldsymbol{M}_0$	magnetisation vector along the z, z'-axis (equilibrium)
$\mathbf{m}_\mathrm{CS}$	reconstructed image (matrix)
$\mathbf{m}_\mathrm{FS}$	fully-sampled image (matrix)
M_R	mobility ratio
M_z	magnetisation component along the z-axis
N	number of the lobe in the imaginary signal
n	number of Bregman iterations (superscript)
n_1, a	fitting constants in the Carreau model
N_{echo}	number of echoes

N_k	number of **k**-space points
N_{phase1}	number of acquired points in the phase1 direction
N_{phase2}	number of acquired points in the phase2 direction
N_q	number of acquired **q**-points
N_{read}	number of acquired points in the read direction
N_s	number of scans
N_{vox}	number of voxels in the image
N_α	number of spins in the high-energy α-state
N_β	number of spins in the high-energy β-state
$\boldsymbol{P}$	vector of local pressure
P_{cap}	capillary pressure
P_{inj}	injection pressure recorded by the pressure transducer
p_M	probability distribution of the image intensities
P_{nw}	pressure in the non-wetting phase
P_w	pressure in the wetting phase
Pe	Péclet number
$\mathbf{q}$	**q**-space wave vector
Q	flow rate
q_{fast}	**q**-data point in the fast-flow regime
q_{slow}	**q**-data point in the slow-flow regime
r	effective radius of oil/water interface
$\boldsymbol{R}$	relaxation matrix containing the T_1 and the T_2 relaxation constants
$\boldsymbol{r}$	vector position
r_H	hydraulic radius
R_{HC}	hydrogen/carbon ratio
r_p	radius of the pore
r_t	radius of the throat
r_{tube}	radius of the tube
ral	fitting function to the Rayleigh distribution
Re	Reynold number
$\boldsymbol{S}$	spin angular momentum
S	phase corrected signal
S_o	oil or dodecane relative saturation
S_p/V_p	surface to volume ratio
S_r	signal detected by the receiver in the x-y plane
S_u	under-sampling pattern
S_w	water or brine relative saturation
S_{wc}	irreducible or connate water saturation
t	time
T	absolute temperature
$T_{2,eff}$	effective transverse relaxation
T_1	longitudinal relaxation
T_2	transverse relaxation
$T_{1,2bulk}$	relaxation of the bulk fluid
t_{echo}	echo time
t_h	gradient stabilisation delay
t_p	duration of a pulse
t_{RD}	recycle delay

t_s	time interval between two successive soft pulses
t_{store}	stimulated echo storage time
t_{VD}	time interval between the 180º and the 90º pulse in the inversion recovery sequence
$\boldsymbol{u}$	local velocity vector
$u(\boldsymbol{r})$	local velocity
u_0	interstitial velocity imposed by the pump
u_D	Darcy interstitial velocity of the displacing phase
u_m	measured velocity from the MRI experiment
u_{min}	minimum detectable velocity
u_{SF}	critical velocity between slow and the fast-flowing regime
V	amount of liquid
V_{sample}	volume of the cylindrical sample
V_{voxel}	volume of each voxel
W	window width factor
w	window function
$\mathbf{y}$	under-sampled k-space data (matrix)

Greek Symbols	**Definition**
α	positive regularisation parameter
α_n	phase contributions that depend on **q**
γ	gyromagnetic ratio
$\dot{\gamma}$	shear rate
$\dot{\gamma}_{eff,max}$	effective maximum shear rate
γ_i	skewness of the distribution for the displacement of the phase i (i stands for polymer or water)
Δ	observation time
$\Delta_\perp$	Laplacian operator
δ	chemical shift
δ_2	gradient stabilisation time
δ_D	Dirac delta function
δ_G	duration of the phase gradient
δ_h	duration of the homospoils
Δf_p	frequency bandwidth of a pulse
Δk	interval of readout points in the **k**-space domain
Δl	pixel size (resolution) of an image
ΔP	pressure drop
ΔP_1	pressure drop across the accumulator and the entrance of the RCH
ΔP_2	pressure drop along the ceramic disc
Δt	Dwell time
Δz	slice thickness
ΔE	energy difference between states
$\Delta\varphi$	phase map
$\Delta\chi$	susceptibility contrast
$\Delta\omega$	offset frequency
ε	normally distributed noise in the image
E	energy of an (eigen)state
ε_τ	error term for automatic background thresholding

ζ_0	displacement imposed by the pump
ζ_i	displacement of the phase i (i stands for polymer or water)
θ	flip angle
θ_R	receding contact angle
λ	critical shear rate in the Carreau model
μ	dynamic viscosity
$\boldsymbol{\mu}$	magnetic moment of a nucleus
μ_0	Newtonian viscosity at zero shear rate
μ_{app}	apparent viscosity
μ_b	mean of the background noise
μ_{eff}	effective viscosity
μ_i	dynamic viscosity of the phase i (i stands for polymer (p), brine (b), displacing (D) and displaced (d) phase)
μ_{inf}	Newtonian viscosity at an infinite shear rate
$\mu_{\mathbf{m}}$	mean of the image intensity
ρ	density of the fluid
$\rho(\boldsymbol{r})$	local magnetisation density
$\rho_{1,2}$	surface relaxivity
ρ_{nw}	density of the non-wetting phase
ρ_w	density of the wetting phase
σ	standard deviation of a distribution
σ_{φ_0}	error for each spin at no-flow conditions
σ_b	standard deviation of the background noise distribution
σ_i	standard deviation of the distribution for the displacement of the phase i (i stands for polymer or water)
$\sigma_{\mathbf{m}}$	standard deviation of the image intensity
σ_n	standard deviation in the noise distribution
σ_u	standard deviation of the velocity
$\sigma_u(\boldsymbol{r})$	error in local velocity
σ_τ	interfacial tension between the two fluids
σ_φ	noise in the phase of the obtained signal
τ	time between 1st, 2nd 90° pulse, and 3rd 90° pulse, STE – in STE sequence
τ_e	inter echo time in the spin-echo sequences
φ	phase angle of spins
ϕ	macroscopic porosity of the sample
ϕ_b	porosity of the bead pack
$\phi_{rel}(\boldsymbol{r})$	relative porosity in each voxel $\boldsymbol{r}$
φ_v	porosity of the vial
ψ	tortuosity
ω_0	Larmor (angular) frequency
ω_1	angular frequency of rotation of the $\boldsymbol{B}_1$ field
ω_{ref}	reference Larmor frequency

Chapter 1 Introduction

This thesis explores the use of MRI techniques to identify the mechanisms of oil extraction from complex reservoir rocks. This is achieved by conducting experimental studies under reservoir-representative conditions and monitoring them with newly developed MRI methods.

1.1 EOR: an Overview

Hydrocarbons are trapped in the subsurface of the Earth within complex networks consisting of pores, throats and fractures. In the oil and gas industry, oil production occurs in three stages; namely primary, secondary and tertiary (EOR) stages. The differential pressure between the reservoir and the production well is the driving force for the primary oil recovery stage. Approximately 10% of the Original Oil Held In Place (OOIP) is recovered during this stage. As the differential pressure is reduced, the oil production is also declining, leading to the stage of secondary oil recovery. Secondary oil recovery is characterised by the injection of external fluids such as gas or water. When injected phase is water (brine), the process is known as waterflooding. The injected phase maintains the differential pressure increasing the rate of oil recovery. An extra 30-50% of the OOIP can be produced during this stage. A significant quantity of hydrocarbons remains trapped in the reservoir. This is why the oil industries implement a tertiary stage in their oil production process. During EOR, the oil can be extracted following four different methods; chemical, thermal, microbial and miscible/ immiscible gas flooding (Gbadamosi et al., 2019; Rellegadla et al., 2017; Terry, 2001). All the applications that enhance the recovery beyond the limits of primary and secondary production are known as EOR applications (Al-Mjeni et al., 2010; Sheng, 2011). EOR techniques can achieve recovery factors between 50 and 70% (Muggeridge et al., 2014).

The efficiency of the oil recovery depends on the characteristics of the reservoir, such as pressure, temperature, wettability, permeability, porosity and brine salinity (Terry, 2001). Large capital investments, long lead times and complex technologies are some of the financial risks related to EOR. Understanding the reservoir's characteristics is of high importance in order to choose the most suitable EOR strategy.

1.2 Digital Rock (DR) Technology

Since the 1980s, universities began digitizing thin sections from rock cores, giving birth to the DR technology (Andersen, 2014). DR is a multidisciplinary tool for computing rock properties (Arns, 2004; Øren et al., 2007) and multiphase fluid flow properties within rocks with the aim of predicting the reservoir's performance (Kalam, 2012). DR models require as input experimental measurements of the rock characteristics and the fluid properties. This is better described in the DR workflow presented in **Figure 1-1** (Al-Mjeni et al., 2010). The workflow is divided into four major categories; (a) characterisation of the rock (steps 1, 2 and 3), (b) characterisation of the fluid (steps 4.1, 4.2), (c) computations (step 5) and (d) validation and calibration (step 6) of the model.

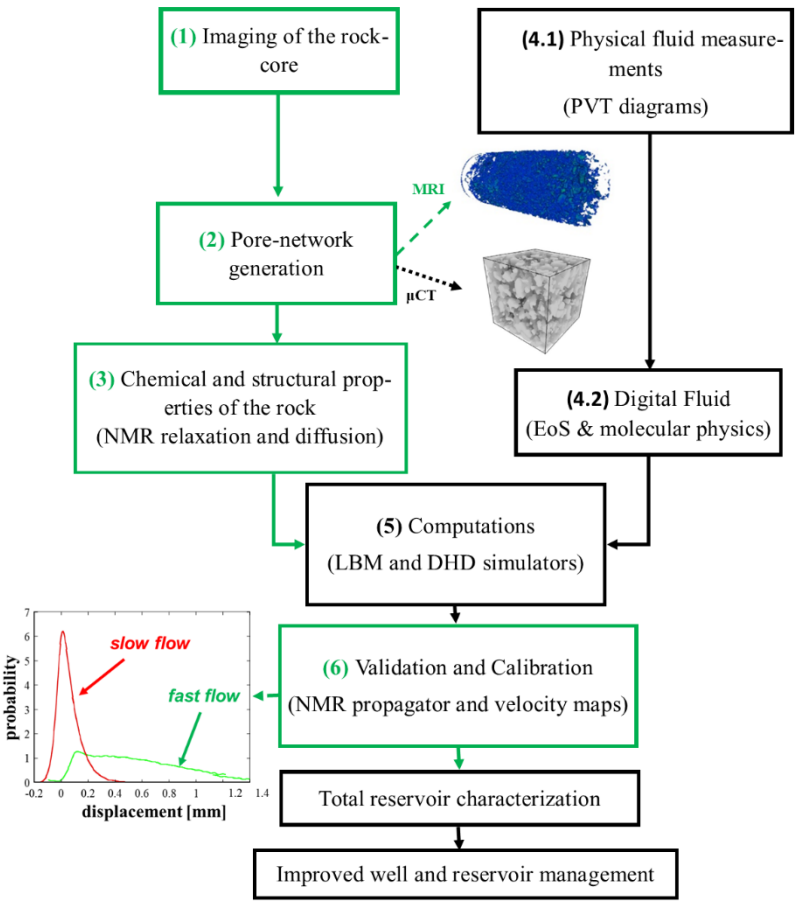

Figure 1-1: DR analysis workflow based on Andersen, (2014); Tahmasebi and Sahimi, (2012). The green blocks represent the steps of the workflow where NMR techniques are used.

MRI and X-ray microcomputed tomography (μCT) are the two most popular non-destructive imaging techniques used in DR (Wildenschild and Sheppard, 2013). The typical μCT spatial resolution is between 0.5 and 2 μm which is higher compared to MRI (Koroteev et al., 2014). Moreover, synchrotron μCT has been used to increase the speed and the resolution of the image (Koroteev et al., 2013). However, μCT cannot describe the full characteristics of the reservoir rock. This is why MRI has been employed for several years as a complementary imaging technique (Vinegar, 1986). Over the last 20 years, MRI has achieved higher spatial resolutions from 23 up to 17 μm pixel^{-1} using smaller samples and stronger field gradients (Doughty and Tomutsa, 1997; Karlsons et al., 2019). Moreover, NMR has been used for the pore size distribution and the wettability characterisation of rocks (Hübner, 2014; Mitchell, 2014; Mitchell and Fordham, 2014). NMR can also give insights into the surface-to-volume ratio (S_p/V_p) of the sample (Latour et al., 1993). NMR has been used as a logging tool for the measurement of the effective porosity and permeability in real reservoirs (Chang et al., 1994). Pressure-Volume-Temperature (PVT) diagrams are used to characterise the propertied of the fluid (Ghiselin, 2014; Koroteev et al., 2013).

The acquired digital representation of the pore network and the fluid characteristics are used as input in the simulation engines. Two of the most popular engines used in DR are the DHD simulator (Koroteev et al., 2014, 2013) and the Lattice-Boltzmann Method (LBM). The LBM has been implemented in complex pore-geometries to

study single and multi-phase flow (Arns et al., 2005; Ferréol and Rothman, 1995; Shikhov et al., 2017). The simulation models are 'validated' and 'calibrated' through comparison with experimental results (Fredrich et al., 2014). For this purpose, core-flooding lab experiments (Andersen, 2014) are monitored with both μCT and NMR techniques. μCT experiments require the addition of dopants for the study of multiphase flow (Vinegar, 1986; Wildenschild and Sheppard, 2013). For this reason, NMR is favoured for the study of multiphase systems. Relative saturation measurements and dynamic monitoring of the secondary oil recovery have been performed with NMR (Jonathan Mitchell et al., 2012; Mitchell et al., 2013b; Ramskill et al., 2018). MRI has also been employed for the acquisition of bulk flow measurements in single and two-phase flow experiments through bead packs and sedimentary rocks (Chang and Watson, 1999; Scheven et al., 2005b; Sederman and Gladden, 2001; Verganelakis et al., 2005). Spatially-resolved flow measurements have been conducted only in single-phase flow systems and under high flow velocities (de Kort et al., 2018b).

1.3 Aims and Scope of This Thesis

This research focuses on identifying the mechanisms of oil displacement during waterflooding and chemical EOR through complex reservoir rocks using novel MRI methods. These MRI strategies are developed to spatially analyse the flow in two-phase porous systems under reservoir-representative velocities (slow flow velocities). The aim is to use the data obtained by these techniques to validate and calibrate numerical models used in DR in future work. The newly developed techniques can detect ultra-slow flow (<10 ft d^{-1}) and two-phase flow through complex rocks. In addition, the strategies for MRI data under-sampling and Compressed-Sensing (CS) reconstruction were optimised reducing the experimental time and enabling dynamic measurements. The novel techniques were tested and validated in ideal porous media (bead packs) and then in sandstones and carbonates. NMR mapped qualitatively, quantitively and dynamically all the mechanisms of immiscible flow displacement at reservoir-representative conditions. Combining the structural images with the flow data in single and two-phase systems can help the development of DR simulators for core systems of a few centimetres.

1.4 Outline of Thesis Chapters

This thesis is structured as follows:

Chapter 1 provides an overview of the EOR and the DR workflow. The benefits of using MRI in DR for structural and flow information are highlighted. The aim and the outline of this thesis are also described.

Chapter 2 underlines the basic principles of NMR and MR in structural imaging and translational motion relevant to this work.

Chapter 3 describes the under-sampling, reconstruction and denoising strategies followed in this thesis for the processing of all the imaging and flow data.

Chapter 4 presents a novel 3D spatially-resolved phase-contrast velocimetry technique and a low-resolution propagator which enable the detection of interstitial velocities lower than 10 ft d^{-1}. Both techniques are tested in a bead pack filled with 4 mm beads and water.

Chapter 5 employs these novel techniques for the analysis of the flow in one sandstone and three carbonate rocks.

Chapter 6 introduces a novel technique with optimised chemical selectivity for multiple-phase systems (water and oil). Chemically-selective images and propagators are analysed for an ideal bead pack and a carbonate rock.

Chapter 7 monitors the primary drainage of a carbonate rock via the short-wait porous plate method. NMR and pressure drop data are used to identify the mechanisms of displacement.

Chapter 8 monitors the imbibition and xanthan gum injection using chemically-selective images and propagators at ultra-slow flows. The mechanisms of displacement are identified and the oil recovery is quantified.

Chapter 9 summarises the conclusions of each chapter and suggests future research areas using the developed novel techniques.

Chapter 2 Theoretical Background

2.1 Principles of NMR

An introduction to the basic principles and the basic pulse sequences implemented in NMR is outlined in this chapter with reference to works by Blumich, (2000); Callaghan, (2014, 1991); Levitt, (2000) and Gladden, (1994), unless stated otherwise. The bold annotation is used for vectors, hence quantities which contain amplitude and direction.

2.1.1 Nuclear Apin and Zeeman Effect

Fundamental particles, such as nuclei and electrons, possess an intrinsic magnetism and according to elementary physics, they have a spin angular momentum $\boldsymbol{S}$. The magnetic moment $\boldsymbol{\mu}$ is related to the spin operator as:

$$\widehat{\boldsymbol{\mu}} = \gamma \cdot \widehat{\boldsymbol{S}}\,, \tag{2-1}$$

where γ is the gyromagnetic ratio which is equal to 2.675×10^8 rad T^{-1} s^{-1} for the proton (^{1}H) nucleus. The 'hat' is used to indicate the quantum mechanical operators. Eq.(2-1) shows that $\boldsymbol{\mu}$ and $\boldsymbol{S}$ point in the same direction. When a static magnetic field $\boldsymbol{B}_0$ is applied along the z-direction, the $\boldsymbol{\mu}$ obtains energy given by the Hamiltonian operator, $\widehat{\boldsymbol{H}}$, as:

$$\widehat{\boldsymbol{H}} = -\gamma\, \widehat{\boldsymbol{S}}\, B_0\, \boldsymbol{i_z}, \tag{2-2}$$

where B_0 is the magnitude of the static magnetic field and $\boldsymbol{i_z}$ is the unit of its direction. From the Schrödinger equation, the eigenvalue of the Hamiltonian operator when Eq.(2-2) is applied to a state ψ leads to:

$$\widehat{\boldsymbol{H}}|\psi\rangle = E|\psi\rangle = -\gamma\, B_0\, \hbar\, m_s|\psi\rangle, \tag{2-3}$$

where E is the energy of an eigenstate, ħ is the Plank's constant divided by 2π, which is equal to 1.05×10^{-34} J s rad^{-1}, and m_s is the spin quantum number which may be either integral or half-integral. Eq.(2-3) is one of the most important equations since it implies the quantization of the energy, a central phenomenon of magnetic resonance. For a proton-nucleus (^{1}H), the m_s is equal to $\pm 1/2$. Thus, this nucleus develops two energy levels, α and β, which are called eigenstates as shown in **Figure 2-1**.

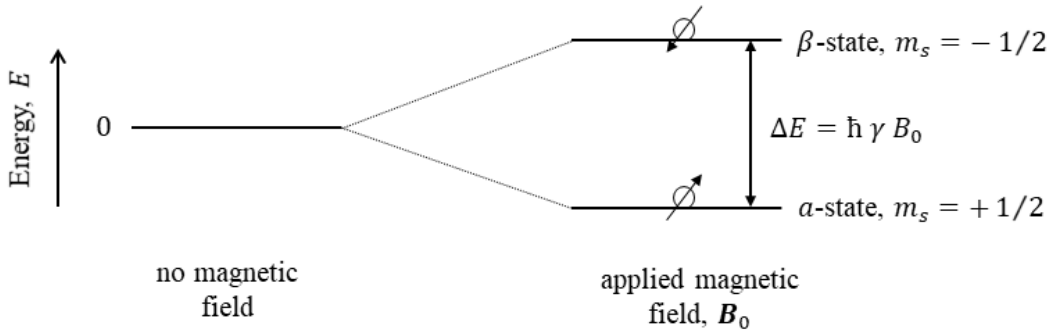

Figure 2-1: Illustration of the Zeeman splitting phenomenon for ^{1}H in the presence of an external magnetic field, $\boldsymbol{B}_0$.

The energy difference, ΔE, in ^{1}H is written as:

$$\Delta E = \hbar\,\gamma\,B_0\,. \tag{2-4}$$

2.1.2 The Bloch Vector Model

When nuclei are in thermodynamic equilibrium, all individual spins occupy the abovementioned eigenstates following the Boltzmann distribution given by:

$$\frac{N_\beta}{N_\alpha} = \exp\left(-\frac{\Delta E}{k_B T}\right), \tag{2-5}$$

where N_α and N_β are the number of spins in α and β eigenstates, respectively, k_B is the Boltzmann constant (1.38×10^{-23} J K^{-1}) and T is the absolute temperature. For a very small energy difference ΔE, a surplus of individual $\boldsymbol{\mu}$ is expected at the lower energy-demanding state α. This distribution of $\boldsymbol{\mu}$ can be visualised as a series of magnetic moments randomly distributed around a precessional cone as shown in **Figure 2-2**.

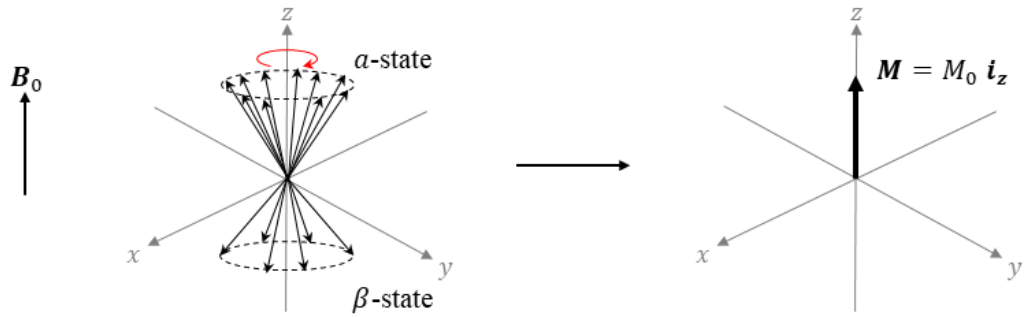

Figure 2-2: Illustration of the Bloch vector model. The red arrow indicates the direction of the precession of the individual magnetic moments $\boldsymbol{\mu}$ in the α and β eigenstate. At thermodynamic equilibrium, the net magnetisation vector $\boldsymbol{M}$ is aligned along the direction of the static magnetic field $\boldsymbol{B}_0$.

This spin population difference between the energy levels gives rise to a net macroscopic nuclear magnetic polarization $\boldsymbol{M}$ which is aligned along the direction of the $\boldsymbol{B}_0$ field. More precisely, $\boldsymbol{M}$ derives from the summation of the all $\boldsymbol{\mu}$ distributed between the two eigenstates. Using Eq.(2-1), the magnetisation in the α-state is equal

to $N_\alpha\,\gamma\,\widehat{\boldsymbol{S}}_\alpha$, while the magnetisation in the β-state is equal to $N_\beta\,\gamma\,\widehat{\boldsymbol{S}}_\beta$, where $\widehat{\boldsymbol{S}}_\alpha$ and $\widehat{\boldsymbol{S}}_\beta$ are the operators of the spin angular momentums in the two states. The eigenvalue of each operator is equal to $\hbar \cdot m_s$ (Gunther, 2013). Hence, the $\boldsymbol{M}$ is written as:

$$\boldsymbol{M} = \sum \boldsymbol{\mu} = \left(N_\alpha - N_\beta\right) \frac{\gamma\,\hbar}{2}\,\boldsymbol{i_z}. \tag{2-6}$$

2.1.3 Larmor Frequency

According to the classical equation of motion when $\boldsymbol{\mu}$ is immersed in $\boldsymbol{B}_0$, it experiences a torque equal to $\boldsymbol{\mu} \times \boldsymbol{B}_0$. This torque is equal to the rate of change of its $\boldsymbol{S}$ and is given by:

$$\frac{d\boldsymbol{S}}{dt} = \boldsymbol{\mu} \times \boldsymbol{B}_0. \tag{2-7}$$

After Eq.(2-1), Eq.(2-7) can be written as:

$$\frac{d\boldsymbol{\mu}}{dt} = \gamma\,\boldsymbol{\mu} \times \boldsymbol{B}_0. \tag{2-8}$$

Eq.(2-8) is known as the Felix-Bloch equation and it is one of the most important equations in NMR experiments. Eq.(2-8) demonstrates that when an individual $\boldsymbol{\mu}$ interact with $\boldsymbol{B}_0$, it starts a precessional motion illustrated in Figure 2-2 until it gets aligned with $\boldsymbol{B}_0$ field. This precession occurs with an angular frequency (in rad s^{-1}) defined as:

$$\boldsymbol{\omega}_0 = -\gamma\,\boldsymbol{B}_0, \tag{2-9}$$

or in the frequency units of Hz as:

$$\boldsymbol{f}_0 = -\frac{\gamma}{2\,\pi}\,\boldsymbol{B}_0\,. \tag{2-10}$$

This frequency of precession is known as the Larmor frequency. The Felix-Bloch equation for the $\boldsymbol{M}$ can be written as:

$$\frac{d\boldsymbol{M}}{dt} = \gamma\,\boldsymbol{M} \times \boldsymbol{B}_0\,. \tag{2-11}$$

Eq.(2-11) is very useful for the analysis of the effect of a time-varying magnetic field such as a pulse on the net magnetisation $\boldsymbol{M}$, which is futher desctibed below.

2.1.4 NMR Experiment

The NMR system consists of a magnet which generates the $\boldsymbol{B}_0$ field. The sample is placed inside a cylindrical probe equipped with radio-frequency (r.f.) circuits for excitation with r.f. waves and detection of the r.f. emissions. In some cases, the probe is equipped with additional coils which generate spatially varying magnetic fields.

These additional coils are employed in the MRI. Moreover, the probe contains additional coils known as the shims. These coils are used to correct the magnetic field inhomogeneities. Finally, the magnet and the performance of the r.f. coils are controlled by a central computer system (Farrar and Becker, 1971; Gunther, 2013).

2.1.4.1 Spin Excitation and the Rotating Frame

Signal detection in NMR experiments is based on the perturbation of the system from the equilibrium state. Energy is induced to the NMR system in the form of a sinusoidal current produced by the r.f. transmitter coil. This oscillating r.f. field, $\boldsymbol{B}_1$, is known as the r.f. pulse. By Faraday's law of induction and after Euler's equation, $\boldsymbol{B}_1$ in the laboratory frame (x, y, z) is described by:

$$\boldsymbol{B}_1(t) = B_1 \cos(\omega_1 t)\, \boldsymbol{i}_x + B_1 \sin(\omega_1 t)\, \boldsymbol{i}_y. \tag{2-12}$$

where B_1 is the magnitude and ω_1 is the angular frequency of rotation of the $\boldsymbol{B}_1$ field. Eq.(2-12) indicates that $\boldsymbol{B}_1$ on the laboratory frame can be viewed as two counter-rotating components of the same amplitude B_1 and frequency ω_1.

To better explain the precession of the $\boldsymbol{M}$, a new coordinate system called the rotating frame (x', y', z') is introduced. The so-called $\boldsymbol{B}_1^+$ is viewed as stationary in the rotating frame when it is on-resonance with $\boldsymbol{B}_0$ as presented in **Figure 2-3**(a) and it follows the precession of the $\boldsymbol{M}$. The condition $\omega_0 = \omega_1$ is needed to disturb $\boldsymbol{M}$ from its equilibrium state. Assuming that the r.f. pulse is applied only for t_p time, the $\boldsymbol{M}$ is moved out from the z'-axis by a flip angle, θ, given:

$$\theta = \omega_1 t_p = \gamma B_1 t_p. \tag{2-13}$$

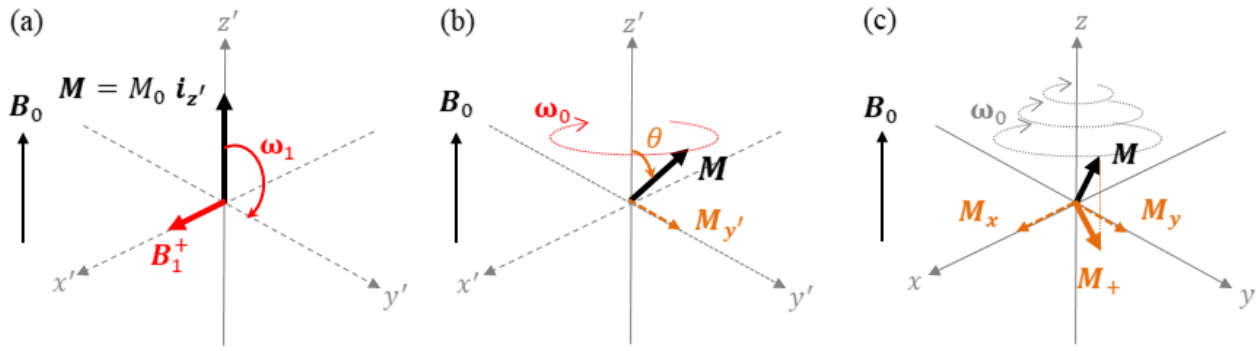

Figure 2-3: Illustration of the effect of $\boldsymbol{B}_1$ on $\boldsymbol{M}$.(a) On resonance, the $\boldsymbol{B}_1^+$ component of the initial $\boldsymbol{B}_1$ field appears static on the rotating frame. (b) When the $\boldsymbol{B}_1^+$ is turned off after t_p, the $\boldsymbol{M}$ is tilt out from the z'-axis by a flip angle θ and it precesses with $\boldsymbol{\omega}_0$.(c) The precession of the flipped $\boldsymbol{M}$ is then viewed in the laboratory frame under the effect of $\boldsymbol{B}_0$. The transverse component $\boldsymbol{M}_+$ rotates with $\boldsymbol{\omega}_0$ and it gets detected by the receiver coil.

The signal is generated by the precession of the flipped $\boldsymbol{M}$ through the receiver coil. In **Figure 2-3**(c), the flipped $\boldsymbol{M}$ precesses with a Larmor frequency $\boldsymbol{\omega}_0$ in the laboratory frame under the effect of the $\boldsymbol{B}_0$ static field. The signal is generated by

detecting the precession of the transverse magnetisation component $\boldsymbol{M}_+$ in the laboratory frame.

2.1.4.2 Hard and Soft Pulses

When $\boldsymbol{B}_0$ and $\boldsymbol{B}_1^+$ are 'on-resonance' the so-called r.f. 90º pulse flips the magnetisation by a θ equal to $\pi/2$. Respectively, the so-called 180º pulse, which is also known as refocusing pulse, flips the magnetisation by a θ equal to π. If the 90º pulse has a short duration, typically in the order of microseconds, it can excite the entire range of Larmor frequencies in the sample. This type of pulse is called a hard or non-selective pulse. If the 90º pulse has a larger duration but a smaller amplitude B_1, it will excite only a narrow range of frequencies Δf_p. These pulses are referred to as soft or selective pulses and they are employed for slice selection or signal suppression. The Δf_p excited by a Gaussian pulse of a t_p duration is defined as:

$$\Delta f_p = \frac{4}{\pi\, t_p}. \tag{2-14}$$

2.1.4.3 Signal detection

Laboratory spectrometers are usually equipped with receiver coils at the x-y plane. This is why only the transverse $\boldsymbol{M}_+$ component can induce an oscillating r.f. current at ω_0 which is known as Free Induction Decay (FID) (**Figure 2-4**(a)). Both M_y and M_x components of the transverse magnetisation, presented in **Figure 2-3**(c), are combined in a complex notation:

$$M_+(t) = M_x(t) + i\, M_y(t) \tag{2-15}$$

The quadrature detector combines the NMR signal of Larmor frequency ω_0 with a reference signal of frequency ω_{ref}, a process known as signal frequency conversion. A signal, $S_r(t)$, which oscillates with an offset Larmor frequency, $\Delta\omega = \omega_0 - \omega_{ref}$, is generated and is given by:

$$S_r(t) \propto M_0\, sin\theta\; e^{i\,\Delta\omega\, t}\; e^{i\,(\varphi_s + \Delta\omega\, \Delta t_s)} \tag{2-16}$$

where M_0 is the highest amplitude of the magnetisation along the z-axis, φ_s is the instrumental phase offset and Δt_s is the signal delay due to signal propagation through various electronic devices or due to finite-length r.f. pulses. The $S_r(t)$ is multiplied by $\exp\{-i\,(\varphi_s + \Delta\omega\, \Delta t_s)\}$, a process known as phase correction. The phase-corrected signal $S(t)$ is then Fourier Transformed (FT) yielding the NMR spectrum, $S(\omega)$. The real part of the $S(\omega)$ follows a Lorentzian distribution with a peak at the sample resonant frequency ω_0 as presented in **Figure 2-4**(b). The NMR spectrum is described by the following equation:

$$S(\omega) = \int_0^{\infty} S(t)\, e^{i\omega t} dt. \tag{2-17}$$

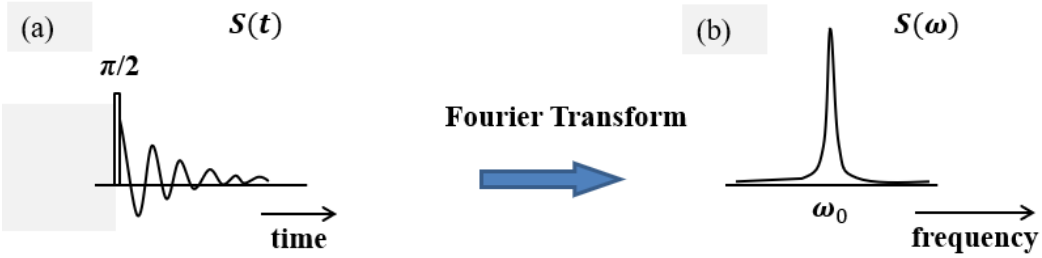

Figure 2-4: Schematic of the free induction decay at a single frequency (FID) after the implementation of a pulse (a) and the real part of the resultant NMR spectrum after FT (b).

2.1.4.4 Chemical Sensitivity

As described above, the resonance frequencies are measured relative to the frequency of a reference sample. Local magnetic fields in a submolecular scale vary due to the distribution of the electron cloud. Hence, in the same molecule, nuclei at two sites can experience a different electronic environment and precess at different frequencies. This effect is known as chemical shift and it is an extremely important tool in NMR since it can provide information regarding the electronic structure of a molecule. In NMR, the reference sample is usually the tetramethyl silane (TMS), and the chemical shift values, δ, in parts per million (ppm) are defined as:

$$\delta = \frac{f - f_{TMS}}{f_{TMS}} \times 10^6\,, \tag{2-18}$$

where f_{TMS} is the frequency of the TMS and f is the frequency of the nucleus of interest.

2.1.5 Relaxation Mechanisms

When a system of spins is distorted from its equilibrium state, it is trying to recover to its initial state following a process known as relaxation. The Bloch-Torrey equation that describes the effect of $\boldsymbol{B}_1$ on $\boldsymbol{M}$ and its relaxation in its equilibrium state is given by:

$$\frac{d\boldsymbol{M}(t)}{dt} = \gamma\, \boldsymbol{M}(t) \times \boldsymbol{B}_1(t) - \boldsymbol{R}\,[\boldsymbol{M}(t) - \boldsymbol{M}_0] \tag{2-19}$$

where $\boldsymbol{M}_0$ is the magnetisation vector along the z, z'-axis and $\boldsymbol{R}$ is the relaxation matrix containing the longitudinal T_1 (along z-axis) and the transverse T_2 (on the x, y-plane) relaxation times. The term $\boldsymbol{R}\,[\boldsymbol{M}(t) - \boldsymbol{M}_0]$ represents the establishment of the thermodynamic equilibrium with time. The T_1, T_2 and T_2^* relaxations are the most common types of NMR relaxation. These time constants and the effect of local susceptibilities are further analysed with reference to works by Callaghan (2014) and Mitchell et al., (2010) except stated otherwise.

2.1.5.1 Spin-Lattice Relaxation

The longitudinal or spin-lattice relaxation is described by the characteristic time T_1 (Bloembergen et al., 1948). Solving Eq.(2-19) for the magnetisation component along the z-axis, M_z, after the implementation of a $\boldsymbol{B}_1$ field gives:

$$\frac{dM_z(t)}{dt} = -\left(\frac{M_z(t) - M_0}{T_1}\right) \tag{2-20}$$

Two of the most popular techniques used for the T_1 estimation are the inversion recovery and the saturation recovery. The inversion recovery sequence is described in **Figure 2-5**(a). M_z is studied under a range of t_{VD} and the detected signal is shown in **Figure 2-5**(b). The curve of the detected signal is given by:

$$M_z(t)/M_0 = 1 - 2\exp\left(\frac{t}{T_1}\right). \tag{2-21}$$

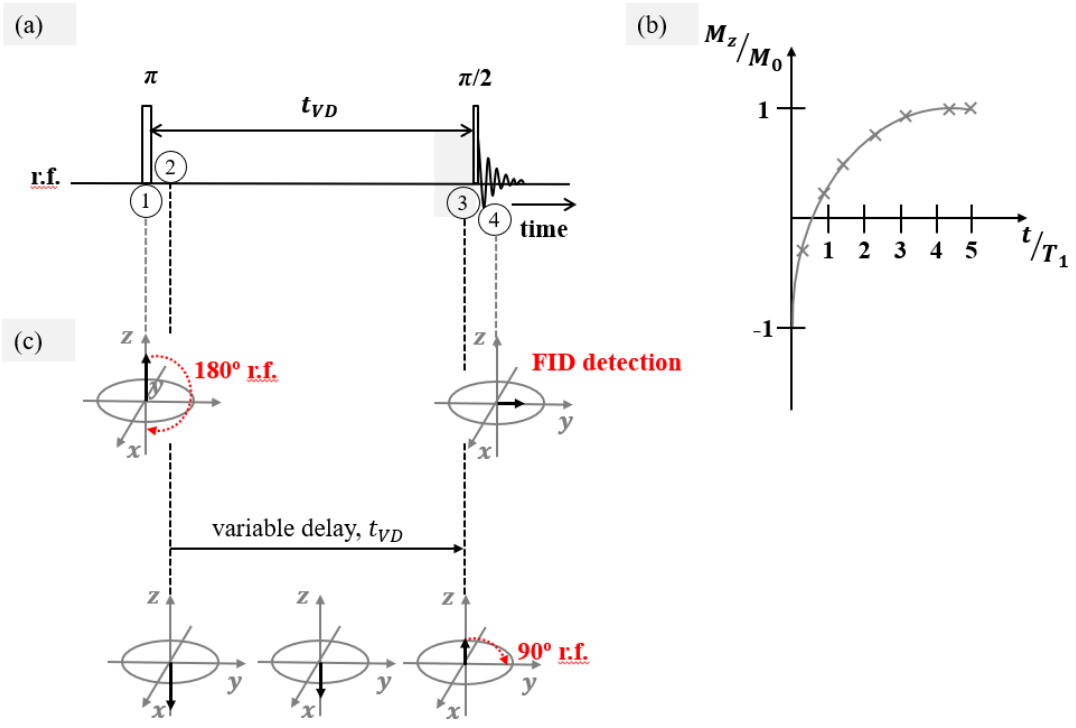

Figure 2-5: Schematic of the T_1 inversion recovery pulse sequence (a). Illustration of the signal development from the application of the inversion recovery sequence (b). Illustration of the ***M*** change during the inversion recovery sequence (c).

T_1 measurement offers a guideline for the assessment of the optimum t_{RD} since ***M*** requires at least $5 \times T_1$ until it returns to its equilibrium state.

2.1.5.2 Spin-Spin Relaxation

Transverse relaxation demonstrates the loss of phase coherence among spins and is characterised by the T_2 spin-spin relaxation time constant. The most common technique for T_2 measurement is the modified Carr-Purcell-Meiboom-Gill (CPMG) (Carr and Purcell, 1954; Meiboom and Gill, 1958) presented in **Figure 2-6**. The pulse sequence starting with the implementation of the 90º pulse until the formation of the first echo is also known as the spin-echo pulse sequence.

Solving Eq.(2-19) for the magnetisation component in the x, y-plane, the rate of change of the transverse magnetisation, M_+, is defined as:

$$\frac{dM_+(t)}{dt} = -\frac{M_+(t)}{T_2} \tag{2-22}$$

The solution of Eq.(2-22) for the initial condition $M_+(t=0) = M_0$, leads to:

$$M_+(t)/_{M_0} = exp\left(-\frac{t}{T_2}\right). \tag{2-23}$$

In a CPMG experiment, a full signal decay is acquired for a constant echo time, t_{echo}, but a variable number of echoes, N_{echo}. In petrophysics, since the T_2 relaxation time is very short, a single-shot CPMG experiment is routinely used. In the single-shot CPMG one complex point in every echo is sampled, hence the N_{echo} after which a full signal decay occurs is observed (Mitchell, 2014).

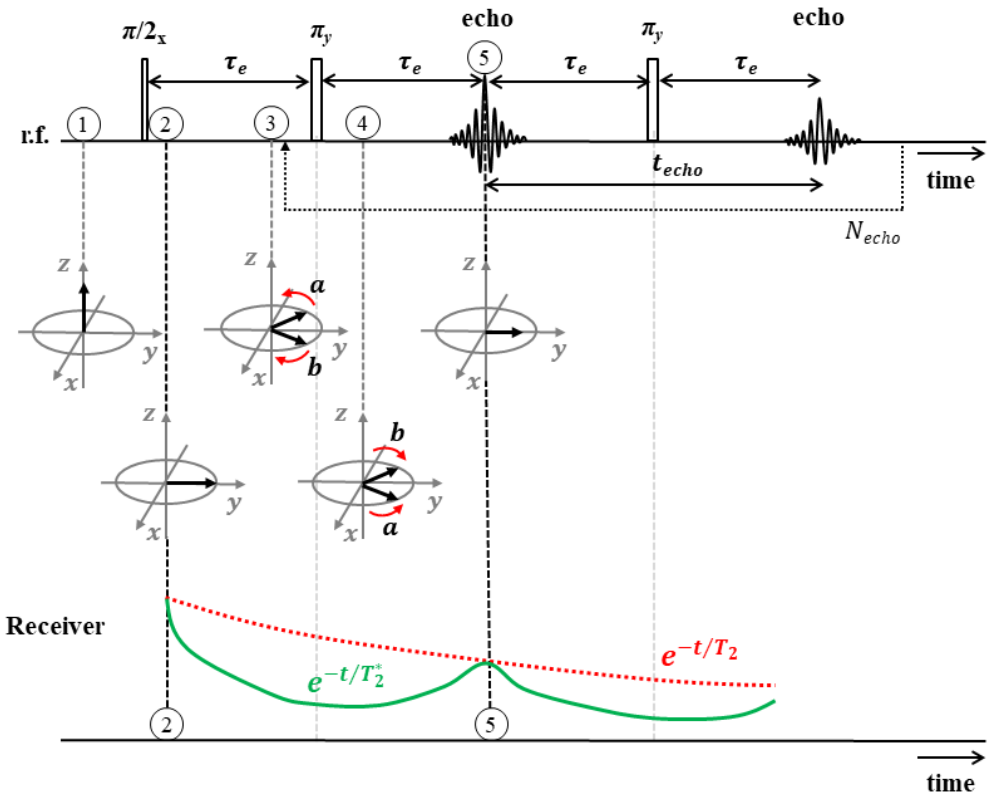

Figure 2-6: Schematic representation of the CPMG spin-echo pulse sequence, the evolution of the ***M*** and the change in the signal intensity detected by the receiver if the full evolution of the magnetisation was recorded.

In all the spin-echo sequences, t_{echo} is equal to twice the inter-echo time, τ_e and it cannot be shorter than 50 times the duration of the 90° pulse.

T_2^* is the effective spin-spin relaxation and it is prone to inhomogeneities of the $\boldsymbol{B}_0$ field (Hahn, 1950). As shown in **Figure 2-6**, if the precession of the isochromats after the implementation of the 90_x^o pulse is measured, an FID signal decaying with T_2^* time constant would be detected. T_2^* can be measured with the simple pulse-acquire sequence presented in **Figure 2-7**. T_2^* is measured from the Full Width at Half Maximum (FWHM) of the $S(\omega)$ as:

$$T_2^* = \frac{1}{\pi \text{ FWHM}}. \tag{2-24}$$

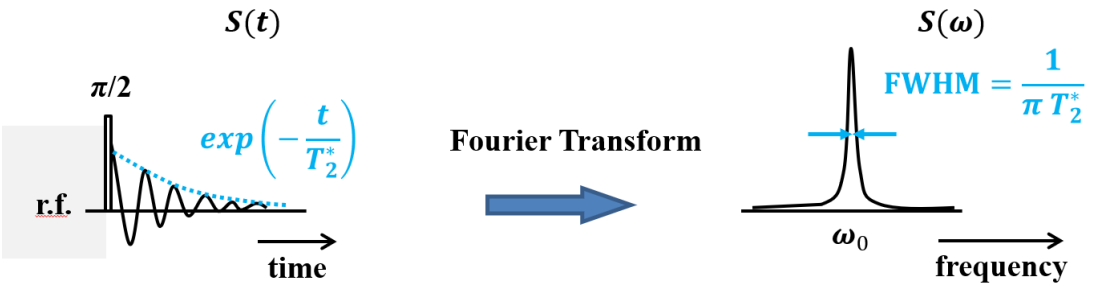

Figure 2-7: Schematic of the FID after the implementation of a 90º pulse showing the T_2^* decay and the resultant NMR spectrum after Fourier Transformation showing the calculation of the T_2^* from the FWHM.

Eq.(2-24) shows that the T_2^* is susceptible to any distortion which can cause line broadening of the real part of the $S(\omega)$. More details regarding these distortions follow below.

2.1.5.3 Relaxation in Porous Media

The relaxation of a fluid inside a porous media can be described by a general physical model. According to this model, the relaxation process is governed by the intrinsic bulk fluid process, the interaction between pore-wall and fluid (surface relaxation) and the diffusion in the presence of internal gradients (Kleinberg et al., 1993). Neglecting, for now, the effect of the internal gradients, both T_1 and T_2 relaxations can be written as:

$$\frac{1}{T_{1,2}} = \frac{1}{T_{1,2bulk}} + \rho_{1,2}\frac{S_p}{V_p}, \tag{2-25}$$

where $T_{1,2bulk}$ is the relaxation of the bulk fluid, $\rho_{1,2}$ is the surface relaxivity. For most fluids, their intrinsic bulk relaxation is much longer compared to their relaxation inside a porous medium ($T_{1,2} \ll T_{1,2bulk}$). The bulk relaxation is controlled by fluid properties such as chemical composition, viscosity, density and temperature (Schön, 2015). The second term represents the relaxation of the fluid molecules adsorbed on the surface.

The relaxation on the surface is divided into two separate processes; the relaxation which occurs at all sites of the surface and the relaxation associated with paramagnetic ion metals of the pore wall, as presented in **Figure 2-8**. The presence of paramagnetic ions in the neighbourhood of protons produces local magnetic fields which are known as 'internal gradients'. The strong gradients generate susceptibility contrast, $\Delta\chi$, between the fluid and the pore wall. These $\Delta\chi(\boldsymbol{r})B_0$ fluctuations can lead to signal attenuation due to diffusion. The measured T_2 relaxation in the presence of internal gradients is also referred as $T_{2,eff}$.

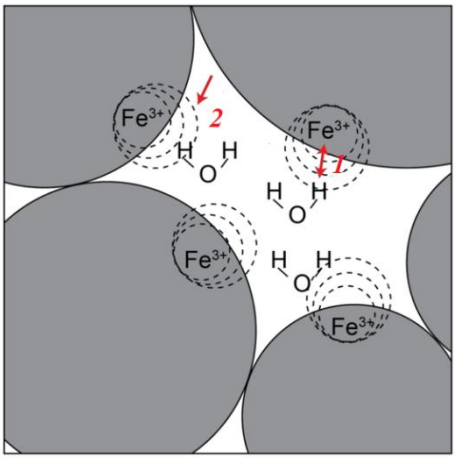

Figure 2-8: Illustration of two mechanisms of the relaxation process in porous media. Gray represents the mineral grains. The interaction of the water molecules confined in a pore body with the paramagnetic centre of the pore wall position is shown at position (1). Diffusion of water molecules due to local magnetic susceptibility at position (2). Adjusted from Daigle et al., (2014).

$\Delta\chi(\boldsymbol{r})B_0$ have a severe effect on the linewidth of the NMR spectrum. Considering ΔB_0 as the inherent inhomogeneity of the applied $\boldsymbol{B}_0$ field, the T_2^* can be written as:

$$\frac{1}{T_2^*} = \frac{1}{T_2} + \gamma\,\Delta\chi\,B_0 + \gamma\,\Delta B_0\,. \qquad (2\text{-}26)$$

When $\boldsymbol{B}_0$ is higher than 5 MHz, the effect of internal gradients is significant.

2.2 Basic Principles of MRI

As was explained above, NMR relaxation techniques obtain properties coming from the whole volume of the sample, whereas MRI enables the acquisition of spatially-resolved information. An overview of MRI theory is provided with references found in Blumich, (2000); Callaghan, (2012); Gladden, (1994) and M. A. Bernstein et al., (2004).

2.2.1 Magnetic Field Gradients

Spatial information can be encoded into the magnetisation by applying a linearly varying magnetic field, the so-called gradient field, $\boldsymbol{G}$, in addition to the main $\boldsymbol{B}_0$. The three gradient functions of frequency encoding, phase encoding and slice selection achieve spatial localisation and are further explained below.

2.2.1.1 Slice Selection Gradients

Slice-selection gradients are used in parallel with soft pulses to achieve the desired spatial localisation. The slice-selection gradient is typically a constant gradient of amplitude G_{slice} which spreads out the resonate spin frequencies along the direction of the gradient. The slice-selection gradient relates Δf_p to the desired image slice of thickness Δz as:

$$\Delta z = \frac{2\pi\, \Delta f_p}{\gamma\, G_{slice}}. \tag{2-27}$$

This equation shows that for a fixed soft pulse, thinner slices can be acquired by increasing the magnitude of the slice-selection gradient.

2.2.1.2 Frequency Encoding

The frequency encoding gradient encodes the spatial information by spatially varying the frequency of precession. The unique frequency of precession assigned to a spin at the vector position $\boldsymbol{r}$ is given by:

$$\omega(\boldsymbol{r}) = \gamma B_0 + \gamma \boldsymbol{G} \cdot \boldsymbol{r}. \tag{2-28}$$

Eq.(2-28) shows that the frequency information contained in the $S(\omega)$ is linearly related to the spatial information along the $\boldsymbol{G}$ direction as presented in **Figure 2-9**.

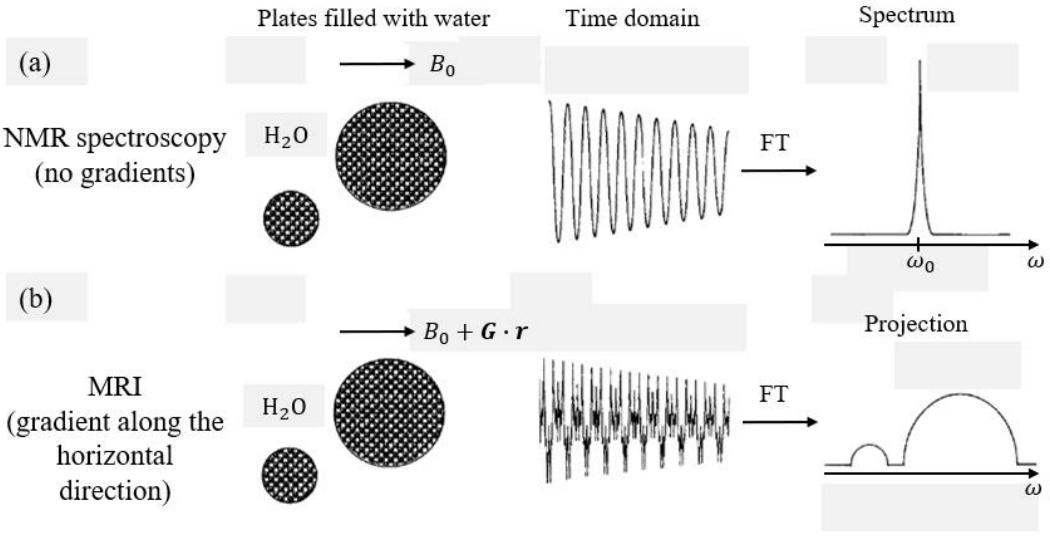

Figure 2-9: Schematic representation of a frequency encoding gradient applied on a system of two plates filled with water. When there is no magnetic field gradient, the time variation of the signal and its Fourier transform are presented in (a). The NMR spectrum will consist of one peak at the Larmor frequency, ω_0. When a magnetic field gradient $\boldsymbol{G}$ is applied along the horizontal position $\boldsymbol{r}$, the Larmor frequenct becomes dependent on the system's position in the standard domain as shown in (b). The resulting frequency signal is called projection or 1D profile of the spin density. Adjusted from Bernstein et al., (2004).

Figure 2-9(a) shows the conventional case of a system placed in a uniform magnetic field $\boldsymbol{B}_0$. The FID as well as its FT do not present any spatial information. The

spectrum is resonated at ω_0. When $\boldsymbol{G}$ is applied as shown in **Figure 2-9**(b), the spatial information becomes linearly related to the frequency of precession and the FID signal presents a range of resonance frequencies. **Figure 2-9** is a good schematical representation showing the difference between the NMR spectroscopy and the MRI.

2.2.1.3 Phase Encoding

Phase encoding is achieved by implementing a gradient lobe when the magnetisation is in the transverse plane to create a linear spatial variation of the phase of the magnetisation as shown in **Figure 2-10**.

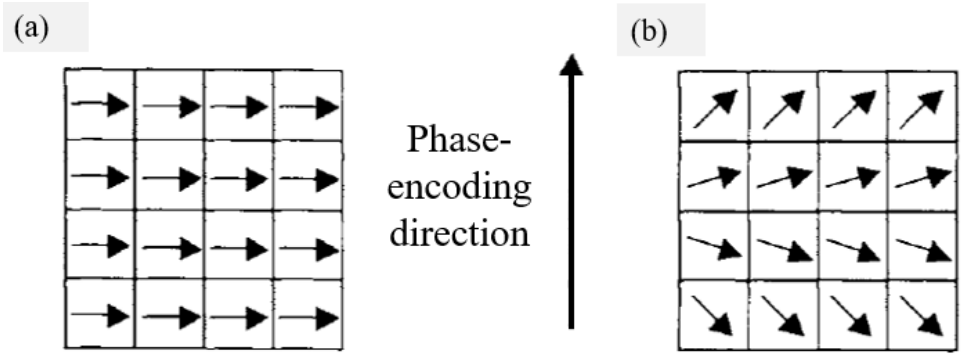

Figure 2-10: The local spins on the transverse plane are represented by arrows at the centre of 16 pixels (a). After the implementation of a 90º pulse, the isochromats have the same direction in each pixel and the magnetisation vector has its maximum amplitude. (b) Then, the phase-encoding gradient introduces phase variation at each pixel along the phase-encoded direction. Adapted from Bernstein et al., (2004).

The phase gradient $\boldsymbol{G}$ of duration t, adds a local phase evolution (in radians), $\varphi(\boldsymbol{r}, t)$, to the transverse M_+ given by:

$$\varphi(\boldsymbol{r}, t) = \gamma\, \boldsymbol{r}\, \cdot \boldsymbol{G}\, t, \tag{2-29}$$

Assuming that relaxation and diffusion effects are negligible and the system is on-resonance in the concept of the rotating frame, the detected signal is written as:

$$M_+(\boldsymbol{r}, t) = \rho(\boldsymbol{r})\, e^{i\, \varphi(\boldsymbol{r},t)}, \tag{2-30}$$

where $\rho(\boldsymbol{r})$ is the local magnetisation density at $\boldsymbol{r}$**,** which can also be written as $M_+(\boldsymbol{r}, 0)$. In the case of a 3D MRI experiment, the signal element, dS, coming from a volume dV at position $\boldsymbol{r}$ is proportional to the $\rho(\boldsymbol{r})$ and can be written as:

$$dS(\boldsymbol{r}, t) \propto \rho(\boldsymbol{r})\, e^{i\, \varphi(\boldsymbol{r},t)}\, dV. \tag{2-31}$$

Neglecting the constant of proportionality, $S(t)$ is given by the sum of signals originating from the nuclei at all positions $\boldsymbol{r}$ and is determined as:

$$S(t) = \iiint \rho(\boldsymbol{r})\, e^{i\,\varphi(\mathbf{r},t)}\, d\boldsymbol{r}, \tag{2-32}$$

where $d\boldsymbol{r}$ represents volume integration and is used instead of $dx\ dy\ dz$. In most MR experiments, the phase encoding is used with the cartesian **k**-space sampling to acquire spatially-resolved information and is applied orthogonally to the frequency-encoded direction as will be described below.

2.2.2 k-Space

From the early days of the MRI, $S(t)$ was related to trajectories that evolve in the 2D or 3D space using the FT. The FT variables were given the symbol **k** and the 2D or 3D domain of trajectories was called **k**-space. As first stated by Mansfield and Grannell, (1973), in analogy with the physics of diffraction the reciprocal space vector **k** (in m^{-1}) is given by:

$$\mathbf{k} = \frac{\gamma}{2\,\pi}\, \boldsymbol{G}\, t. \tag{2-33}$$

Comparing Eq.(2-29) with Eq.(2-33), it can be deduced that the vector **k** can be written as the spatial rate of change in the phase accumulated by the stationary spins as a result of the applied gradients. In other words, the vector **k** can be defined as:

$$\mathbf{k} = \frac{1}{2\,\pi}\, \boldsymbol{\nabla_r}\varphi(\boldsymbol{r}, t). \tag{2-34}$$

Incorporating Eq. (2-34) in Eq. (2-32), the acquired NMR signal in the **k**-space domain, $S(\mathbf{k})$, is defined as the Fourier transform of the local spin density $\rho(\boldsymbol{r})$, written as:

$$S(\mathbf{k}) = \iiint \rho(\boldsymbol{r}) e^{i2\pi\mathbf{k}\cdot\boldsymbol{r}}\, d\boldsymbol{r}. \tag{2-35}$$

Implement an inverse Fourier transform on the $S(\mathbf{k})$, the local magnetisation density at location $\boldsymbol{r}$ is given by:

$$\rho(\boldsymbol{r}) = \iiint S(\mathbf{k}) e^{-i2\pi\mathbf{k}\cdot\boldsymbol{r}}\, d\boldsymbol{r} \tag{2-36}$$

showing that $S(\mathbf{k})$ and $\rho(\boldsymbol{r})$ are a mutually conjugate Fourier transform pair.

2.2.3 Nyquist Theorem

According to the Nyquist theorem, the spectrum of a discretely sampled signal is replicated in the Fourier conjugate domain. In other words, if the signal is sampled at a dwell time Δt, the Fourier transform of the sampled signal is replicated at intervals $1/\Delta t$. If the frequency bandwidth of the spectrum, f_s, is greater than $1/\Delta t$, signal aliasing will occur since the replicates will overlap. Signal aliasing can be prevented by windowing the spectrum bandwidth before sampling so that $f_s \leq 1/\Delta t$. The

threshold frequency of $1/\Delta t$ is also known as Nyquist frequency (Hennig, 1999; Nyquist, 1928).

The Nyquist theorem is applied in both the phase and the frequency-encoding domain. The interval of readout points in the **k**-space domain, Δk, is related to the temporal Nyquist sampling requirements as:

$$\Delta k = \frac{1}{\mathrm{FOV}}. \tag{2-37}$$

where FOV is the Field-Of-View in the real space domain. In the frequency-encoding domain, Δt is also known as the duration of each step in the readout lobe. In this case, the Nyquist theorem is expressed as:

$$\mathrm{FOV}_{\mathrm{freq}} = \frac{2\,\pi}{\gamma\, G\, \Delta t}, \tag{2-38}$$

while in the phase-encoding domain the Nyquist theorem is described as:

$$\mathrm{FOV}_{\mathrm{phase}} = \frac{2\,\pi}{\gamma\, \Delta G\, t}, \tag{2-39}$$

where ΔG is the amplitude and t is the duration of the $\boldsymbol{G}$ phase-encoding gradient. If the Nyquist theorem is breached in the phase domain, replicates of the sample will appear in the image. To avoid these wrap-around artefacts the phase-encoding gradient lobe has the same shape (in this thesis trapezoid) and duration in each step.

2.2.4 Resolution in MRI

N_k phase-encoding gradients of different amplitudes need to be used to obtain N_k points along its direction. The full extent of the **k**-space will be described by:

$$N_k \cdot \Delta k = 2\, k_{max} = \frac{N_k}{\mathrm{FOV}} = \frac{1}{\Delta l} \tag{2-40}$$

where k_{max} is the Fourier conjugate **k**-data obtained using the gradient of largest amplitude and Δl is the image resolution, in other words, the pixel size after FT. N_k is also called matrix size along the direction of the chosen FOV. High values of Δl mean low spatial resolution.

The coordinates in the **k**-space domain depend on the phase angle as shown in Eq.(2-34). As a consequence, the maximum achievable resolution in an MRI acquisition is limited not only by the specifications of the MRI system but also by mechanisms that affect the phase of the signal (Hennig, 1999). Some physical properties that influence the phase of the signal are the T_2^* relaxation, the local magnetic susceptibilities $\Delta\chi(\boldsymbol{r})$ and the diffusion through internal gradients. These physical properties cause broadening of the linewidth and signal attenuation. More information regarding the effect of these physical properties on the resolution can be found in the literature (Gladden, 1994).

2.2.5 k-Space Trajectories

In most clinical applications, the **k**-space is visualised as a rectangular and normally even square grid in which each dot represents a sampling point in the **k**-space. All the lines in the raster, also known as Cartesian raster, are parallel and equidistant in the **k**-space. The Cartesian raster of an even number of equidistant **k**-space data enables the use of fast FT (FFT) which reduces the reconstruction time of an image. The **k**-space trajectory is the path formed by **k**-points and it illustrates the acquisition strategy. The first 'vehicle' for travelling along each line of the **k**-space is the frequency-encoding sequence. The second 'vehicle' for travelling between lines is the phase-encoding gradient lobe.

2.2.6 RARE

One of the most used techniques in this thesis is the RARE sequence (Hennig et al., 1986). RARE employs an r.f. excitation pulse followed by a train of refocusing pulses which produce a train of spin echoes. Each spin echo is spatially-resolved so that multiple **k**-space lines are sampled.

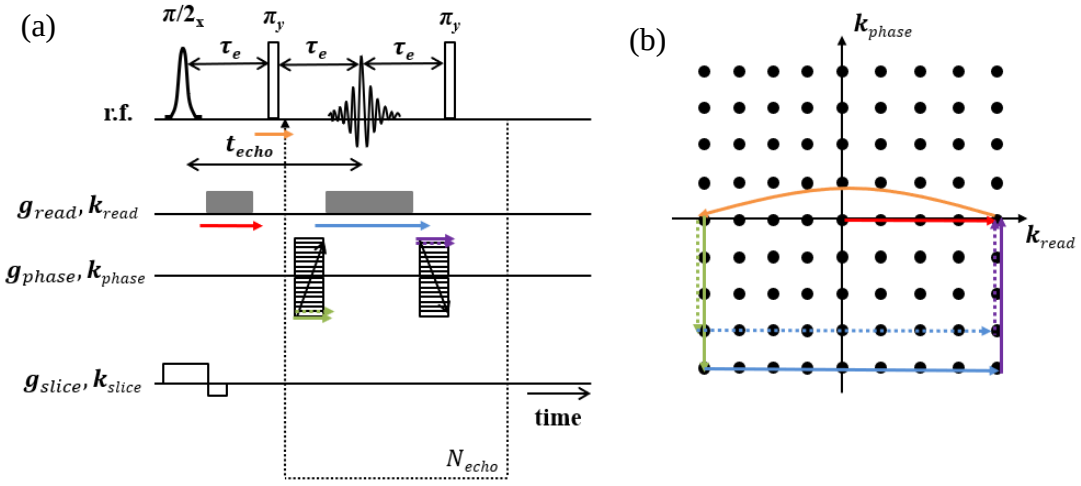

Figure 2-11: Schematic representation of the 2D RARE sequence (a) and the Cartesian raster showing the **k**-space trajectories transversed and sampled during the data acquisition (b). A soft 90º pulse is applied in parallel with a $\boldsymbol{g}_{slice}$ slice-selective gradient to flip the magnetisation within the selective slice into the transverse plane. Then, the prephasing lobe of the frequency-encoding sequence ($\boldsymbol{g}_{read}$; red arrow) is applied moving the magnetisation to the right-hand side of the raster at $(+k_{read,max}, 0)$. Then, a refocusing pulse (orange arrow) inverts the magnetisation to the left-hand side of the raster at $(-k_{read,max}, 0)$. The first phase-encoding gradient ($\boldsymbol{g}_{phase}$; green arrow) moves the magnetisation at the bottom left-hand corner of the raster at $(-k_{read,max}, -k_{phase,max})$. The bottom **k**-space line is sampled by implementing a readout frequency-encoding gradient ($\boldsymbol{g}_{read}$; blue arrow) along the first echo and then the second phase-encoding gradient ($\boldsymbol{g}_{phase}$; purlple arrow) of same amplitude but opposite polarity compared to the first, returns the magnetisation at the right-hand side of the raster at $(+k_{read,max}, 0)$. At this point the second 180º pulse is applied and the same process is repeated for a pair of bipolar phase-encoding gradients of smaller amplitude ($\boldsymbol{g}_{phase}$; green and purple dotted arrow). The second echo of lower intensity is sampled using a readout frequency-encoding gradient ($\boldsymbol{g}_{read}$; blue dotted arrow) and the process is repeated until N_{echo} **k**-space lines are sampled. The intensity difference between consecutive echoes in the formed echo train illustrates the T_2 decay. The echo time t_{echo} is defined as twice the interecho time τ_e.

Figure 2-11 illustrates how the frequency-encoding, phase-encoding and slice-selective gradients are combined to sample quickly the full **k**-space in a Cartesian raster in the 2D RARE sequence.

In the case of a 3D acquisition, the soft excitation pulse is replaced by a hard 90º pulse and the slice-encoding gradient is replaced by one phase-encoding gradient g_{phase2}. The 3D RARE sequence used in all the imaging experiments of this thesis is shown in **Figure 2-12**.

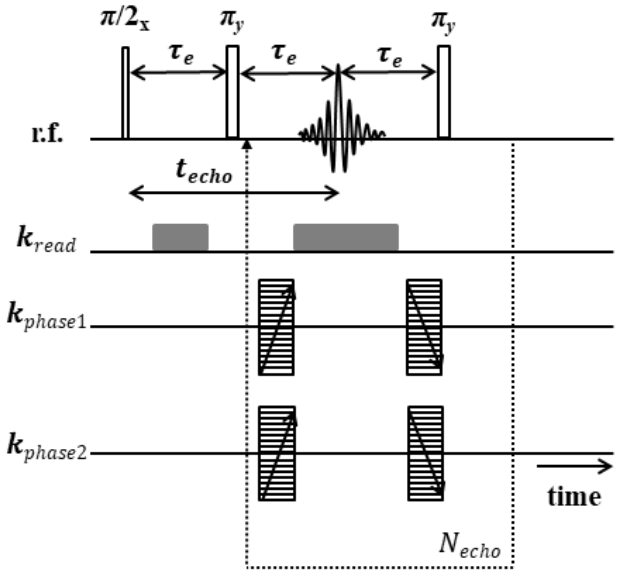

Figure 2-12: Schematical representation of the 3D RARE pulse sequence.

2.2.6.1 Suppression of the Artefacts Arising from the RARE Sequence

The echoes produced during the train of refocusing pulses are generally not in phase due to system imperfections such as nonideal 180º pulses or eddy currents. This phase inconsistency can cause ghosting. Applying coherent successive pulses and shifting the phase of the 180º pulse train by 90º compared to the phase of the first 90º pulse leads to echoes of the same phase (Meiboom and Gill, 1958). Implementing the modified CPMG in the RARE sequence ensures that the echoes will occur at the desired position in the pulse sequence and that they will carry the same phase. Calibration of the flip angle of the refocusing pulse train can stabilize the echo train amplitude reducing further ghosting and blurring artefacts. Blurring in RARE can also occur due to T_2 decay. The larger the echo train, the more vulnerable the system becomes to blurring. It is therefore important to carefully choose the N_{echo} for each excitation. Ghosting and blurring artefacts can also be eliminated by phase correcting the data during image reconstruction. One way of phase correcting the data is by estimating the phase of the central **k**-space data. It is considered that at the centre of the **k**-space, the phase distortion is minimum. Therefore, the phase of that **k**-point is used to phase correct all the **k**-space data before reconstruction.

Except for ghosting, other types of artefacts present in 3D images are truncation artefacts. Truncation artefacts can arise from insufficient spatial resolution which cannot reproduce spatial variations. It is often found near sharp edges. The truncation

is equivalent to multiplying **k**-space data by a rectangle function. One solution to reduce the effect of truncation is to decrease Δl. Another method is to window the sampled **k**-points prior to FT at the expense of the spatial resolution. Several types of window functions have been proposed. The Gaussian window function is the most efficient for the suppression of artefacts in 3D data sets (de Kort et al., 2018a; Harris, 1978).

Other types of distortions can arise from the spectrometer's imperfections. These imperfections can be suppressed by applying appropriate phase cycling. Since the experiment is repeated several times, the increment (scan) phase of the r.f. pulse is altered. The resultant signals from each scan are combined in a way that eliminates the unwanted distortions. CYCLOPS is one of the most popular phase cycling techniques and is designed to erase amplitude and phase errors related to quadrature detection (Hoult and Richards, 1975). All these techniques have been applied for the suppression of distortions in the data acquisition and processing of this thesis.

2.2.7 SNR in NMR and MRI

The peak in an NMR spectrum or the structure of the sample in an MR image cannot be observed if the achievable Signal-to-Noise Ratio (SNR) is not acceptable. SNR is a metric of the quality of the NMR or MRI experiment. Developments in the r.f. coil design and higher $\boldsymbol{B}_0$ field improve significantly the SNR of the obtained data. Another way for improving the SNR is by increasing the number of scans, N_s. The SNR is increased proportionally to $\sqrt{\Delta t}$ (Redpath, 1998). In MRI, SNR is proportional to the Δl along each direction and to the square root of the experimental time. In other words, SNR is increased proportionally to the $\sqrt{t_{RD}}$ and the $\sqrt{N_k}$ along each direction (Edelstein et al., 1986).

2.3 Basic Principles of MRI in Translational Motion

2.3.1 Self-Diffusion

The term diffusion is deliberately used to describe both mutual and self-(translational) diffusion. The driving force in mutual diffusion is the concentration gradient, while in self-diffusion the thermal fluctuations (Willis et al., 2016). The random walk of molecules in self-diffusion is a stochastic process also known as Brownian motion and is described by the self-diffusion coefficient, D_s(Uhlenbeck and Ornstein, 1991). NMR has been employed to study D_s by analysing the relaxation data and by using Pulsed-Field Gradient (PFG). The relaxation method requires several assumptions, while PFG-NMR has been deliberately used estiamating the D_s (Price, 1997).

2.3.2 PFG-NMR for Studying Translational Motion

The Pulsed-Gradient Spin Echo (PGSE) sequence, introduced by Stejskal and Tanner (1964), is illustrated in **Figure 2-13**(a). A phase encoding gradient of duration δ is used to label the motion of molecules by assigning a φ to each spin. At the end of the first τ_e, a 180_y^o pulse is applied to inverse the direction of the spins. The 180_y^o pulse is followed by a second identical gradient. The time between the first and the second

gradient is known as the observation time, Δ. If there is no translation motion, the phase effects of the gradients are cancelled out leading to full signal recovery as shown in **Figure 2-13**(b). However, if there is a translational motion to a new $\boldsymbol{r'}$ position, the net phase shift is:

$$\varphi(\boldsymbol{r}) = \gamma\,(\boldsymbol{r'} - \boldsymbol{r}) \cdot \boldsymbol{G}\,\delta. \tag{2-41}$$

PFG-NMR is used to monitor both coherent (flow) and incoherent (diffusive) motion. In the diffusive motion, the echo signal presents an attenuation due to the average of all the random phase shifts (incoherent distribution of phase shifts) as shown in **Figure 2-13**(c). In the case of directed flow, the detected signal intensity is reduced due to the net phase shift of the isochromats as presented in **Figure 2-13**(d) (Callaghan et al., 1988).

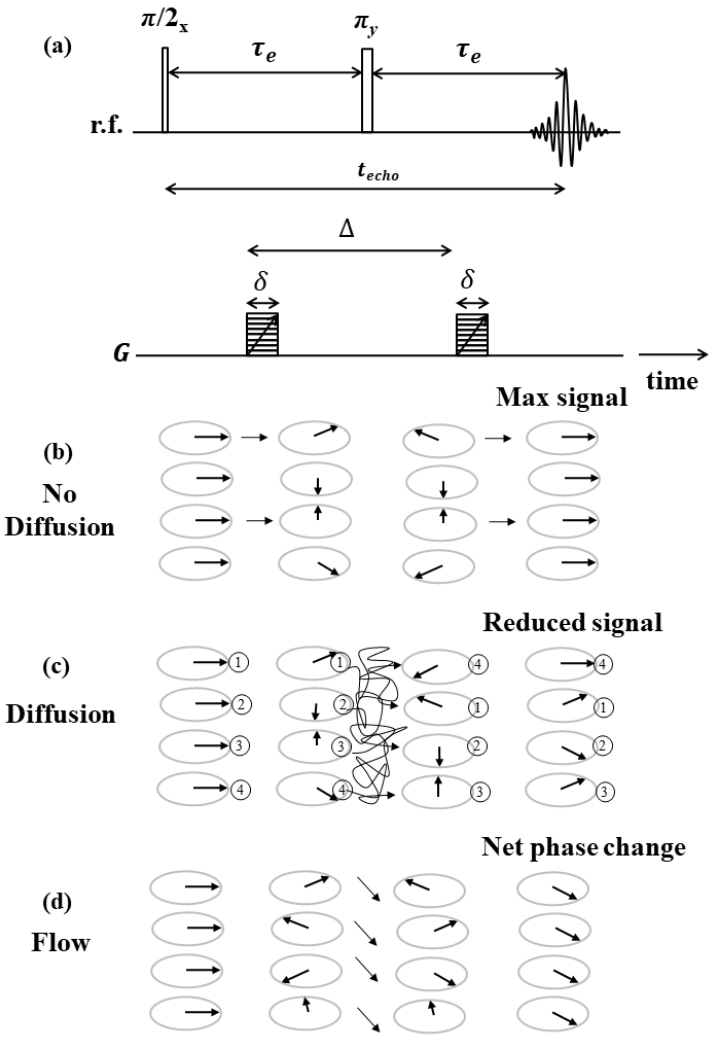

Figure 2-13: Schematic representation of the PGSE pulse sequence (α) in parallel with the spin phase change when there is no translational motion (b), when there is motion due to diffusion (c) and when there is motion due to flow (d). Adapted from Price, (1997).

2.3.3 Conditional Probability, Echo Attenuation and Q-Space

Assuming an isotropic self-diffusion coefficient, D_s, the mutual diffusion is driven by the flux of particles due to a concentration gradient described by Fick's second law:

$$\frac{\partial c(\boldsymbol{r},t)}{\partial t} = D_s\, \boldsymbol{\nabla^2} c(\boldsymbol{r},t), \tag{2-42}$$

where $c(\boldsymbol{r},t)$ is the local concentration. The self-diffusion is driven by Brownian motion and is described by the probability that a particle needs to transit from $\boldsymbol{r}$ to $\boldsymbol{r}'$ in time t. $P(\boldsymbol{r}|\boldsymbol{r}',t)$ is known as Conditional or Markovian probability. Einstein proved that the probability density can replace $c(\boldsymbol{r},t)$ in Eq.(2-42) leading to:

$$\frac{\partial P(\boldsymbol{r}|\boldsymbol{r}',t)}{\partial t} = D_s\, \boldsymbol{\nabla^2} P(\boldsymbol{r}|\boldsymbol{r}',t). \tag{2-43}$$

Eq.(2-43) is solved by considering a Dirac, δ_D, probability, giving (Stilbs, 1987):

$$P(\boldsymbol{r}|\boldsymbol{r}',t) = \frac{1}{\left(\sqrt{4\,\pi\, D_s\, t}\right)^3} \exp\left(-\frac{(\boldsymbol{r}'-\boldsymbol{r})^2}{4\, D_s\, t}\right). \tag{2-44}$$

As first stated by Callaghan et al., (1988), in analogy with the neutron scattering the reciprocal space vector **q** (in rad m^{-1}) for moving spins is given by:

$$\mathbf{q} = \gamma\, \boldsymbol{G}\, \delta. \tag{2-45}$$

Removing the relaxation effects by implementing the normalisation process, the amplitude of the echo at its centre is given by (Karger et al., 1988):

$$E(\mathbf{q},t) = \iint \rho(\boldsymbol{r})\, P(\boldsymbol{r}|\boldsymbol{r}',t)\, e^{i\,(\boldsymbol{r}'-\boldsymbol{r})\cdot\mathbf{q}}\, d\boldsymbol{r}' d\boldsymbol{r}. \tag{2-46}$$

2.3.4 Restricted Diffusion

Although D_s is independent of the chosen Δ, diffusion becomes dependent on the time when spins are confined in a pore system (Latour et al., 1993). Neglecting the relaxation on the pore wall, the displacement in the case of restricted diffusion is written as $\boldsymbol{r}(\Delta) - \boldsymbol{r}(0)$ and the effective diffusion coefficient as D_{eff}. If Δ is not long enough, spins will not collide with the boundary, hence D_{eff} is equal to D_s. This is known as short-time (ST) or free diffusion regime and is characterized by $l_D \ll d_p$, where l_D is the diffusion length and is equal to $\sqrt{D_s\Delta}$. If Δ is finite, a fraction of molecules will feel the effect of the boundaries. If Δ is too long, molecules will be able to sample the whole volumet of the sample. More details about the restricted diffusion regimes can be found in the literature (Mitchell et al., 2013a; Scheven and Sen, 2002).

2.3.5 Techniques for Measuring Restricted Diffusion in Porous Media

Implementing rectangular gradients of duration δ as shown in **Figure 2-13** has several advantages such as no-line broadening in the spectrum, measurement of short D_{eff} and separation between the diffusion and the T_2 relaxation effects on the echo signal (Price, 1997). In the low-q limit, D_{eff} is equal to the apparent diffusion, D_{app}, of the whole porous medium. Since porous media suffer from fast T_2 relaxation, stimulated echoes were integrated into the PGSE (Tanner, 1970). To reduce even further the effect of diffusion through internal gradients, bipolar gradients were employed to develop the 13-interval sequence, also known as Alternating Pulsed Gradient Stimulated Echo (APGSTE), shown in **Figure 2-14** (Cotts et al., 1989).

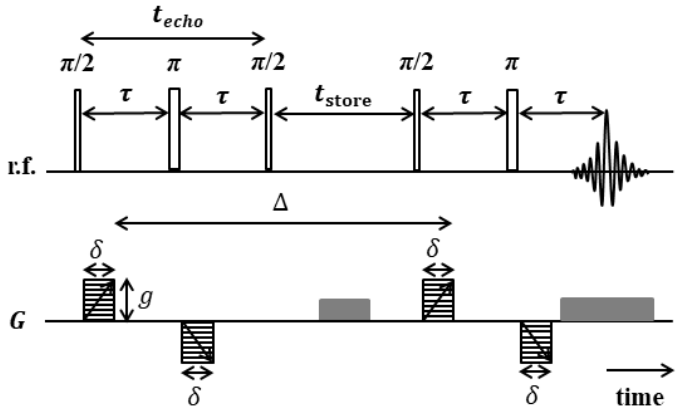

Figure 2-14: Schematic representation of the APGSTE sequence which combines bipolar phase-encoding gradients with stimulated echo to detect the diffusion and flow of spin in complex porous systems with strong internal gradients and short T_2 relaxation times. Homospoils are indicated by the small grey rectangles and the readout lobe by the large grey rectangle.

Chapter 3 Digital Image Processing

3.1 Introduction

The first MRI image was published by Lauterbur, (1973) who acquired 2D images of water in tubes using projection imaging. Since then high-quality superconducting magnets have been coupled with improvements in electronics, computing and novel image processing techniques leading to images of higher quality. Quantitative information such as liquid concentration, flow and diffusion can also be derived from clinical MRI (Glover and Mansfield, 2002). Further, the applications of MRI have now expanded to plant biology, food, polymers and porous media with a big focus on petrophysics (Mitchell et al., 2014; Scheenen et al., 2000; Shutang et al., 1995).

In order to extract reliable petrophysical information from MRI images and flow measurements, significant processing of the acquired data needs to be performed. This is because the MRI data are often corrupted by noise and interference leading to artefacts in the measured images or errors in the calculated values (Andris and Frollo, 2016). To assess the accuracy of the results, the noise level and the noise variance need to be addressed to determine the quality of the image and the consistency of the image processing technique (Coupé et al., 2010). Accurate modelling of the signal and noise statistics has been used to assess the randomness of the noise across the image (Aja-Fernandez and Tristan-Vega, 2013). The level of noise affects the SNR which can result in quantitative errors (Macovski, 1996). Hence, image enhancement techniques have been implemented for contrast enhancement and image quality improvement (Senthilkumaran and Thimmiaraja, 2014). Since noise reduces the sensitivity of the instrument, the observation of ultra-slow flow in complex porous media such as low-permeability rocks becomes difficult. To overcome all these challenges, analysis of the background noise and intensity thresholding have been implemented in the structural images and the flow maps acquired in this thesis (Brummer et al., 1993).

To speed up the acquisition time, MRI systems often subsample the **k**-space covering local phase distortions. This under-sampling of the **k**-space data imports aliasing artefacts in the real space image after the application of FFT in the raw data. Therefore, several reconstruction techniques have been studied (Aja-Fernandez and Tristan-Vega, 2013; Donoho, 2006). In this thesis, the compressed sensing approach has been chosen as the most adequate reconstruction technique for the experimental requirements.

In this chapter, the technique for the acquisition of the optimum under-sampling pattern will be described. Then, the compressed sensing reconstruction and the optimisation of the regularisation parameters are described. Last but not least, denoising techniques that are relevant to this thesis for the MRI images, velocity maps and propagators are discussed.

3.2 Under-Sampling in 3D RARE

The main imaging technique that was used to acquire spatially resolved 3D images was the 3D RARE. Hard pulses were employed instead of Gaussian-shaped pulses as presented in **Figure 2-12** (Hennig et al., 1986). The advantage of using hard pulses is that shorter τ_e can be applied, decreasing the signal loss due to T_2 relaxation. RARE has several advantages over other fast imaging techniques described in the literature (Xiao and Balcom, 2012). The uniform rectilinear **k**-space sampling enables the combination of RARE with CS since the magnetization is always returned at the centre of k-space. The combined approach of CS with RARE is known as the CS-RARE sequence and aims to reduce the acquisition time by giving quantitative results with high structural quality (Donoho, 2006; Lustig et al., 2008, 2007). CS-RARE imaging has already been applied by Ramskill et al., (2016). However, the under-sampling pattern and the reconstruction process were not optimal.

3.2.1 Under-Sampling Patterns

For RARE imaging, the density sampling pattern is applied to the $\boldsymbol{k}_{phase1}$ and $\boldsymbol{k}_{phase2}$ dimensions, whereas the $\boldsymbol{k}_{read}$ lines are fully-sampled (de Kort et al., 2018a). RARE implies **k**-space sampling on the Cartesian grid and a simple inverse FFT is required for image reconstruction (Lustig et al., 2008). The highest intensity **k**-space points are usually in the central region of **k**-space and contain information about the contrast and the SNR of the real space image. The periphery of the **k**-space presents lower energy, including information about the spatial details of the real space image. Lustig et al., (2007) recommend a variable density sampling pattern based on the probability density function (pdf). This pseudo-random sampling scheme results in incoherent aliasing artefacts but a sub-optimal choice of the constant can decrease the quality of reconstruction.

This is why data-driven sampling strategies involving learning from MRI data have been adopted. Since the intensity of the **k**-space data contains information about the morphological structure of the real space image, the fully-sampled **k**-space can be used as input for the selection of the optimum sampling pattern. Karlsons et al., (2019) developed the so-called μCT-VDS method which takes as input a μCT image and results in a relatively large fully-sampled central region. All the sampling patterns in this thesis were generated using this strategy having as input a fully-sampled MR image of 437.5 μm pixel^{-1} isotropic resolution instead of a μCT image. This method can be referred to as MRI-VDS. The steps followed can be summarised as:

1) *Obtain the MRI input image*. A fully-sampled MR image is obtained. The **k**-space data are then phase-corrected with the angle of the highest intensity point (centre of **k**-space) and then the intensity of all the **k**-data is integrated along the read direction.
2) *Obtain a pdf*. The 2D **k**-space data are radially averaged to the corner of the raster creating a 1D **k**-space array. Considering that N_{phase} is the number of elements in each direction of the 2D **k**-space raster of the reference image, the length of the obtained 1D array is equal to the round number of $N_{phase}/2\sqrt{2}$. The 1D array is interpolated through a 2D mesh grid to form the 2D pdf,

including the central **k**-point with an intensity of 1. The number of elements in each direction of this 2D pdf is equal to $2\,N_{phase}/2\sqrt{2}+1$ and the grids outside the radius $N_{phase}/2\sqrt{2}$ are replaced by 0. This is known as azumuthial averaging process and the obtained 2D pdf represents the magnitude distribution of the **k**-space for any porous medium.

3) *Cropping of the pdf*. The generated 2D pdf is then cropped homogeneously around the central area of the highest intensity **k**-points to the desired matrix size, i.e. to the size of the final under-sampled image.
4) *Scaling the pdf*. By setting all the intensities higher than 1 to be equal to 1 and implementing a weighted parameter towards the centre of the k-space, a scaled 2D pdf is generated. The scaled 2D pdf presents a fully-sampled central region and its integral is equal to the number of **k**-space points that need to be acquired for the chosen under-sampling rate.
5) *Sampling point selection*. Monte-Carlo simulation is employed to generate the final 2D logical matrix that represents the sampling pattern. More precisely, in each loop, a Cartesian grid of the same size as the scaled 2D pdf is created with uniformly distributed random numbers. The 2D logical matrix has the same size as the scaled 2D pdf and the value of a square becomes equal to 1 when the value of the scaled 2D pdf in the adequate square is higher than the randomly generated value. The loop is completed when the desired sampling rate matches the result of the random point selection procedure. This loop is repeated more than 1000 times and the sampling pattern with the greatest incoherence is chosen as the optimum. The incoherence is estimated using the density-compensated Point Spread Function (PSF) as detailed in Lustig et al., (2007).

The same process was followed to obtain the sampling pattern for the under-sampled +q and -q phase images in the 3D velocity mapping.

3.2.2 k-Space Sampling Trajectories

A **k**-space sampling pattern shows which data points in the **k**-space raster need to be sampled to achieve the optimum qualitative and quantitative result after reconstruction. **Figure 3-1**(a) shows a typical sampling pattern that has been used in CS-RARE acquisition for a sampling fraction of 0.25. However, it does not indicate the trajectory followed to acquire these **k**-points. In this project, the sampling trajectories used for all the 3D CS experiments are based on the previous work by Ramskill et al., (2018). The most popular trajectory of sampling is the Scheme A trajectory presented in **Figure 3-1**(b) for a N_{echo}=32. In Scheme A the edges of the **k**-space are sampled first and the centre of the **k**-space later. In contrast, the Scheme B trajectory presented in **Figure 3-1**(c) is based on the sampling of the central **k**-point first while the edges are sampled at the end of the echo train. The reconstructed CS-RARE images acquired with Scheme A present a better contrast, but a larger T_2 relaxation weighting compared with the CS-RARE images acquired with Scheme B. Consequently, the CS-RARE images acquired with Scheme B present better SNR and have been proved quantitative when measuring relative saturations. In this thesis,

Scheme B has been used for the first time in the acquisition of 3D CS phase-contrast and propagator data.

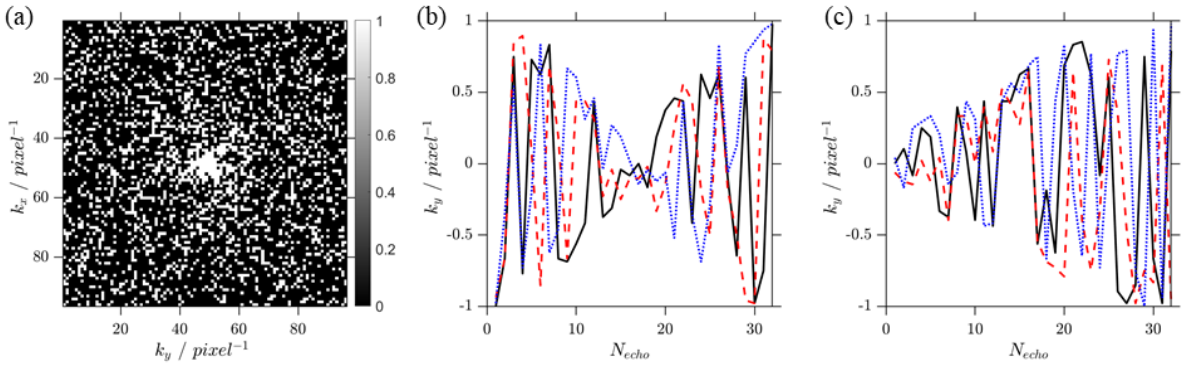

Figure 3-1: (a) Variable density **k**-space sampling pattern for an under-sampling fraction of 0.25 in both k_x and k_y directions. The white pixels correspond to the sampled **k**-space data. Scheme A(b) and Scheme B(c) trajectories for the k_y with an echo train length of N_{echo}=32 for the 1st (solid black line), 37th (dashed red line) and 73rd (last) (dotted blue line) echo train.

3.3 Under-Sampling in 3D Propagators

The under-sampling strategy used for all the 3D propagators acquired in this thesis using the APGSTE-RARE sequence was developed by de Kort et al., (2018). In short, the 2D pdf function was generated from a fully-sampled MRI as described from step 1 until step 3. The 2D pdf was then replicated for each **q**-space point forming a 3D pdf. The **q**-space is the result of the 1D propagator obtained with the APGSTE sequence under the same conditions as the 3D propagator. A Gaussian window function was then implemented on the 3D pdf. Then, a sampling pattern was applied to the 3D pdf weighted towards the centre of both **k** and **q**-space as shown in **Figure 3-2**. There are two constraints for implementing this strategy of under-sampling. The first is that for each **q**-space point, the number of $\boldsymbol{k}_{phase}$ data points should be a multiple of the number of odd and echo pairs, hence of the $N_{echo}/2$. The second constraint is that the sampling pattern in the **q**, $\boldsymbol{k}_{phase}$-dimensions should be symmetrical around **q**=0 m^{-1} and the central **q**-point should be sampled. The Monte-Carlo simulation described in step 5 is modified for these constraints and the sampling pattern with the greatest incoherence is chosen after 1000 iterations. In these iterations, the sampling rate is modified to approximate the desired value for the optimum PSF.

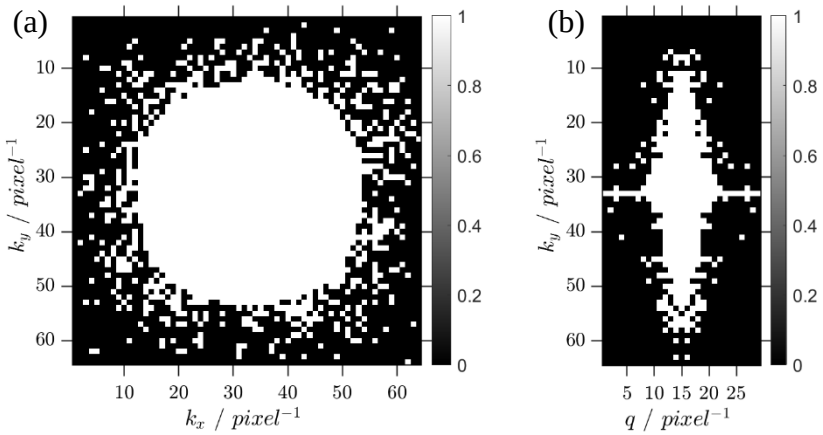

Figure 3-2: Variable density **k**-space sampling pattern in the two phase-encoding dimensions (a), k_y and k_x, and in the k_y and q-dimensions (b) for a sampling fraction of 13%.

3.4 Compressed Sensing Reconstructions

The final step is to reconstruct the acquired under-sampled **k**-space data. All CS reconstructions in this thesis were performed using an in-house Matlab toolbox, Object-Oriented Mathematics for Inverse Problems (OOMFIP), for which the implementation is presented by Benning et al., (2014). In this thesis, Total Variation (TV) is employed as the appropriate regulariser for the image reconstruction and has demonstrated a good reconstruction quality in structural images (Karlsons et al., 2019; Ramskill et al., 2016), velocity images (Benning et al., 2014; Holland et al., 2010) and spatially-resolved propagators (de Kort et al., 2018b) due to its edge-preserving properties and the isotropic regularisation. The Tikhonov regularisation scheme used in this thesis is written as:

$$\begin{aligned} \mathbf{m}_{\mathrm{CS}}^{n} \in \arg\min_{\mathbf{m}} \left\{ \frac{1}{2} \|\mathbf{y}^{n-1} - S_u \mathcal{F}_u \mathbf{m}\|_2^2 + \alpha J(\mathbf{m}) \right\}, \\ \boldsymbol{y}^{n} = \boldsymbol{y}^{n-1} + \boldsymbol{y} - S_u \mathcal{F}_u \mathbf{m}_{\mathrm{CS}}^{n}, \end{aligned} \tag{3-1}$$

where $\mathbf{m}_{\mathrm{CS}}$ is the reconstructed image, **m** is the complex image which should be recovered from the noisy sub-sampled **k**-space data, **y** the sub-sampled **k**-space data, S_u the sampling pattern, $\mathcal{F}_u$ the linear operator for the discrete 2D FT, J the regularisation functional, α is a positive regularisation parameter that balances the weight between the fidelity and the regularisation term. Bregman iterations enhance image contrast by solving Eq.(3-1) n times. Although Bregman iterations increase the reconstruction time, they can improve significantly the image quality

3.4.1 Optimisation of Image and Velocity Map Reconstruction Parameters

To quantify the quality of the CS reconstructed image, $\mathbf{m}_{\mathrm{CS}}$, with respect to the fully-sampled reference image, $\mathbf{m}_{\mathrm{FS}}$, two standard image quality metrics are defined. The Peak Signal-to-Noise Ratio (PSNR) measures the error between the reconstructed and the reference image as:

$$\mathrm{PSNR}(\mathbf{m}_{\mathrm{CS}}, \mathbf{m}_{\mathrm{FS}}) = 10 \log_{10} \left(\frac{(\max|\mathbf{m}_{\mathrm{FS}}|)^2}{\|\mathbf{m}_{\mathrm{CS}} - \mathbf{m}_{\mathrm{FS}}\|_2^2 / N_{vox}} \right), \qquad (3\text{-}2)$$

where N_{vox} is the number of voxels in the image. Higher values of PSNR correspond to better quality reconstructions. The Structural Similarity Index (SSIM) is a robust metric of the structural differences between the reconstructed and the fully-sampled image. The Local SSIM (LSSIM) is given by:

$$\mathrm{LSSIM}(\mathbf{m}_{\mathrm{CS}}, \mathbf{m}_{\mathrm{FS}}) = \frac{(2\mu_{\mathbf{m}_{\mathrm{CS}}}\mu_{\mathbf{m}_{\mathrm{FS}}} + C_1)(2\sigma_{\mathbf{m}_{\mathrm{CS}}}\sigma_{\mathbf{m}_{\mathrm{FS}}} + C_2)}{(\mu_{\mathbf{m}_{\mathrm{CS}}}^2 + \mu_{\mathbf{m}_{\mathrm{FS}}}^2 + C_1)(\sigma_{\mathbf{m}_{\mathrm{CS}}}^2 + \sigma_{\mathbf{m}_{\mathrm{FS}}}^2 + C_2)}, \qquad (3\text{-}3)$$

where $\mu_{\mathbf{m}}$ and $\sigma_{\mathbf{m}}$ are the mean and standard deviation of the image intensity in a local Gaussian window and constants C ($C_1 = (0.01 \max|\mathbf{m}_{\mathrm{FS}}|)^2$ and $C_2 = (0.03 \max|\mathbf{m}_{\mathrm{FS}}|)^2$) are used to avoid instabilities. The global SSIM is derived by averaging the LSSIM over the whole image area. A perfect reconstruction would give an SSIM=1 (Wang et al., 2004).

In this thesis, a fully-sampled and an under-sampled image with a 0.25 sampling fraction were always obtained at the beginning of the experimental procedure. The under-sampled image is reconstructed for ten different values of $\alpha \in \{0.001, 0.0043, 0.0084, 0.01, 0.03, 0.05, 0.08, 0.1, 0.126, 0.18\}$. Each α value was varied for one up to fifteen Bregman iterations. The final PSNR and SSIM coming from an under- and a fully-sampled 3D RARE image for an Indiana limestone sample are illustrated as 2D bar plots in **Figure 3-3**.

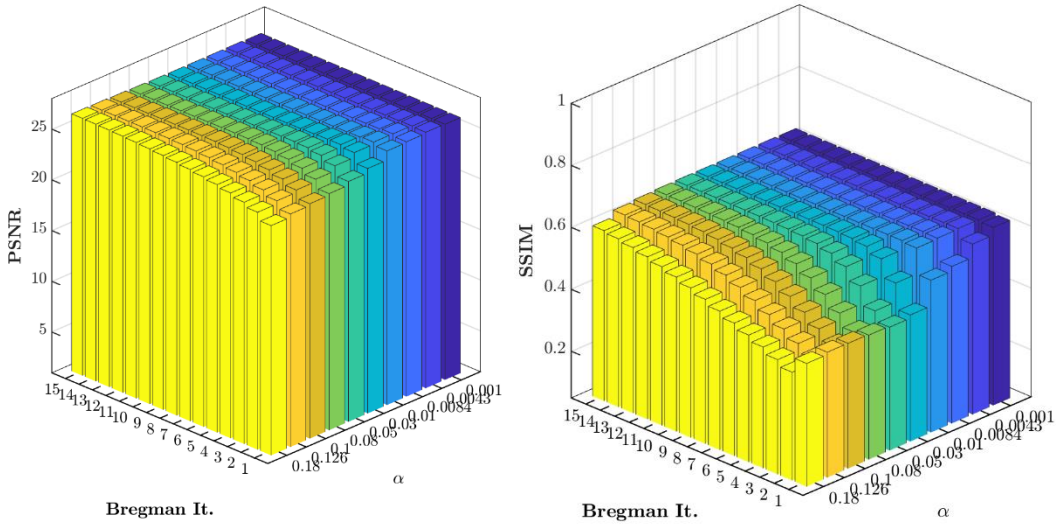

Figure 3-3: 2D plots for PSNR and SSIM for reconstructed CS-RARE images using ten different α values and one up to fifteen Bregman iterations.

Figure 3-3 shows that for each value of α the Bregman iterations improve significantly both the PSNR and the SSIM metrics. In addition, for the small values of α from 0.001 up to 0.08 and varying the Bregman iterations from 1 up to 15, a plateau of high PSNR and SSIM is observed. Isolating that area and fitting a fifth-order

polynomial surface to the data leads to the optimum α and Bregman values as indicated by the red sphere in **Figure 3-4**.

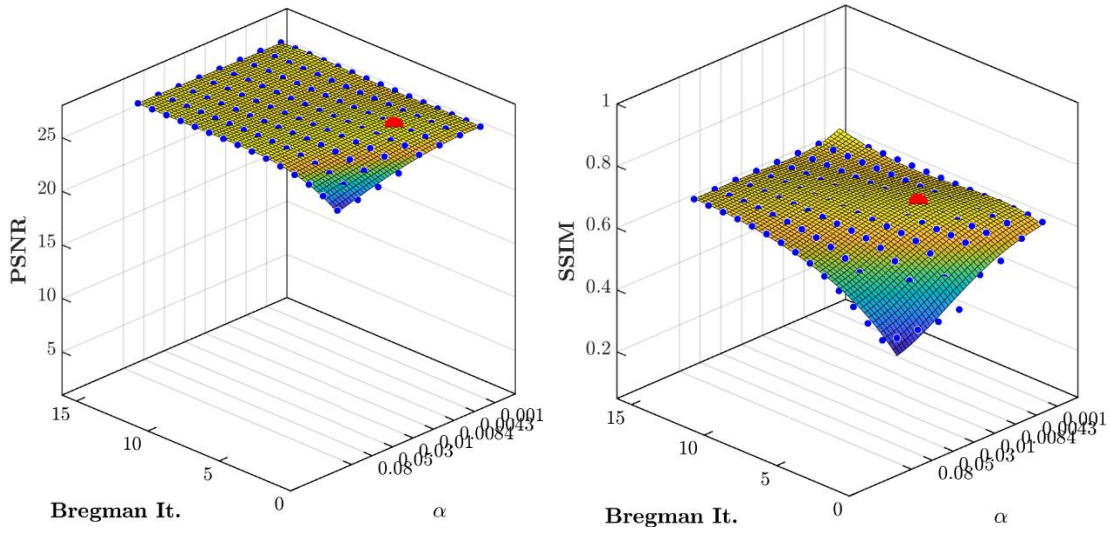

Figure 3-4: Polynomial fitting to the plateau area observed in the 2D plot in Figure 3-3 for PSNR and SSIM and optimum α and Bregman value (red sphere).

Figure 3-4 shows that the PSNR and the SSIM present their optimum value for a similar α value. The optimum α comes from the mean of these two values and is equal to 0.00867 for that CS process. The optimum Bregman for PSNR is 3 while for SSIM is 6. The highest value of Bregman iterations is chosen as the optimum since Bregman only improves the contrast of the image. The logic behind surface fitting in a plateau area of high PSNR and SSIM is that most of the systems studied in this thesis are dynamic. Therefore, it is not possible to acquire fully-sampled images for each dynamic stage and repeat the process described above. By choosing α and Bregman in the plateau area, we know that each reconstructed CS-RARE image will present a high enough PSNR and SSIM.

The same procedure is followed for the optimisation of the α and Bregman regularisation parameters in the CS velocity mapping. As will be described in Chapter 4, velocity maps are calculated by four different complex images; an odd and an even image of the positive +q point and an odd and an even image of the negative -q point. The PSNR and the SSIM 2D plots are created for all these four images separately. The optimum α comes from the mean of all the α values estimated by each polynomial fitting. The highest value of Bregman iterations is chosen as the optimum Bregman.

3.4.2 Optimisation of Propagator Reconstruction Parameters

The acquisition of fully-sampled propagators with the APGSTE-RARE sequence is time-consuming (~ 4 d). As a result, Morozov's discrepancy principle is used to optimise the parameter α for one Bregman iteration (Morozov, 1965). Considering that $\mathbf{m}$ is the complex noisy spatially-resolved propagator and $\mathbf{m}_{CS}$ is the reconstructed propagator, Morozov's discrepancy principle is written as:

$$\mathbf{m}_{\text{cs}} \in \arg\min_{\sigma} J(\mathbf{m}) \text{ subject to } \|S_u \mathcal{F}_u \mathbf{m} - \mathbf{y}\|_2 \leq \sigma_n \sqrt{N_k}. \quad (3\text{-}4)$$

The inequality constraint invokes that there is consistency with the sampled **q**, **k**-space data. In practice, several CS propagators for different α values are reconstructed and the optimum α is chosen as the maximum α that satisfies Eq.(3-4).

3.5 Denoising Procedures

3.5.1 Distribution of Noise in MRI Images

The spatial distribution of noise in MR images was initially studied by Murphy et al., (1993) by comparing the noise variance between matched images of the same object and it was later modelled by Aja-Fernandez and Tristan-Vega (2013). It is assumed that the real and the imaginary parts of a signal are corrupted by a white additive Gaussian noise (i.e. zero-mean uncorrelated Gaussian noise) when it is measured from a quadrature detector. This Gaussian noise follows a Rician distribution in magnitude images and is given by:

$$p_M(IM) = \frac{IM}{\sigma_n^2} e^{-(IM^2+A^2)/2\sigma_n^2} I_0\left(\frac{A\, IM}{\sigma_n^2}\right), \quad (3\text{-}5)$$

where A is the original voxel intensity without the presence of noise, I_0 is the zeroth-order Bessel modified function, σ_n is the standard deviation of the Gaussian noise in the real and imaginary images and IM is the measured voxel intensity or the magnitude of the complex number corresponding to each voxel. the shape of the Rician distribution changes a lot as indicated by Eq.(3-5). The SNR is defined as A/σ_n. This model is adopted by the majority of noise estimation methods which can be divided into two categories; the background-based and the object-based methods.

The first category focuses on the background area of the image where the signal is usually considered as zero, i.e. SNR = 0. For this area, the Rician distribution is converted into a Rayleigh distribution described by:

$$p_M(IM) = \frac{IM}{\sigma_n^2} e^{-IM^2/2\sigma_n^2}. \quad (3\text{-}6)$$

Based on the properties of the Rayleigh distribution, the mean μ_b and the variance σ_b^2 of the noise in the background can be related to the σ_n as:

$$\begin{aligned} \mu_b &= \sqrt{\frac{\pi}{2}}\, \sigma_n \\ \sigma_b^2 &= \frac{4-\pi}{2}\, \sigma_n^2. \end{aligned} \quad (3\text{-}7)$$

The Rayleigh distribution model can fail when ghosting artefacts are present or by implementing wrong filters or suppressing the signal (Coupé et al., 2010).

The second approach is valid only when the signal intensity in the area of the sample is high (SNR > 2). In this approximation, the Rician distribution can be well approximated by a Gaussian curve defined as:

$$p_M(IM) \approx \frac{1}{2\,\pi\,\sigma_n^2} exp\left(-\frac{\left(IM-\sqrt{A^2+\sigma_n^2}\right)^2}{2\,\sigma_n^2}\right). \quad (3\text{-}8)$$

Other approximations using the Median Absolute Deviation for the measurement of the Gaussian noise have been studied, but are beyond the scope of this thesis (Aja-Fernández et al., 2008; Coupé et al., 2010; Gudbjartsson and Patz, 1995).

3.5.2 Automatic Background Thresholding

For the quantification of the MRI data reported in this work, it is important to define a background intensity threshold which will allow us to mask the background and the low-intensity voxels where noise is dominant. A method for automatic threshold determination is employed to generate an intensity threshold mask. This mask is generated for all the structural images as well as the 3D velocity and propagator data. According to Brummer et al., (1993), a least-square fit of a scaled Rayleigh curve can be fitted to the histogram of the lowest grayscale values using the Levenberg-Marquardt minimisation algorithm given by:

$$\sum_{IM=0}^{IM_c}\left(hist(IM)-K\frac{IM}{\sigma_n^2}e^{-IM^2/2\sigma_n^2}\right)^2, \quad (3\text{-}9)$$

where $hist(IM)$ is the curve from the histogram of the magnitude image, K is a scaling factor and IM_c is the cut-off intensity value. Searching for the first local maximum, a first estimate of σ_n is acquired. The first cutoff value is defined as 2 σ_n. The best fit for the Rayleigh function is denoted as $ral(IM)$. To find the optimum threshold value, a bimodal distribution is generated as:

$$fun(IM) = hist(IM) - ral(IM), \quad (3\text{-}10)$$

where $fun(IM)$ is the function representing all the non-background voxels. Minimising the ε_τ error term given by:

$$\varepsilon_\tau = \sum_{IM=0}^{IM_c-1} fun(IM) + \sum_{IM=IM_c}^{\infty} ral(IM), \quad (3\text{-}11)$$

leads to the optimum IM_c value (Zhan and Zhang, 2019).

3.5.3 Experimental Results of the Automatic Background Thresholding

Initially, the automatic background thresholding was applied to a 3D RARE fully-sampled image with Scheme B sampling trajectory and 437.5 μm pixel^{-1} resolution of

a bead pack filled with water and borosilicate spheres of 4 mm. This is an ideal porous model with a significant partial volume effect. This effect is a common source of error and is caused due to limits in image acquisition which blurs the transition between phases and features. In the presented system, the resolution of 437.5 μm pixel^{-1} enables pore-scale analysis which results in an important partial volume effect. That means that several voxels contain both the fluid and the solid phase of the bead (Tang et al., 1993). **Figure 3-5**(a) presents the area of the partially- and fully-filled voxels in the histogram of the image. **Figure 3-5**(b) shows the Rayleigh fitting from Eq.(3-9) and the first cutoff value at $2\,\sigma_n$. Then, **Figure 3-5**(c) indicates the optimum IM_c coming from the minimsation of the error term ε_τ in Eq.(3-11). Finally, **Figure 3-5**(d) differentiates the cropped area corresponding to background noise (light blue) and the histogram of the voxels that belong to the sample (red area).

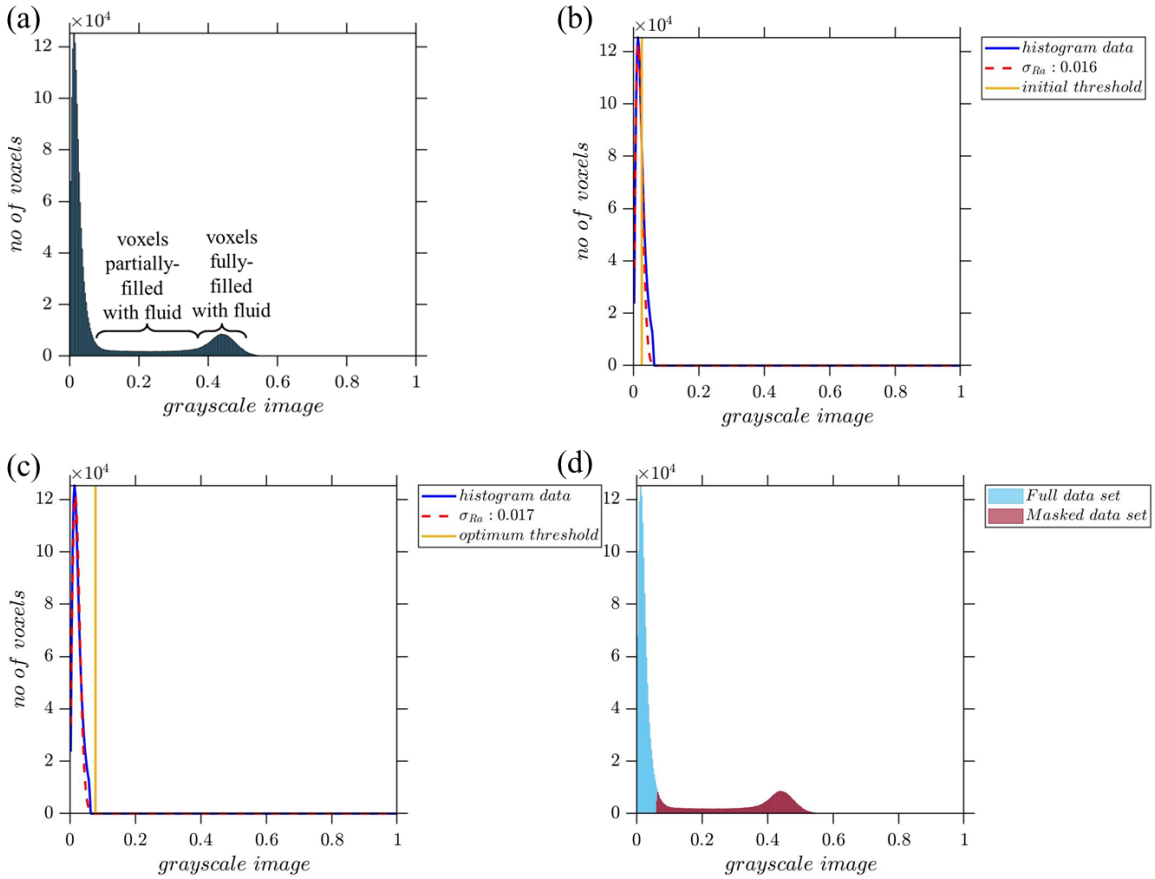

Figure 3-5: Steps of automatic background thresholding for the fully-sampled 3D image of a bead pack filled with water and 4 mm borosilicate beads. Histogram of the grayscale intensity images (a), Rayleigh fitting to the histogram of the background data and first cut-off (yellow line) at $2\,\sigma_n$(b), optimum cut-off value from the improved Otsu algorithm (c) and histogram after implementation of the optimum threshold intensity mask separating the background and low-intensity data (blue area) from the important data of the sample (red area) (d).

3D RARE fully-sampled images following the Scheme B sampling trajectory with 437.5 μm pixel^{-1} resolution were obtained for more complex porous media. **Figure 3-6** presents the optimised masked histogram of an Estaillades(a) and an Indiana limestone(b) after applying the automatic background thresholding method. Each voxel in the area of the sample (red area) contains a range of water-filled pores. The

pore size is smaller than 10 μm, hence pore-scale resolution cannot be achieved in these samples. This is why these voxels present lower grayscale values compared to the histogram of the bead pack. Although Scheme B sampling strategy was followed, T_2 relaxation has a significant effect on the magnitude of the acquired **k**-space data.

The Gaussian curve that corresponds to the area of the sample (red region) is apparent in the Estaillades histogram shown in **Figure 3-6**(a). This makes easier the separation between the background noise and the high-intensity area. However, low-permeability rocks like the Indiana limestone in **Figure 3-6**(b) do not show any clear separation between the two areas. Automatic background thresholding is an important denoising tool in such systems with a high number of low-intensity voxels.

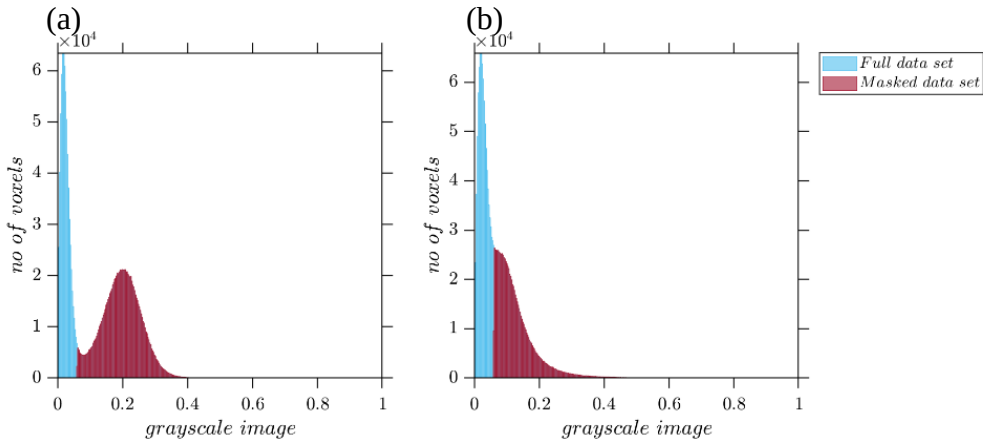

Figure 3-6: Histogram of the grayscale intensity images acquired following the Scheme B trajectory for the acquisition of the whole of the **k**-space for an Estaillades (a) and an Indiana limestone core-plug (b) saturated with water. The red area corresponds to the masked area after the application of the optimum IM_c cutoff while the light blue area represents the background noise.

In the case of velocity maps, the mean intensity coming from the odd and even images for +q and -q is converted into a grayscale image and the same automatic intensity threshold is applied. In the case of spatially-resolved propagators, the intensity is average for all the obtained **q**-space values and is then converted into a grayscale image.

3.5.4 Methods for Measuring SNR

One technique for measuring the SNR is based on the analysis of the histogram of the image. By fitting Eq.(3-8) to the histogram that is related to the intensity of the sample, a Gaussian mean equal to $\sqrt{A^2 + \sigma_n^2}$, and a standard deviation of σ_n can be measured (Gudbjartsson and Patz, 1995). Therefore, the value of SNR is:

$$\text{SNR} = \frac{A}{\sigma_n}. \tag{3-12}$$

Another very popular technique for SNR estimation was recommended by Andris and Frollo, (2016). This technique was used for measuring the noise in the image of a plastic bottle filled with water. The SNR was estimated as the ratio of the average

intensity in a Region-Of-Interest (ROI) of the water areas divided by the standard deviation of the intensities in an ROI outside the plastic bottle.

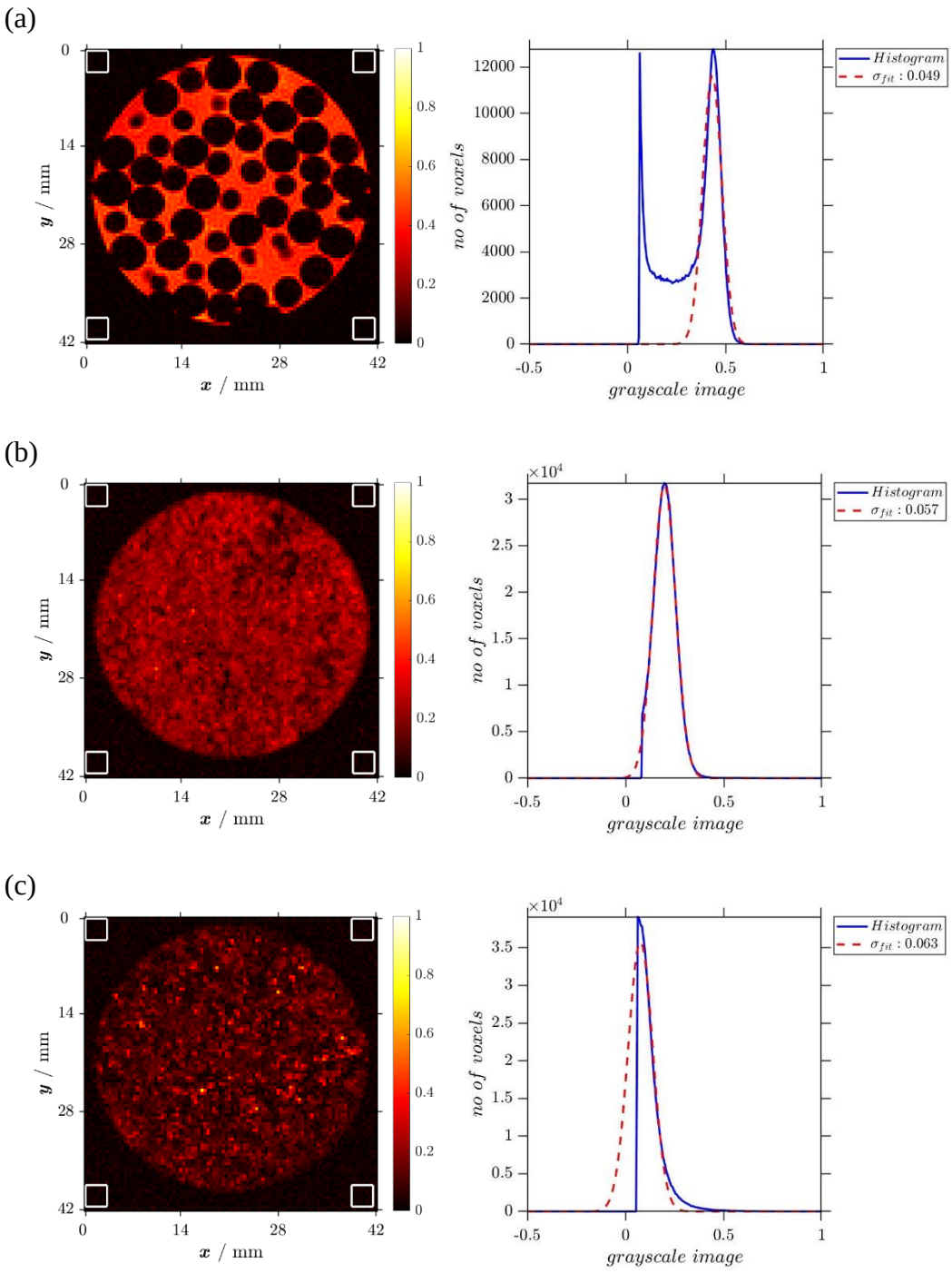

Figure 3-7: Four regions of background intensity (white squares) in the xy slice of 3D RARE image acquired following the Scheme B trajectory for the acquisition of the whole of the **k**-space and fitted-Gaussian curve (dashed red line) to the histogram curve (blue line) of the grayscale values coming from the highest intensity region for a bead pack filled with 4 mm borosilicate beads (a), an Estaillades (b) and an Indiana limestone core-plug (c) saturated with water. The histogram curve corresponds to the masked dataset after the application of the optimum IM_c cutoff as shown from the red area in **Figure 3-6**.

Figure 3-7(a) shows the x-y slice at the centre of the 3D image with four selected ROI outside the sample. **Figure 3-7**(b) presents the histogram curve which

corresponds to the highest intensity voxels (blue) and the Gaussian fit (red dashed line) to it for the bead pack. In both cases, the 3D image had been normalised by the mean intensity of 7 voxels around the highest intensity voxel. In the first figure, four background areas of 16 pixels each were chosen along each axial position. The standard deviation of these background areas was averaged. Then, the mean intensity of 7 voxels around the highest intensity voxel was divided by the standard deviation giving an SNR of 58. In the second figure, the SNR coming from the Gaussian fit method was measured as equal to 8.8.

Figure 3-7(b) and (c) present the corresponding images and histograms for water-saturated Estaillades and Indiana limestone cores, respectively. For the Estaillades rock, the SNR measured with the second technique was 3.1 and the SNR measured with the third technique was 32. **Figure 3-7**(c) shows that the histogram method is hard to implement since the grayscale of the masked image region does not present a Gaussian curve due to the large number of low-intensity voxels. The SNR of Indiana measured using equation (3-12) was 0.6, while the SNR derived from the final method was 7.

Several parameters can affect the SNR such as relaxation, imperfections in the hard pulses, voxel inhomogeneities etc. In 3D imaging, the SNR is proportional to the product of the voxel size and the square root of the acquisition time (Macovski, 1996).

3.6 Removal of Artefacts

As discussed in Section 2.2.6.1, MR images are susceptible to artefacts that can create ghosting and poor SNR. To reduce the truncation artefacts, the raw **k**-space data were phase-corrected and then convolved with a window function, w, which smoothly rolls off toward zero. This w attenuates the high spatial frequencies reducing truncation artefacts (M. Bernstein et al., 2004; Harris, 1978). In this thesis, a Gaussian window was employed to reduce the effect of truncation due to low-resolution in the 3D propagator measurements (de Kort et al., 2018b). The Gaussian window can be defined as:

$$w(m) = e^{-\frac{1}{2}\left(\frac{m-m_{\boldsymbol{k}_0}}{\sigma}\right)^2}, \tag{3-13}$$

where σ is the standard deviation of the Gaussian distribution, $m_{\boldsymbol{k}_0}$ is the index of the central point of the **k**-space and m is an array representing the number of **k**-space data along a chosen direction. The σ is of the Gaussian function is defined as:

$$\sigma = \frac{size(m)}{W \cdot 2\sqrt{2\,log2}}, \tag{3-14}$$

W is a window width factor which is always a positive number, $size(m)$ is the size of the m array, hence the number of **k**-space data along that direction. Increasing the window width factor means a smaller value of σ, hence a narrower Gaussian window (M. Bernstein et al., 2004).

Chapter 4 Ultra-Slow Flow in a Bead Pack

4.1 Introduction

Fluid flow through porous rock is of considerable interest to the petroleum industry. Understanding the displacement mechanisms in these complex pore networks can help to improve the recovery and develop accurate simulation models. NMR has been used to detect local flow processes within the opaque solid structure since it is a non-invasive technique which requires no tracers and can give a better description of the flow regime than the macroscopic properties. PFG NMR is one of the first experiments employed for the study of spin displacement due to flow and diffusion (Callaghan et al., 1980; Stejskal and Tanner, 1964). In complex porous media, the spins will not have the same displacement over a given time interval due to restricted diffusion, flow variations and limited pore space interconnectivity. As a result, PFG has been combined with imaging modules to enable direct 3D measurements of flow in heterogeneous structures (Callaghan et al., 1988; Dijk et al., 1999; Seymour and Callaghan, 1997a).

There are two main techniques which enable the detection of motion; the propagator and the phase-contrast velocimetry. Spatially-resolved propagators capture the motion of molecules from both diffusion and flow offering a full characterisation of the hydrodynamic dispersion. Nonetheless, they are costly in terms of experimental time since they require the acquisition of a range of **q**-points. Accelerating the acquisition through under-sampling of the **q**-space has been recommended (Colbourne et al., 2016). Under-sampling of both the **q**- and **k**-space has been proved more efficient for local propagator measurements with great accuracy (de Kort et al., 2018a). Phase-contrast velocimetry can be derived from a minimum of two **q**-points and when combined with CS can lead to fast velocity measurements (Benning et al., 2014).

To evaluate the suitability of each method, it is important to distinguish two regimes of flow based on the experimental spatial resolution. The first regime is characterised by pore-scale resolution meaning that the voxel size is smaller than the pore body. This is achieved in packed beds filled with large beads. In this regime, both propagator and phase-contrast velocimetry have shown great agreement (Manz et al., 1999b). The second regime involves measurements with a voxel size higher than the equivalent pore size. This regime is met in all the core plugs, especially the low-permeability ones. Phase-contrast velocimetry has shown deviations in the measured velocity compared to the externally measured velocity when implemented in flow experiments through rocks (Chang and Watson, 1999). This is because the accuracy of phase-shift measurements depends on the symmetry of the local dispersion (Shukla et al., 2016; Vallatos et al., 2018) and the suppression of the induced phase coming from local susceptibilities between the solid and liquid phase (Waggoner and Fukushima, 1996). Therefore, propagator measurements are deliberately used for the study of transport phenomena through rock samples (de Kort et al., 2018b). Both phase-contrast and propagator methods observe the molecules' displacement over a time interval Δ which is limited by the relaxation rate. The fast relaxation rate in the rock system poses obstacles to the detection of ultra-slow velocities (<10 ft d^{-1}) which dominate the oil recovery process in real reservoirs (Williamson et al., 2020).

The petrochemical industry is interested in the study of velocities lower than 10 ft d^{-1} which is equivalent to 35 μm s^{-1}. Therefore, it is important to understand the limits in flow detection using NMR. Packer, (1969) first studied slow coherent motion with CPMG-based NMR sequences. Flow as low as 1 μm s^{-1} has been detected for water flow through a tube (Magdoom et al., 2019). NMR velocity measurements at the order of 60 μm s^{-1} (Spindler et al., 2011) and 25 μm s^{-1} have been recorded for water displacement inside plants (Windt et al., 2006). Williamson et al., (2020) derived the equations for slow flow limits using the PGSE sequence for phase-contrast velocimetry. In the current chapter, we have modified the same equations for the case of the APGSTE sequence. APGSTE has been combined with the RARE imaging sequence for 3D spatial measurements. The strategy of **k**-space sampling has been modified to reduce the signal losses and the whole sequence has been combined with CS enabling measurements in less than 1 h. Ultra-slow velocities from 3.5 up to 53 μm s^{-1} are studied for the first time in a packed bed with pore-scale resolution using this fast technique of velocimetry. The same system is also studied with 3D propagators without spatial resolution which are obtained at the same experimental time as the velocity images and are employed for the first time to detect such slow flows.

4.2 Theoretical Background

4.2.1 Single-Phase Flow in Porous media

There are two different approaches to describing particle flow. On the one hand, the fixed particle approach, also known as the Lagrangian approach, describes motion as the displacement of individual particles. On the other hand, the fixed point approach, also known as the Eulerian approach, describes motion by assigning a time-dependent velocity to each particle. Using the Eulerian approach, the rate of increase of the total momentum of a fluid depends on the bulk flow (advection), its molecular motion (diffusion) and the externally applied forces. The equation of the kinetic energy for an incompressible fluid is described by the Navier-Stokes equation as:

$$-\boldsymbol{\nabla P} + \rho\, \boldsymbol{g}_r + \mu\, \boldsymbol{\nabla}^2 \boldsymbol{u} = \rho \left(\frac{\partial \boldsymbol{u}}{\partial t} + \boldsymbol{u} \cdot \boldsymbol{\nabla u} \right), \tag{4-1}$$

where ρ is the density of the fluid, $-\boldsymbol{\nabla P} + \rho\, \boldsymbol{g}_r$ describes the driving forces of pressure gradient and gravity and $\boldsymbol{u}$ is the local velocity vector (Bird et al., 1987). The combination of these three mechanisms of flow defines the flow behaviour of the fluid.

Figure 4-1 illustrates the types of flow fields. In laminar flow, particles move in smooth layers (laminae) and there is no mixing between the streamlines. Laminar flow is an inherently steady state. In turbulent flow, the streamlines present chaotic fluctuations due to fluid inertia at high flow rates. In dispersive flow, particles that are initially placed at nearby locations follow diverging paths, although the fluid flow may be steady-state. Such dispersive flow behaviour is seen in flow through porous systems and has been studied with simulations (Reynolds et al., 2000).

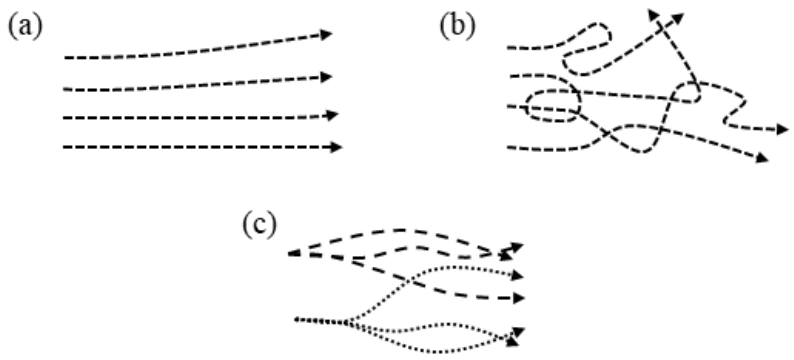

Figure 4-1: Types of flow fields: (a) steady-state laminar flow, (b) turbulent flow and (c) dispersive flow with particles starting on the same streamline and following divergent paths. The different dashed paths represent flow trajectories from different starting points. Adapted from Callaghan, (2011).

4.2.1.1 Dispersion in Bead Packs

Dispersion in microscopically disordered porous media is a stochastic process driven by a kinematic and a dynamic mechanism. The kinematic mechanism arises from the streamlines which divide and rejoin repeatedly along the flow direction. The varying orientations of the flow paths and the coordination numbers of the pore space affect the length and the transverse separation of the streamlines. The dynamic mechanism is based on the flow resistance, the local pressure gradient and the orientation. These two mechanisms recommend two geometrical aspects of dispersion; the longitudinal and the transverse dispersion. The longitudinal dispersion is related to the gradient of velocity along the flow. More precisely, the longitudinal movement of molecules create local velocity variations along the tortuous paths, a process known as mechanical dispersion. Transverse dispersion is related to the gradient of the orthogonal components of the velocity (Scheven, 2013). The transverse dispersion or else self-diffusion affects the kinematic and dynamic mechanisms of dispersion by allowing particles to move from one streamline to another, a process known as asymptotic Taylor dispersion. At the pore level, self-diffusion enables particles to move from boundary layers (slow velocity regions) or dead-end pores to nearby streamlines, a process known as holdup dispersion. The pore structure affects these mechanisms of dispersion since it controls the separation of the streamlines and the local velocities, while it acts as a barrier to diffusion (Sahimi, 2010). The ratio between advection and diffusion is described by the Péclet given by:

$$Pe = \frac{\langle u \rangle \, l_{char}}{D_s}, \tag{4-2}$$

where l_{char} is the effective pore spacing or transport diameter and $\langle u \rangle$ is the average pore space velocity (Manz et al., 1999a; Seymour and Callaghan, 1997b). In a monodisperse bead pack, l_{char} is defined by $d_s \, \phi_b/(1-\phi_b)$, whereas in real rocks, l_{char} is equal to $2\sqrt{8\,F\,k}$, where k the absolute permeability and F is the formation factor. Both of these properties are characteristics for each core plug (Singer et al., 2016). $Pe > 1$ shows that advection is the dominant dispersion mechanism while $Pe < 1$ indicates that diffusion controls the spreading of particles. The dispersion coefficient scales with Pe in mechanical mixing, with Pe^2 in Taylor dispersion and with $Pe \ln Pe$ in the hold-up dispersion (Seymour and Callaghan, 1997b).

The viscous forces of the fluid should also be taken into account to understand better the flow behaviour. A comparison between the viscous and advective forces is achieved by the Reynolds number defined as:

$$Re = \frac{\langle u \rangle \, l_{char} \, \rho}{\mu}, \tag{4-3}$$

where μ is the dynamic viscosity. For water flow through a smooth pipe, laminar flow is epxected at the low Re while the turbulent flow regime is expected at Re >1000-2000 (Callaghan, 2014).

Another important metric, which should be introduced for the description of the flow at the macro-scale, is the dispersivity length, L_v, which demonstrates the distance over which the fluid molecules must travel to sample all the heterogeneities of the porous rock system (Singer et al., 2016). When the particles have scanned the full length of the heterogeneities, the dispersion transits from the pre-asymptotic to the asymptotic regime. In a monodisperse bead pack, $L_v \approx 1.8 \times l_{char}$ and for a mean porosity of 0.36, $L_v \approx d_s$ (Lebon et al., 1997). In the asymptotic regime, mechanical mixing has reached a steady state and the propagator looks like a Gaussian shifted from zero. In this case, the D_s in Eq.(2-44) can be replaced by the $D_{//}$ which is the coefficient of the longitudinal (mechanical) dispersion (Scheven and Sen, 2002).

4.2.1.2 Darcy Flow Behaviour

As shown by Eq.(4-2) and (4-3), the flow behaviour depends not only on the fluid characteristics but also on the properties of the porous medium (l_{char}). Rock properties in petroleum reservoirs are divided into the static properties such as porosity, ϕ, pore size distribution, pore-throat diameter etc and into the dynamic properties such as permeability, k, wettability, fluid saturation and capillary pressure, P_{cap} (Satter and Iqbal, 2016). Permeability indicates how easily the reservoir fluids can pass through a porous medium and it is the main parameter of distinction between convention (k > 0.1 mD) and unconventional reservoirs (Canadian Society for Unconventional Resources, 2012; DeSorcy et al., 1994). For a laminar flow field through a homogeneous porous medium, the interstitial velocity of the fluid also known as Darcy velocity is given by (Darcy, 1856):

$$\boldsymbol{u} = -\frac{k}{\mu} \nabla \boldsymbol{P}. \tag{4-4}$$

In assumption of laminar flow, $\boldsymbol{u}$ does not present any change with time or space.

4.2.2 Flow MRI at Ultra-Slow Velocities

4.2.2.1 Pulse Sequences for Spatially-Resolved Flow MRI

As mentioned in Section 2.3, phase encoding gradients are employed in PFG methods to quantify fluid displacement. In this work, two different spatially-resolved techniques were used to detect fluid flow; the velocity mapping and the spatially-resolved propagators. The same pulse sequence was utilized for both of these techniques. As descussed in L. Wang et al., 2019, low-velocity non-Darcy phenomena appear in low-permeability rocks. Low-permeability rocks dominate oil reservoirs. This is why it is important to employ these techniques for systems with fast T_2 relaxation times and strong internal gradients. As a

result, the APGSTE-RARE sequence presented in **Figure 4-2** was chosen as the most appropriate for slow flow spatially-resolved measurements. The use of bipolar gradients in the APGSTE sequence reduces the effect of echo attenuation due to diffusion, while the stimulated echo enables the use of a large Δ which is necessary for slow liquid flow (Cotts et al., 1989). In the subsequent RARE module, crusher gradients of 2% g_{max} around all the refocusing pulses were used to remove unwanted phase incoherence. The $\boldsymbol{k}_{read}$ dimension is frequency encoded while the $\boldsymbol{k}_{phase1}$ and $\boldsymbol{k}_{phase2}$ dimensions are phase encoded. This is achieved by applying two identical phase encoding gradients within the inter-refocusing interval. The RARE echo train was obtained with the XY-8 phase cycling (Gullion et al., 1990) which has presented the same echo stability and phase coherence as the modified CPMG sequence (Carr and Purcell, 1954; Meiboom and Gill, 1958). The phase encoding gradients are incremented after the acquisition of each pair of odd and even echoes. The combination of echoes leads to better accuracy of the velocity measurements as shown by Huang et al., (2017). For each **q**-space point, two identically phase-encoded datasets are obtained for each odd and even echo. Thus, the total experimental time is inversely proportional to $N_{echo}/2$ instead of N_{echo} as the conventional RARE sequence. More details regarding the APGSTE-RARE sequence are provided by de Kort et al., (2018) who developed the sequence.

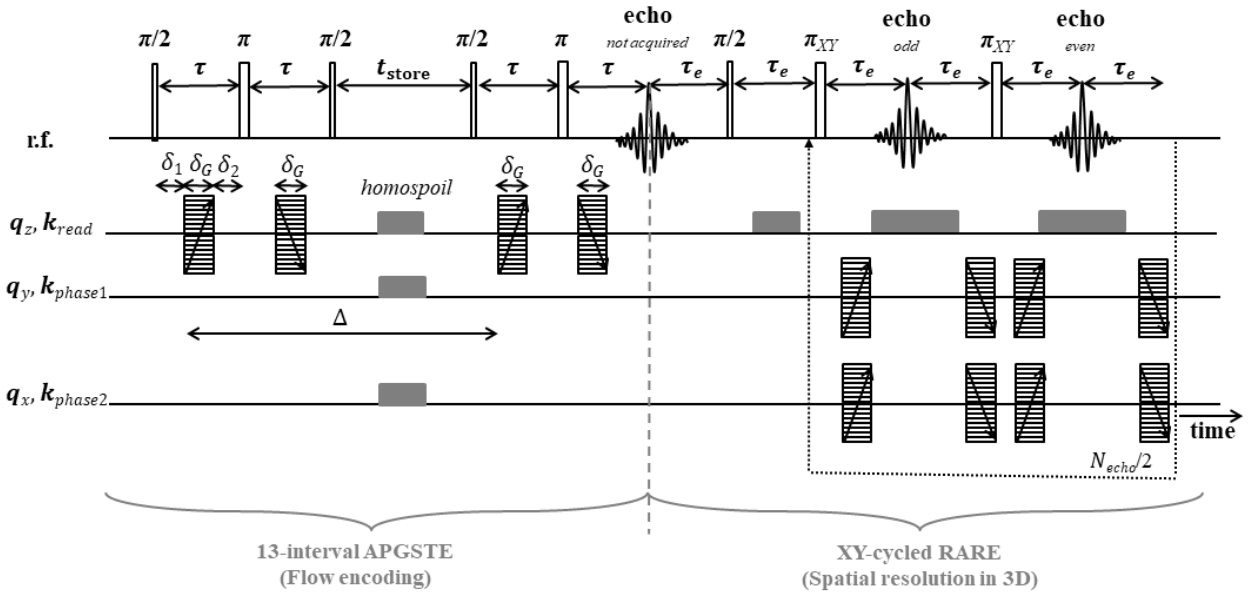

Figure 4-2: Schematical representation of the APGSTE-RARE sequence used to acquire 3D spatially-resolved velocity maps and propagators. The 13-interval APGSTE sequence is followed by a RARE echo train with XY phase cycling. Each pair of odd and even echoes is identically phase-encoded so that two individual datasets for each **q**-space point can be obtained and averaged during post-processing. Adapted from de Kort et al., (2018).

4.2.2.2 Theory of Phase Contrast Velocimetry

Advective (coherent) flow is related to a phase angle φ which is the angle between the real and imaginary channels of the receiver. The linear relationship between the phase angle and the mean velocity $\langle u \rangle$ for the APGSTE-RARE sequence shown in **Figure 4-2** is given by:

$$\varphi = \mathrm{q}\,\langle u\rangle \Delta, \tag{4-5}$$

where $\mathrm{q} = \gamma\,(2\,\delta) g$. The measured phase shift is affected by additional experimental parameters such as α_n which accounts for phase contributions that depend on q and σ_φ which is the noise in the phase of the obtained signal. If the in-phase and quadrature components are assumed to have equal and uncorrelated noise in each complex image then the noise can be measured as:

$$\sigma_\varphi^2 = \frac{\sigma_n^2}{|S|^2} = \frac{1}{\mathrm{SNR}^2}, \tag{4-6}$$

where σ_n^2 is the standard deviation of the background noise measured from four regions on the background of the image as described in Section 3.5.4 and $|S|$ is the mean magnitude of the signal for a ROI inside the sample (Pelc et al., 1991).

The phase-contrast velocimetry is based on the subtraction of the phase image acquired at g_1 from the phase image acquired at g_2 for a Δ observation time. This technique cancels phase contributions not related to flow such as to eddy current distortions (Shukla et al., 2016). The difference between two **q**-data points is known as the 'two-point' method and enables the measurement along one direction to examine the motion in that direction. The phase shift with the inherent noise measured using this method is written as:

$$\varphi_2 - \varphi_1 \approx \gamma\ 2\ \delta_G\ (g_2 - g_1)\Delta\ \langle u\rangle + \alpha_n + \sigma_\varphi. \tag{4-7}$$

One way to remove phase contributions that are not related to the flow is the acquisition of a zero flow phase-shift map, φ_0. Considering $\Delta\varphi = \varphi_2 - \varphi_1$, the resulting phase shift map after subtracting the no-flow phase image can be written as:

$$\Delta\varphi - \varphi_0 = \gamma\ 2\ \delta_G\ (g_2 - g_1)\ \Delta\ \langle u\rangle + \sigma_\varphi - \sigma_{\varphi_0}. \tag{4-8}$$

where σ_{φ_0} is the imparted error for each spin at no-flow conditions. In most experiments, the gradients are of equal but opposite amplitude g. Therefore Eq.(4-8) can be written as:

$$\Delta\varphi - \varphi_0 = -\gamma\ (2\ \delta_G)\ (2\ g)\ \ \Delta\ \langle u\rangle + \sigma_\varphi - \sigma_{\varphi_0}. \tag{4-9}$$

As shown by Eq.(4-9), the measurement of the phase map, $\Delta\varphi$, depends on the σ_φ and therefore on the SNR of the velocity image. Working in slow flow rates results in a lower phase imparted in each isochromat, making the measurements prone to phase errors (Magdoom et al., 2019). Except for SNR, linearity between the imposed velocity-encoding gradient and the phase of the NMR signal should be tested in these slow-flow regimes. This is because the φ-g linearity is distorted as Δ and g are increased (Shukla et al., 2016).

4.2.2.3 Challenges in Ultra-Slow Flow Detection with MRI

Williamson et al., (2020) derived all the mathematics for the detection of the slow flow regime using the PGSE sequence. The same analysis is made here for the equations used in the '13-interval' APGSTE sequence which is the sequence deliberately used in this thesis for diffusion and flow measurements.

To better understand the limits in flow detection, it is necessary to separate the slow- from the fast-flowing regime. There is a critical velocity, u_{SF}, which can separate the slow- from the fast-flowing regime defined as:

$$u_{SF} = \frac{\pi}{2}\sqrt{\frac{2\,D_{app}}{\Delta}}. \tag{4-10}$$

If the mean velocity of the spins is given by $\langle u \rangle$, the echo attenuation from flow and diffusion using the 13-interval APGSTE is written as:

$$E_{diff}(\mathrm{q}) = \exp\left(i\,\langle u\rangle\,\Delta\,\mathrm{q}\; - D_{app}\frac{\mathrm{q}^2}{4}\left(4\,t_{store} + 6\,\tau - 2\frac{\delta_G}{3}\right)\right), \tag{4-11}$$

while the echo attenuation coming from T_1 and T_2 relaxation can be written as:

$$E_{relax} = \frac{1}{2}\exp\left(-{}^{t_{store}}/_{T_1}\right)\exp\left(-{}^{2\tau_e}/_{T_2}\right), \tag{4-12}$$

where the factor $1/2$ appears in the formula for the stimulated echo (Tanner, 1970) showing that half of the initial signal amplitude is returned. The total echo attenuation in the APGSTE part of the sequence is:

$$E(\mathrm{q}) = E_{diff}(\mathrm{q}) \cdot E_{relax}. \tag{4-13}$$

Considering the free water regime, where D_{app} is equal to D_s (2.29 10^{-9} m^2s^{-1} at 25 °C) , δ_G is 1.9 ms, Δ is 750 ms and g is scaled for 101 increments between -9.09 up to +9.09 mT m^{-1}, the signal attenuation indicated by Eq.(4-11) is plotted for interstitial velocities of 1, 10, 20 and 80 ft d^{-1} in Figure 4-3. For this experiment, the separation between the two regimes occurs at u_{SF}= 35 ft day^{-1}. Figure 4-3 shows that for $\langle u \rangle \leq 35$ ft d^{-1} the imaginary signal lobes (red line) are slightly higher than the noise. For the chosen parameters, it is difficult to measure flow velocities of 1 ft d^{-1} because the signal attenuates before showing any detectable phase shift. For the higher velocities of 10 and 20 ft d^{-1}, the heights and the depths of the imaginary lobes are easily distinguishable, enabling the measurement of the flow in the presence of noise with good precision.

In the fast-slow regime, multiple imaginary lobes are resolvable and the peak of each lobe can be found at:

$$\mathrm{q} = \pm\,\pi\frac{1 + 2\,N}{2\,\langle u\rangle\,\Delta}, \tag{4-14}$$

where N is the number of the lobe defining the first lobe as zero. The parameters in the fast-flowing regime should be chosen so that phase wrapping is avoided. To avoid flow aliasing the **q**-data point should be sampled following the condition:

$$\mathrm{q}_{fast} = \frac{\pi}{\langle u \rangle \, \Delta}. \tag{4-15}$$

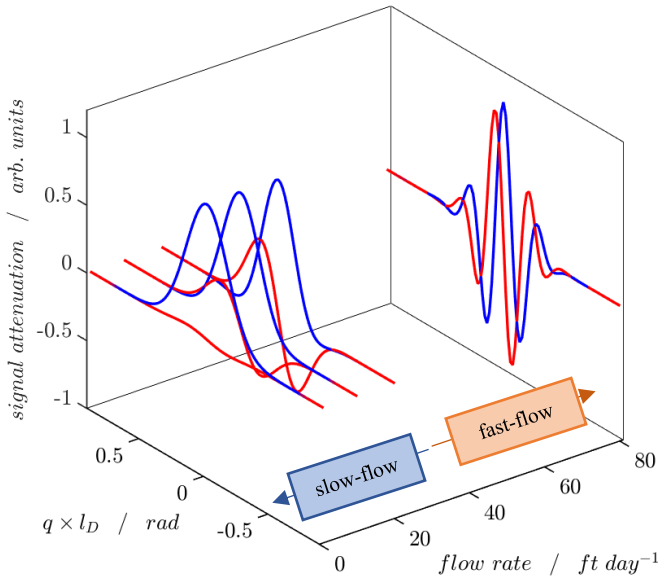

Figure 4-3: Schematic representation of the real and imaginary part of the echo attenuation signal simulated for 101 **q**-data points acquired with the 13-interval APGSTE sequence for an interstitial flow of 1, 10, 20 and 80 ft d^{-1} in the free water system. Adapted from Williamson et al., (2020).

In this case, the standard deviation of the velocity, σ_u, measured from the 'two-points' method (Pelc et al., 1991) using gradients of the equal amplitude but opposite direction defined as $\mathrm{q}_2 = -\mathrm{q}_1 = \mathrm{q}_{fast}$ is given by:

$$\sigma_u = \frac{1}{\sqrt{2}\,\mathrm{SNR}\,\mathrm{q}_{fast}\,\Delta}. \tag{4-16}$$

This σ_u is the minimum detectable velocity, $\langle u_{min} \rangle$, for the fast-flowing regime and it has been divided by $\sqrt{2}$ to account for the acquisition of two **q**-points which are necessary for the phase contrast and for the doubling of the variance when using the two-point method.

However, when $\langle u \rangle < u_{SF}$, measuring q from Eq.(4-15) leads to an overestimation of the q-point required for the detection of the slow-flow regime. This is because diffusive attenuation shifts the first imaginary lobe inwards and attenuates $E_{diff}(\mathrm{q})$ before more additional lobes are resolved as seen in **Figure 4-3**. The **q**-value which corresponds to the highest lobe presents the greatest sensitivity to flow. From Euler's formula, the imaginary component of Eq.(4-11) can be written as:

$$Im\{E_{diff}(\mathrm{q})\} = \sin(\langle u\rangle\, \Delta\, \mathrm{q}) \exp\left(-D_{app}\frac{\mathrm{q}^2}{4}\left(4\, t_{store} + 6\,\tau + 2\frac{\delta_G}{3}\right)\right) \quad (4\text{-}17)$$

The local maximum of Eq.(4-17) is found from the first derivative as:

$$\frac{\langle u\rangle\, \Delta}{\mathrm{q}\frac{D_{app}}{2}(4t_{store} + 6\tau - \frac{2\delta_G}{3})} - \tan(\langle u\rangle\, \mathrm{q}\, \Delta) = 0, \quad (4\text{-}18)$$

which is valid for both the slow- and fast-flowing regime. In the slow-flow regime, $\tan(\langle u\rangle\, \mathrm{q}\, \Delta)$ is very small since the interstitial velocity coming from the pump is small, so the approximation of $\tan(\langle u\rangle\, \mathrm{q}\, \Delta) \approx \langle u\rangle\, \mathrm{q}\, \Delta$ can be valid. Solving Eq.(4-18) for the slow-flow approximation, the optimum **q**-data point is given by:

$$\mathrm{q}_{slow} = \frac{1}{\sqrt{\frac{D_{app}}{2}\left(4t_{store} + 6\tau - \frac{2\delta_G}{3}\right)}}. \quad (4\text{-}19)$$

The slowest detectable velocity, u_{min}, is estimated by the noise σ_φ. Combining Eq.(4-17) with Eq.(4-19) results in signal attenuation of $\exp(-1/2) \approx 0.6$ in the case of D_{app} with narrow distribution. Neglecting this signal attenuation of 0.6 and setting the combination of Eq.(4-17) and (4-19) equal to σ_φ given by Eq.(4-6), the $\langle u_{min}\rangle$ is estimated as:

$$\langle u_{min}\rangle = \sin^{-1}\left(\frac{1}{\mathrm{SNR}}\right)\sqrt{\frac{D_{app}}{4\,\Delta^2}\left(4t_{store} + 6\tau - \frac{2\delta_G}{3}\right)}. \quad (4\text{-}20)$$

In other words, the velocity is detectable when $\langle u\rangle$ in the voxel is higher than $\langle u_{min}\rangle$. It can also be said that the difference $Im\{E_{diff}(\mathrm{q}_1)\} - Im\{E_{diff}(\mathrm{q}_2)\}$ should be greater than the standard deviation of the noise to detect the slow velocities.

All these approximations are valid in a system of coherent flow with D_{app} independent of the time and a propagator represented by a shifted Gaussian. A symmetrical Gaussian propagator is an important parameter for the accuracy of phase-contrast velocimetry (Shukla et al., 2016; Vallatos et al., 2018). For this reason, Δ is optimised so that the mean displacement based on the pump flow rate $\langle\zeta\rangle_0 = Q\,\Delta/(A_c\,\phi)$ is lower than the l_D which for a Gaussian propagator is $\sqrt{2\,D_s\,\Delta}$. This condition is easily achievable for the ultra-slow velocities expected in the low-permeability reservoirs.

In this chapter, the detection of ultra-slow flow velocities will be tested in an ideal porous medium. The choice of the optimum **q**-point for spatially-resolved velocity images was made following the method described above. Validation of the slow flow technique and conclusions regarding the behaviour of the spins at this ultra-slow flow regime are drawn. In addition, 3D propagators were obtained for the same flow rates and the local dispersion coefficients are analysed.

4.3 Materials and Methods

4.3.1 Materials

A cylindrical bead holder was firstly filled with deionised (DI) water and then borosilicate glass beads (Q.A. Equipment Ltd., UK) of 4.0 mm nominal diameter, d_s, were added. The packed bed was connected to a closed flow loop with a syringe pump (Quizix QX-1500HC dual-cylinder syringe pump). Water was flowing through the bead pack for several hours at different flow rates, while the bead holder was held perpendicular to remove all the trapped air bubbles. The internal diameter and length of the bead holder were 38.5 mm and 58 mm, respectively. The porosity of the bead pack, ϕ_b, was measured as 37.6 ± 0.6 % gravimetrically and by implementing mathematical models for a loose random packing of spheres (Roshani, 1990). It is hard to define a unique 'pore size' in a random packing of spheres. A metric of twice the hydraulic radius, r_H, has been defined in the literature as the adequate 'pore size' of a bead pack (Fayed and Otten, 1984). For the current set-up:

$$r_H = \frac{d_s}{6}\frac{\phi_b}{1-\phi_b} \tag{4-21}$$

was measured as 402 μm (Scheven et al., 2004). Hence, the 'pore size' of this bead pack can be considered as ~ 804 μm.

4.3.2 Methods

4.3.2.1 Water Flooding Protocol

The bead holder was connected into a closed flow loop with a syringe pump and was centred inside the birdcage coil and then inside the cylindrical bore of the magnet. Uniform flow was achieved by placing two porous polyethylene distributors plates (SPC Technologies Ltd) at the entrance and the exit of the bead holder. The inner diameter of the tubes between the pump and the bead holder was 1/16″ (1.6 mm). The flow rate was turned on for 1h before the beginning of data acquisition for each separate flow rate.

4.3.2.2 NMR Protocol for Slow Flow Through a Bead Pack

All NMR experiments were conducted at room temperature (20 ± 1°C) in a 2 T (85 MHz for ^{1}H nuclei) horizontal bore superconducting magnet, controlled by a Bruker AV spectrometer. A 63 mm inner diameter r.f. birdcage coil, tuned to 85.2 MHz, was used for excitation and signal detection. Spatial resolution in three orthogonal x, y and z-directions was achieved using a magnetic field gradient, capable of a maximum gradient strength, g_{max}, of 10.7 G cm^{-1}. The z-direction was defined as the direction of superficial flow through the sample. Water flow through the bed was monitored based on the following experimental protocol:

i. spatially-unresolved measurement of T_1 (inversion-recovery sequence)
ii. spatially-unresolved measurement of T_2 (one-shot CPMG sequence)
iii. a high spatially-resolved 3D RARE image of 437.5 μm pixel^{-1} isotropic resolution to generate the under-sampling pattern
iv. a spatially-resolved 3D RARE image of 656.3 μm pixel^{-1} isotropic resolution to measure the relative porosity map for the sample

v. APGSTE-RARE fully-sampled experiments of 2.63 mm pixel^{-1} for 11 **q**-points to prove the linear relationship between the phase and the amplitude of the gradients
vi. 3D spatially-resolved velocity maps of 656.3 μm pixel^{-1} isotropic resolution using APGSTE-RARE with compressed sensing for different slow flows
vii. a fully-sampled velocity map with the same parameters as experiment vi for 15 ft d^{-1} to find the optimum α and Bregman iterations for reconstruction
viii. 3D spatially-resolved propagators of 2.63 mm pixel^{-1} isotropic resolution using APGSTE-RARE with compressed for the same flow rates
ix. a 3D spatially-resolved propagator of 656.3 μm pixel^{-1} isotropic resolution using APGSTE-RARE with compressed sensing for one flow rate to compare with the adequate velocity map

Experiment (i) was acquired to determine the signal loss during t_{store} stimulated echo storage time which depends on Δ, while experiment (ii) was acquired to define the signal attenuation due to the τ inter echo time which changes with δ_G. Signal losses from the RARE part of the sequence were not taken into account since the Scheme B **k**-space acquisition (Section 3.2.2) can guarantee very small losses due to T_2 (Ramskill et al., 2018). 3D propagators of 2.63 mm pixel^{-1} resolution (viii) were designed to obtain flow measurement within the same experimental time as the velocity maps of 656.3 μm pixel^{-1} resolution (vi). Both techniques give useful information for the slow flow regime. The aim is to speed up the acquisition and to use these techniques in the dynamic fast-changing system of a rock sample. In addition, velocity maps encoded along the x, y and z directions were obtained for 3, 6 and 15 ft d^{-1} to give a better understanding of the fluid behaviour by comparing the connected streamlines.

4.3.2.3 Multi-Objective Optimisation Toolbox for Experimental Parameters in Velocity Imaging

To separate flow from noise in the slow-flow regime, the experimental parameters for the slow-flow velocity maps (vi) were chosen carefully. More precisely, Δ, g and δ_G were optimised using a MATLAB multi-objective optimisation function which solves Eq.(4-19) and maximises Eq.(4-13). One important constraint added in the optimisation process is that the mean interstitial velocity coming from the pump,$\langle u \rangle_0 = Q\ /(A_c\ \phi)$, where A_c is the cross-sectional area, should be greater than $\langle u_{min} \rangle$ measured by Eq.(4-20) for the adjustable parameters. Solving the system of Eq.(4-13) and Eq.(4-19) requires knowledge of T_1, T_2 and D_{app} of the sample which are measured by the experiments (i) and (ii), while D_{app} was considered equal to the D_s of the bulk water.

4.3.2.4 NMR Experimental Parameters

A hard 90º pulse of 39.3 μs and a refocusing 180º pulse of 78.7 μs were used. The inversion recovery (**Figure 2-5**) experiment was performed for 16 different t_{VD}. The t_{RD} was defined as 7.25 s ($3\times T_1$) for all the experiments. Then one-shot CPMG (**Figure 2-6**) was obtained for a τ_e of 1.97 ms (50×duration of 90º pulse) for a long echo train until $\boldsymbol{M}$ fully decayed. The FOV for all the 3D spatially-resolved experiments was 84 mm in the $\mathbf{k}_{read}$ dimension and 42 mm in both $\mathbf{k}_{phase}$ dimensions. The Scheme B **k**-space trajectory was implemented in all the spatially-resolved measurements. The parameters chosen for the 3D velocity maps and the 3D propagators were adjusted for each separate flow rate.

The high-resolution image (iii) was obtained with the 3D RARE sequence using 32 echoes, a t_{echo} of 3.4 ms and 4 scans. The number of points acquired in the read dimension, N_{read}, was 192, while N_{phase1} and N_{phase2} were 96 giving an isotropic resolution of 437.5 μm pixel^{-1} along each dimension. The image acquired at the same resolution as the velocity maps (iv) used 32 echoes, a t_{echo} of 2.8 ms and 4 scans. The N_{read} was 128, while N_{phase1} and N_{phase2} were 64 giving an isotropic resolution of 656.3 μm pixel^{-1}. Image (iii) required almost 3 h while image (iv) needed 2 h. Both images have pore-scale resolution since the r_H from Eq.(4-21) was measured as 804 μm.

In the velocity mapping, the matrix of **k**-points was defined the same as in the 656.3 μm pixel^{-1} image. The **k**-space was under-sampled by 25% following the Scheme B trajectory of sampling. The $\boldsymbol{k}_{read}$ was defined as the flow-encoding dimension and is the same as the flow direction. Based on Section 4.3.2.3, the optimum experimental parameters for all the applied flow velocities are summarized in **Table 4-1**. The total acquisition time for each experiment was 56 min for 4 averages and 32 echoes.

Table 4-1: Experimental parameters for phase-contrast imaging.

$\langle \boldsymbol{u_0} \rangle$ (ft d^{-1})	$\boldsymbol{\Delta}$ (ms)	$\boldsymbol{\delta_G}$(ms)	$\boldsymbol{g_{factor}}$
1	201.4	1.4	35.5%
3	80	5.0	17.3%
6	91.4	1.6	47.6%
10	62.7	1.2	74.1%
15	24	1.5	96%

For 6, 10 and 15 ft d^{-1}, the above-mentioned optimum Δ and δ_G were employed to acquire 11 different **q**-points by changing the g_{factor} from -96% up to +96%. All the **k**-space data were obtained following the Scheme B trajectory and each acquisition required ~ 2.4 h.

Propagators were obtained with the parameters presented in **Table 4-2**. The selection of the suitable **q**-points for the propagator measurements has been described by Scheven et al., (2005). The **q**-space is a reciprocal space like the **k**-space, hence the same rules apply to it. The distance between the **q**-data, Δq, is related to the FOV of the flow field, FOV$_{prop}$, as:

$$\frac{\Delta \mathrm{q}}{2\,\pi} = \frac{1}{\mathrm{FOV}_{prop}}. \tag{4-22}$$

The FOV$_{prop}$ is defined as $5\times\langle\zeta\rangle_0$ for the bead pack system. The **q**-space was scaled up to $2\pi/\sqrt{D_s\Delta}$ and the constraint of maximum $E(\mathrm{q})$ for q=0 rad m^{-1} was added to the optimisation code. The number of **q**-points, N_q, was set to fulfil Eq.(4-22) and to require the minimum time of acquisition. In the current system, 25 **q**-points were encoded along the flow direction (z-direction) for all the different flow rates. The 3D propagator acquired at the same resolution as the velocity maps required ~4 h, while the low-resolution one needed ~40 min for an under-sampling rate of 11%.

Table 4-2: Experimental parameters for spatially-resolved propagator measurements.

$\langle u_0 \rangle$ (ft d^{-1})	Δ(ms)	δ_G(ms)	g_{factor}
1	2070	5.0	96%
3	1100	4.8	96%
6	1250	3.0	67.5%
10	1070	2.4	96%
15	442	3.7	96%

4.3.2.5 Data Procession for Relaxation and Diffusion Coefficient Data

The One-Dimensional (1D) inversion is used for T_1 and T_2 relaxation measurements while the 2D inversion is used for D-T_2 NMR measurements. The numerical methods employed for the data acquired in these sample rocks are the ones included in the in-house code of the Magnetic Resonance Research Centre (MRRC) (J. Mitchell et al., 2012; Mitchell et al., 2013a). More details regarding the inversion process can be found in Bush, (2018).

4.3.2.6 Data Processing of Phase-Contrast Maps

All the velocity maps were reconstructed for an α of 0.095 and 6 Bregman iterations following the optimisation procedure described in Section 3.4.1. In the current experiments, data post-processing is similar to the one described by Huang et al., (2017) and is summarised in the following steps:

1. MR raw datasets of odd and even echoes were measured with the pump switched on and off for the parameters defined for each chosen flow rate.
2. In each flow and no-flow experiment, two velocity encoding gradients of equal magnitude but the opposite direction and the same δ_G were employed.
3. For a single flow rate, the four individual MR raw data are Fourier Transformed yielding a complex-valued MR image.
4. The magnitude of the complex images was averaged to generate a single structural image.
5. By implementing automatic background thresholding in the magnitude image as described in Section 3.5.2, a binary mask was determined for nulling low-intensity areas. Simultaneously a cylindrical mask defined by the 3D RARE image of the same resolution was applied to the FT data.
6. Phase-contrast maps were acquired from the difference between the positive and the negative encoding step for each odd and even echo to remove eddy current phase contributions which are independent of q.
7. Phase unwrapping was performed separately for each odd and even echo at each velocity encoding step. More precisely, the per voxel phase difference between the flow and the no-flow even echo velocity image at +q was compared with an upper and a low bound of phase. For $\varphi_{even,+\mathrm{q}} - \varphi_0 > \pi$ a phase of $2\,\pi$ was subtracted and for $\varphi_{even,+\mathrm{q}} - \varphi_0 < -\pi$ a phase of $2\,\pi$ was added to the total phase difference. The same procedure was followed for the even echo velocity image acquired at -q. The same phase unwrapping process was followed for the odd velocity images acquired at +q and -q. Then the phase map of the -q image was subtracted from the

phase map of the +q image generating $\Delta\varphi - \varphi_0$ (Eq.(4-9)) for both odd and even echoes. This process removes the noise dependency on q.

8. The total phase contrast of the even echoes image was averaged with the negative phase contrast of the odd echoes image to acquire the total phase contrast, $\Delta\varphi_{total}$.
9. The per voxel noise was measured from Eq.(4-20) using as $|S|$ the intensity of each voxel.

The binary mask applied in all the velocity maps was obtained with a signal threshold of approximately 9.2% of the maximum voxel signal.

4.3.2.7 Data Processing of Spatially-Resolved Propagators

Initially, a Gaussian window function with a W of 3.5 was used to erase the truncation artefacts from the under-sampled **q**,**k**-space. The rate of under-sampling was ~11%. Then, the raw data were phase-corrected by the phase of the maximum intensity **k**-point for the central **q** = 0 m^{-1} to prevent the appearance of ghosting artefacts. Finally, CS reconstruction was employed to obtain the FT data as described in Section 3.4. Further denoising was achieved by multiplying the spatially-resolved data with a binary mask. The optimum intensity threshold for the denoising mask was set as 25% times the normalisation intensity.

Nonetheless, several local propagators present small artefacts around the main displacement curve which affect significantly their statistical analysis. To suppress these artefacts of local field distortion, a denoising method was introduced. This method begins by first identifying the data points at approximately $1/2$ of the maximum value of the curve. A random local propagator in the middle of the vial was picked and the two data points which represent the initial ROI are shown in **Figure 4-4**(a). Then the ROI was expanded by 4 points toward the negative and the positive direction of the displacement axis, respectively. **Figure 4-4**(b) shows the final ROI. Then, all the points outside the ROI were set equal to zero smoothening the effect of the artefacts. To account for user mistakes in the definition of the optimum ROI, the arbitrary limit of 4 was changed from 3 up to 10. Then, the standard deviation among all the statistical metrics for all the new ROIs was estimated and integrated into the local error analysis.

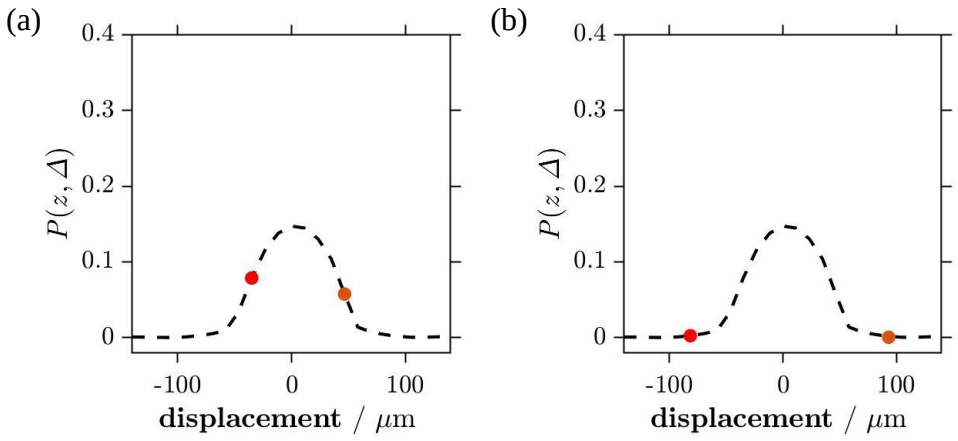

Figure 4-4: (a) Gaussian-shaped curve of the local propagator (black dashed line) and points at approximately $1/2$ of the maximum value (red and orange circles). The left and the right data points of the FWHM were expanded by 4 points towards the negative and the positive direction of the displacement axis creating an ROI as shown in (b).

When the local propagators are skewed, the limit of expansion towards the positive displacement axis is much larger compared to the negative expansion making sure that it covers the full length of the tail.

After implementing all the above-mentioned denoising techniques, more reliable local measurements can be extracted. Given the large amount of data for local propagators, it is mandatory to define some quantitative statistical descriptors to describe the heterogeneity of the flow and to compare the complexity of different flow systems (de Kort et al., 2018a). The key statistical metrics used in this propagator analysis are the mean displacement ζ_i, the broadness of the peak which is given from the standard deviation σ_i and the skewness γ_i of the curve for the phase i. Considering as $P(\boldsymbol{r}, \Delta)$ the local propagator curve and $\boldsymbol{r}$ the displacement along the flow-encoded direction over an observation time Δ, the statistical metrics are given by:

$$\zeta_i = \frac{\int P(\boldsymbol{r}, \Delta)\, \boldsymbol{r}\, d\boldsymbol{r}}{\int P(\boldsymbol{r}, \Delta)\, d\boldsymbol{r}} \tag{4-23}$$

$$\sigma_i = \sqrt{\frac{\int P(\boldsymbol{r}, \Delta)(\boldsymbol{r} - \mu)^2\, d\boldsymbol{r}}{\int P(\boldsymbol{r}, \Delta)\, d\boldsymbol{r}}} \text{ and} \tag{4-24}$$

$$\gamma_i = \frac{\int P(\boldsymbol{r}, \Delta)\, (\boldsymbol{r} - \mu)^3 d\boldsymbol{r}}{\sigma_i^3 \int P(\boldsymbol{r}, \Delta)\, d\boldsymbol{r}}. \tag{4-25}$$

These statistical metrics were used to analyse all the propagators acquired with the 3D APGSTE-RARE sequence in this thesis. In the case of slow flow through a bead pack, all the local propagators present a Gaussian shape tilt from zero. The local σ for each propagator was measured from Eq.(4-24). In a Gaussian-shaped propagator described by Eq.(2-44), the local σ is related to the coefficient of the longitudinal-mechanical dispersion, $D_{//}$, from the advection-diffusion equation as:

$$D_{//} = \sqrt{\frac{\sigma^2}{2\,\Delta}}. \tag{4-26}$$

4.3.2.8 Data Processing for Relative Porosities and Measured Flow Rates

The relative porosity in each voxel $\boldsymbol{r}$, $\phi_{rel}(\boldsymbol{r})$, was measured from the 3D RARE image of 656.3 μm pixel^{-1} resolution as:

$$\phi_{rel}(\boldsymbol{r}) = I(\boldsymbol{r}) \frac{\phi\, V_{sample}}{V_{voxel} \sum I(\boldsymbol{r})}, \tag{4-27}$$

where V_{sample} is the volume of the cylindrical sample, V_{voxel} is the volume of each voxel, $I(\boldsymbol{r})$ is the intensity of each voxel, $\sum I(\boldsymbol{r})$ is the total intensity coming from all the voxels which belong to the sample area and ϕ is the macroscopic porosity of the sample. In the bead pack, some voxels contained only the water phase and some others both the water and the solid phase of the bead. In this case, ϕ was defined as 1 and not as ϕ_b.

The measurement of $\phi_{rel}(\boldsymbol{r})$ was important for the measurement of the mean volumetric velocity. To calculate the volumetric velocity, the measured per-voxel $u(\boldsymbol{r})$ from the velocity maps or the local propagators is multiplied by the $\phi_{rel}(\boldsymbol{r})$ and the voxel cross-sectional area. Then, all these local flux measurements are summed along the z-direction resulting in the 1D mean volumetric velocity. In the case of the bead pack, $\phi_{rel}(\boldsymbol{r})$ used in the mean volumetric velocity coming from the propagator results was considered as equal to ϕ_b since there is no pore-scale resolution. In the mean volumetric velocity coming from the phase-contrast imaging, $\phi_{rel}(\boldsymbol{r})$ derived from Eq.(4-27). Moreover, the mean volumetric velocity can be compared to the Q set by the pump in the bead pack experiment since relaxation effects are negligible.

4.4 Results

4.4.1 Relaxation Measurements

Figure 4-5 shows that only a unique peak is observable for the system of the bead pack. The small peak in the T_2 distribution is considered an artefact. The measured T_1 was 2.34 s while the long T_2 was 2.2 s.

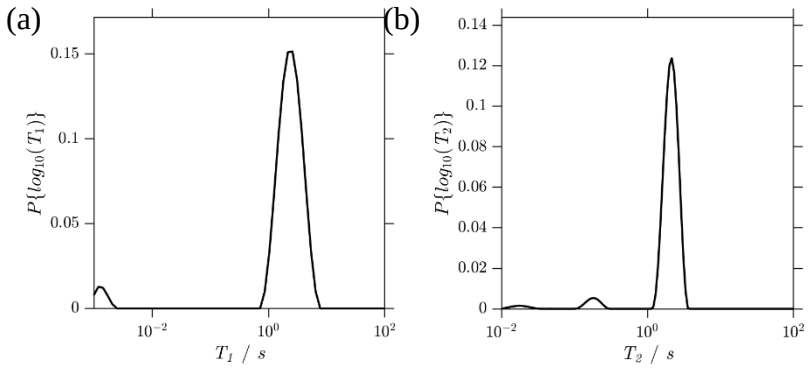

Figure 4-5: T_1(a) and T_2(b) distributions coming from the inversion recovery and the CPMG sequence for the bead pack filled with water and 4 mm beads in diameter.

4.4.2 Linear Relationship Between the Phase and the Gradients

It is important to assess the validity of the linear relationship between the imparted φ and the applied g in a flowing system (Shukla et al., 2016; Vallatos et al., 2018). **Figure 4-6** shows the average phase, $\langle\varphi\rangle$, for a ROI of 16 voxels in the middle of the FOV as a function of g for three different flow rates.

The values of Δ and δ_G were derived from the multi-objective optimisation as described in Section 4.3.2.3, while was g scaled. The value of $\langle\varphi\rangle$ for each g was measured from the phase of the complex signal. Eq.(4-5) shows the linear relationship between $\langle\varphi\rangle$, Δ and g. A dashed line was fitted to the linear region. Shukla et al., (2016) have shown that the linear relationship is lost for large values of Δ and g as well as for increased flow rates if all the experimental parameters are kept constant. In **Figure 4-6**(a), the change of $\langle\varphi\rangle$ with g is presented for 6 ft d^{-1} velocity using a Δ of 91.4 ms and a δ_G of 1.6 ms. The optimum g was 47.6 % × g_{max} (red diamond) and is inside the linear region (dashed line). Similarly, **Figure 4-6**(b) and (c) show that the optimum g defined by the optimisation process (red diamond) for 10 and 15 ft d^{-1} were inside the limits of the linear area.

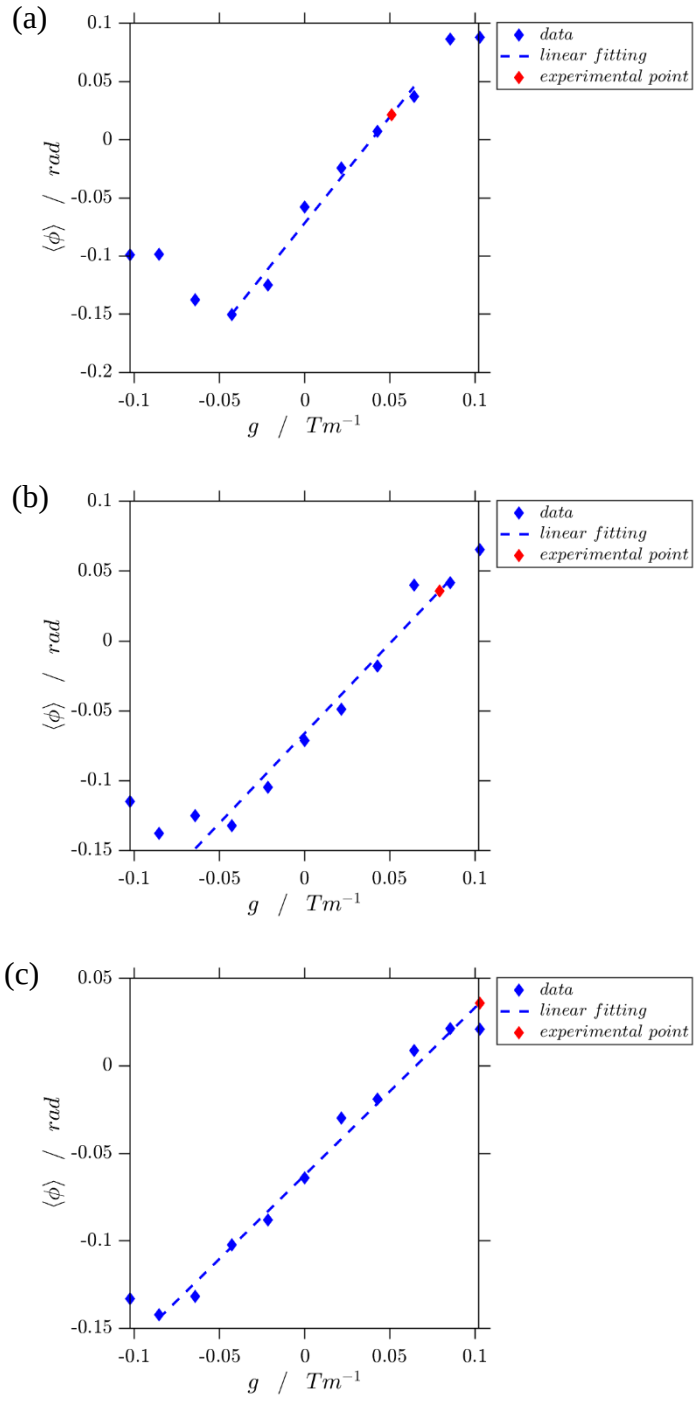

Figure 4-6: Phase shift as a function of the gradient amplitude for 6(a), 10(b) and 15(c) ft d^{-1} water flow through a bead pack. The red data point shows the optimum g defined for the slow flow velocity maps by the multi-objective optimisation and the dashed line indicates the area where φ and g are linear.

4.4.3 Noise Analysis in Phase-Contrast Imaging

After confirming the linear relationship between the phase and the g, it is important to assess the local noise in the velocity measurements. One way of assessing the local noise is by acquiring five successive velocity maps under the same experimental conditions and for the same parameters (Murphy et al., 1993). Then, the per voxel standard deviation of the

local velocity is assessed for each experiment. **Figure 4-7**(a) shows the standard deviation among five successive velocity maps for 6 ft d^{-1} and **Figure 4-7**(b) for 15 ft d^{-1}. The colourmap in both velocity maps is scaled between ± 5×$\langle u \rangle_0$. It can be seen that both figures are dominated by the green colour which indicates a standard deviation of the velocity around 0 μm s^{-1}.

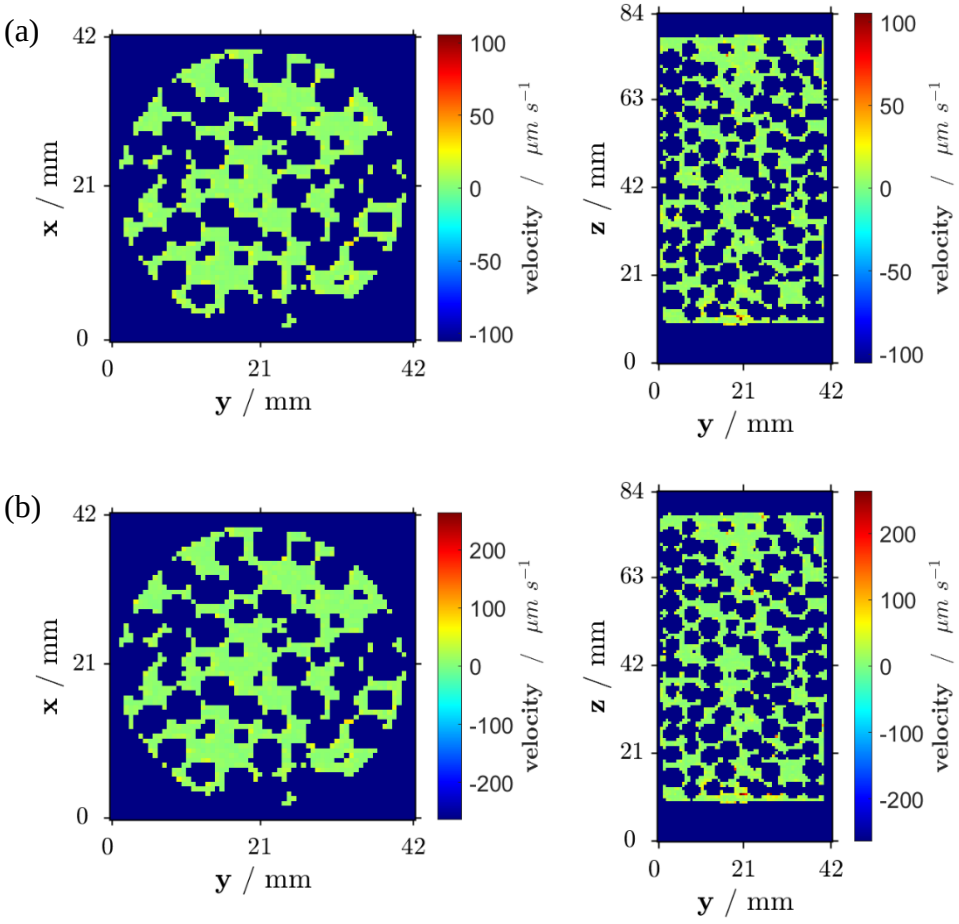

Figure 4-7: The middle *x*-*y* slice and *z*-*y* slice of the standard deviation between 5 velocity maps acquired under the same conditions using the same experimental parameters for 6(a) and 15(b) ft d^{-1}.

A further assessment of the local noise in the velocity for 1 ft d^{-1} is given in **Figure 4-8**. Firstly, the magnitude of the complex images for the odd and even echoes acquired for the +q and -q points was averaged. The intensity image at no-flow conditions coming from the average of the intensity of each is presented in **Figure 4-8**(a). Four regions in the background were selected and are indicated by the squares. The standard deviation of the voxel intensity within these squares was considered as the σ_n. In this case, the SNR of each voxels was measured by Eq.(3-12), considering A equal to the intensity of each voxel, $I(\boldsymbol{r})$. Based on these, the local error in the velocity, σ_u, was measured from Eq.(4-20) and is shown in **Figure 4-8**(b). Thirdly, the velocity map for the same *x*-*y* slice derived from the process described in Section 4.3.2.5, is shown in the **Figure 4-8**(c), while the $\phi_{rel}(\boldsymbol{r})$ map is presented in **Figure 4-8**(d). The voxels at the interface of the liquid and the solid phase are partially filled with water and they are coloured differently than dark red.

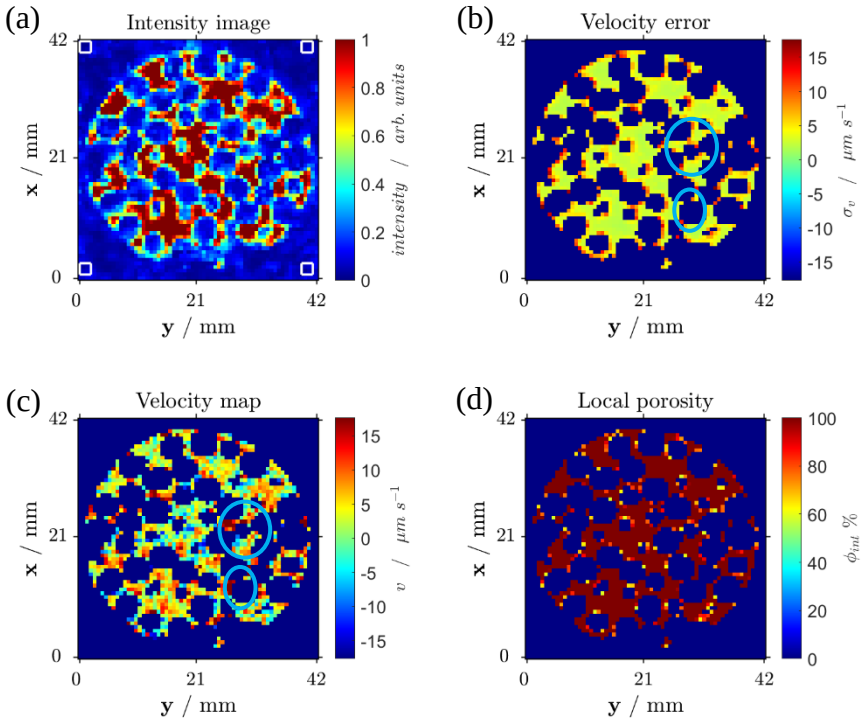

Figure 4-8: The middle x-y slice of the bead pack is analysed for its average intensity for the odd and even echoes and the -q and +q acquisitions showing the four background regions accounted in the standard deviation of the background noise in the SNR measurements (a), its local velocity error σ_u (b), its velocity maps (c) and its relative porosity (d) for 1 ft d^{-1}.

The 1 ft d^{-1} is the experiment with the highest noise since the imparted phase-shift of the spins is the smallest tested. Both σ_u and $u(\boldsymbol{r})$ maps have been coloured in a similar way to allow easy visual comparison. **Figure 4-8**(b) shows that σ_u is larger for the voxels that belong in the interface between the water and the beads phase. However, by comparing **Figure 4-8**(b) and (c), it can be concluded that in the area of the bulk liquid (between the beads), the measured local velocity, $u(\boldsymbol{r})$, is significantly higher than the corresponding $\sigma_u(\boldsymbol{r})$. Therefore, the novel technique enables the measurement of the local velocities with small noise even at 1 ft d^{-1}. The same noise analysis was conducted for the higher flow regimes, showing an even smaller $\sigma_u(\boldsymbol{r})$ compared to the measured $u(\boldsymbol{r})$. The results for the other flow regimes are not analysed here due to space limitations.

4.4.4 Velocity Maps from Phase-Contrast Imaging

After proving that local noise is minor in most of the areas of bulk liquid, all the velocity maps are presented in **Figure 4-9** and **Figure 4-10** and the colourmaps are scaled as ± 5×$\langle u \rangle_0$. The l_{char} for this monodisperse bead pack was 2.4 mm, the μ for the water at 25°C is 8.9 10^{-4} Pa·s and the ρ is 997 10^{-3} g cm^{-3}. Figure 4-9 shows the velocity map for 1(a) and 3 ft d^{-1}(b). In both cases, the large σ_u in the solid/liquid interface leads to large error in the mean value.

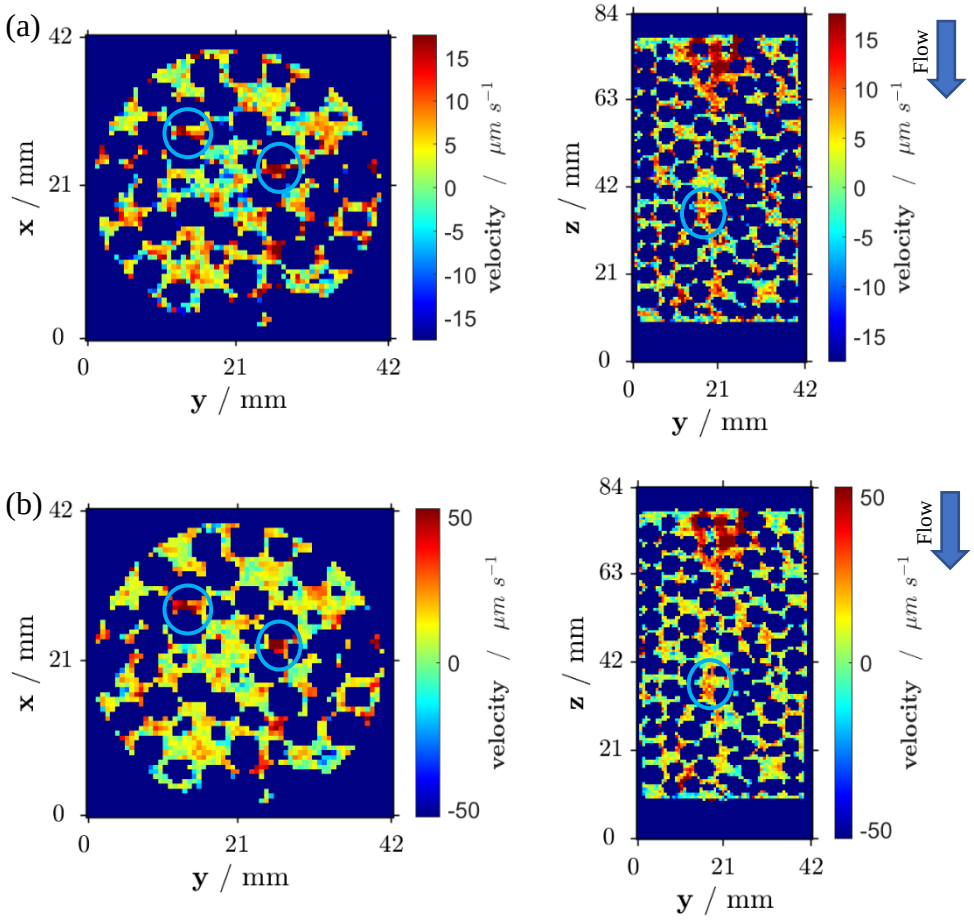

Figure 4-9: The middle x-y and z-y slices of the velocity maps for water flow through the bead pack at 1(a) and 3(b) ft d^{-1}. Interesting areas for comparison are shown by the light blue circles.

Figure 4-10 indicates the velocity map for 6(a), 10(b) and 15 ft d^{-1}(c). The results for the mean measured velocity, $\langle u_m \rangle$, from the phase-contrast velocity maps presented in **Figure 4-9** and **Figure 4-10** and the corresponding Pe and Re for each applied Q are summarized in **Table 4-3**. All the velocity maps present a red region of high-velocity flow paths in the middle area of the bead pack. A great agreement between the externally imposed and the measured velocities can be seen in **Table 4-3**. The large mean error in the $\langle u_m \rangle$ for the 1 and 3 ft d^{-1}, is mainly due to the high values of σ_u in the solid/liquid interface. This error is also an indication of the $\langle u_{min} \rangle$ that can be detected for the chosen optimum parameters. Interesting high velocity areas have been circled by the light blue line and are observed in all the flow regimes.

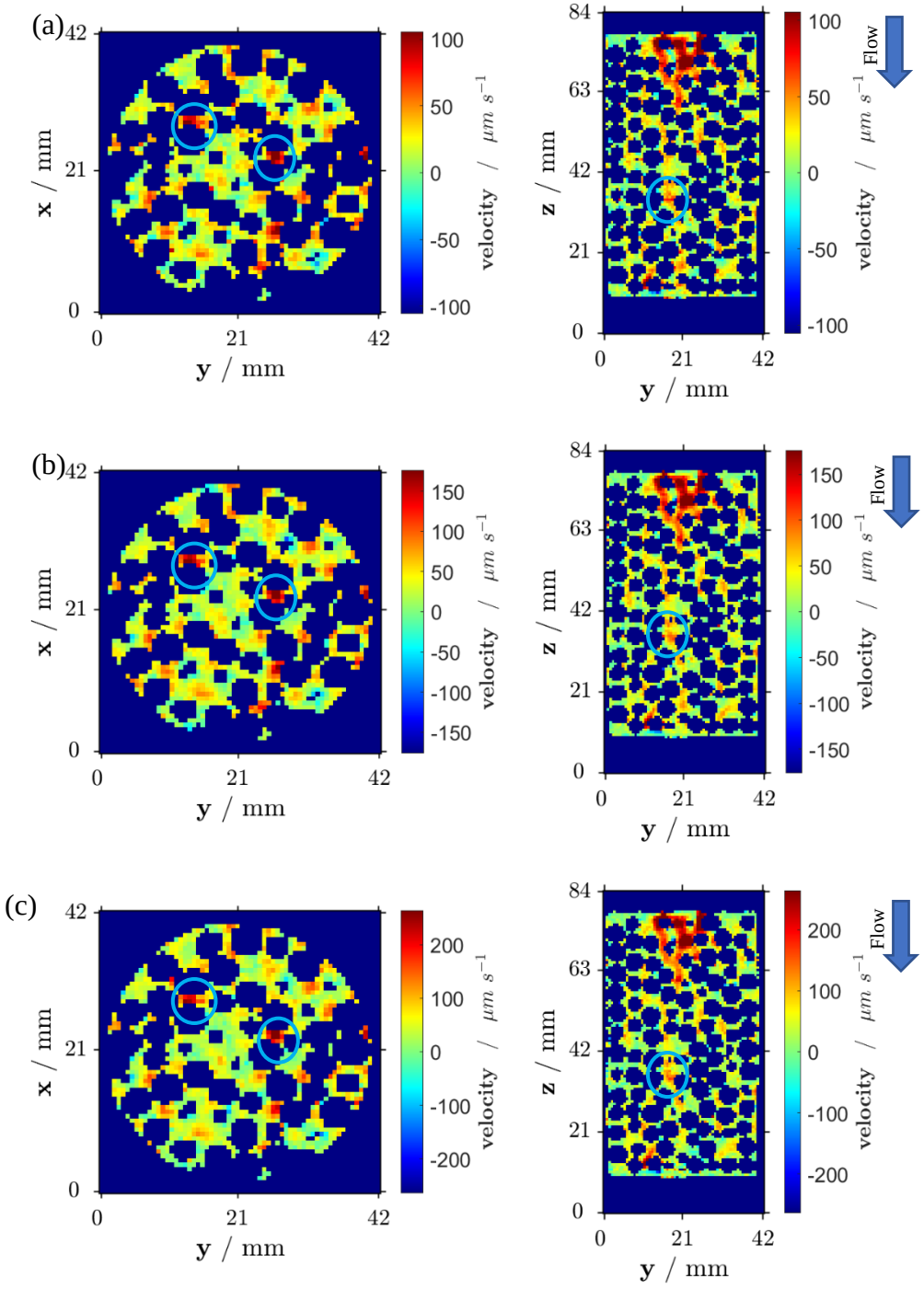

Figure 4-10: The middle *x*-*y* and *z*-*y* slices of the velocity maps for water flow through the bead pack at 6(a), 10(b) and 15(c) ft d^{-1}. Interesting areas for comparison are shown by the light blue circles.

Table 4-3: Summary of the Q, Pe, Re and the mean measured interstitial velocity, $\langle u_m \rangle$, from the phase-contrast imaging for 1, 3, 6, 10 and 15 ft d^{-1}.

$\langle u_0 \rangle$ (ft d^{-1})	Q (mL min^{-1})	Pe	Re (10^{-3})	$\langle u_0 \rangle$ (μm s^{-1})	$\langle u_m \rangle$ (μm s^{-1})
1	0.09	3.7	9.5	3.5 ± 0.1	3.5 ± 3.3
3	0.28	11.2	28.6	10.6 ± 0.2	10.2 ± 4.8
6	0.56	22.3	57.3	21.1 ± 0.4	19.4 ± 4.9
10	0.93	37.2	95.5	35.3 ± 0.7	31.9 ± 8.1
15	1.36	55.8	143.3	52.9 ± 1.0	43.7 ± 9.8

4.4.5 Average Volumetric Velocity Profile from Phase-Contrast Imaging

Figure 4-11 presents the mean volumetric velocity profile measured by the phase-contrast velocimetry in parallel with the flow rate imposed by the pump (dashed yellow line). The great agreement between the measured and externally imposed Q is another proof for the great accuracy of the phase-contrast imaging in measuring ultra-slow velocities.

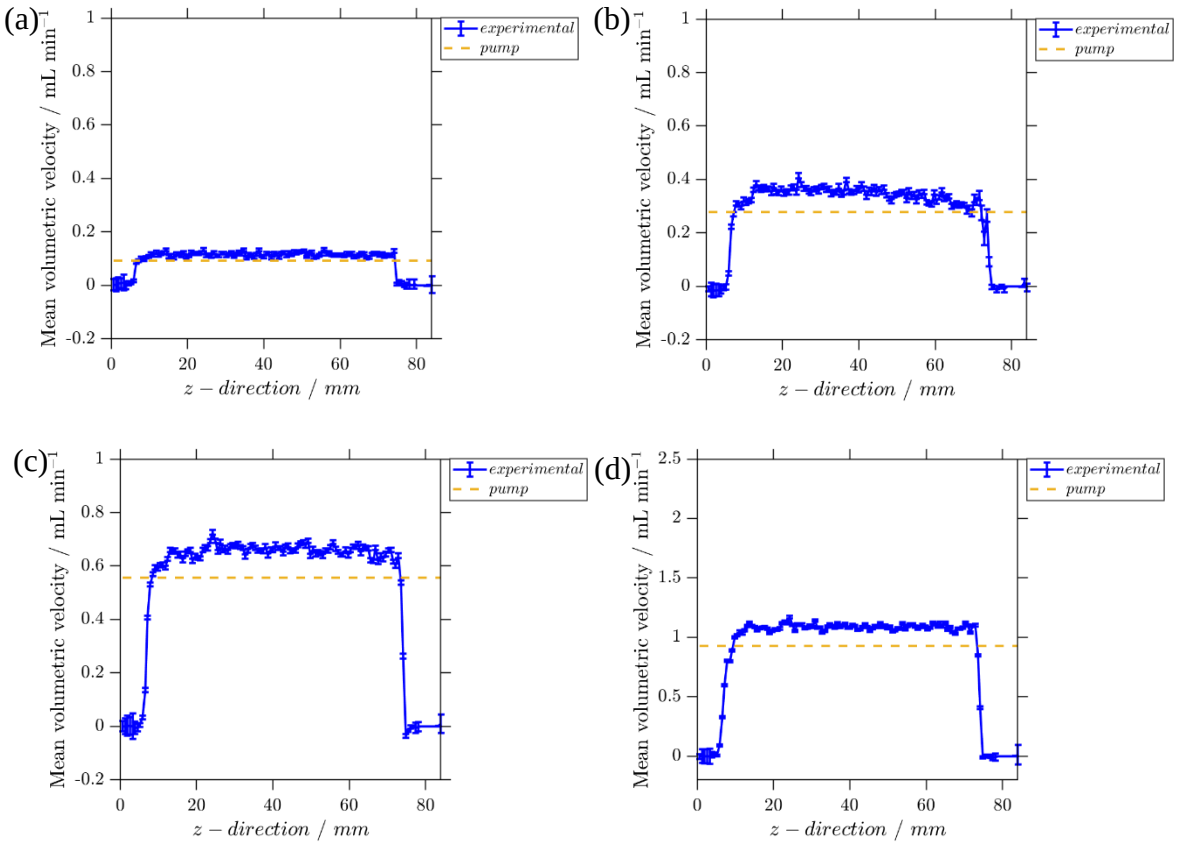

Figure 4-11: Mean volumetric velocity profiles measured by the phase-contrast velocimetry for water flow through the bead pack at 1(a), 3(b), 6(c) and 10(d) ft d^{-1}.

4.4.6 Spatially-Resolved Propagator Measurements

The spatially-resolved propagators have been used for the analysis of $D_{//}$. The $D_{//}$ map and its distribution across the bead pack are presented in **Figure 4-12** and **Figure 4-13**.

The $D_{//}$ maps were acquired in the same bead pack as the velocity maps in **Figure 4-9** and **Figure 4-10**. However, the propagator measurements cannot be directly compared to the velocity maps since they were not obtained at pore-scale resolution. Each voxel contains information on both the liquid phase and the solid phase. **Figure 4-12**(a) and (b) show the results obtained for 1 and 3 ft d^{-1}, respectively. The measured values of $D_{//}$ appear similar across the whole sample. In both cases, the $D_{//}$ presents narrow distributions around 1.95 10^{-9} and 2.2 10^{-9} m^2 s^{-1}. $D_{//}$ is slightly lower than D_s due to the effect of restricted diffusion coming from presence liquid and the solid phase within a single voxel.

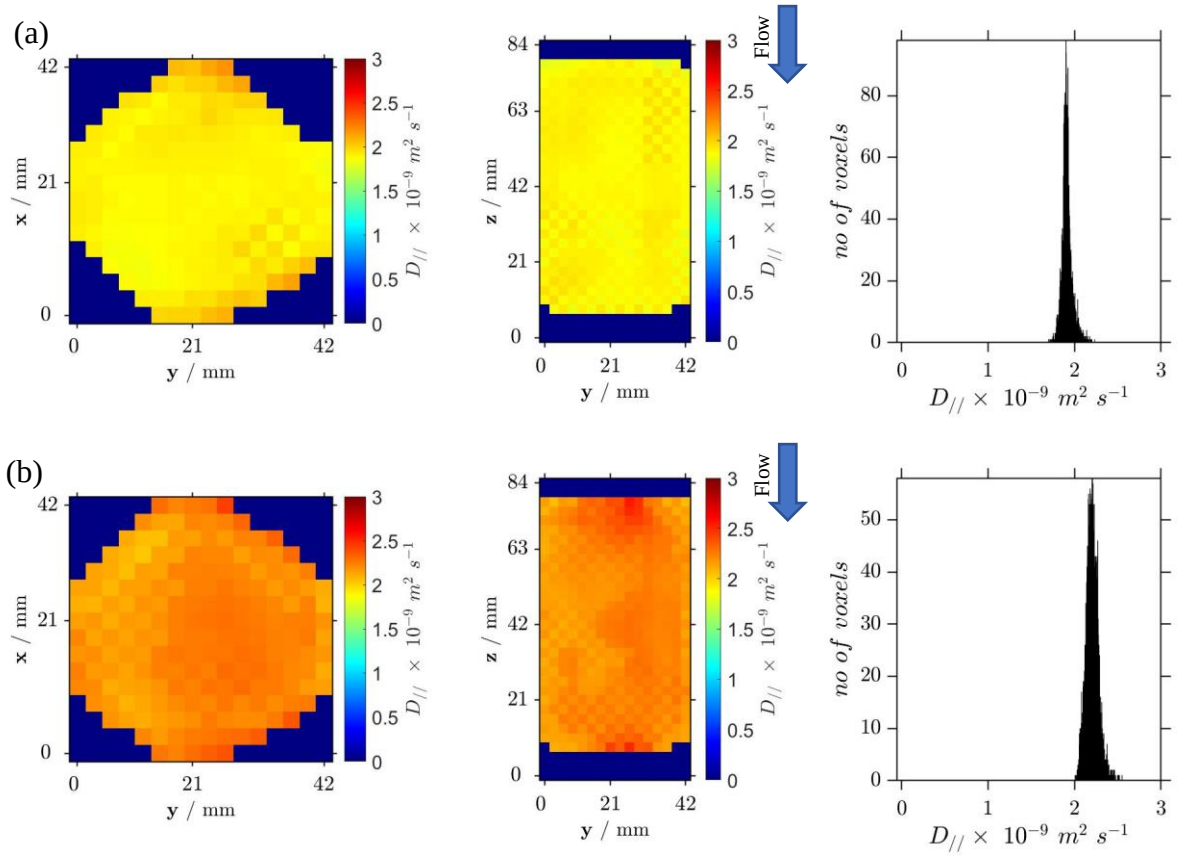

Figure 4-12: Local $D_{//}$ along the flow direction measured from the Gaussian-shaped propagators for water flow through the bead pack at 1(a) and 3(b) ft d^{-1}.

Figure 4-13 illustrates the $D_{//}$ map for the velocities of 6, 10 and 15 ft d^{-1}. A broad distribution of $D_{//}$ was seen, with the highest values in the middle area of the inlet and close to the right side of the outlet. The mean $D_{//}$ in **Figure 4-13**(a) was 2.6 10^{-9} m^2 s^{-1} , in **Figure 4-13**(b) was 2.9 10^{-9} m^2 s^{-1} and **Figure 4-13**(c) was 3.2 10^{-9} m^2 s^{-1}.

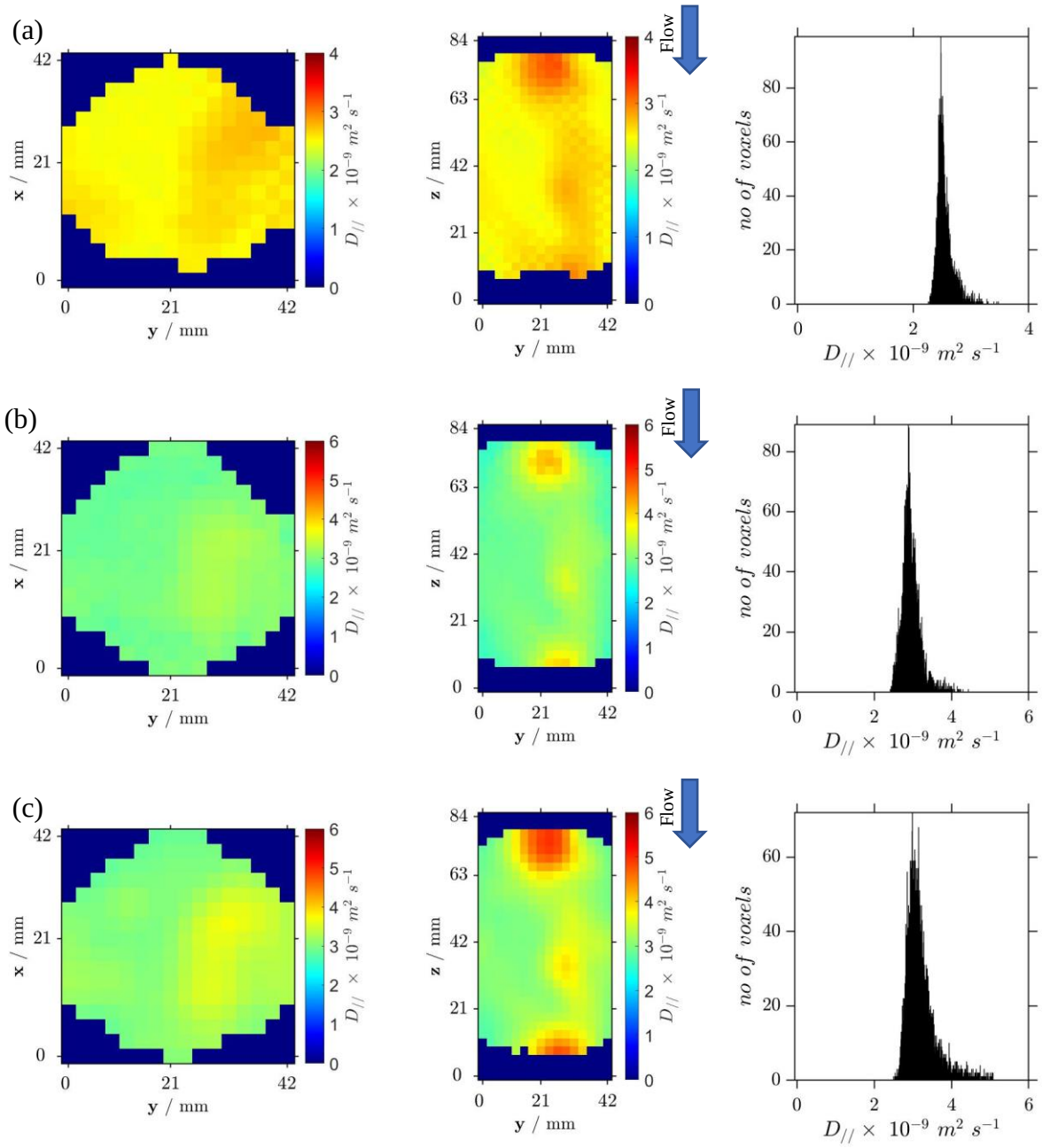

Figure 4-13: Local $D_{//}$ along the flow direction measured from the Gaussian-shaped propagators for water flow through the bead pack at 6(a), 10(b) and 15(c) ft d^{-1}.

4.4.7 Velocity Map and 3D Propagator of Same Resolution

Figure 4-14 exhibits the velocity maps coming from the phase-contrast imaging(a) and the propagator experiment(b) for 15 ft d^{-1} with 656.3 μm $pixel^{-1}$ resolution. The $D_{//}$ map and its distribution(c) are also portrayed. The regions confined in the red circles represent areas of velocities higher than 90 μm s^{-1}, while areas of very slow or no flow are identified by the green colour in the velocity maps. In these no-flow areas $D_{//}$ was equal to the D_s. A great agreement between the phase-contrast and the propagator results for the same resolution can be noticed. Nonetheless, propagators required 8 times more experimental time and an extra 1h for data reconstruction compared to the phase-contrast imaging.

Therefore, high-resolution propagators are more time-consuming and they cannot be used to map dynamic changes in the system.

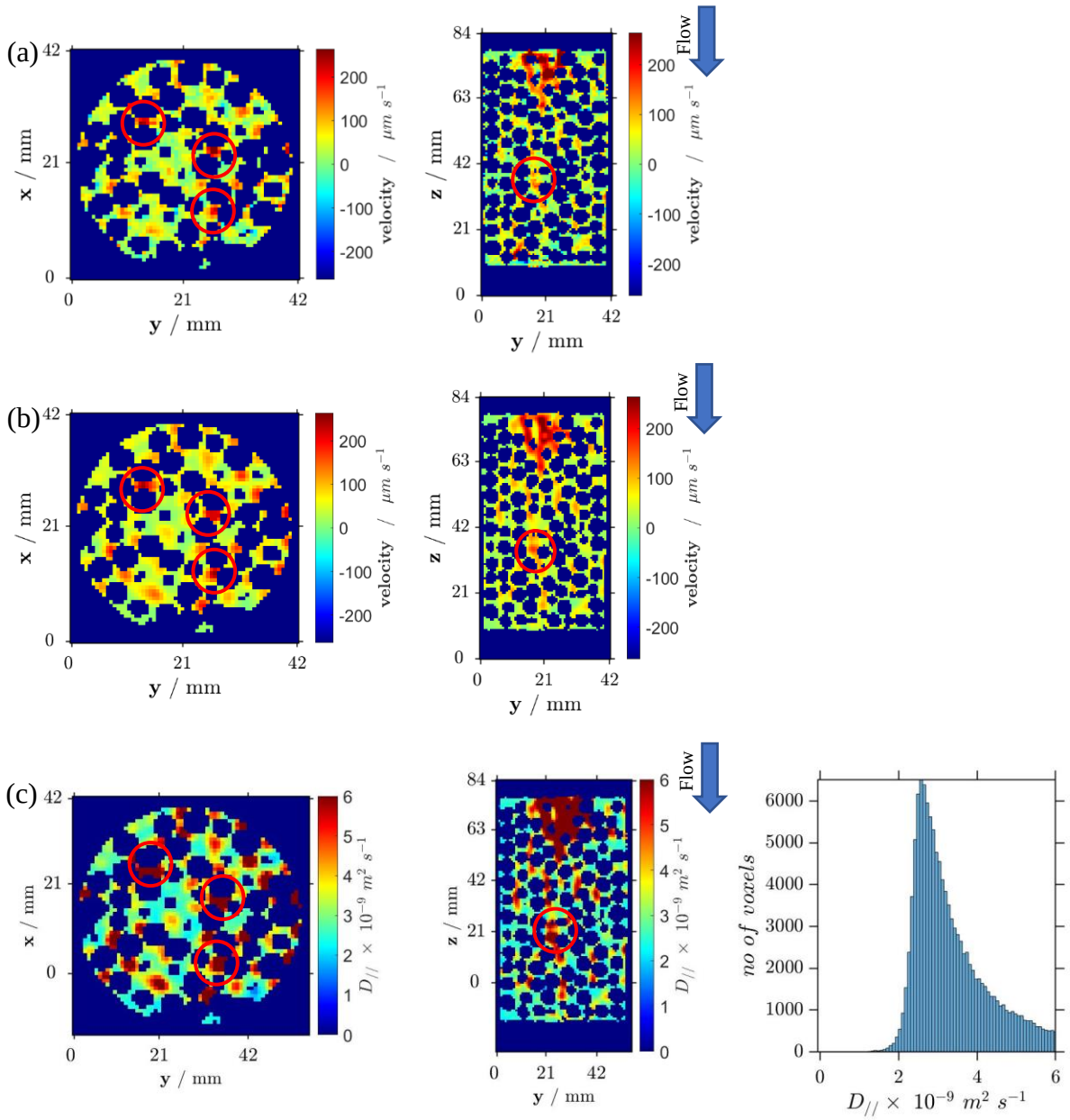

Figure 4-14: Velocity maps from phase-contrast velocimetry(a) propagator(b) and local $D_{//}$ derived from the Gaussian-shaped propagators) for water flow through the bead pack at 15 ft d^{-1}. Interesting areas for comparison are shown by the red circles.

Figure 4-15 highlights that the 1D volumetric velocities coming from the local propagators are higher than the ones coming from the velocity map for 15 ft d^{-1}. This difference can be related to the fact that the propagator captures both flow and diffusion displacement, while phase-contrast velocimetry can measure only the flow displacement.

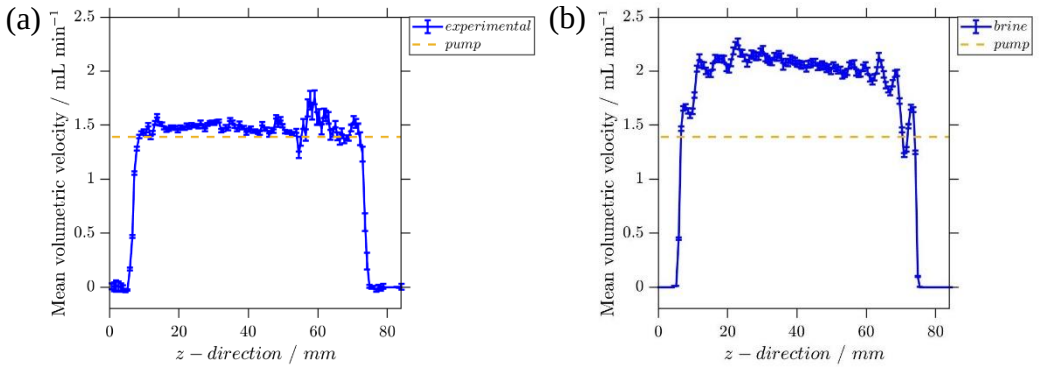

Figure 4-15: Mean volumetric velocity measurement obtained by the velocity map(a) and the 3D propagators(b) for water flow through the bead pack at 15 ft d^{-1}.

4.5 Discussion

To validate the accuracy of the measured ultra-slow velocities using the novel phase-contrast imaging technique, it is important to identify the local error in the velocity measurements. **Figure 4-8** demonstrates that the local error $\sigma_u(\boldsymbol{r})$ is small compared to local measured $u(\boldsymbol{r})$ verifying the robustness of the newly developed optimisation technique. Even at the small velocities of 1 ft d^{-1}, the measured velocity in the area of bulk flow imparts a small amount of noise. For all the velocity experiments, the parameters were chosen so as $\langle\zeta\rangle_0 < \sqrt{2}\, l_D$ which is important for the accuracy of the velocity measurements (Vallatos et al., 2018). The $\langle u_m\rangle$ is inside the error interval of the externally applied $\langle u_0\rangle$ proving that the multi-objective optimisation tool can detect with great accuracy the ultra-slow velocities within an ideal porous network.

Comparing the voxels inside the light blue circles for all the tested flow regimes, it can be concluded that the high-velocity areas for 1 and 3 ft d^{-1} are wider and broader compared to the same areas for 6, 10 and 15 ft d^{-1}. The very small Pe and Re values show that diffusion has a significant contribution to the displacement of the molecules. The significant contribution of the transverse dispersion for these ultra-slow flow regimes was also verified by the $D_{//}$ map. **Figure 4-12** shows a homogenous distribution of $D_{//}$ values close to the D_s which is characteristic of the Taylorian (transverse) dispersion. In contrast, the velocity maps for 6, 10 and 15 ft d^{-1} (**Figure 4-10**) present areas of high velocities among adjacent spheres forming clear paths towards the exit. The same paths were mapped by the $D_{//}$ maps in **Figure 4-13**. The inlet of the bead pack where all the streamlines were aligned and the highest $u(\boldsymbol{r})$ were recorded in **Figure 4-10**, is illustrated by the highest values of $D_{//}$. Then, the streamlines were dispersed along the bead holder due to the presence of beads. Several paths of lower $D_{//}$ and of $D_{//}$ equal to D_s were apparent along the flow as shown in **Figure 4-13**. All these dispersed paths were again reconnected at the outlet forming an area of high values of $D_{//}$. In these higher flow regimes, mechanical (longitudinal) dispersion is the dominant mechanism of displacement in most areas of the bead pack. However, there are still some areas of low $D_{//}$, where Taylorian dispersion was present.

Combining phase-contrast velocity maps (**Figure 4-10**) with $D_{//}$ maps (**Figure 4-13**) provide a better understanding of the mechanical and Taylorian mixing. Each experiment

requires less than 1 h giving useful insights into the flow mechanisms. Obtaining phase-contrast imaging and propagators with the same resolution (**Figure 4-14**) shows that both methods give a similar representation of the flow behaviour at the pore-scale resolution. However, local propagators can also map the local $D_{//}$. Areas of mechanical and Taylorian displacement are better mapped. However, the acquisition and the reconstruction time are significantly higher. As a result, low-resolution propagators can be considered a credible and fast experiment which in combination with velocity maps can contribute to the understanding of the fluids flow behaviour in these ultra-slow regimes.

4.6 Conclusions

In this chapter, two techniques for observing spatially-resolved velocities at ultra-slow velocities in less than one hour were tested in an ideal porous system of beads. The first technique enables pore-scale resolution and is based on the acquisition of two phase-contrast images. The second technique is based on the acquisition of spatially-resolved propagators without pore-scale resolution in order to capture both the flow and diffusion of molecules in these ultra-slow flow regimes. The aim of this study is to show that ultra-slow velocities can be captured with MRI, the displacement mechanisms can be identified and the total acquisition time can be reduced without loss of quantitative information enabling measurements at the dynamic scale.

An optimisation code was built in MATLAB requiring as input data the T_1, T_2 and D_{app} of the system to adjust the optimum Δ, δ_G and g for the acquisition of the **q**-point which is more sensitive to the flow. The accuracy of the technique is verified by adjusting the error in the local velocity measurements taking into consideration the local SNR and the standard deviation among successive velocity maps. Interstitial velocities as low as 1 ft d^{-1} (3.5 μm s^{-1}) were detected for the first time within 56 min having a pore-scale resolution. The mean interstitial velocities measured with MRI were in agreement with the interstitial velocity set by the pump. In addition, the mean volumetric velocity measured with MRI was very close to the pump flow rate, showing that the optimisation technique is reliable for measurements in an ideal porous system.

Velocity maps resulting from propagator measurements with the same resolution are almost identical to the ones acquired from the fast phase-contrast technique. However, propagators provide extra information on the $D_{//}$ giving a better mapping of the areas where mechanical mixing is the dominating mechanism of displacement and of the areas where spins are moving due to self-diffusion. Fast spatially-resolved propagators were also acquired for the same ultra-slow flow regimes. For 1 and 3 ft d^{-1}, the $D_{//}$ is very close to the D_s proving that diffusion across the streamlines had a significant role in the displacement of the molecules. For $Pe \geq 22.3$ and $Re \geq 57.3\ 10^{-3}$, mechanical mixing across the streamlines was dominant in most areas of the sample. This is the first time that the Taylor dispersion is separated from the mechanical mixing through MRI measurements at ultra-slow velocities. In Chapter 5, the two methods were used for ultra-slow flow measurement through a sandstone and three low-permeability carbonate rocks.

Chapter 5 Ultra-Slow Flow in Sedimentary Rocks

5.1 Introduction

Low-permeability rocks are of great interest in recent years. Low permeability oil reservoirs contain a significant amount of oil and are widely distributed around the world. Almost 50% of the total oil reserves in China are trapped in low-permeability reservoirs. The production of oil and gas from these reservoirs will be increased. In these low-permeability reservoirs, the pressure gradients far away from the wellbore region are much smaller than close to it. The ultra-slow flow rates typically used in hydrocarbon recovery result in deviation of the fluid behaviour from Darcy to non-Darcy (Panfilov and Fourar, 2006). Low-velocity non-Darcy flow phenomena are an emerging area of research (Dou et al., 2014) since they influence the production rate. The detection of ultra-slow velocities in the area of the non-Darcy regime is not possible with conventional laboratory experiments (Wang and Sheng, 2017). Therefore, various numerical models have been employed to describe this regime (Diwu et al., 2018; Luo et al., 2019). Wang et al., (2019) designed a filtration column which enabled ultra-slow flow measurements in the laboratory using different sand beds. It was proved that the nonlinear effects depend on the interaction between the fluid and the solid phase. Therefore, a different bottom limit of Re under which nonlinear phenomena are present, is expected for each rock sample. Understanding the mechanism of the non-Darcy flow regime in parallel with field research and downhole logging are crucial for implementing economically feasible EOR techniques in low permeability reservoirs (Davletbaev and Ivaschenko, 2014).

Both propagator and phase-contrast velocimetry have been employed to study flow through bead packs (Kutsovsky et al., 1996). Phase-contrast velocimetry has given good results for water flow through sedimentary rocks at flow rates in the order of 1 and 2 mL min^{-1} (Li et al., 2009; Romanenko et al., 2012; Shukla et al., 2016). Waggoner and Fukushima, (1996) accurately measured velocities as low as 40 μm s^{-1} for water flow through a sandstone with both velocity images and bulk propagators using the ‘13-interval’ Cotts sequence and suitable phase cycle to suppress the induced phase incoherence. This chapter focuses on detecting slow velocities through one sandstone and three low-permeability carbonate rocks. The first goal of this chapter is to validate that phase-contrast velocimetry and propagators capture the ultra-slow displacement of the molecules. The second goal is to identify the changes in the flow mechanisms as the injection rate increases. For this purpose, the APGSTE-RARE sequence with CS was used to obtain spatially-resolved phase-contrast measurements and 3D propagators in less than 30 min.

5.2 Theoretical Background

5.2.1 NMR Techniques to Assess the Pore Throat Distribution in the Presence of Internal Gradients in Low-Permeability Rocks

According to Mitchell et al., (2010), in most porous media T_1 distribution provides better understanding of the pore size distribution than T_2 distribution which inherits the attenuation coming from the diffusion (Eq.(2-31)). As described in Section 2.1.5.3, susceptibility contrast between the liquid and the pore wall generate local magnetic fields creating distortions in the $\boldsymbol{B}_0$ field. These local distortions are responsible for phase accumulation in the local spins making the phase-contrast velocimetry more challenging. In addition, the existence of very small pores and throats increases the mechanisms of relaxation which affect the signal attenuation, hence the SNR. A comparison between T_1 with T_2 distributions obtained in high-field magnets can show if the effect of internal gradients in the porous system is important (Price, 2017). The signal decay due to diffusion and T_2 relaxation can be studied by simultaneously encoding D_{app} and T_2. This can be detected by adding a CPMG echo train right after the APGSTE sequence as shown in **Figure 5-1** (Mitchell et al., 2013a).

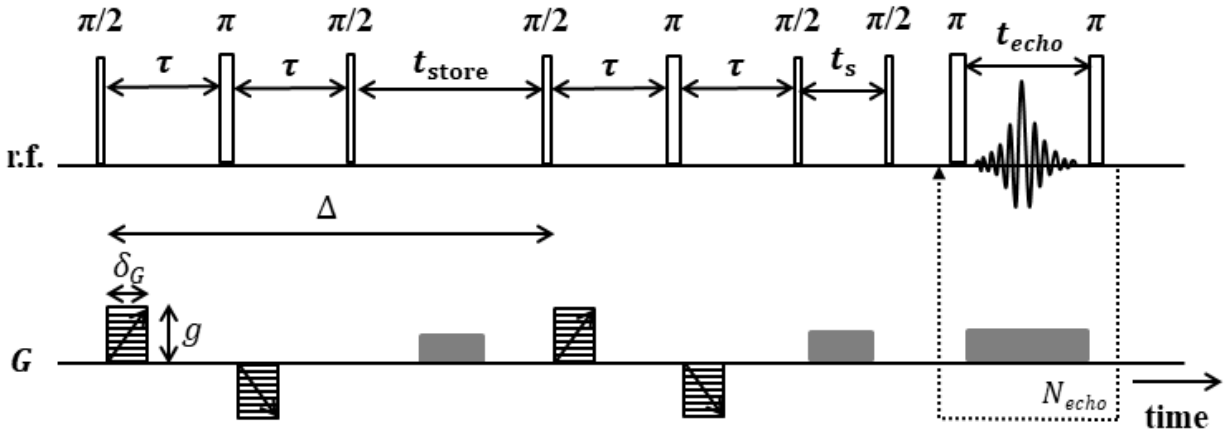

Figure 5-1: Schematic representation of the APGSTE-CPMG sequence based on the '13-interval' Cotts et al., (1989) combined with the standard CPMG echo train. On the diffusion encoding sequence, the echo time is 2τ and the observation time Δ. The rectangular phase-encoding gradient pulse have a duration δ and an amplitude g. Homospoils are indicated by the small grey rectangles and the readout lobe by the large grey rectangle. Data are acquired during the CPMG echo train of N_{echo} echoes separated by t_{echo} time. A stimulated echo of t_s duration is used before the CPMG sequence.

The APGSTE-CPMG sequence results in the acquisition of D-T_2 correlations. D-T_2 can give insights into the pore structure of heterogeneous porous media (Bernin and Topgaard, 2013; Callaghan et al., 2003; Zhang and Blümich, 2014). Measuring the relaxation times and the D_{app} of the system is important for estimating the maximum SNR and therefore the u_{min} of the system as described by Eq.(4-20).

5.2.2 Propagator Measurements in Sedimentary Rocks

In real core plugs, the maximum observation time Δ is not sufficient for the scanning of the rock heterogeneities $L_v \approx l_{char}$. As a result, only the preasymptotic regime is

expected in flowing experiments through rocks. Propagators present a long tail which is characteristic of the core heterogeneity. **Figure 5-2** shows the formed tail in the propagator curve for short (small displacement) and long Δ (large displacement) time intervals. In this case, the flow behaviour does not obey Eq.(2-44) and it is known as non-Fickian flow (Bijeljic et al., 2013; Scheven et al., 2005b). In the case of the bead pack, small displacements are defined as $\langle u \rangle \Delta < d_s$ (Scheven et al., 2004).

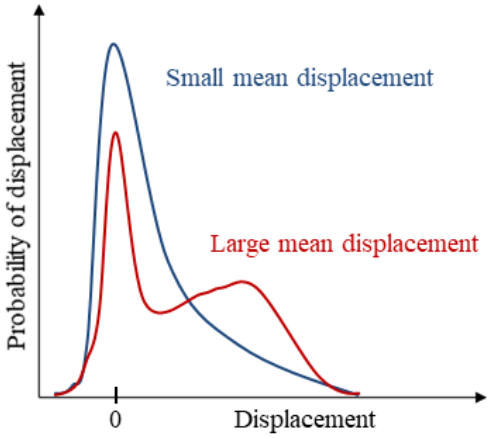

Figure 5-2: Schematical representation of bulk propagators for flow through a core plug for small and large mean displacements. Adapted from Shukla et al., (2016).

For oil reservoirs a good approximation is that k above 1000 mD is related to high permeability reservoirs, k of ~100 mD corresponds to low permeability and k below 10 mD to extra-low permeability reservoirs.

5.3 Materials and Methods

5.3.1 Materials

The core plugs provided by STCA had an average length of 7.00 ± 0.01 cm and diameter of 3.80 ± 0.01 cm and their properties are presented in **Table 5-1**. The samples were dried under vacuum for 1 hour and then saturated in DI under vacuum for 3 hours.

Table 5-1: Porosity and absolute permeability of four different core plugs.

Names	ϕ (%)	k (mD)
Bentheimer	22.9 ± 0.7	1000 ± 10.4
Estaillades	30.0 ± 0.7	113 ± 5.6
$IND4_33$	18.10 ± 0.09	165 ± 8.3
$COR1_7$	20.20 ± 0.10	3.37 ± 0.17

5.3.2 Methods

5.3.2.1 Core Flooding Protocol

The inlet lines of the Rock Core Holder (RCH) were filled with water to remove the air and they were attached to the fixed end platen. The PEEK RCH flow cell (ErgoTech, Conwy, UK) was filled with water and the core was loaded in the Aflas

sleeve enclosed in the RCH to avoid the formation of air bubbles. Then, the adjustable platen was placed at the outlet end as shown in **Figure 5-3**. The confining pressure was monitored at 6.3 MPa using 3M Fluorinert FC-43 and water was injected with a constant flow rate of 1 mL min^{-1} for 1 h to remove any trapped air bubbles. The RCH was connected in a closed flow loop.

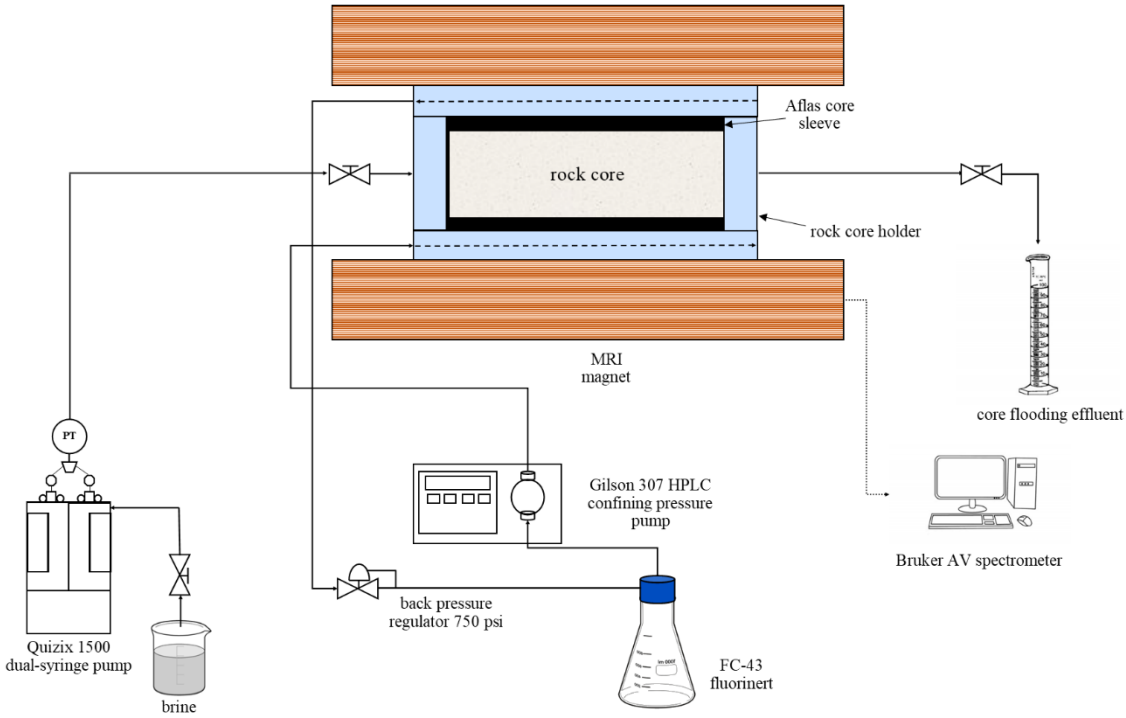

Figure 5-3: Schematic representation of the CFS set-up used during the water injection at various flow rates through different core plugs.

5.3.2.2 NMR Protocol

All NMR experiments were conducted at the same magnet following the NMR protocol described in Section 4.3.2.2 with an extra step after the experiment (ii). D-T_2 correlation maps following the APGSTE-CPMG sequence described in Section 5.2.1 were obtained using different Δ times. D-T_2 maps were used to give insights into the heterogeneity of each core plug. The high-resolution 3D CS propagators are not analysed for the core plugs since they do not provide any interesting insight into the flow.

5.3.2.3 NMR Experimental Parameters

The duration of the hard 90º and 180º pulses were adjusted for each sample separately. The inversion recovery and the one-shot CPMG experiments were conducted as described in Section 4.3.2.4. The D-T_2 correlations were performed with 24 **q**-points in the fast Δ acquisition and with 16 **q**-points in the long Δ acquisition. The g scaled up to 96% $\times g_{max}$ when incremented 24 times and up to 70% $\times g_{max}$ when incremented 16times. The duration δ of each bipolar gradient was defined as 4.2 ms, while τ_e ($t_{echo}/2$) was chosen as fifty times the duration of the 90º pulse as in the one-shot CPMG experiment.

The FOV for all the 3D spatially-resolved experiments was kept the same and the Scheme B **k**-space trajectory was followed. The parameters chosen for the 3D velocity maps and the 3D propagators were adjusted for each separate flow rate and each sample as described in Sections 4.3.2.3 and 4.3.2.4. The propagators for all the samples were acquired for 29 **q**-points encoded along the flow direction (z-direction). The exact experimental parameters for each rock are presented below.

Betheimer: A hard 90º pulse of 38.3 μs and a refocusing 180º pulse of 76.6 μs were used for the Bentheimer rock. The t_{RD} for all the experiments in this rock was defined as 3.2 s. The velocity maps were reconstructed for an α of 0.043 and 5 Bregman iterations. The parameters for phase-contrast imaging and propagator measurement in Bentheimer are summarized in **Table 5-2**. The acquisition time for each velocity map was 26 min for an under-sampling rate of 25%. The acquisition time for the low-resolution propagators was 38 min, whereas for the high-resolution one was 5 h for an under-sampling rate of 18%.

Table 5-2: Parameters for phase-contrast imaging and propagator measurements in Bentheimer.

$\langle u_0 \rangle$ (ft d^{-1})	Δ(ms)	δ_G(ms)	g_{factor}
Phase-contrast imaging			
6	134.1	0.6	93.1%
10	41.3	4.8	24.3%
15	24	5.0	29.4%
Propagators			
6	597	4.2	82%
10	353	4.4	80%
15	239	4.2	80.7%

Estaillades: A hard 90º pulse of 36.8 μs and a refocusing 180º pulse of 73.6 μs were used for the Estaillades rock. The t_{RD} for all the experiments in this rock was defined as 2.8 s. The velocity maps were reconstructed for an α of 0.024 and 4 Bregman iterations. The parameters for phase-contrast imaging and propagator measurement in Estaillades are summarized in **Table 5-3**. The acquisition time for each velocity image was 24 min for an under-sampling rate of 25%. The acquisition time for the low-resolution propagators was 44 min, whereas for the high-resolution one was 6.2 h for an under-sampling of 21%.

Table 5-3: Parameters for phase-contrast imaging and propagator measurements in Estaillades.

$\langle u_0 \rangle$ (ft d^{-1})	Δ(ms)	δ_G(ms)	g_{factor}
Phase-contrast imaging			
6	79.1	0.8	96%
10	52.7	3.8	33%
15	24	5.0	29.4%
Propagators			
6	800	5.0	24%
10	672	1.9	96%
15	800	1.1	96%

***IND*4_33**: A hard 90º pulse of 39.7 µs and a refocusing 180º pulse of 79.4 µs were used for the $IND4_33$ rock. The t_{RD} for all the experiments in this rock was defined as 4.5 s. The velocity maps were reconstructed for an α of 0.028 and 4 Bregman iterations. The parameters for phase-contrast imaging and propagator measurement in $IND4_33$ are summarized in **Table 5-4**. The acquisition time for each velocity image was 38 min for an under-sampling of 25%. The acquisition time for the low-resolution propagators was 1.31 h, whereas for the high-resolution one was 10.3 h for an under-sampling of 29%. For 6, 10 and 15 ft d^{-1}, the optimum Δ and δ_G indicated in **Table 5-4** for phase-contrast imaging were employed to acquire 11 different **q**-points by changing the g_{factor} from -96% up to +96%. All the **k**-space data were obtained following the Scheme B trajectory and each acquisition required ~ 2.3 h. These results were used to assess the linear relationship between φ and $\langle u \rangle$.

Table 5-4: Parameters for phase-contrast imaging and propagator measurements in $IND4_33$.

$\langle u_0 \rangle$ (ft d^{-1})	Δ(ms)	δ_G(ms)	g_{factor}
Phase-contrast imaging			
6	86.5	0.7	96%
10	59.8	4.4	22.3%
15	24	5.0	29.4%
Propagators			
6	1000	4.8	42.6%
10	900	1.4	96%
15	896	2.5	37%

***COR*1_7**: A hard 90º pulse of 38.7 µs and a refocusing 180º pulse of 77.4 µs were used for the $COR1_7$ rock. The t_{RD} for all the experiments in this rock was defined as 2.3 s. The velocity maps were reconstructed for an α of 0.047 and 4 Bregman iterations. The parameters for phase-contrast imaging and propagator measurement in $COR1_7$ are summarized in **Table 5-5**. The acquisition time for each velocity image was 20 min for an under-sampling rate of 25%. The acquisition time for the low-resolution propagators was 50 min, whereas for the high-resolution one was 7.4 h for an under-sampling of 29%.

Table 5-5: Parameters for phase-contrast imaging and propagator measurements in $COR1_7$.

$\langle u_0 \rangle$ (ft d^{-1})	Δ(ms)	δ_G(ms)	g_{factor}
Phase-contrast imaging			
6	67	0.8	96%
10	53.8	4.5	66%
15	24	5.0	29.4%
Propagators			
6	611.5	4.9	69%
10	720	1.8	96%
15	720	1.2	96%

All the results were processed as described in Sections 4.3.2.5, 4.3.2.6 and 4.3.2.7. In the case of the rocks, ϕ was defined as the porosity of each rock for the measurement of the $\phi_{rel}(\boldsymbol{r})$.

5.4 Results

5.4.1 Validation of the Applied Techniques

5.4.1.1 Validation of D-T_2 Sequence in the Bead Pack

The D-T_2 sequence described in Section 5.2.1 should be validated. For that reason, the bead pack studied in Chapter 4 was used. **Figure 5-4** shows the echo attenuation for different Δ values. For Δ set as 24 ms, 24 **q**-points were acquired, while for Δ set as 50, 100 and 200 ms, 16 **q**-points were obtained. The measured D_{app} was close to the D_s for water for all the different applied Δ, as expected. Moreover, the decay lines are overlapping, proving that the relaxation effects were negligible in the system.

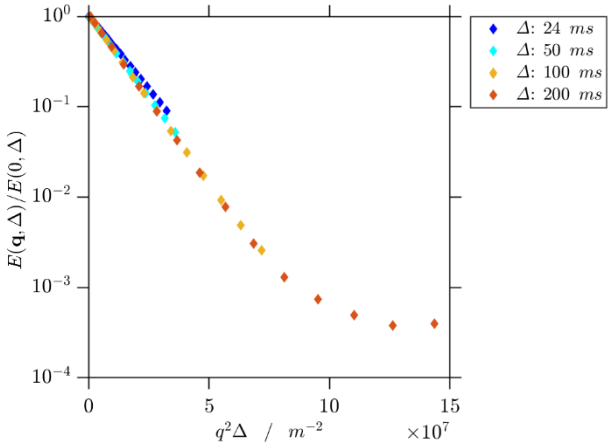

Figure 5-4: Echo attenuation for four different Δ measuring the value of D_{app}.

As explained in Section 2.3, D_{app} can be considered equal to the D_{eff} when short bipolar gradients are employed. **Figure 5-5** shows the 2D correlation between the D_{eff}, and the effective T_2 also referred as $T_{2,eff}$ for Δ equal to 24 and 200 ms. The D-T_2 map presents a single peak for both D_{eff} and T_2 (Hürlimann and Venkataramanan, 2002). However, the peak is broader for the short Δ equal to 24 ms. This is because spins from all the T_2 relaxation times contributed to the diffusion. On the other hand, for Δ equal to 200 ms, spins close to the interface with the beads or the walls of the bead holder had relaxed without contributing to the D_{eff} distribution (Zhang and Blümich, 2014). In both cases, the T_2 is evenly distributed around 2.2 s, which was also measured by the single-shot CPMG experiment in Section 4.4.1.

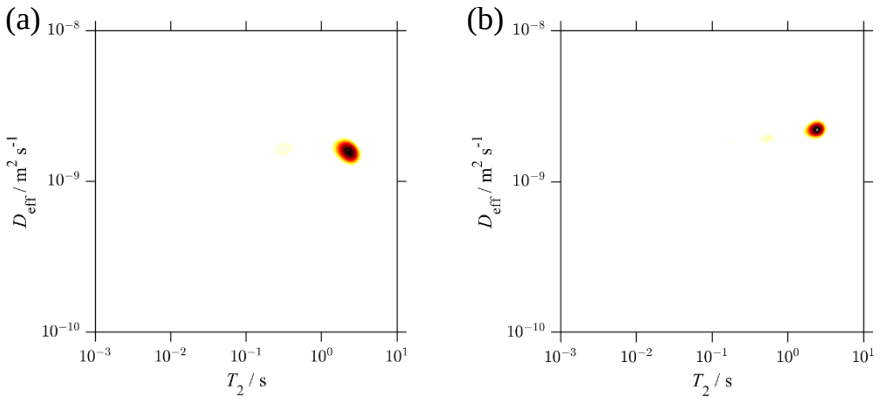

Figure 5-5: D-T_2 maps coming from the APGSTE-CPMG sequence for the bead pack filled with water and 4 mm beads in diameter for Δ equal to 24(a) and 200 ms(b).

5.4.1.2 Linear Relationship Between Phase and Gradients for One of the Core Samples

Another important relationship that should be examined is the linear relationship between the imparted φ and the applied g in a flowing system through the rocks. For that reason, experiment (v) was performed for each rock using the optimum Δ and δ_G derived by the multi-objective optimisation for each flow rate (Section 4.3.2.3). **Figure 5-6** shows the $\langle\varphi\rangle$, for a ROI of 16 voxels in the middle of the FOV as a function of g for 6, 10 and 15 ft d^{-1} of water flow through $IND4_33$. A dashed line was fitted in that linear region. **Figure 5-6**(a) shows the change of $\langle\varphi\rangle$ with g for 6 ft d^{-1} velocity using a Δ of 86.5 ms and a δ_G of 0.72 ms. The optimum g used in the velocity map was 96% × g_{max} (red diamond) and is inside the linear region (dashed line). Similarly, **Figure 5-6**(b) and (c) show that the optimum g defined by the optimisation process (red diamond) for 10 and 15 ft d^{-1} is inside the limits of the linear area for the corresponding values of Δ and δ_G used in the velocity mapping. This proves that the optimum g, Δ and δ_G used in the velocity map of each rock are in the linearity area enabling the use of Eq.(4-5) for the measurement of the $u(\boldsymbol{r})$.

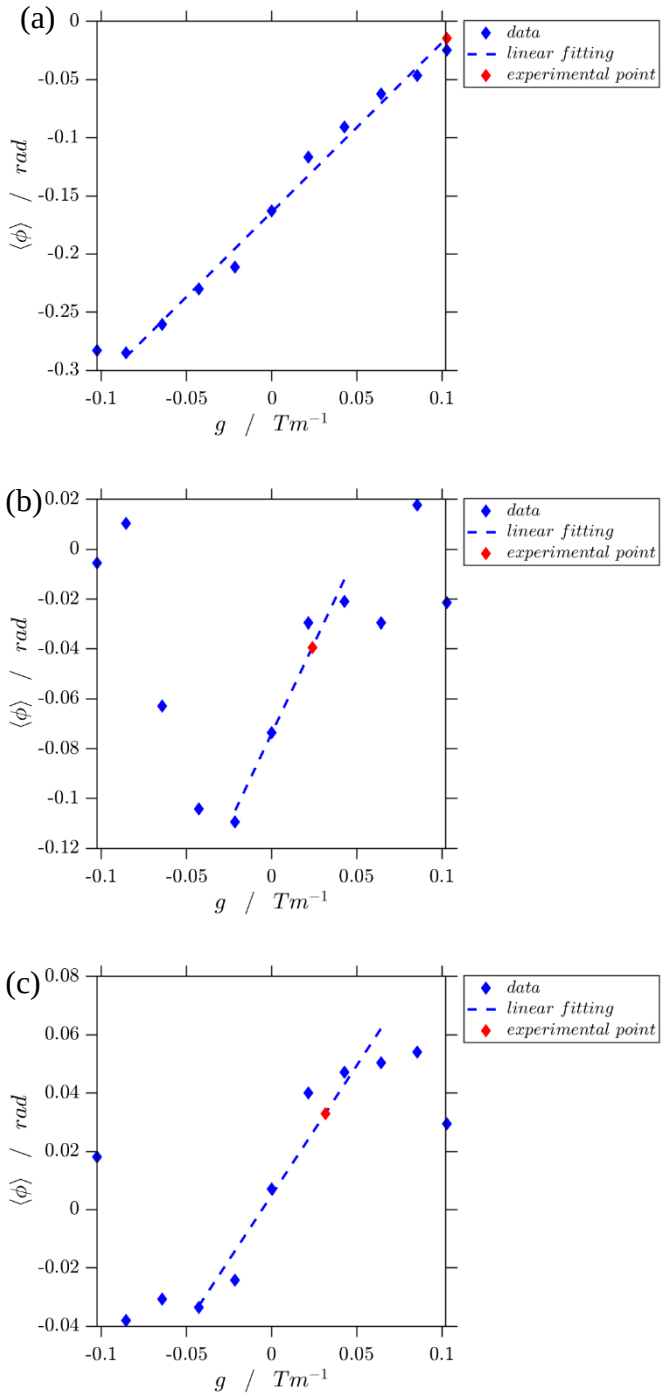

Figure 5-6: Phase shift as a function of the gradient amplitude for 6(a), 10(b) and 15(c) ft d^{-1} water flow through IND4_33. The red data point shows the optimum g defined for the slow flow velocity maps by the multi-objective optimisation and the dashed line indicates the area where φ and g are linear.

The same experiments were performed for all the core plugs used in this chapter, but only the results coming from the $IND4_33$ rock are presented. The goal of this analysis was to verify that Eq.(4-5) can be used for the measurement of the $u(\boldsymbol{r})$ for each complex pore structure and each flowing regime.

5.4.2 Relaxation and Diffusion Measurements for all the Core Plugs

Bentheimer: Figure 5-7(a) shows that the T_1 distribution in Bentheimer is mainly unimodal with a large peak around 1 s. The small peak around 96 ms can be attributed to water confined within chlorites. In the literature, T_1 distribution is considered as a reflection of the pore body distribution. On the other hand, the T_2 distribution presented in **Figure 5-7**(b) is much broader with a large peak around 196 ms and several small peaks. This broad distribution indicates that T_2 is affected by the presence of internal gradients (Mitchell et al., 2010a).

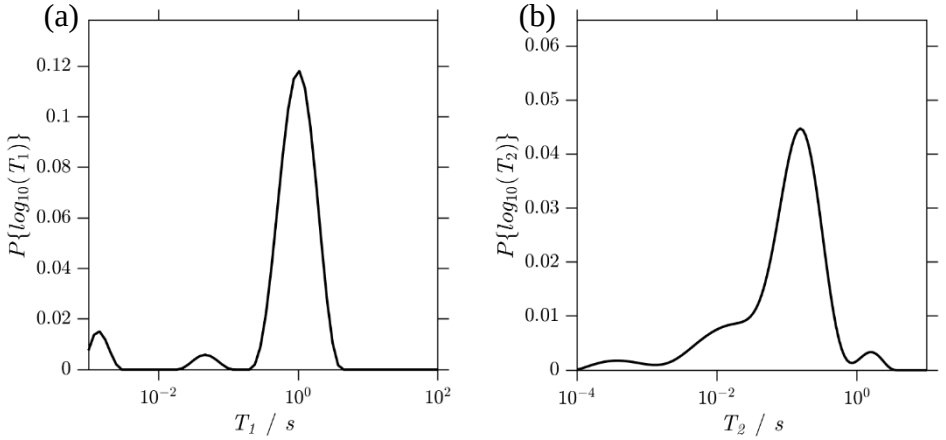

Figure 5-7: T_1(a) and T_2(b) distributions coming from the inversion recovery and the CPMG sequence for the water-saturated Bentheimer.

Diffusion through internal gradients affects the short T_2 components and leads to fast signal decay. Diffusion through internal gradients is also responsible for the artificial peak which appeared at long T_2 (Mitchell and Fordham, 2014). **Figure 5-8** shows that the shape of the D-T_2 correlation map is different for Δ equal to 24 and 220 ms. In **Figure 5-8**(a), there is an area of fast T_2 components with small D_{eff}. This area is related to the presence of very small pores. The spins in these narrow pores have fully decayed in the 220 ms regime. In **Figure 5-8**(b), fast T_2 components present high values of D_{eff} and T_2 components around 110 ms present a broad D_{eff} distribution. These high D_{eff} measurements are related to the presence of high susceptibility effects in these narrow pores (Zhang and Blümich, 2014).

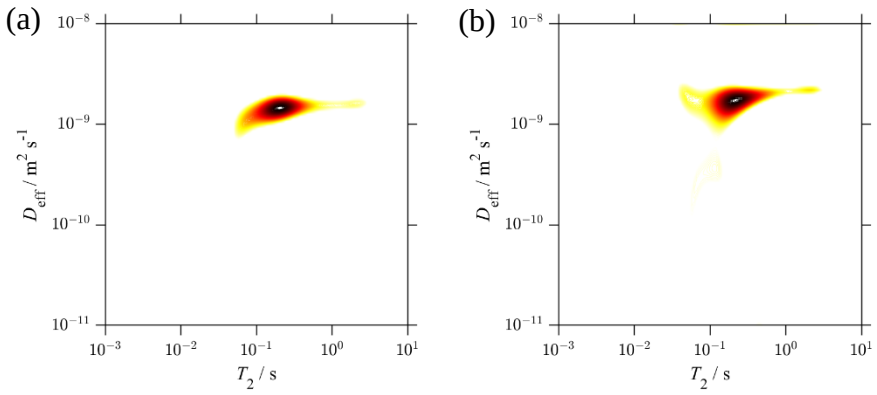

Figure 5-8: D-T_2 maps coming from the APGSTE-CPMG sequence for the Bentheimer core plug saturated with water for Δ equal to 24(a) and 220 ms(b).

Estaillades: Figure 5-9(a) shows the T_1 distribution in Estaillades as a bimodal distribution around 927 and 192 ms. **Figure 5-9**(b) demonstrates that this bimodal system is replaced by a broad T_2 peak and several small peaks around it. This phenomenon is observed due to the diffusive coupling between large and small pores which is important, especially in high-field magnets. Diffusive coupling results in a decrease of the peak associated with the long T_2 around 164 ms which is connected to the macropores. In addition, the peak related to the short T_2 values and therefore the micropores become wider and the highest peak is around 38 ms. The small peaks at the longest (1.4 s) and shortest (10^{-2} s) T_2 areas are artefacts.

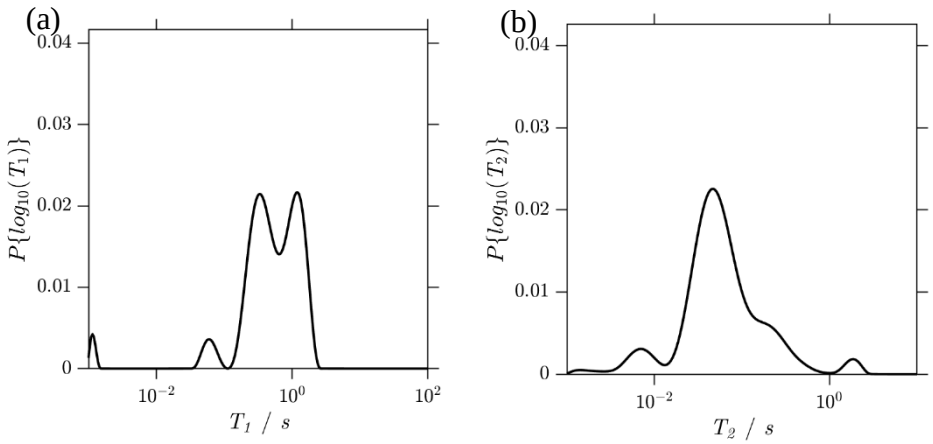

Figure 5-9: T_1(a) and T_2(b) distributions coming from the inversion recovery and the CPMG sequence for the water-saturated Estaillades.

This bimodal T_2 distribution in Estaillades is better observed in the D-T_2 correlation map presented in **Figure 5-10**. D-T_2 map presents different shapes for Δ equal to 24 and 100 ms. Fast T_2 components with small D_{eff} which are attributed to the small pores, were apparent only in the 24 ms experiment. These fast components have fully relaxed in the 100 ms regime which exhibits a narrower D_{eff} distribution.

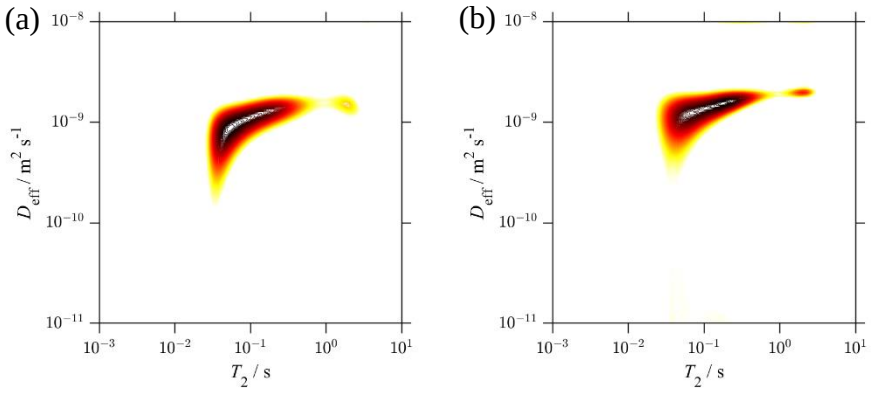

Figure 5-10: D-T_2 maps coming from the APGSTE-CPMG sequence for the Estaillades core plug saturated with water for Δ equal to 24(a) and 100 ms(b).

***IND4_33*: Figure 5-11**(a) shows the T_1 distribution in $IND4_33$ as a bimodal distribution around 1.2 s and 144 ms. This bimodal distribution is in agreement with the pore body size distribution seen in the literature for the Indiana limestone (Bijeljic et al., 2013). **Figure 5-11**(b) presents a multicomponent T_2 distribution. This presence of multiple effective T_2 peaks in a high-field magnet which do not follow the T_1 distribution is characteristic of the presence of different internal gradient environments (Mitchell, 2014; Mitchell et al., 2010b).

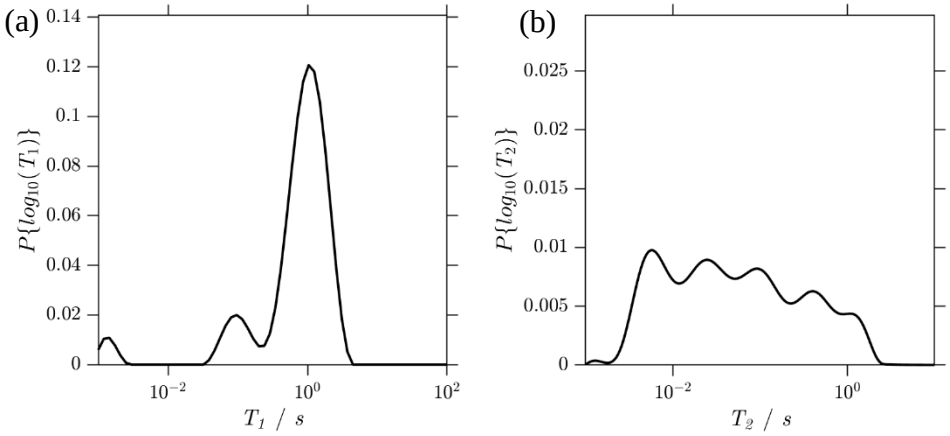

Figure 5-11: T_1(a) and T_2(b) distributions coming from the inversion recovery and the CPMG sequence for the water-saturated IND4_33.

Since the APGSTE sequence limits the effect of internal gradients, the multiple peaks below T_2 of 0.1 ms are not apparent in **Figure 5-12**. In contrast to what was seen above for Bentheimer and Estaillades, the D-T_2 map of $IND4_33$ presents similar shapes for Δ equal to 24 and 80 ms. This means that D_{eff} is independent of Δ. Even though the T_2 distribution is wide, the D_{eff} distribution is narrow and concentrated around 1.4×10^{-9} m^2 s^{-1}. The small pores with the fast T_2 present small D_{eff} values confirming the microporosity that dominates the pore structure of Indiana. According to the literature, Indiana limestone cores present very few connected flow paths and several dead ends (Ji et al., 2012; Singer et al., 2016) which makes them difficult to study with NMR.

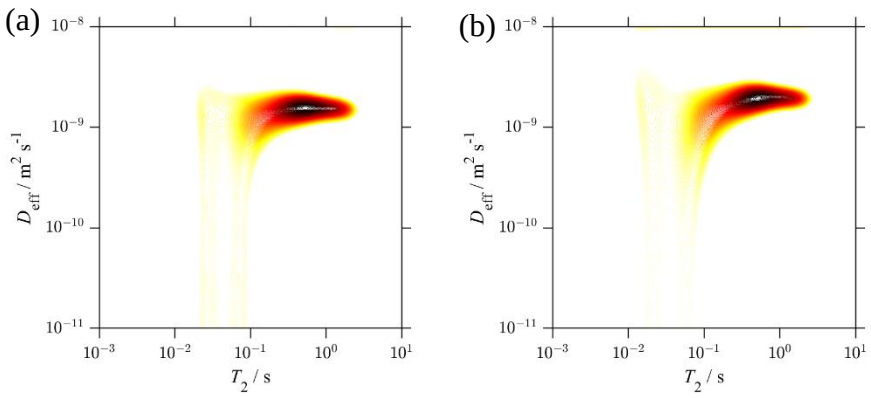

Figure 5-12: D-T_2 maps coming from the APGSTE-CPMG sequence for the $IND4_33$ core plug saturated with water for Δ equal to 24(a) and 80 ms(b).

COR1_7: **Figure 5-13**(a) shows the expected bimodal T_1 distribution in $COR1_7$. The two peaks are observed around 716 and 223 ms. The T_2 distribution in **Figure 5-13**(b) is similar to the one acquired for Estaillades. The long T_2 of 1.6 s and the fast T_2 below 10^{-2} s are artefacts. Diffusive coupling results in a decrease of the peak around 83 ms which is associated with the macropores and broadness of the peak around 20 ms which is associated with the micropores.

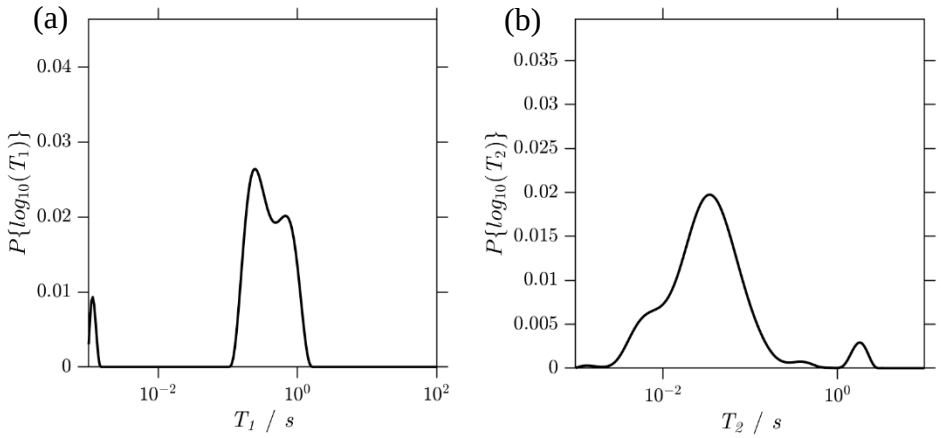

Figure 5-13: T_1(a) and T_2(b) distributions coming from the inversion recovery and the CPMG sequence for the water-saturated $COR1_7$.

The same T_2 distribution in $COR1_7$ is better observed in the D-T_2 correlation map presented in **Figure 5-14**. D-T_2 maps present similar shapes for Δ equal to 24 and 100 ms. Fast T_2 components with small D_{eff} which are attributed to the small pores, were apparent only in the 24 ms experiment. These fast components have fully relaxed in the slow 100 ms regime. In both cases, the D_{eff} distribution is centered around 1.25×10^{-9} m^2 s^{-1}. The fast T_2 relaxation measured in this sample is responsible for the poor SNR in the MRI measurements, as will be discussed below.

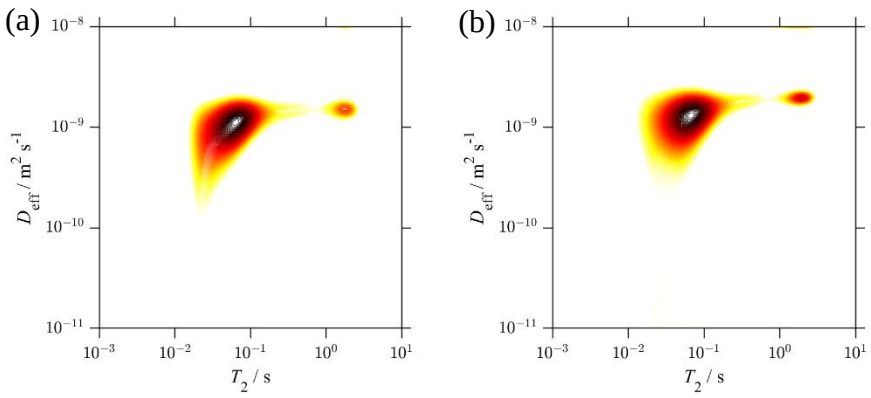

Figure 5-14: D-T_2 maps coming from the APGSTE-CPMG sequence for the $COR1_7$ core plug saturated with water for Δ equal to 24(a) and 100 ms(b).

5.4.3 Noise Analysis in the Phase-Contrast Imaging for all the Core Plugs

Internal gradients have a significant effect on the velocity measurements for all the studied core plugs. To investigate the local error in the obtained velocity maps from the phase-contrast imaging technique, the 6 ft d^{-1} regime for all the samples is analysed. The slowest velocity regime carries the highest per cent of noise. Therefore, the standard deviation among five successive velocity maps and the $\sigma_u(\boldsymbol{r})$ map are displayed for the slowest flow regime of each rock.

Bentheimer: Figure 5-15(a) shows the standard deviation among five successive velocity maps at 6 ft d^{-1} flow. The colourmap in all the measurements has been scaled between ± 5×$\langle u \rangle_0$. The green colour dominates the image proving that the standard deviation of the measured velocities is close to 0 μm s^{-1}. The red stripes seen in the z-y slice of the core are attributed to external artefacts of the magnetic field.

Figure 5-15(b) presents the same analysis made for the bead pack in **Figure 4-8**. The intensity image coming from the phase-contrast imaging obtained at no-flow conditions (top left) is presented along with the $\sigma_u(\boldsymbol{r})$ map (top right) measured by Eq.(4-20), the $u(\boldsymbol{r})$ map (bottom left) and the $\phi_{rel}(\boldsymbol{r})$ map (bottom right) coming from the fully-sampled 3D RARE image for the Bentheimer rock. Comparing the $u(\boldsymbol{r})$ map with the $\sigma_u(\boldsymbol{r})$ map and the standard deviation, it can be concluded that the detected local velocities carry a small amount of error when measuring ultra-slow flow at 6 ft d^{-1} through Bentheimer. The same measurements were repeated for 10 and 15 ft d^{-1}, showing that the local error is even smaller for these higher flow regimes.

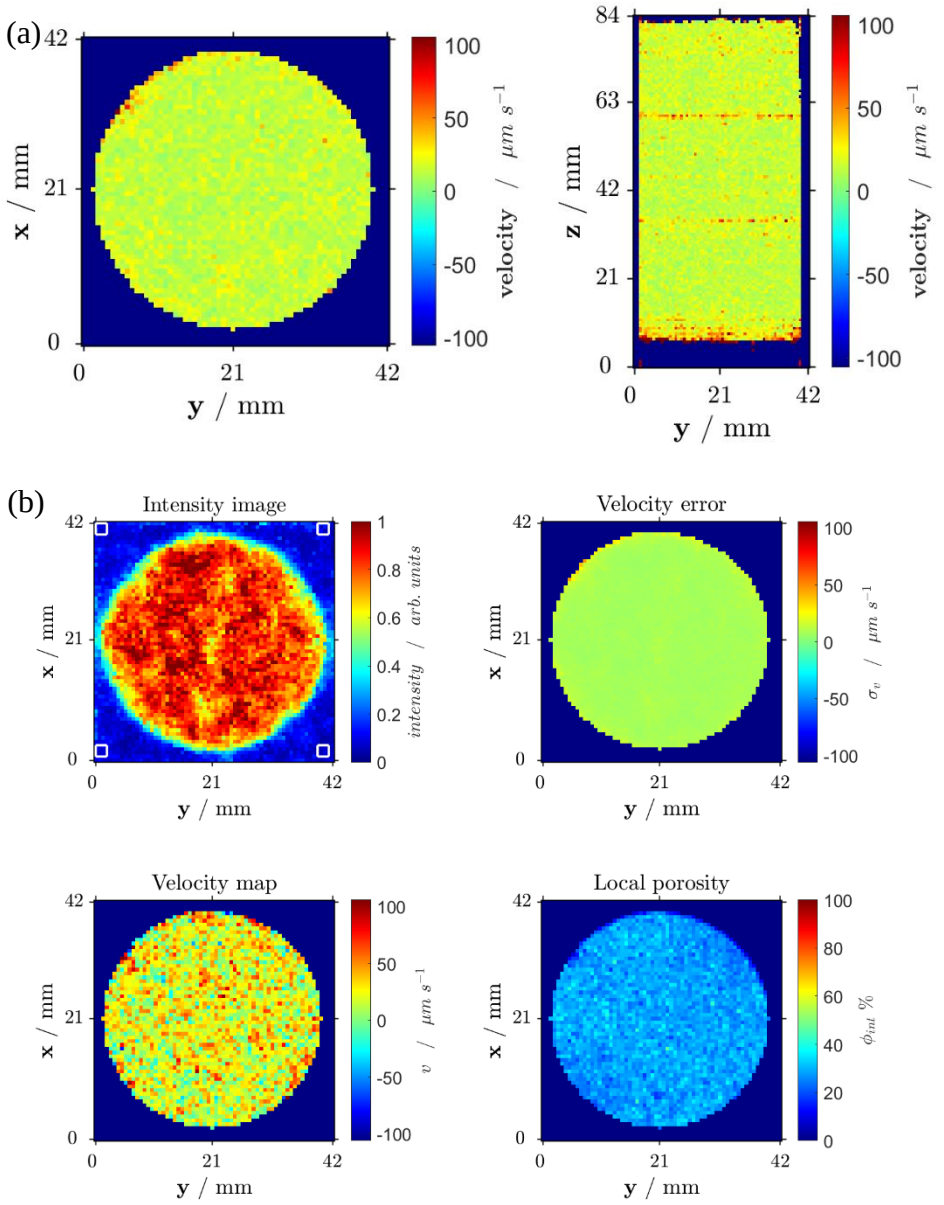

Figure 5-15: The middle x-y slice and z-y slice of the standard deviation between 5 velocity maps acquired under the same conditions using the same experimental parameters(a). The middle x-y slice for the average intensity image coming from the phase-contrast imaging, the local velocity error σ_u, the measured velocity map and the relative porosity coming from the 3D RARE image(b) for water flow at 6 ft d^{-1} through the Bentheimer core plug.

Estaillades: The same type of analysis was conducted for Estaillades and is presented in **Figure 5-16**. The colourmap in all the measurements has been scaled between ± $5\times\langle u\rangle_0$. Both the standard deviation and the $\sigma_u(\boldsymbol{r})$ map present a uniform green colour, showing that the error in the measured local velocities in the $u(\boldsymbol{r})$ map is small.

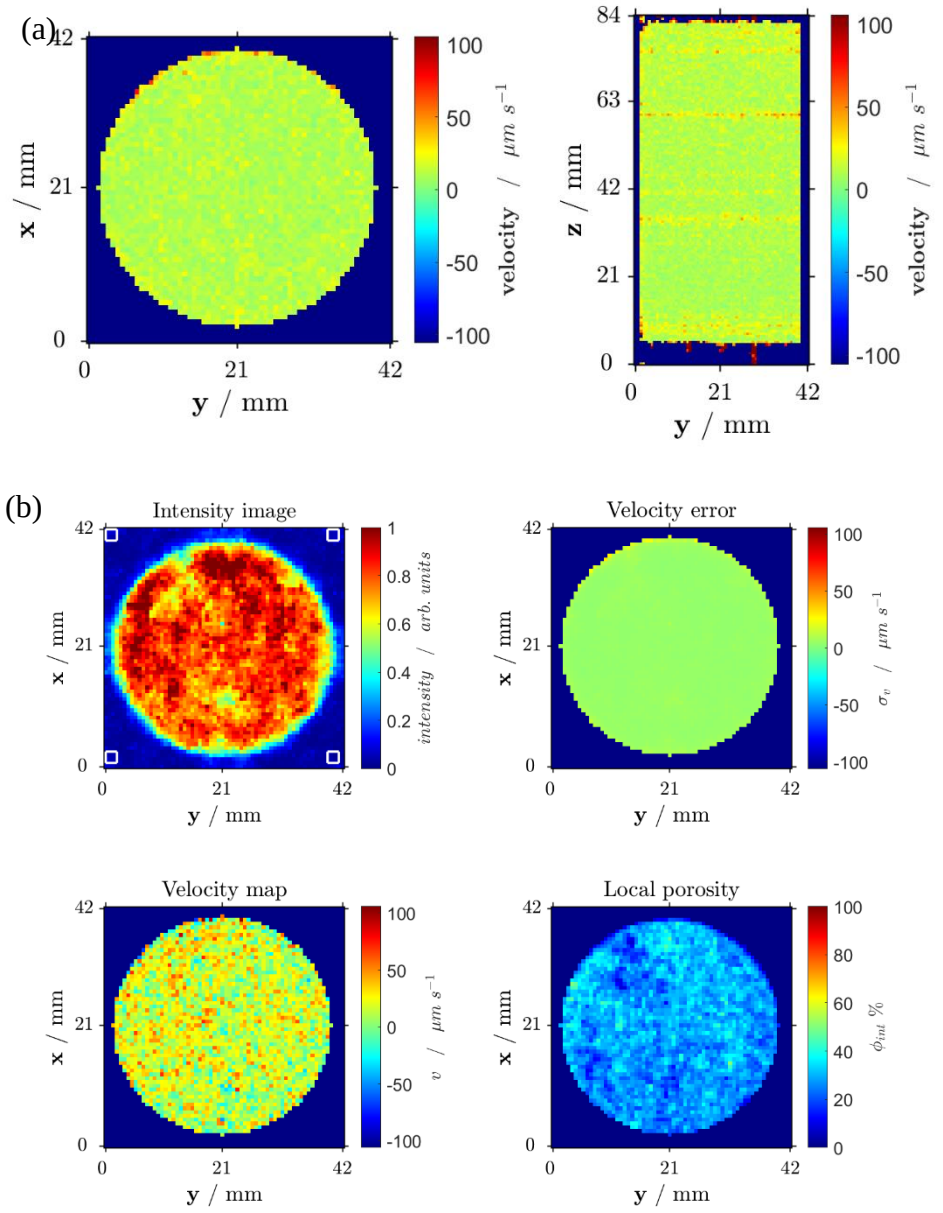

Figure 5-16: The middle x-y slice and z-y slice of the standard deviation between 5 velocity maps acquired under the same conditions using the same experimental parameters(a). The middle x-y slice for the average intensity image coming from the phase-contrast imaging, the local velocity error σ_u, the measured velocity map and the relative porosity coming from the 3D RARE image(b) for water flow at 6 ft d^{-1} through the Estaillades core plug.

***IND4_33*: Figure 5-17** presents the same noise analysis for $IND4_33$. The colourmap for all the measurements has been scaled between ± 10×$\langle u \rangle_0$. Even though, the green colour is dominant in both the standard deviation and the $\sigma_u(\boldsymbol{r})$ map, there are more region of yellow and red colour in this carbonate rock, compared to Estaillades. The intensity image coming from the phase-contrast map at the top left corner in **Figure 5-17**(b) indicates that the background noise is high and that there are several low intensities inside the sample. A characteristic area of low signal intensity can be seen in the middle of the x-y slice. The same region presents very low values of $\phi_{rel}(\boldsymbol{r})$ as seen in **Figure 5-17**(b) (bottom right). These voxels have low SNR and therefore

significant $\sigma_u(\boldsymbol{r})$ as shown by the yellow areas in the middle of the x-y slice in **Figure 5-17**(b) (top right).

However, the velocity map in **Figure 5-17**(b) (bottom left) presents several voxels with high measured velocities (yellow, orange and red colour) outside this area of high error. This proves that even in this very noisy system, the detected local velocities import a small amount of noise.

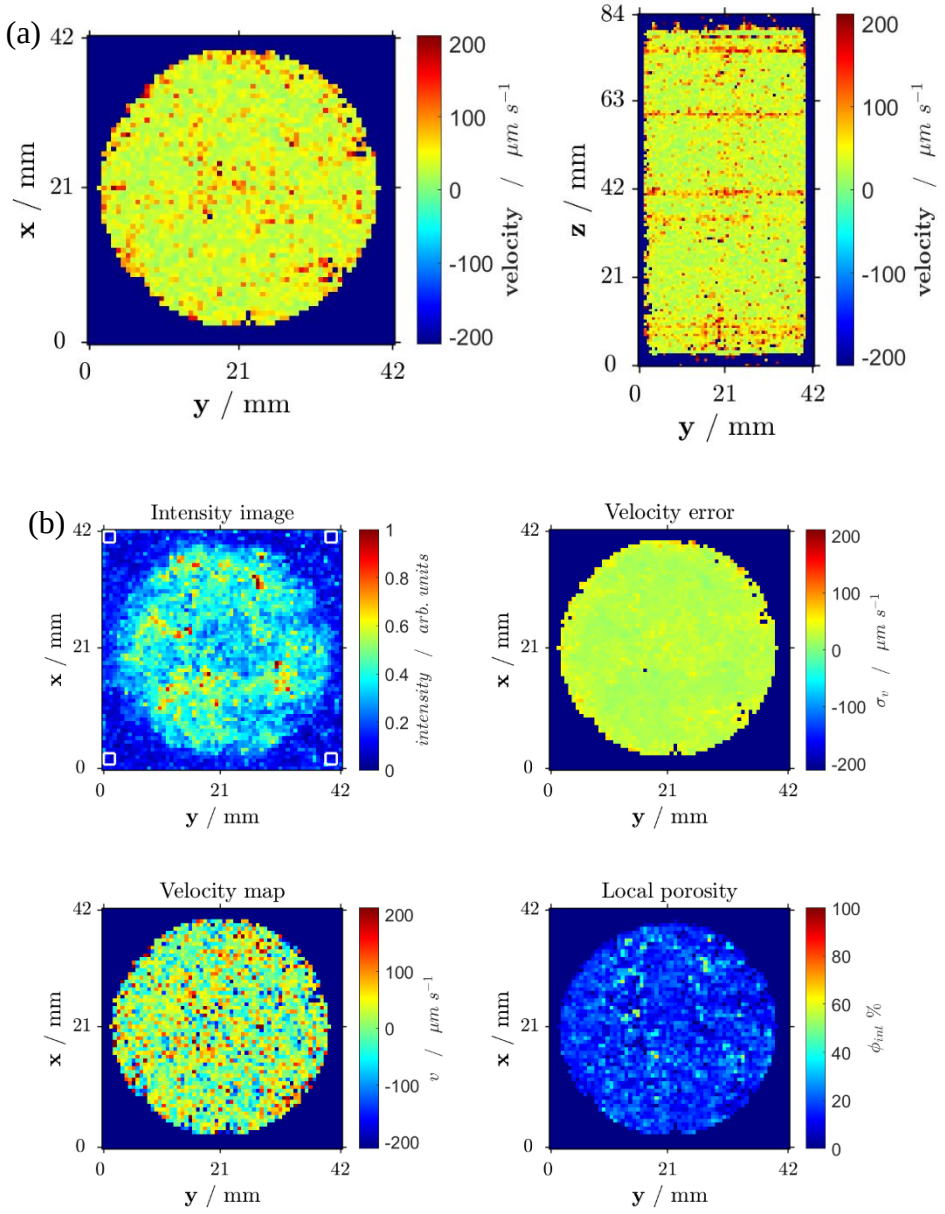

Figure 5-17: The middle x-y slice and z-y slice of the standard deviation between 5 velocity maps acquired under the same conditions using the same experimental parameters(a). The middle x-y slice for the average intensity image coming from the phase-contrast imaging, the local velocity error σ_u, the measured velocity map and the relative porosity coming from the 3D RARE image(b) for water flow at 6 ft d^{-1} through the $IND4_33$ core plug.

***COR1_7*: Figure 5-18** presents the same noise analysis for the lowest permeability rock. The colourmap for all the measurements has been scaled between ± 10×$\langle u \rangle_0$. In this rock, there are also some regions of high noise indicated by yellow and red

colours. These regions are represented by a long thick stripe across the centre of the x-y slice of the rock as clearly seen in the intensity image in **Figure 5-18**(b) (top left). This area is also characterised by very small values of $\phi_{rel}(\boldsymbol{r})$ as presented in **Figure 5-18**(b) (bottom right) and higher $\sigma_u(\boldsymbol{r})$. However, most of the areas of high velocities are located outside this noisy area as seen in the $u(\boldsymbol{r})$ map in **Figure 5-18**(b) (bottom left). Therefore, local ultra-slow velocities were measured accurately even at this extra-low permeability rock.

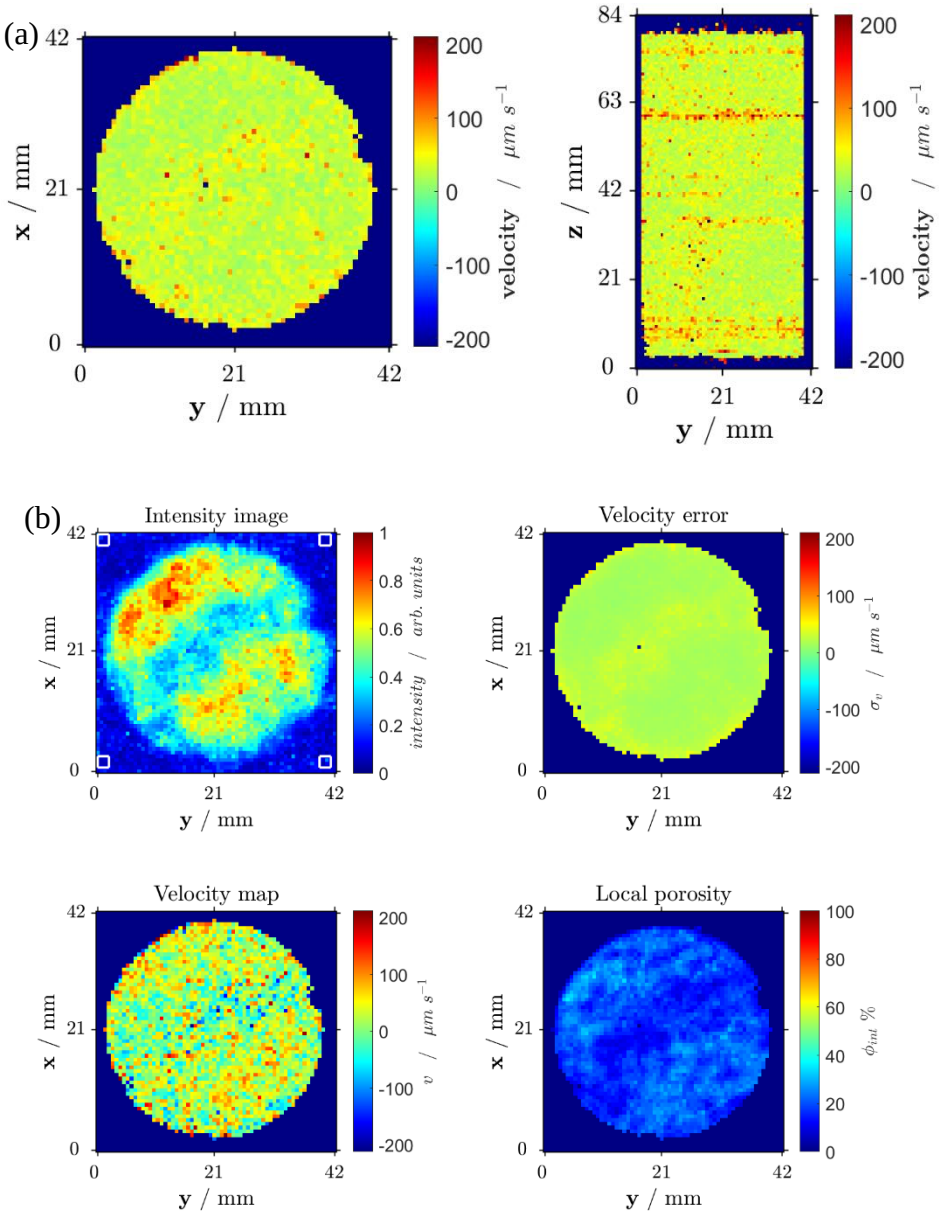

Figure 5-18: The middle x-y slice and z-y slice of the standard deviation between 5 velocity maps acquired under the same conditions using the same experimental parameters(a). The middle x-y slice for the average intensity image coming from the phase-contrast imaging, the local velocity error σ_u, the measured velocity map and the relative porosity coming from the 3D RARE image(b) for water flow at 6 ft d^{-1} through the $COR1_7$ core plug.

5.4.4 Velocity Maps from Phase-Contrast Imaging and 3D Propagators

The velocity maps coming from both the phase-contrast imaging and the 3D propagators for each different rock are presented below.

Bentheimer: Figure 5-19 shows the velocity maps coming from the phase-contrast imaging for 6 (a), 10 (b) and 15 ft d^{-1}(c) in Bentheimer. Bentheimer is a homogeneous sandstone and the flow field at this resolution appears homogeneous across the core for 6 and 10 ft d^{-1}. For 15 ft d^{-1}, there are two areas of high velocities close to the outlet of the sample, circled with a light blue line.

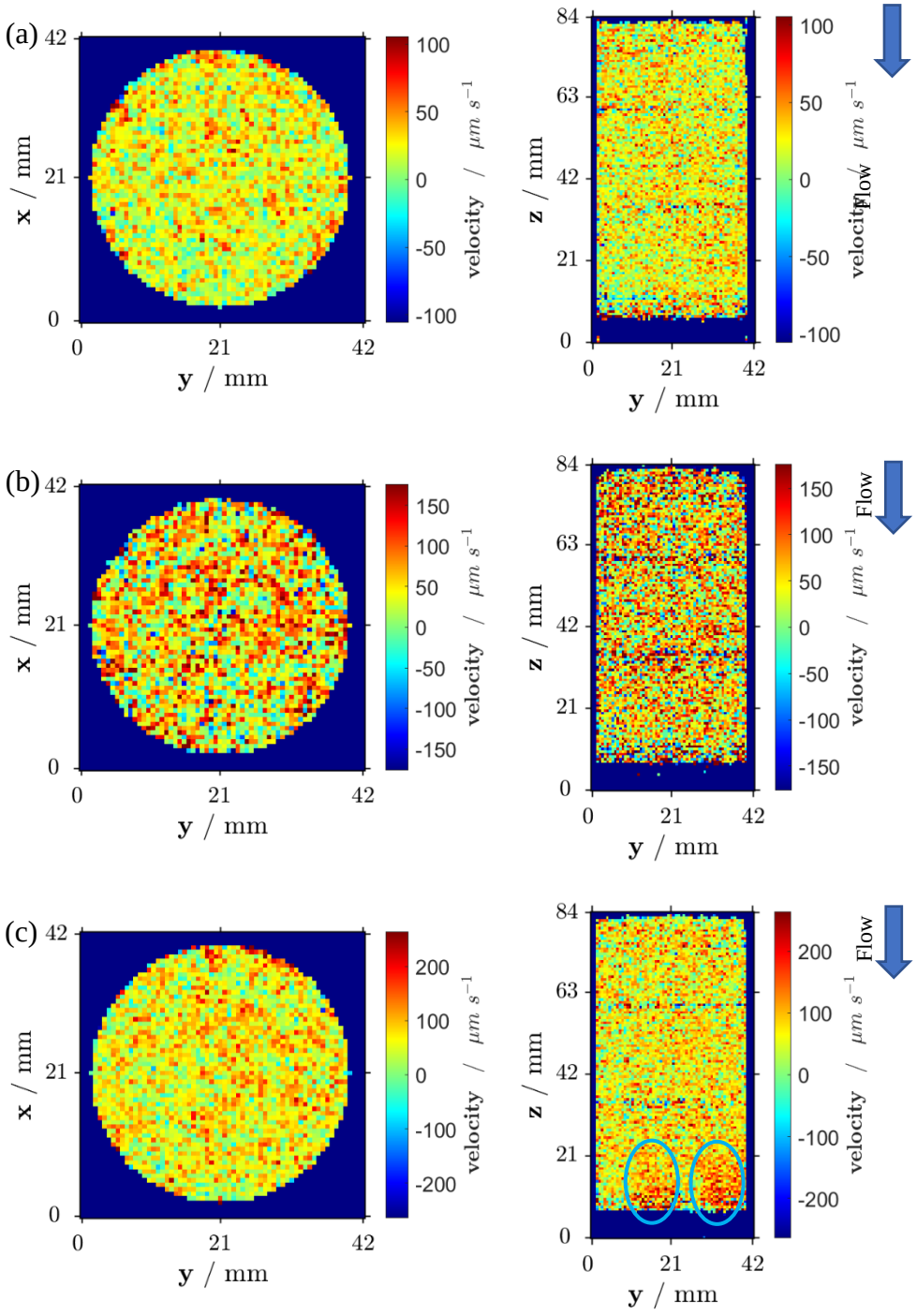

Figure 5-19: The middle *x-y* and *z-y* slices of the velocity maps coming from the phase-contrast imaging for water flow through the Bentheimer core plug at 6(a), 10(b) and 15(c) ft d^{-1}. Interesting areas are highlighted by the light blue circles. In the *z-y* slices, parallel 'zipping' lines which correspond to artefacts are present.

The velocity maps of 656.3 μm $pixel^{-1}$ resolution presented in **Figure 5-19** were averaged to a resolution of 2.63 mm $pixel^{-1}$ and are presented in **Figure 5-20** and **Figure 5-21**. **Figure 5-20** presents the comparison between the velocity maps of the same resolution coming from the phase-contrast(a) and the propagator(b) techniques

for 6 ft d^{-1}. In both *z-y* slices, an area of high velocities is present on the middle right side of the outlet and is circled by a light blue line.

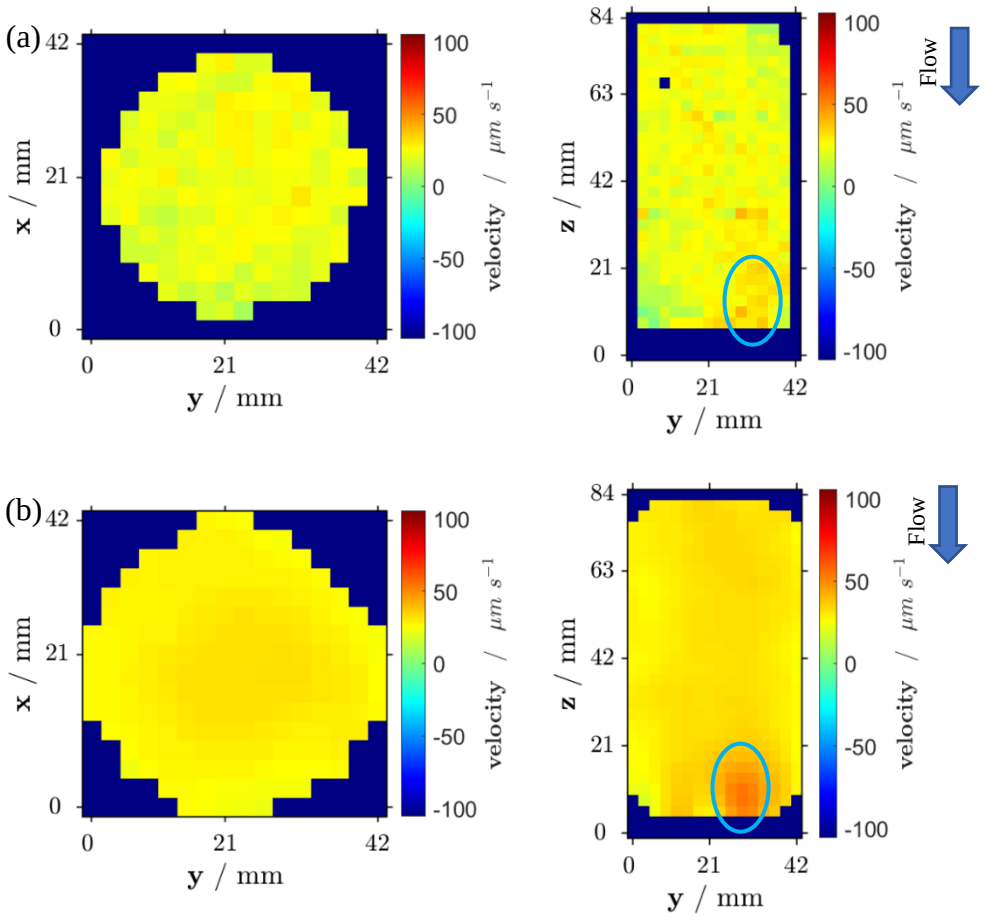

Figure 5-20: The middle *x-y* and *z-y* slices of the velocity maps coming from the phase-contrast imaging average at 2.63 mm $pixel^{-1}$ resolution(a) and from the 3D propagators for water flow through the Bentheimer core plug at 6 ft d^{-1}.

Figure 5-21 shows the results obtained for 15 ft d^{-1}. Both the phase-contrast(a) and the 3D propagator(b) velocity images presented two areas of high velocity close to the outlet. These two areas are circled by a light blue line in the *z-y* slice proving that both the phase-contrast and the propagator sequence recorded a similar pattern of flow.

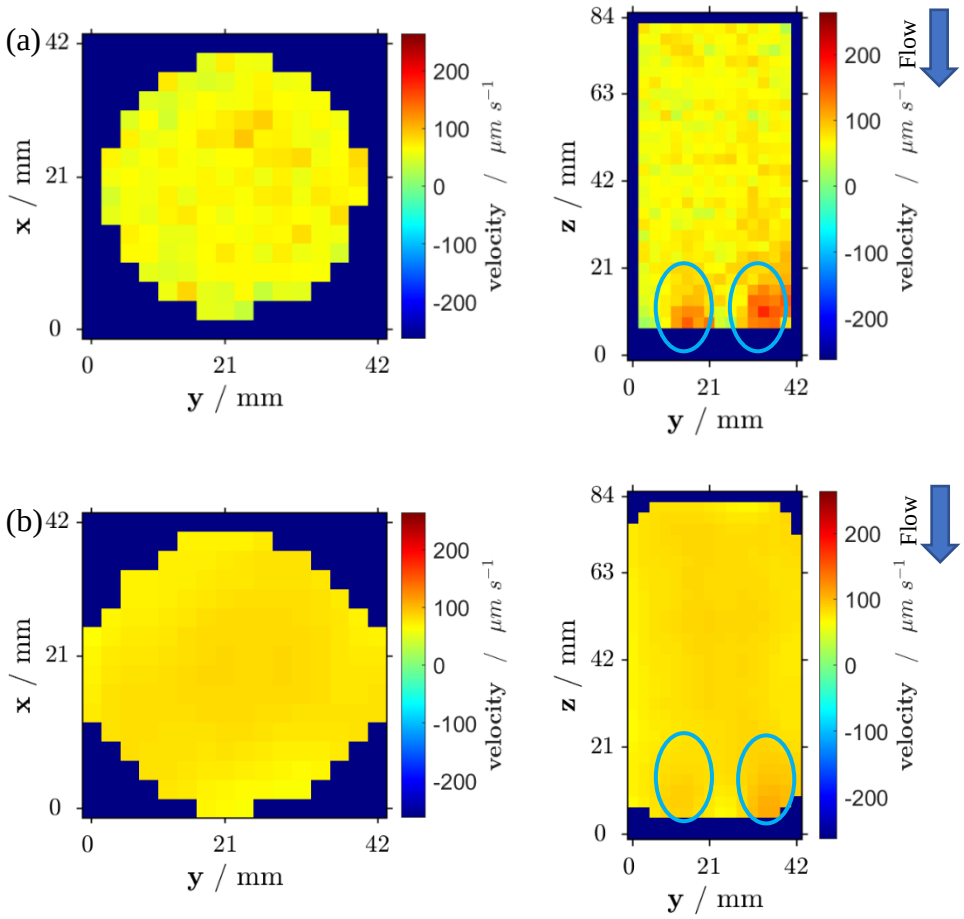

Figure 5-21: The middle *x-y* and *z-y* slices of the velocity maps coming from the phase-contrast imaging averaged at 2.63 mm pixel^{-1} resolution(a) and from the 3D propagators for water flow through the Bentheimer core plug at 15 ft d^{-1}.

Table 5-6 has summarised the $\langle u \rangle_m$ coming from both the phase-contrast and the propagator acquisitions. Although the phase-contrast imaging resulted in a $\langle u_m \rangle$ very close to the $\langle u_0 \rangle$ for all the flow velocities, the propagator measurement resulted in higher $\langle u_m \rangle$.

Table 5-6: Mean measured velocities coming from the phase-contrast imaging and the propagator measurements from the different flows through the Bentheimer core plug.

$\langle u_0 \rangle$ (ft d^{-1})	Q (mL min^{-1})	$\langle u_0 \rangle$ (μm s^{-1})	$\langle u_m \rangle$-phase-contrast (μm s^{-1})	$\langle u_m \rangle$ - propagators (μm s^{-1})
6	0.33	21.2	20.9 ± 7.1	28.6 ± 0.7
10	0.55	35.3	23.8 ± 7.9	51.8 ± 0.4
15	0.83	52.9	42.8 ± 2.8	76.9 ± 0.7

Estaillades: Figure 5-22 presents the velocity maps coming from the phase-contrast imaging for 6(a), 10(b) and 15 ft d^{-1}(c) in Estaillades. Even though Estaillades has a bimodal pore-throat distribution, the velocity maps coming from the phase-contrast imaging present a homogeneous distribution of high and low velocities. The same homogeneity in the velocity distribution is seen in the velocities coming from the

propagator measurements presented in **Figure 5-23**. An area of high velocities is highlighted by the light blue circle and is located at the same area of the core plug for all the different flow velocities.

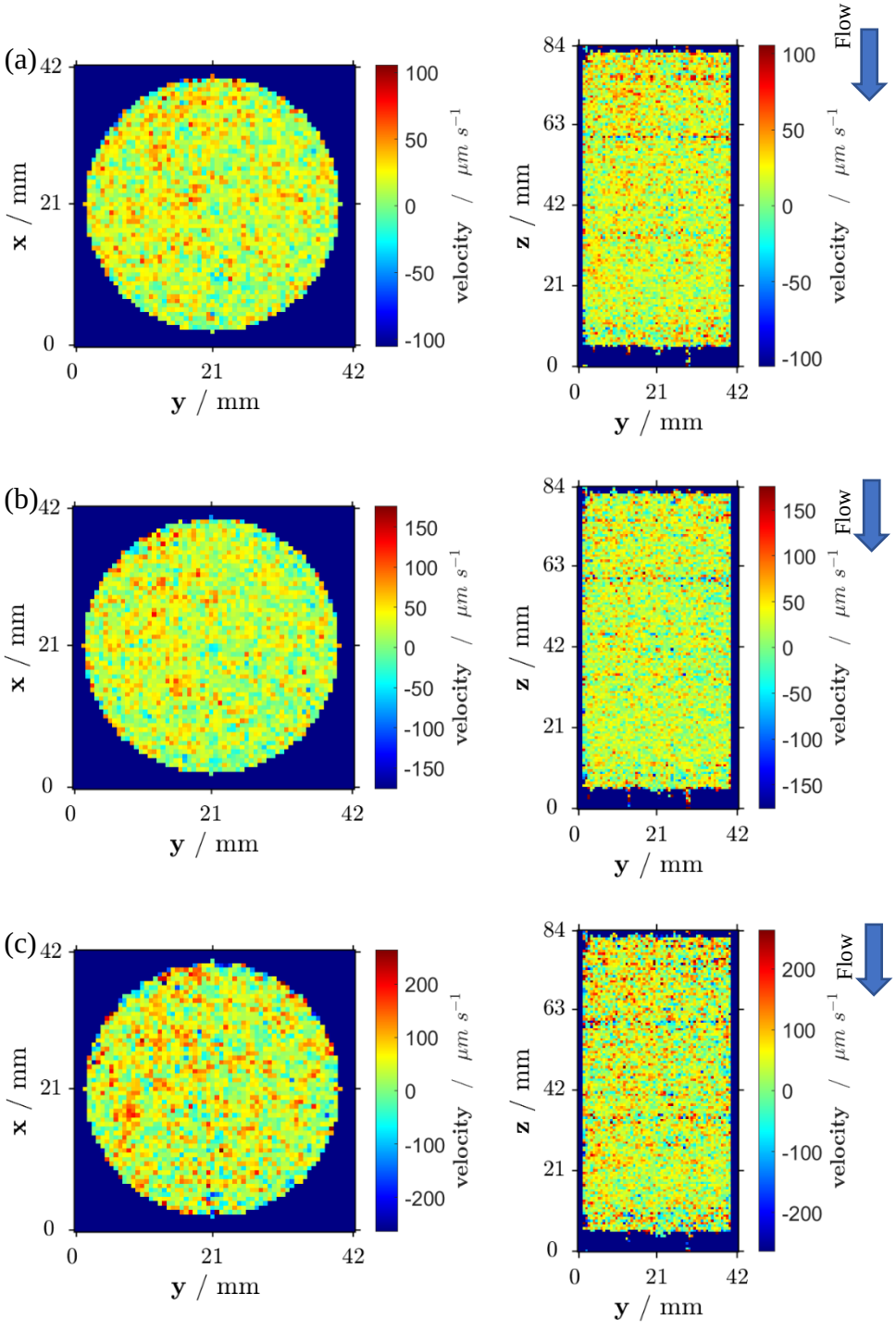

Figure 5-22: The middle *x-y* and *z-y* slices of the velocity maps coming from the phase-contrast imaging for water flow through the Estaillades core plug at 6(a), 10(b) and 15(c) ft d^{-1}. In the z-y slices, parallel 'zipping' lines which correspond to artefacts are present.

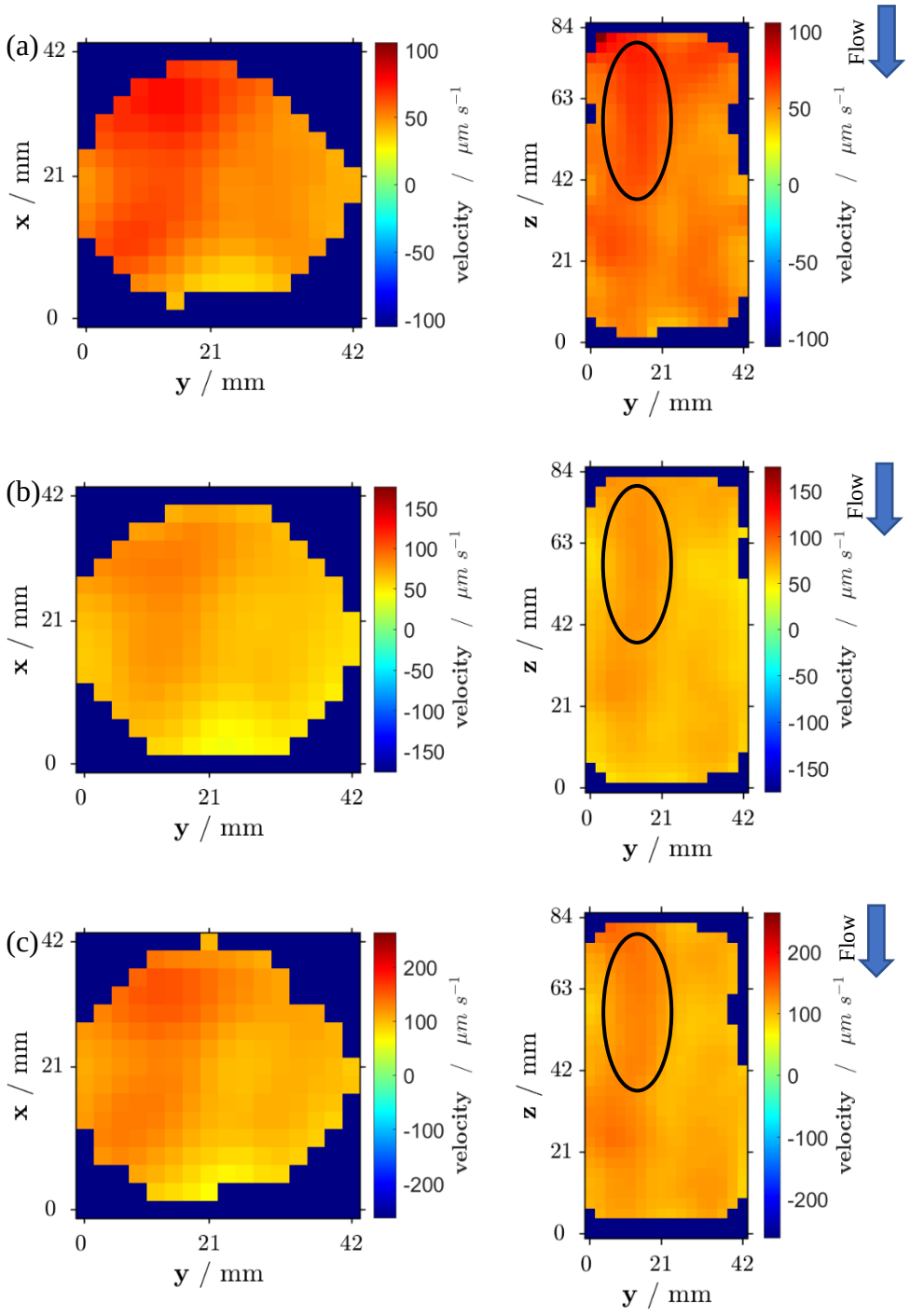

Figure 5-23: The middle *x-y* and *z-y* slices of the velocity maps coming from the propagator measurements for water flow through the Estaillades core plug at 6(a), 10(b) and 15(c) ft d^{-1}. Interesting areas are highlighted by the black circles.

Table 5-7 has summarised the $\langle u_m \rangle$ coming from both the phase-contrast and the propagator acquisitions. On the one hand, the phase-contrast imaging resulted in a $\langle u_m \rangle$ slightly lower than the $\langle u_0 \rangle$ for all the flow velocities. On the other hand, the propagator measurements resulted in $\langle u_m \rangle$ higher than the $\langle u_0 \rangle$.

Table 5-7: Mean measured velocities coming from the phase-contrast imaging and the propagator measurements from the different flows through the Estaillades core plug.

$\langle u_0 \rangle$ (ft d^{-1})	Q (mL min^{-1})	$\langle u_0 \rangle$ (μm s^{-1})	$\langle u_m \rangle$-phase-contrast (μm s^{-1})	$\langle u_m \rangle$ - propagators (μm s^{-1})
6	0.43	21.2	17.4 ± 6.1	54.2 ± 0.8
10	0.72	35.3	23.8 ± 6.9	64.8 ± 1.2
15	1.08	52.9	42.8 ± 2.8	109.8 ± 2.4

***IND4_33*: Figure 5-24** presents the velocity maps coming from the phase-contrast imaging for 6(a), 10(b) and 15 ft d^{-1}(c) in $IND4_33$. The areas of low SNR within the sample have been masked and several high-velocity voxels were detected. Due to its very short T_2 relaxation times, $IND4_33$ is one of few Indiana Limestone rocks whose velocity has been mapped successfully for different ultra-slow flow regimes. **Figure 5-25** shows homogeneous velocity profiles coming from all the propagator measurements. This homogeneous mapping across the core and around zero is a result of several parameters which will be discussed later.

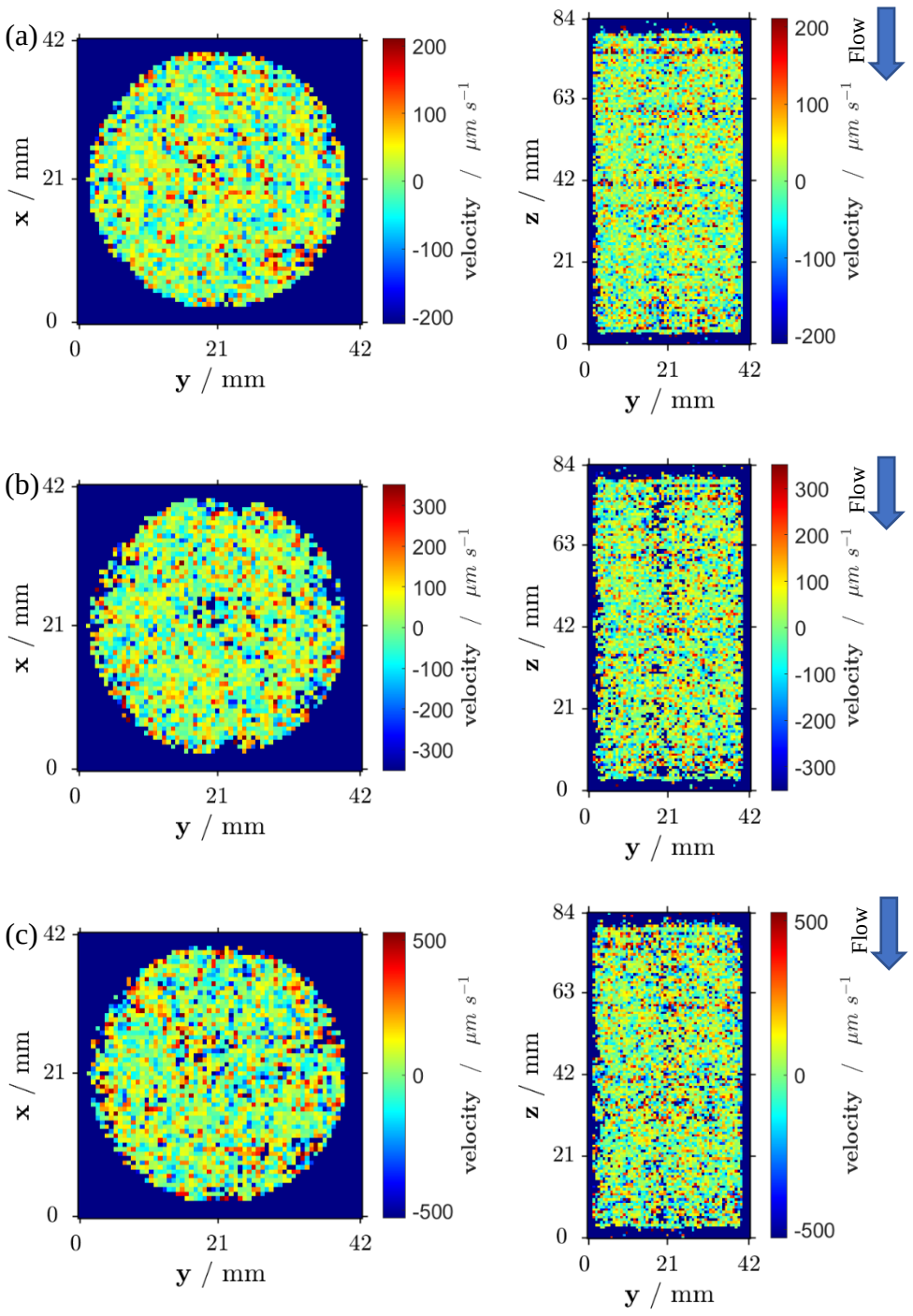

Figure 5-24: The middle x-y and z-y slices of the velocity maps coming from the phase-contrast imaging for water flow through the $IND4_33$ core plug at 6(a), 10(b) and 15(c) ft d^{-1}. In the z-y slices, parallel 'zipping' lines which correspond to artefacts are present. In the z-y slices, parallel 'zipping' lines which correspond to artefacts are present.

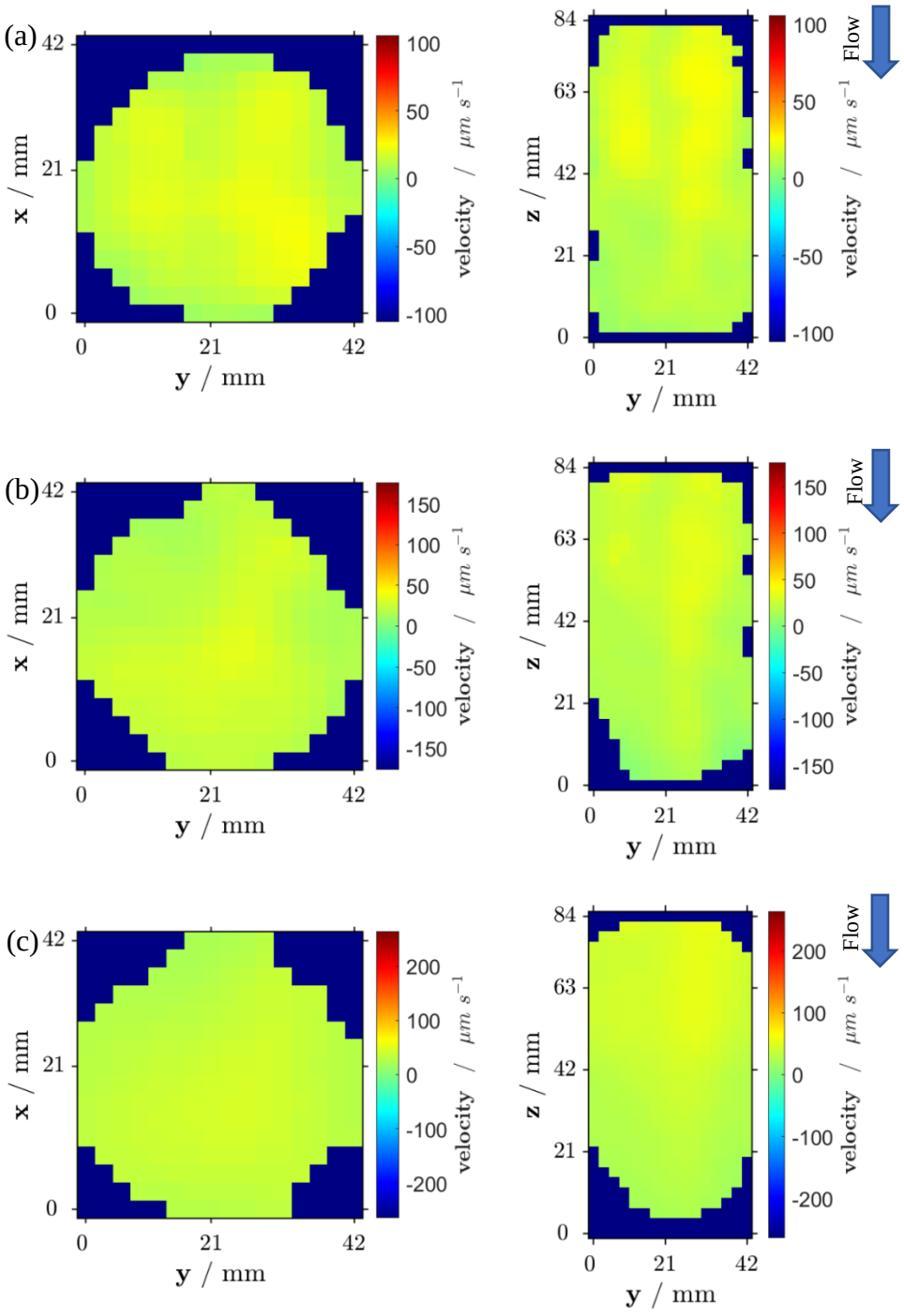

Figure 5-25: The middle x-y and z-y slices of the velocity maps coming from the propagator measurements for water flow through the $IND4_33$ core plug at 6(a), 10(b) and 15(c) ft d^{-1}.

Table 5-8 displays the $\langle u_m \rangle$ coming from both the phase-contrast and the propagator acquisitions. Both the phase-contrast and the propagator measurements resulted in $\langle u_m \rangle$ lower than the $\langle u_0 \rangle$.

Table 5-8: Mean measured velocities coming from the phase-contrast imaging and the propagator measurements from the different flows through the $IND4_33$ core plug.

$\langle u_0 \rangle$ (ft d^{-1})	Q (mL min^{-1})	$\langle u_0 \rangle$ (μm s^{-1})	$\langle u_m \rangle$ - phase-contrast (μm s^{-1})	$\langle u_m \rangle$ - propagators (μm s^{-1})
6	0.26	21.2	8.4 ± 3.4	17.0 ± 0.6
10	0.43	35.3	14.5 ± 2.4	25.6 ± 0.9
15	0.65	52.9	23.3 ± 3.2	42.1 ± 1.7

COR1_7: **Figure 5-26** presents the velocity maps coming from the phase-contrast imaging for 6 (a), 10 (b) and 15 ft d^{-1}(c) in $COR1_7$. The left side of the z-y slice is dominated by areas of low SNR and several voxels have been masked. However, the right side of the z-y slice demonstrates several regions of high velocities which are highlighted by the black circles. In the x-y slice, the thick stripe of low SNR at the centre of the core plug has been masked and the areas of high velocities have also been circled. The same high-velocity areas were also observed in the velocity maps coming from the propagator measurements which are exhibited in **Figure 5-27**. It can be seen that in propagator measurements, the results suffer from low SNR and a large among of voxels have been masked, especially in **Figure 5-27**(c). $COR1_7$ is an ultra-low permeability rock and this is the first time that velocity has been detected in such a difficult to study sample.

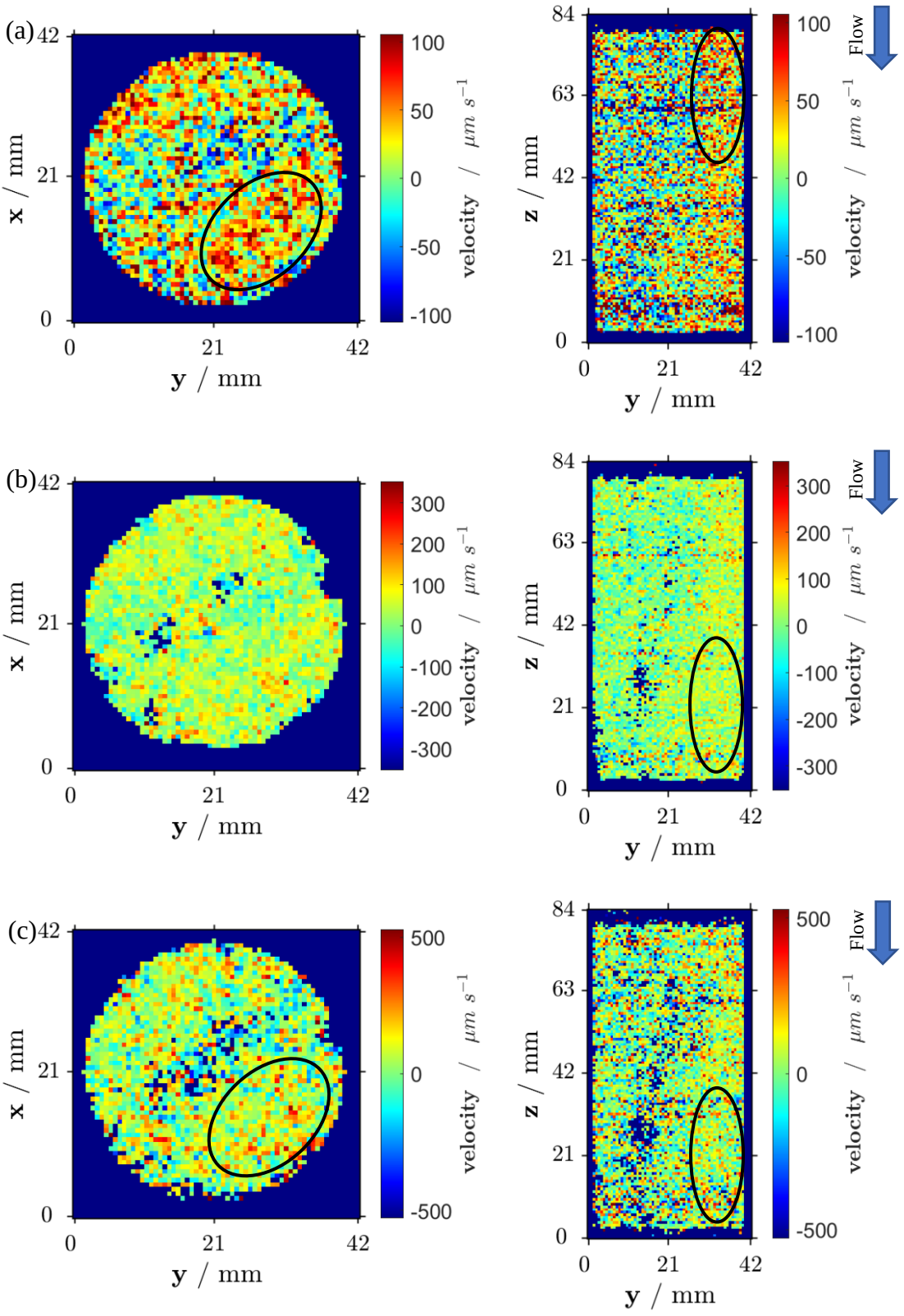

Figure 5-26: The middle x-y and z-y slices of the velocity maps coming from the phase-contrast imaging for water flow through the $COR1_7$ core plug at 6(a), 10(b) and 15(c) ft d^{-1}. In the z-y slices, parallel 'zipping' lines which correspond to artefacts are present.

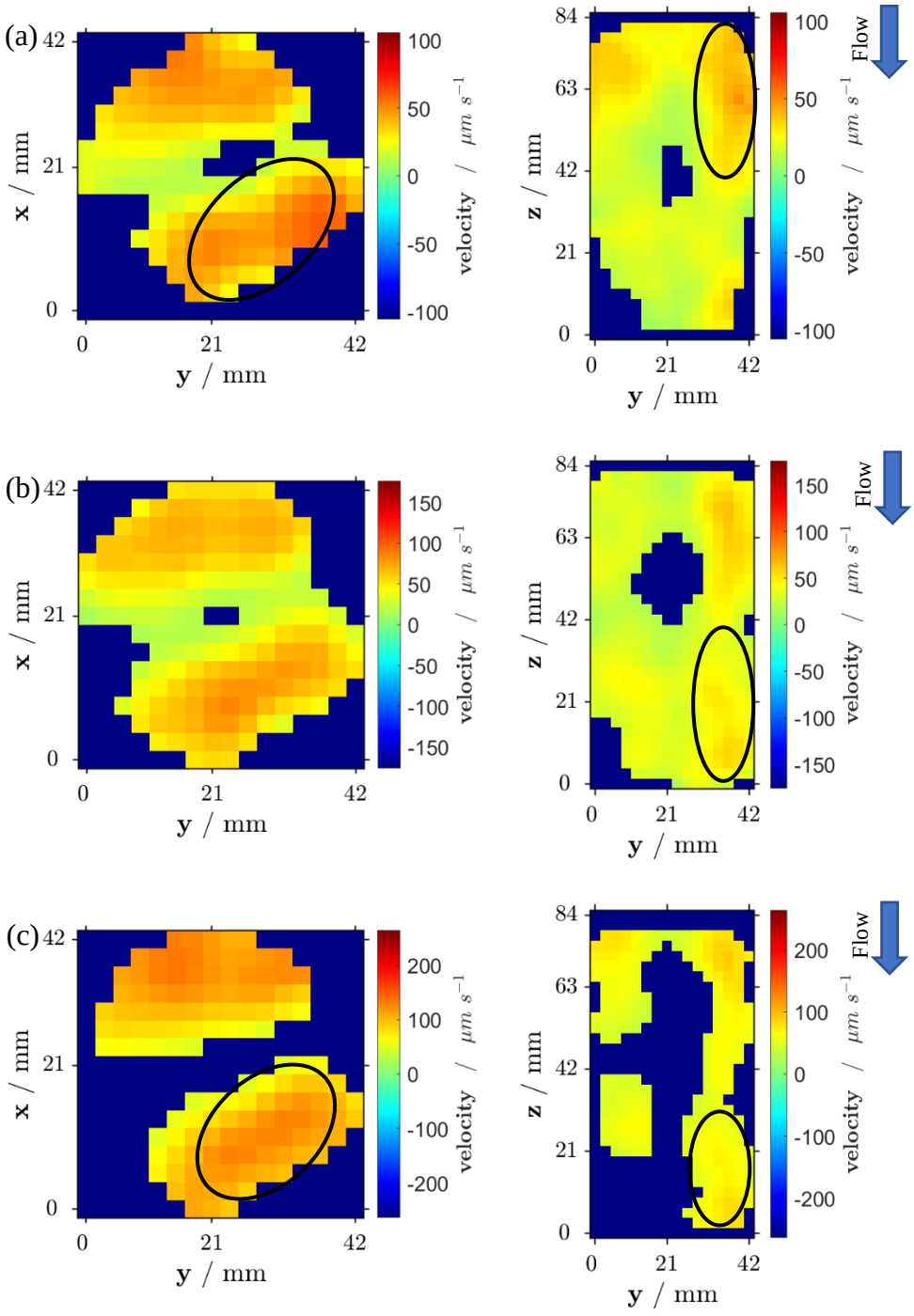

Figure 5-27: The middle x-y and z-y slices of the velocity maps coming from the propagator measurements for water flow through the $COR1_7$ core plug at 6(a), 10(b) and 15(c) ft d^{-1}. Interesting areas are highlighted by the black circles.

Table 5-9 gathers the $\langle u_m \rangle$ coming from both the phase-contrast and the propagator measurements for the $COR1_7$ sample. The phase-contrast imaging resulted in a $\langle u_m \rangle$ similar to the $\langle u_0 \rangle$, whereas the propagator measurements derived a much larger $\langle u_m \rangle$. It should be pointed out that in the propagator measurements, a large number of voxels had been masked. This means that many voxels of low SNR or low velocity have been excluded from the measurement.

Table 5-9: Mean measured velocities coming from the phase-contrast imaging and the propagator measurements from the different flows through the $COR1_7$ core plug.

$\langle u_0 \rangle$ (ft d^{-1})	Q (mL min^{-1})	$\langle u_0 \rangle$ (μm s^{-1})	$\langle u_m \rangle$ - phase-contrast (μm s^{-1})	$\langle u_m \rangle$ - propagators (μm s^{-1})
6	0.29	21.2	16.2 ± 6.2	32.6 ± 0.8
10	0.48	35.3	29.8 ± 7.4	48.4 ± 0.7
15	0.73	52.9	46.9 ± 9.3	85.5 ± 1.4

5.4.5 Flow Paths Formed from the Phase-Contrast Images

Figure 5-28 presents the flow paths derived by the velocity vectors for 15 ft d^{-1} through the Bentheimer (a) and the Estaillades (b) rocks. The three data acquisitions were combined using the 'streamslice' function of MATLAB. **Figure 5-28** shows that for the same velocity, the homogeneous pore structure of the Bentheimer enables the formation of long straight flow paths towards the exit. In contrast, the bimodal pore structure of the Estaillades causes tortuosity in the detected flow paths towards the outlet.

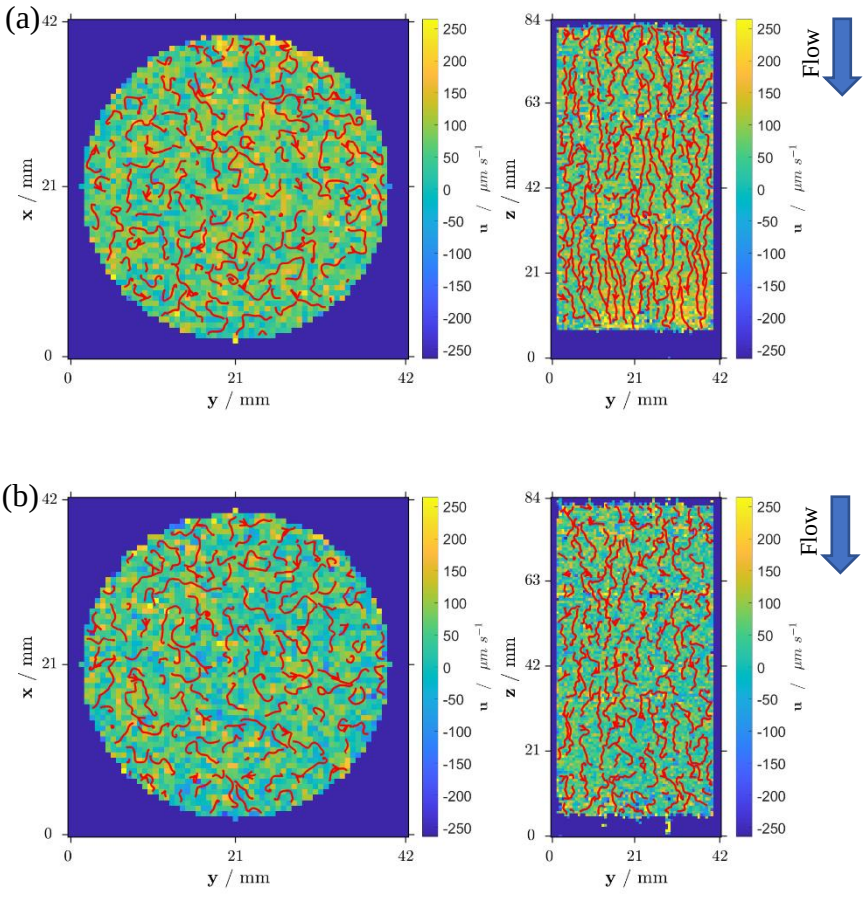

Figure 5-28: The middle x-y and z-y slices of the velocity maps with the flow paths (red lines with arrows showing the direction) for water flow through the Bentheimer (a) and the Estaillades(b) core plug at 15 ft d^{-1}.

Figure 5-29 presents the flow paths derived by the velocity vectors for 15 ft d^{-1} through the two Indiana limestones, the $IND4_33$(a) and the $COR1_7$(b) rocks. In contrast to Bentheimer and Estaillades, the narrow pore throats met in Indiana

Limestones are responsible for the presence of several unconnected and tortuous flow paths along the flow direction. In **Figure 5-29**(b), some longer tortuous flow paths, similar to the ones observed in Estaillades, can be seen close to the outlet of the z-y slice of the $COR1_7$. These areas are highlighted by the black line and indicate the presence of connected pores in this area.

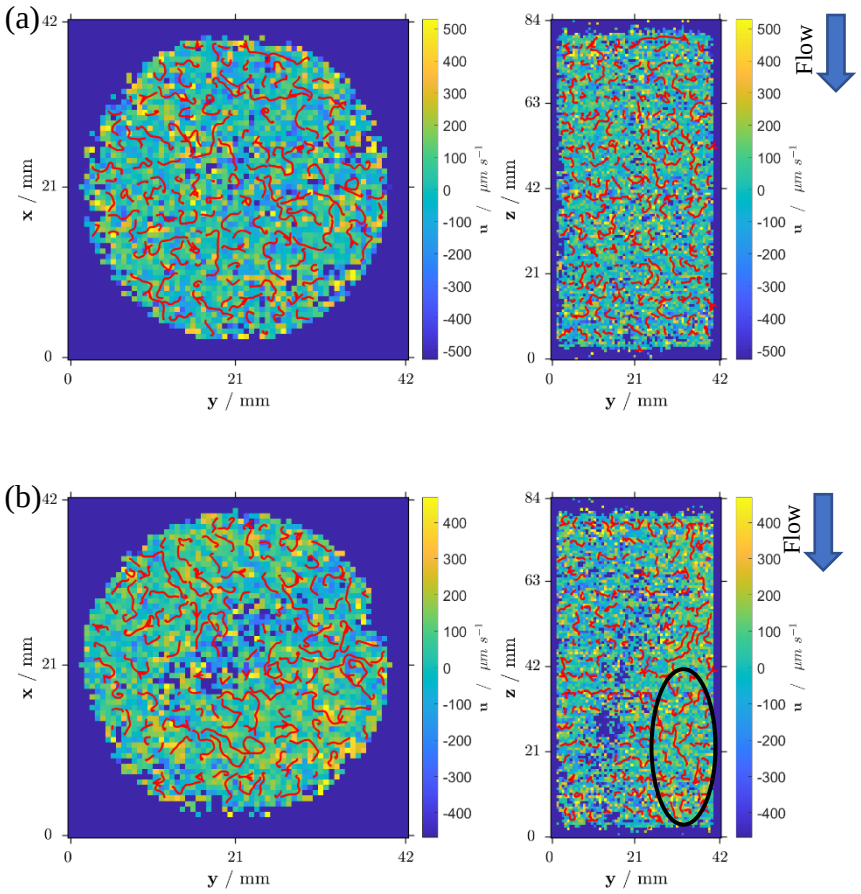

Figure 5-29: The middle x-y and z-y slices of the velocity maps with the flow paths (red lines with arrows showing the direction) for water flow through the $IND4_33$(a) and the $COR1_7$(b) core plug at 15 ft d^{-1}.

5.5 Discussion

As discussed in Chapter 4, it is important to analyse the T_1 and T_2 relaxations for each rock, as well as the D_app before finding the optimum experimental parameters for the slow-flow experiments. By analysing the relaxations and the diffusion coefficient interesting observations can be made about the rocks. Bentheimer presented a strongly unimodal pore structure with strong internal gradients. Estaillades exhibited a bimodal T_1 distribution which is in agreement with the pore body size distribution seen in the literature for Estaillades (Dautriat et al., 2011; Mitchell and Fordham, 2014). The short T_1 is related to the microporosity of the core (< 2 μm), while the long T_1 corresponds to the macroporosity. Its T_2 distribution demonstrates strong diffusive coupling between the pores (Mitchell et al., 2014). $IND4_33$ is an Indiana Limestone presenting bimodal pore structure and strong internal gradients. According to the literature, the variation in the pore size creates distinct regions with stronger and

weaker local magnetic field gradients. The spins diffuse between these distinct regions, giving rise to multiple T_2 times (Mitchell and Fordham, 2014). This explains the multiple peaks T_2 distribution measured in the $IND4_33$. In addition to that, the sample is dominated by microporosity with fast T_2 relaxations which deteriorate the SNR in the velocity measurements. The other Indiana Limestone, $COR1_7$, presented T_1 and T_2 relaxations faster than the $IND4_33$. Faster T_1 means the pore throats in this limestone were narrower. $COR1_7$ is an extra-low permeability rock with stroing diffusive coupling which make it hard to study.

Comparing the $\phi_{rel}(\boldsymbol{r})$ map among the samples, a homogeneous distribution can be seen in Bentheimer, while areas of low intensity mixed with the high-intensity ones can be noticed in the other three carbonates. This agrees with the multi-modal peak T_1 distribution recorded in the carbonate samples. Analysing the standard deviation among successive velocity maps and the $\sigma_u(\boldsymbol{r})$ maps measured for the 6 ft d^{-1} regime in all the studied rocks, it was proved that the noise imported in the local velocity measurements was small. Therefore, the optimisation toolbox proved valid for the measurement of the ultra-slow velocities through rocks. The two Indiana Limestone samples presented higher values of noise in some regions within the sample. This high noise was related to the low local SNR due to the fast T_2 relaxation. The areas of low SNR and high local noise were also mapped in the $\phi_{rel}(\boldsymbol{r})$ map and in the intensity image of the velocity map.

For the case of water flow through the Bentheimer, the velocity mapping coming from the averaged phase-contrast imaging presented a similar pattern of flow to the one detected with the 3D propagator sequence. The velocity distribution was relatively homogeneous along the core with some areas of concentrated high-velocity voxels close to the outlet. Estaillades also presented a relatively homogeneous distribution of the velocity field along the core using both velocity imaging techniques. Both Betheimer and Estaillades presented long connected flow paths for the 15 ft d^{-1} regime presented in **Figure 5-28**. On the other hand, $IND4_33$ and $COR1_7$ presented several areas of low SNR within the rock which were related to the fast T_2 relaxation. $IND4_33$ presented a homogeneous velocity map coming from the propagator measurement. The long Δ in addition to the low-resolution of the propagator measurements resulted in the green colour which dominates **Figure 5-25**. In other words, the high-velocity voxels detected in **Figure 5-24** were merged with the low or no-velocity voxels, presenting that homogeneous green colour. As shown by the flow paths in **Figure 5-29**(a), $IND4_33$ is a rock dominated by dead ends and unconnected paths. Similar flow path patterns have also been detected by Romanenko et al., (2012) in higher flow rates of 2 mL min^{-1}. In $COR1_7$, the propagator measurements mapped the areas of higher velocities and the results were aligned with the phase-contrast imaging results. However, the propagator measurements were governed by voxels of low SNR which were masked in the data processing. This resulted in an important loss of information as seen in **Figure 5-27**. The $\langle u_m \rangle$ obtained by the propagator measurements was higher than the $\langle u_m \rangle$ measured by the phase-contrast imaging because propagator captures movement from both flow and diffusion. Moreover, some of the slow flowing spins especially in the Indiana Limestones may have relaxed due to surface relaxation.

The novel phase-contrast imaging was proved less sensitive to noise even though the measurements were obtained at higher resolution. Acquisition of high-resolution propagators which can detect the ultra-slow flow was very difficult for the two Indiana Limestone samples since noise dominated the measurements.

5.6 Conclusion

In this chapter, the two techniques of phase-contrast imaging and low-resolution propagators developed in Chapter 4 for observing ultra-slow flowrates in less than one hour were tested in a homogeneous sandstone and in three heterogeneous carbonates. None of these techniques had pore-scale resolution. The aim of this study is to show that the multi-objective optimisation and the new propagator technique can capture for the first time ultra-slow flows in the complex pore space of different rocks and to identify areas of high velocity flow paths as the externally applied flow from the pump was changing.

The same noise analysis was conducted for all the samples and all the flow rates. The standard deviation among consecutive velocity maps and the measurement of the $\sigma_u(\boldsymbol{r})$ proved that in most areas within the volume of each sample, the detected velocities were much higher compared to the local noise. In Bentheimer, a homogeneous velocity distribution with some areas of higher velocity close to the outlet were recorded by both propagator and phase-contrast imaging. The flow paths recorded for flow through this homogenous sandstone were long and straight in contrast to the more tortuous paths detected in Estaillades. The heterogeneity in the pore-throat distribution affected the formed flow paths for the same externally applied velocity of 15 ft d^{-1}. $IND4_33$ and $COR1_7$ were dominated by unconnected flow paths and areas of low SNR. The novel phase-contrast imaging was proved as the most suitable and less noise-sensitive technique for the acquisition of velocity measurements in these rocks.

This is the first time that the transverse and the longitudinal dispersion have been recorded for flow through the same core plug at different flow rates. Moreover, this is the first time that flow through a rock at reservoir-like interstitial velocities has been recorded with MRI. The utter goal is to use these two techniques to identify the changing behaviour of polymers when flooded through these rocks and identify the optimum flow rate which will result in the highest oil recovery in a two-phase system. In Chapter 6, a new method for capturing two-phase flow in a water-oil system was developed and was applied in an ideal and in an Estaillades.

Chapter 6 Two-Phase Flow in an Ideal and in a Rock-Porous System

6.1 Introduction

Chemical shift sensitivity is one of the key advantages of MR as it allows us to distinguish the signal coming from different chemical species, whereas other imaging techniques such as micro-CT require the addition of dopants in order to map multiphase flow distribution. The addition of dopants is considered costly and corrosive to the equipment. In addition, bulk properties are influenced by the presence of dopants leading to inaccurate results (Lin et al., 2018; Vinegar, 1986; Wildenschild and Sheppard, 2013). NMR techniques rely on good spectroscopic chemical shift separation between the chemical compounds. Several methods based on the spin-echo sequence have been employed to distinguish between oil and water signals (Tessier and Packer, 1998). Other techniques based on the different relaxation times or different diffusion coefficients of the species have also been proposed. Bulk $T_1 - T_2$, $D_{app} - T_2$ measurements as well as spatially-resolved sequences such as $L - T_2$, $L - T_1 - T_2$ and SESPI (T_2 maps) have been applied in both low- and high-field magnetic fields to map the remaining oil phase during or after water-flooding (Bush, 2018a; Jonathan Mitchell et al., 2012; Mitchell et al., 2013b). Another famous technique is the WATERGATE pulse sequence in which a selective π pulse is used to affect only the water resonance (Liu et al., 1998).

In porous media, T_2 relaxation is very fast making the signal suppression scheme look like the most prominent technique for chemical selection in porous media. Pre-saturation of the solvent resonances by a low-power selective r.f. pulse is a common suppression technique that presents several drawbacks as described by Zheng and Price (2010). Selective water excitation followed by gradient dephasing is a standard technique initially used for suppression of the T_1 and B_1 inhomogeneities in the single-scan localisation methods such as STEAM (90°–TE/2–90°–TM–90°–TE/2–Acq) (Frahm et al., 1987) and PRESS (90°–TE_1–180°–TE_{1+2}–180°–TE_2– Acq) (Bottomley, 1982). Single water- and oil-suppression sequence has been combined with pulse-acquire and RARE sequence and has been used in water-flooding through dodecane saturated Estaillades rock (Ramskill et al., 2018). A more efficient method of multiple frequency-selective r.f. pulses followed by dephasing gradients of changing amplitude has been proven insensitive to T_1 and B_1 inhomogeneities. This n-pulse variable angle sequence is called WET (Water suppression Enhanced through T_1 effects) method. This method is independent of intervoxel T_1 and B_1 inhomogeneities and therefore spatial homogeneity in suppression is achieved (Ogg et al., 1994; Smallcombe et al., 1995). This suppression technique is used in the current experiment for dodecane and water suppression and is combined for the first time with pulse-acquire, RARE and APGSTE-RARE for spatially-resolved two-phase flow in an ideal porous medium and in a complex carbonate rock.

6.2 Methods for Achieving Chemical Selectivity

6.2.1 Chemically-Selective Pulse-Acquire Experiment

NMR spectra are considered a quantitative and fast measurement of the bulk presence of a chemical species in the sample. It has been stated that a single Gaussian pulse leads to non-uniform excitation of frequencies (Callaghan, 2014; Gladden, 1994). This is why this chapter focuses on multiple Gaussian pulses known as the WET scheme are used for the chemical shift selectivity of the oil and the water phase in combination with several sequences. Figure 6-1 presents a new pulse sequence where the WET scheme is combined with the pulse-acquire experiment. Discrimination between chemical species is achieved by four selective excitation pulses at x-, y-, y- and y-direction, respectively. The flip angle θ for each pulse was optimised to account for T_1 and B_1 inhomogeneities following the method described by Ogg et al. (1994). Each selective pulse is followed by a dephasing homospoil gradient at the transverse plane. The homospoils are applied along with the three (z, x, y) orthogonal directions. The duration of the homospoils was defined as δ_h, the gradient stabilisation delay as τ_h and the time interval between the soft pulses as τ_s. The amplitude of each subsequent homospoil gradient is halved yielding g_h, $1/2\ g_h$, $1/4\ g_h$ and $1/8\ g_h$where g_h is the amplitude of the first homospoil gradient. This change in amplitude has been proved more efficient for the minimisation of the gradient echoes (Smallcombe et al., 1995). Then, the un-suppressed phase can be manipulated from the pulse sequence that follows.

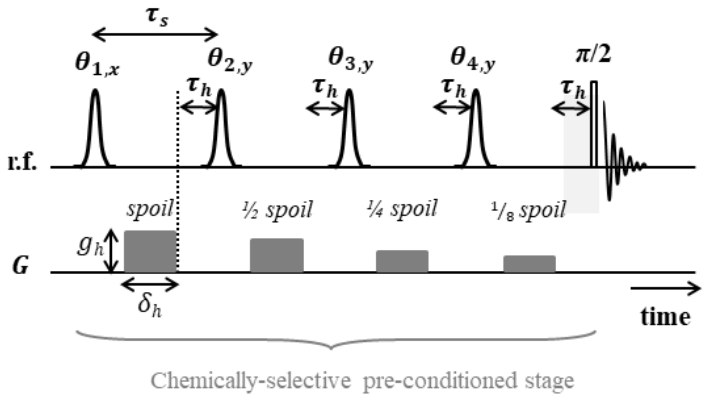

Figure 6-1: Schematic of the chemically-selective pulse-acquire experiment. Chemical suppression is based on the WET pre-conditioned sequence which consists of four soft pulses with variable flip angles (<180°) and with x, y, y, y phases respectively. The amplitude of each subsequent gradient pulse is halved and the gradient stabilisation delay is denoted as τ_h. The time duration between two successive soft pulses is τ_s.

6.2.2 Chemically-Selective and Spatially-Resolved Spectra

The four pulses WET suppression scheme was also integrated into the 1D spatially-resolved Chemical Shift Imaging (CSI) pulse sequence as shown in Figure 6-2. Acquiring spatially-resolved spectra can give an extra validation for the effectiveness of the WET scheme when the information is spatially-resolved since the sequence is based on the peak suppression. Acquiring spectra along the full length of the sample shows that at each pixel the one peak is fully-suppressed and only the signal from the

selected chemical compound is detected. This step can be used before the acquisition of 3D RARE images with chemical suppression, to test the efficiency of the peak suppression when it is applied spatially.

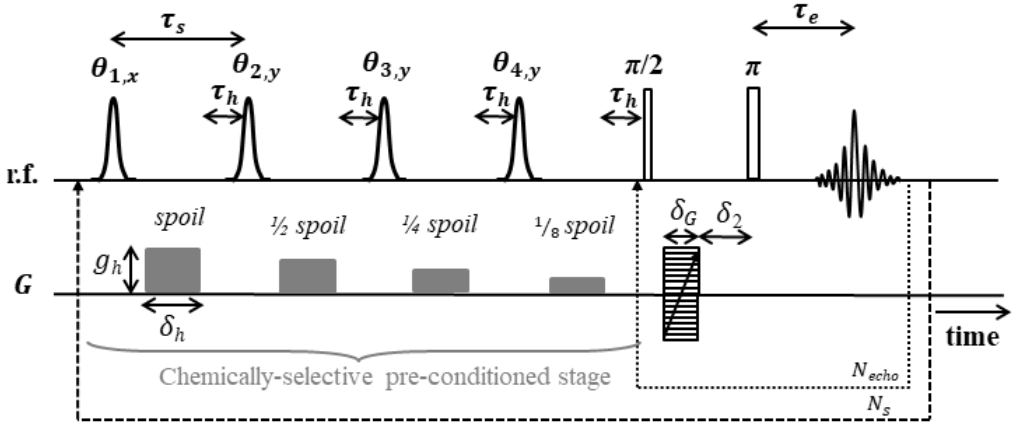

Figure 6-2: Schematic of the chemically-selective CSI experiment. Chemical suppression is achieved by adding the WET pre-conditioned sequence in front of the chemical shift imaging module. The spatial information is achieved using the changing amplitude gradient of duration δ_G.

Chemically-selective 1D or 3D CSI experiments can be used in complex systems such as catalytic reactions (Yuen et al., 2002), where multiple peaks are present and the acquisition of the spectrum at each voxel suppressing only one peak is required. In the current research, the effectiveness of the pulse sequence was compared to volumetric measurements and to the results coming from 3D RARE images.

6.2.3 Chemically-Selective RARE Images

For the acquisition of chemically-selective images, a pre-conditioning stage of four selective pulses was added in front of the 3D RARE imaging sequence (Hennig et al., 1986) as shown in Figure 6-3. Even though the application of a 3D CS-RARE sequence in combination with a chemical suppression scheme has already been used by Ramskill et al. (2018) to study the multi-phase flow in a core-plug, the WET-based suppression scheme in combination with the improved under-sampling and reconstruction method, improved the accuracy and reliability of the quantitative results which is important for the two-phase flow analysis.

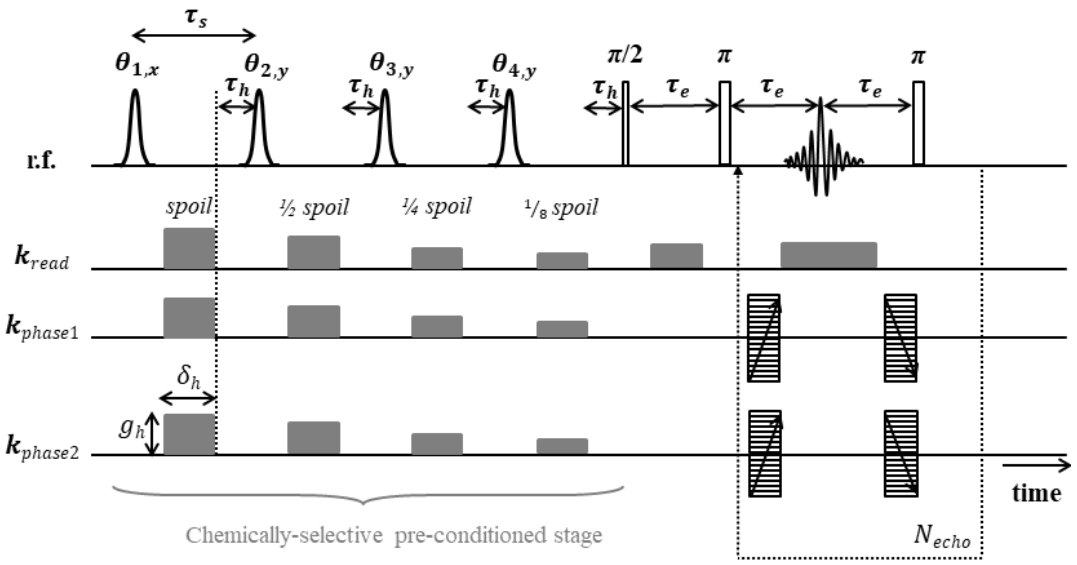

Figure 6-3: Schematic of the chemically-selective RARE experiment. Chemical suppression is achieved by adding the WET pre-conditioned sequence in all three orthogonal directions (z,x,y) in front of the RARE imaging module.

In the current chapter, results from both fully-sampled and under-sampled RARE images with chemical selection will be presented and will be compared to the results coming from the single-selective pulse suppression scheme used by Ramskill et al. (2018).

6.2.4 Chemically-Selective and Spatially-Resolved Flow Propagators

As explained in Chapter 4, the APGSTE sequence is more suitable for the study of flow through porous media of fast T_2 relaxation. Implementing the chemically-selective stage during the t_{store} time interval, as shown in Figure 6-4, was proven ideal for the chemical selection under flow conditions. By placing the selective pulses during the t_{store} time interval, the chemical selection was achieved without increasing the experimental time. Moreover, there are no limitations in the choice of Δ. The one phase is suppressed during the t_{store} time interval, while the un-suppressed phase-encoded in the q_z-space. Then, they experience the RARE sequence which provides 3D spatial resolution.

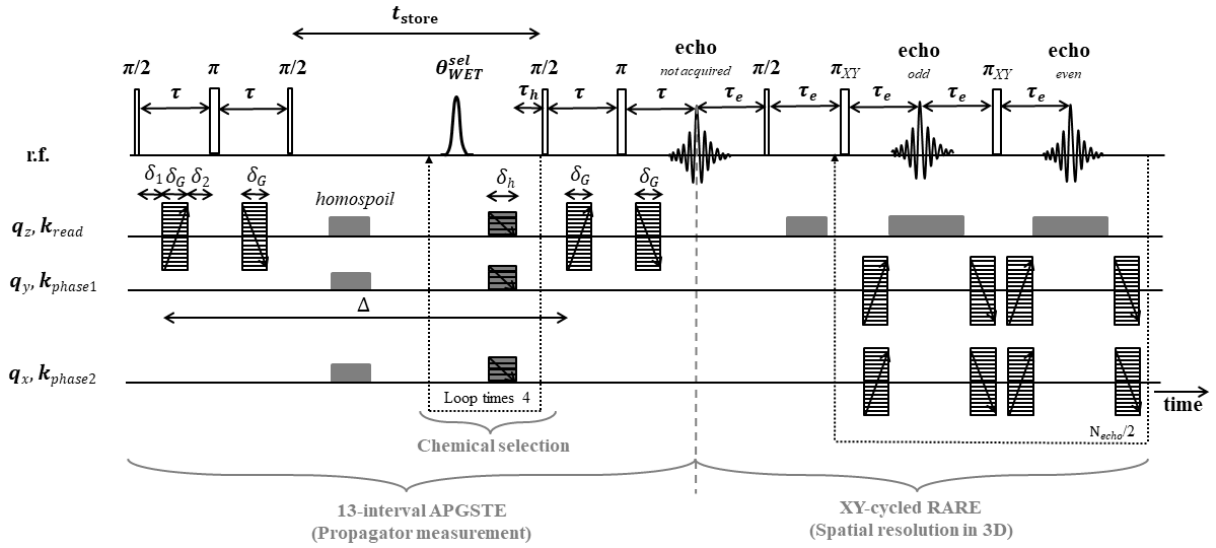

*Figure 6-4: Schematic of the chemically-selective APGSTE-RARE experiment. Chemical suppression is achieved by adding the WET sequence in all three orthogonal directions (z,x,y) during the t_{store} duration when the magnetisation is stored along the longitudinal position before the **q**-encoding stage which is followed by the 3D RARE pulse sequence.*

Both chemically-selective RARE and APGSTE-RARE sequences can be combined with the CS and Scheme B (Section 3.2.2) trajectory of sampling. The aim of this chapter is to show the quantitative nature of the four-pulses selective scheme with the pulse-acquire, the CSI, the RARE and the APGSTE-RARE sequence. It is the first time that chemical selection is implemented in the APGSTE-RARE sequence and its validity is proved in the ideal porous set-up designed for this experiment.

6.3 Materials and Methods

6.3.1 Materials

6.3.1.1 Bead holder filled with beads and a vial with dodecane

A cylindrical bead holder was filled with DI water, large borosilicate glass beads (Q.A. Equipment Ltd., UK) and a vial filled with dodecane (99%, Acros Organics) and smaller beads. The large spheres were of d_s equal to 4.0 mm and the small spheres in the vial of d_s equal to 2.0 mm. Dodecane was in the hydrocarbon phase and was trapped in the 10 mL vial. The internal diameter and length of the bed were 37.1 mm and 70 mm, respectively and the whole apparatus is illustrated in Figure 6-5. The packed bed was connected to a closed flow loop with a syringe pump (Quizix QX-1500HC dual-cylinder syringe pump). Water was flowing through the bead pack for several hours at different flow rates, while the bead holder was held perpendicular to remove all the trapped air bubbles. The blue arrows demonstrate the direction of water flow.

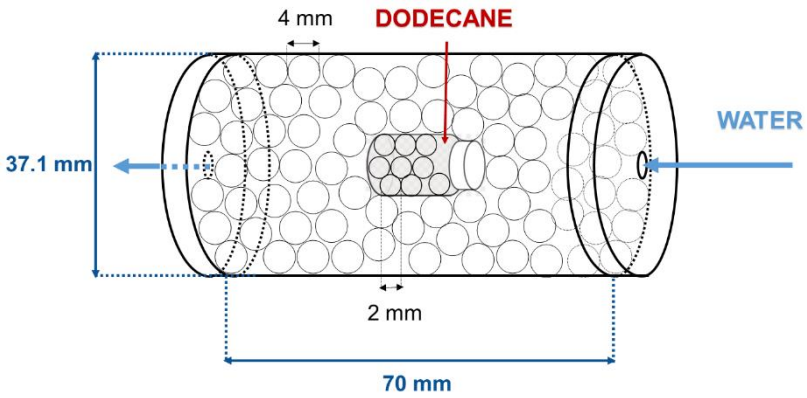

Figure 6-5: Schematical representation of the bead holder of 70 mm length and 37.1 mm diameter packed with borosilicate glass spheres of 4 mm diameter and a 10 mL vial filled with dodecane and borosilicate glass spheres of 2 mm diameter. Water flows from the right to the left as shown by the blue arrows (mobile phase) while dodecane remains static (stagnant phase) inside the vial.

The ϕ_b was measured as 39.5 ± 0.6 % gravimetrically and by implementing mathematical models for a loose random packing of spheres (Roshani, 1990). Following Eq.(4-21), the r_H of the area filled with water was 436 μm (Scheven et al., 2004). Hence, the pore size of the bead holder outside the vial can be considered as ~ 873 μm. Similarly, the porosity inside the vial, ϕ_v, was defined as 39 % and the hydraulic radius as 213 μm, hence the expected pore size was considered as ~ 426 μm.

6.3.1.2 Estaillades carbonate rock

A cylindrical plug of an Estaillades (EST1_102) carbonate rock (provided by STCA) with an average length of 7.01 ± 0.01 cm and an average diameter of 3.81 ± 0.01 cm was studied. The core was placed in the oven for 1 h at 90°C to remove molecules of water captured in the pores. Increasing the temperature higher than 100°C, which is the boiling point of water, could damage the sample. Therefore, the temperature of 90°C was considered suitable for at least partial removal of water particles captivated in the pore structure. Then, the core plug and the semi-permeable disc were dried under vacuum for 2 h and then they were both saturated in synthetic brine under vacuum. Low salinity, synthetic brine was prepared using sodium chloride (99 %, Sigma Aldrich) and Deionised water (DI) to a concentration of 3.0 ± 0.1 g NaCl litre^{-1}. The DI water used for every study in this thesis was obtained from a laboratory purification system (ELGA, DV25, Pure Lab Option), to a concentration of 1.075 ± 0.001 g GdCl3 /litre deionised water. The core P.V. was measured as 23.64 ± 0.50 mL by gravimetric analysis, corresponding to a porosity of 29.62 ± 0.67 %. This measurement agrees with the porosity given by STCA equal to 29.6 %. The permeability of the rock was measured with nitrogen adsoprion in the laboratories of STCA and was equal to 113 mD. The core was then placed in the RCH and a 6.3 ± 0.3 MPa confining pressure was applied using 3M Fluorinert FC-43. The RCH was placed in a closed-loop system with a back-pressure regulator, and the confining pressure was maintained using a Gilson model 307 pump. The rock was analysed in two different states of saturation. The first state was 15 ± 0.7% brine and 85 ± 0.7% dodecane and is known as the ‘end of primary drainage’. The second state was 67 ± 2% brine and 33 ± 2% dodecane and is known as ‘end of imbibition’. More information about these states follows in Chapter 7 and Chapter 8. The brine was

prepared with deionised (DI) water to a concentration of 3.0 ± 0.1 g NaCl L^{-1}. Both phases had a uniform distribution along the length of the core.

6.3.2 Methods

6.3.2.1 NMR Protocol for Chemically-Selective Experiments in the Bead Pack

All NMR experiments were conducted at room temperature (20 ± 1 °C) in the same 2 T magnet. The transmitter/receiver offset was set at the peak of the chemical compound that we want to observe. The offset frequency of each selective pulse was set at a 0.75 ppm distance from the peak of the chemical compound that we want to suppress. The amplitude of the first homospoil was defined as g_h and it was set at 24 % of the g_{max}. The amplitude of each successive homospoil was halved as shown in Figure 6-1.

Firstly, the WET suppression scheme was tested in the bead pack shown in Figure 6-5. In the pulse-acquire experiment, the vial was filled only with oil and not with spheres. Then, the 2 mm beads were added to the vial. Multiple pulse-acquire experiments with and without chemical selection were acquired to test for the reproducibility of the novel pulse sequence. Fully-sampled 3D RARE images were acquired using the same WET scheme. Finally, water was injected at a flow rate of 7 mL min^{-1} and fully-sampled 3D spatially-resolved propagators were acquired for the water and the oil phase separately.

6.3.2.2 NMR Experimental Parameters for the Bead Pack

In the pulse-acquire with chemical selection experiment, δ_h was chosen as 3.1 ms and t_h as 2 ms. The t_{RD} was set as 8 s to allow the full recovery of the magnetisation. The duration of the hard 90° pulse was 19 μs. The duration of all the Gaussian-shaped excitation pulses was 8192 μs which is related to a bandwidth of 155 Hz as derived from Eq.(2-14). The flip angles were optimised following the method described by Ogg et al. (1994). The optimum flip angles were 91.7°, 92.1°, 95.6° and 173.9°. The t_s was measured as 9.2 ms and the N_s was set as 8 to achieve a full phase cycle. The same parameters were used for both water and dodecane suppression changing only the offset frequency of the pulses. More precisely, the offset frequency was set at 0.55 ppm for the dodecane suppression and at 5.55 ppm for the water suppression.

In the 3D RARE experiments, the parameters of the pre-saturated stage remained the same. The t_{RD} was changed to 0.5 s and 24 scans were taken. The FOV in the $\boldsymbol{k}_{read}$ dimension was 96 mm and in both $\boldsymbol{k}_{phase1}$ and $\boldsymbol{k}_{phase2}$ was 48 mm. The N_{echo} in the RARE loop was 16 with a t_{echo} of 3.7 ms. The N_{read} was 256, while N_{phase1}, N_{phase2} were 128 giving an isotropic resolution of 375 μm $pixel^{-1}$. This enabled pore-scale resolution inside the vial where the r_h (Eq.(4-21)) was measured as ~ 426 μm and in the area around the vial where the r_h was measured as ~ 873 μm. Scheme A **k**-space sampling trajectory (Section 3.2.2) was implemented. The acquisition time for one image was approximately 4 h.

The same Scheme A **k**-space sampling trajectory was followed in the 3D propagator. The FOV along the three dimensions was the same as in the images. In this experiment, the N_{read} was 80 and the N_{phase1}, N_{phase2} were 40 giving an isotropic

spatial resolution of 1.2 mm pixel^{-1}, almost 3 times lower than the image resolution. A τ_e of 2.2 ms was defined for the spatial encoding while a τ of 4.1 ms was determined for the flow-encoding part of the sequence. A Δ of 200 ms was applied, while the length of a single **q**-encoding gradient was settled at 3.7 ms. The **q**-points were encoded along the superficial flow direction, i.e. z-direction, and the N_{echo} was set at 40. A total of 65 **q**-points were sampled by applying flow encoding gradients between -10.16 $\times 10^{-2}$ and 10.16 $\times 10^{-2}$ Tm^{-1} (94.92% of g_{max}) in equidistant steps; i.e., symmetrically around the centre of **q**- space, with the 33rd point at **q**=0 m^{-1}. The duration of the homospoil during the t_{store} time interval was 10 ms while its amplitude was set at 30% of the g_{max}. To avoid the effect of eddy currents while the magnetisation was stored at the longitudinal position a delay of 2 ms was placed before and after the large homospoil of 10 ms, right before the chemically-selective scheme as shown in Figure 6-4. Sixteen signal averages were used with a t_{RD} of 1.03 s, resulting in a total acquisition time of 30 h.

6.3.2.3 NMR Protocol for Chemically-Selective Experiments Estaillades

A series of pulse-acquire experiments were performed to optimise the t_{RD}, δ_h and t_h parameters. To optimise the t_{RD}, T_1 relaxation time was needed. Therefore, an inversion recovery experiment was acquired. Based on that value, seven non-chemically selective pulse-acquire experiments were performed changing the t_{RD}, i.e. the time between consecutive scans. Then, we needed to optimise the WET suppression scheme. For that reason, five chemically-selective pulse-acquire experiments for the water and five chemically-selective pulse-acquire experiments for the oil phase changing initially the δ_h and then the t_h value.

The optimised suppression scheme was employed for the acquisition of 3D fully-sampled and under-sampled RARE images for the oil and the water phase following the Scheme B trajectory of **k**-space sampling. The same sampling trajectory was followed for all the spatially-resolved experiments. The images were compared with 1D CSI experiments to prove the quantitative nature of the acquisition. Then, brine was injected at 5 ft d^{-1} through the rock and 3D APGSTE-RARE experiments with under-sampling were obtained.

6.3.2.4 NMR Experimental Parameters for the Estaillades

The inversion recovery experiment was performed with a hard 90º pulse of 40.7 μs and 8 scans, choosing 16 points for signal decay. In the non chemically-selective pulse-acquire experiment, the duration of the hard 90º pulse was 40.7 μs. The t_{RD} varied from 0.8 s up to 7.7 s (5×T_1) between 8 scans. The duration of all the Gaussian-shaped excitation pulses was chosen as 8192 μs which is related to a bandwidth of 155 Hz. For this soft pulse duration, the power level of the 180º pulse was calibrated as 18.6 dB. Hence, the flip angles for the soft pulses were manually calibrated for the chemically-selective experiment and they were set up as 68º, 84.7º, 91.8º and 103º. The offset frequency for the selective pulses was set at 0.55 ppm for dodecane suppression and at 5.43 ppm for water suppression. After choosing t_{RD} equal to 3 s and τ_h of 0.58 s, the value of the duration of the homospoil δ_h varied from 0.5 up to 4 ms. Then, choosing a t_{RD} of 3 s and a δ_h of 3 ms, the value of τ_h varied from 0.58 up

to 3.08 ms. All this calibration occurred at the state called 'end of the primary drainage', therefore the oil phase was dominant.

After defining the optimum values of t_{RD}, δ_h and τ_h for the WET scheme, one reference spectrum was compared with the two chemically-selective spectra. At this point, the rock was in the 'end of imbibition saturation state. Therefore, the brine peak was larger. The hard 90º pulse was calibrated at 41.9 μs. The duration and the flip angle of the suppression scheme were again calibrated and the optimum values were found the same as before. Then spatially-resolved spectra along the axial position of the rock were acquired implementing the same suppression scheme. The duration of the gradient δ_G shown in Figure 6-2 was 0.18 ms while its amplitude was chosen as 95 % of the g_{max}. Therefore, the resolution of the CSI spectra along the axial position was 656.3 μm pixel^{-1}. The gradient stabilisation delay δ_2 was defined as 1.8 ms while the duration of the hard 180º was 83.8 μs.

Fully-sampled 3D RARE images chemically-selective for the oil and the brine phase were compared to a reference fully-sampled 3D RARE image for the same state of saturation. All images were acquired following the Scheme B acquisition trajectory. The FOV in the $\mathbf{k}_{read}$ dimension was 84 mm, and in both $\mathbf{k}_{phase}$ dimensions 42 mm. The number of echoes in the RARE loop, N_{echo}, was 32 with an echo time, τ_e, of 2.9 ms. The N_{read} was 128 and the N_{phase1}, N_{phase2} were 64 giving an isotropic resolution of 656.3 μm pixel^{-1} along each dimension. The acquisition time of each image for 4 averages was 26 min. Then, two chemically-selective fully-sampled 3D RARE images of higher resolution were acquired. More precisely, the N_{read} was 192 while the N_{phase1} and N_{phase2} were 94 giving an isotropic resolution of 437.5 μm pixel^{-1} along each dimension. The acquisition time of each image for 4 scans was 1 h. The water fully-sampled image following the Scheme B trajectory was used to generate a sampling pattern. Several under-sampling ratios were used and it was found that the lowest ratio of under-sampling which led to quantitative measurement was 25% of all **k**-space data points. Therefore, two under-sampled images using the same pulse sequence settings as for the fully-sampled experiments were obtained. For 4 scans, the required time was reduced from 1 h down to 15 min for each chemically-selective image.

The Scheme B acquisition trajectory for the sampling of the **k**-space was also followed in the 3D propagators with chemical selection. The FOV in the $\mathbf{k}_{read}$ dimension was 84 mm and in both $\mathbf{k}_{phase}$ dimensions 42 mm as in the imaging. However, the N_{read} was 96 and the N_{phase1}, N_{phase2} were 48 giving an isotropic spatial resolution of 875 μm pixel^{-1}, almost 2 times lower than the resolution of the under-sampled images. The N_{echo} was set at 32, the τ_e was defined as 2.5 ms for spatial encoding and the τ was measured as 2.2 ms for flow-encoding. A Δ of 1.8 s was chosen, while δ_G was settled at 3.4 ms. A total of 87 **q**-points were encoded along the superficial flow direction, i.e. z-direction. The **q**-points were sampled by applying flow encoding gradients between -9.2 ×10^{-2} and 9.2 ×10^{-2} T m^{-1} (86% of g_{max}) in equidistant steps; i.e., symmetrically around the centre of **q**- space, with the 44th point at **q**=0 m^{-1}. The duration of the homospoil during the t_{store} time interval was 10 ms while its amplitude was set at 30% of the g_{max}. To avoid the effect of eddy currents

while the magnetisation was stored at the longitudinal position a delay of 1.1 ms was placed before and after the large homospoil of 10 ms, right before the chemically-selective scheme as shown in Figure 6-4. Eight signal averages and two dummy scans were implemented with a time between excitations of 3.0 s, resulting in a total acquisition time of 20 h for an under-sampling rate of 24% in the **k**,**q**-space.

6.3.2.5 NMR Data Processing

To demonstrate the quantitative nature of the improved MRI techniques, it is important to measure the relative saturation of water (S_w^k) and dodecane (S_o^k) in the core plug given by:

$$S_w^k = \frac{HI \cdot I_w^k}{HI \cdot I_w^k + I_o^k} \; and \tag{6-1}$$

$$S_o^k = \frac{I_o^k}{HI \cdot I_w^k + I_o^k}. \tag{6-2}$$

HI is the hydrogen index of the dodecane, I_w is the integral of the water phase, I_o is the integral of the oil phase and k stands for ref (reference spectrum), $supp$ (chemically-selective spectrum) and MRI (images acquired with 3D RARE). HI is defined as the ratio of the amount of hydrogen in the sample over the amount of hydrogen in pure water at Standard Temperature and Pressure conditions (STP) (Appel, 2004). More precisely HI is given by:

$$HI = \frac{\rho\,[R_{HC}/(Ar_C + Ar_H\,R)]}{[H]_{water}^{STP}}, \tag{6-3}$$

where ρ is the density of the chemical compound, in this case, the dodecane (0.75 g/cm^3), Ar_C is the relative atomic mass of ^{13}C, Ar_H is the relative atomic mass of ^{1}H, $[H]_{water}^{STP}$ is the concentration of hydrogen in pure water at STP and R_{HC} is the hydrogen/carbon ratio which is equal to 2.17 for dodecane. In the dodecane-water experiment, the value of HI was calculated as 1.03 ± 0.01.

The CS-RARE images of the Estaillades were reconstructed for an α of 0.13 and 12 Bregman iterations. The 3D CS propagators were treated as described in Section 4.3.2.7.

6.3.2.6 Gravimetric and Volumetric Measurements

The NMR and the MRI measurements were compared to the gravimetric measurements S_w^{grav} and S_o^{grav} in the ideal bead pack system and to the volumetric measurement S_w^{vol} and S_o^{vol} in the rock system.

The relative saturation of a fluid is defined as the volume of that fluid, normalized by the whole pore volume (Schön, 2015). In the system presented in Figure 6-5, there is no pore volume neither in the sense of a saturated rock nor in the sense of a conventional saturated bead pack. Since dodecane and water were present in the system in separate set-ups without being in contact, the whole pore volume was considered as the sum of the water and the dodecane volume. Gravimetric

measurements took place after the NMR measurements. The bead pack was weighed and then it was decomposed. The beads of 4 mm in diameter and the vial filled with dodecane and water were dried and weighed giving the mass of the water present in the bead pack. Knowing that the density of water at 20°C is 0.998 ± 0.02 g cm^{-3}, a water volume of 29.3 ± 0.6 mL was derived. The same method was followed for the gravimetric measurement of the dodecane included in the vial filled with beads of 2 mm in diameter. The empty vial and the beads of 2 mm were dried in the oven and then they were weighted extracting a dodecane volume of 3.9 ± 0.1 mL. Volumetric measurements were acquired by measuring the effluent of the imbibition process. More precisely, brine was injected into the core and the effluent was collected. Knowing that the rock was saturated by 85% with dodecane, we could derive the final saturation by measuring the effluent dodecane.

6.4 Results and Discussion

6.4.1 Chemical Selectivity of the Pulse-Acquire Sequence in the Bead Pack

Figure 6-6 is a comparison between the WET scheme with one selective pulse(a) and four selective pulses(b). The reference spectrum is plotted in parallel with the water peak to illustrate the difference in the suppression of the dodecane peak. The sample studied here was the bead pack filled with the large beads of 4 mm and the 10 mL vial filled with dodecane. The inverse peak seen in the one pulse WET scheme suppression has also been mentioned by Ramskill et al. (2018). This inverse peak affects the integration limits increasing the uncertainty of the saturation measurements. The four pulses WET scheme suppresses more efficient the signal coming from the oil phase.

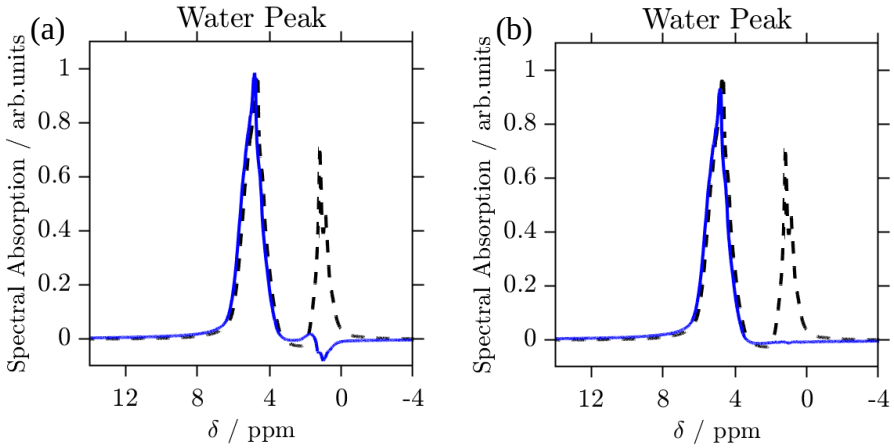

Figure 6-6: Standard (non-chemically-selective) NMR spectrum (dashed black line) in parallel with chemically-selective spectra for the phase of water (blue solid line) using one (a) and four soft pulses(b) during the pre-conditioned stage in the system of a bead pack filled with water, 4 mm beads and a 10 ml vial filled with dodecane.

Implementing the four pulses WET scheme in the sample presented in Figure 6-5, the resulting reference spectrum is plotted along with the water and the oil peak in Figure 6-7.

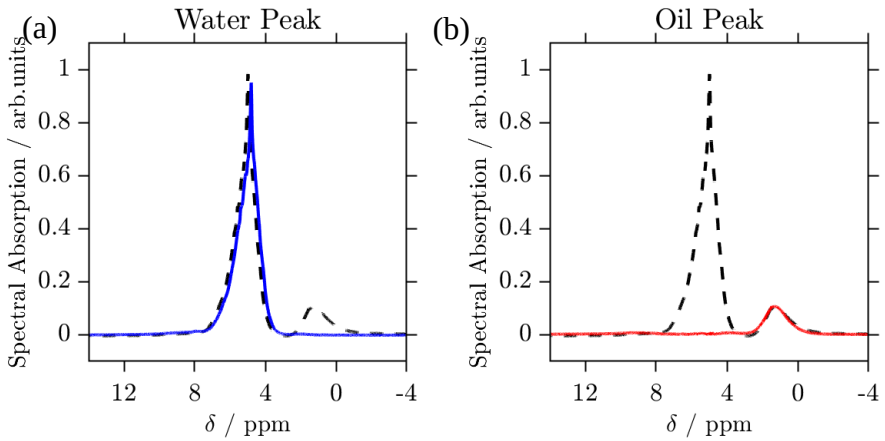

Figure 6-7: Standard (non-chemically-selective) NMR spectrum (dashed black line) in parallel with chemically-selective spectra for the phase of water (blue solid line)(a) and the phase of the oil (red solid line)(b) using the four pulses WET pre-conditioned scheme in a system of a bead pack filled with water, 4 mm in diameter beads and a vial of 10 ml filled with dodecane and 2mm in diameter beads.

6.4.1.1 Optimum Peak Integration

The presence of oil and water in the system can be determined using the relative concentration determination method (Amin and Claridge, 2017). The integration area around each peak was adjusted as the summation of its FWHM and an extension of 1.2 ppm on each side of the curve. The integrals between the reference ($I_i^{ref}, i = w, o$) and the suppressed (I_i^{supp}) spectrum for both phases was compared. Comparing I_w^{ref} with I_w^{supp} in Figure 6-7(a), the percent of water suppression was calculated as 1.0 %, while the oil peak was suppressed by 98.8 %. Similarly, comparing I_o^{ref} with I_o^{supp} in Figure 6-7(b), the oil peak was suppressed by 2.5 %, while the water peak was suppressed by 97.8 %.

6.4.1.2 Reproducibility of the Spectrum

Seven reference, seven chemically-selective for the water phase and seven chemically-selective for the dodecane phase spectra are plotted in Figure 6-8. The overlap among all these spectra proves the excellent reproducibility of the chemically and non-chemically selective experiments.

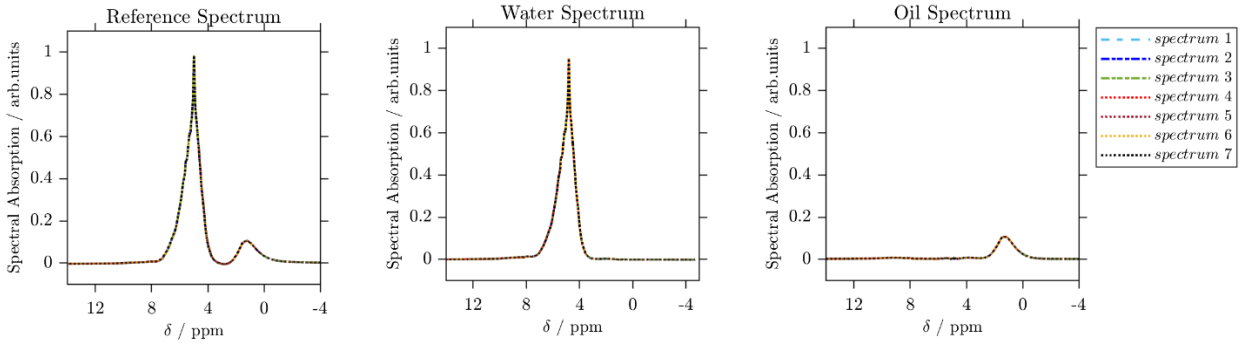

Figure 6-8: Seven reference, seven chemically-selective for the water phase and seven chemically-selective for the dodecane phase spectra are plotted in parallel in a system of water and dodecane placed in a bead holder.

6.4.1.3 Error Analysis of the Pulse-Acquire Experiments

From the suppression analysis an error of 1.0% × I_w^{ref} and 2.5% × I_o^{ref} were assigned to the I_w^{supp} and I_o^{supp}, respectively. The standard deviation among all the spectra presented in Figure 6-8 was also integrated into the error analysis. Another parameter that can bring error in the peak integration is the extension area of 1.2 ppm around the FWHM of each peak. That is why this extension limit was varied from 0.9 ppm up to 1.8 ppm. The standard deviation among these different integration areas was integrated into the error analysis of the I_w and I_o.

6.4.1.4 Quantification of the Chemical Selectivity of the Pulse-Acquire Sequence

Figure 6-9 compares the relative saturation measurements coming from the reference and the suppressed spectra with the gravimetric results. The relative saturation measurements coming from the NMR spectra were measured from Eq.(6-1) and (6-2) and the error analysis followed the process described above. Analysing the reference spectrum, S_w^{ref} was measured as 0.88 ± 0.01 and S_o^{ref} as 0.12 ± 0.01. Analysing then the suppressed spectrum data, S_w^{supp} was found equal to 0.87 ± 0.01 and S_o^{supp} equal to 0.13 ± 0.01. These measurements are in great agreement with the S_w^{grav} of 0.88 ± 0.002 and the S_o^{grav} of 0.12 ± 0.004.

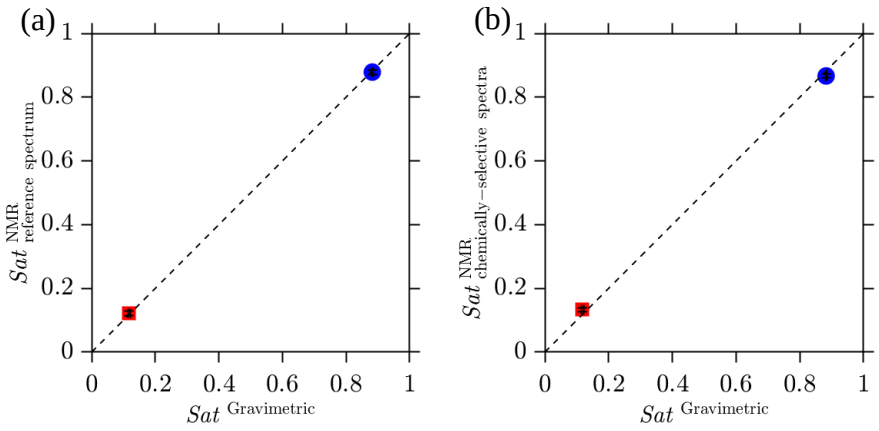

Figure 6-9: Comparison of the NMR and the gravimetric determination of the relative saturation of the dodecane S_o (red square) and the water S_w (blue circles) from the NMR spectra acquired from the non-chemically-selective (a) and the four pulses WET chemically-selective (b) pulse-acquire experiment.

6.4.2 Chemical Selectivity in the 3D RARE Images of the Bead Pack

Figure 6-10 illustrates the reference image of the bead holder represented in Figure 6-5 with both the oil and the water phase (a), the image of the water phase (b) and the image of the oil phase (c). All the images were normalised by the mean intensity coming from 16 voxels around the voxel of maximum intensity in the reference image.

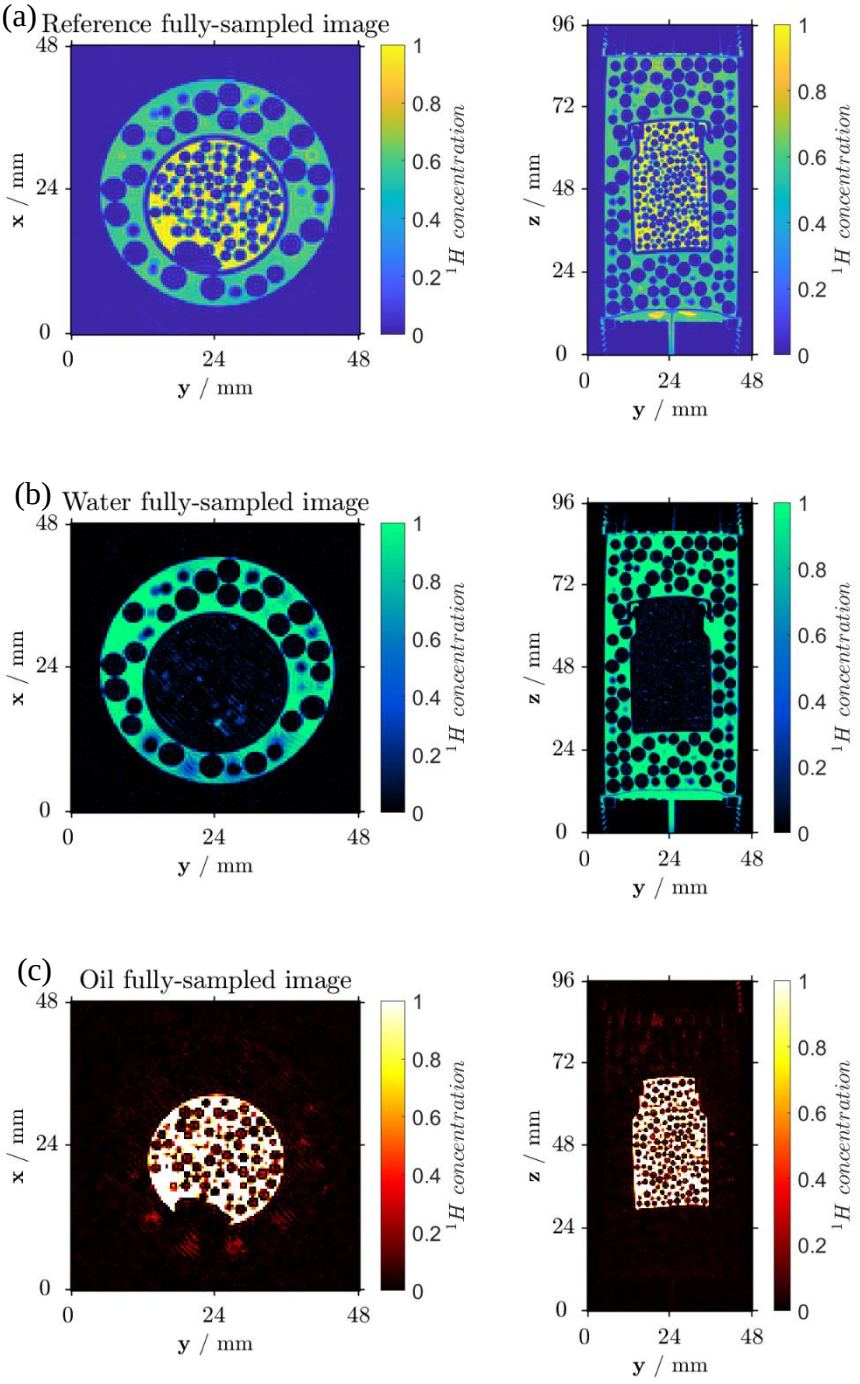

Figure 6-10: 3D fully-sampled RARE images acquired with the non-chemically-selective (a) and with the four pulses WET scheme for the water (b) and the oil phase (c). The **k**-space was sampled following the Scheme A trajectory.

Comparing Figure 6-10(b) with (c), we can easily observe that the four pulses suppression scheme has worked. However, there are some small intensities in the oil area in Figure 6-10(b) and in the water area in Figure 6-10(c). Comparing the intensities in an area of 1331 voxels in the region of oil in Figure 6-10(b) with the same area in Figure 6-10(a), a suppression of 87% of the oil phase was attained. Similarly comparing the area of 1331 voxels in the region of water in Figure 6-10(c) with the same area in Figure 6-10(a), a suppression of 79% of the water phase was

achieved. This suboptimal suppression led to a S_w^{MRI} of 0.80 ± 0.046 and a S_o^{MRI} of 0.20 ± 0.046. These values deviated by 9% from the gravimetric measrements. The reason for the sub-optimal suppression in these images was very short t_{RD} of 0.5 s. According to the theory $5 \times T_1$ is needed for the full recovery of the magnetisation and the T_1 relaxation of the water in a system of large pores is ~ 2.1 s, close to its bulk relaxation. Similarly for the oil phase trapped in the vial, the T_1 relaxation can be considered as 1.4 s (Reci et al., 2017). The very short t_{RD} was employed to reduce the acquisition time and to qualitatively see if the novel WET scheme was working. There was no intension for quantification of the 3D RARE images of the bead pack. The 3D RARE images of the Estaillades rock were obtained with the optimum parameters and they were quantified as we will describe later.

6.4.3 Chemically-Selective Propagators Following the APGSTE-RARE Sequence in the Bead Pack

To quantify the suppression in the local propagators, we focused on the measurement of the displacement coming from the global propagator for each phase and on the measurement of the D_s using Eq.(2-44) for the oil phase. Since the oil phase is confined in a porous system, D_s is also called D_{app}. The oil phase is stagnant, therefore the measured D_s is expected equal to the D_s of the oil phase which is 0.845 10^{-9} m^2 s^{-1} (at 25°C) (Marbach and Hertz, 1996).

Firstly, for a flow rate of 7 mL min^{-1}, $\langle\zeta\rangle_0$ for the given Δ was 54.6 ± 5 μm. Figure 6-11(a) presents the global propagator of the water phase, in other words, the summation of all the local water propagators. This skewed shape with the large peak around the stagnation point gave a $\langle\zeta\rangle_{water}$ of 57.2 ± 4 μm. The error attributed to the $\langle\zeta\rangle_{water}$ derived from the denoising method described in Section 4.3.2.6. The agreement between $\langle\zeta\rangle_0$ and $\langle\zeta\rangle_{water}$ is a first indication of the reliability of the chemical selection in the flow measurements. In addition, the global propagator of the oil phase presented a Gaussian curve well defined around zero as expected.

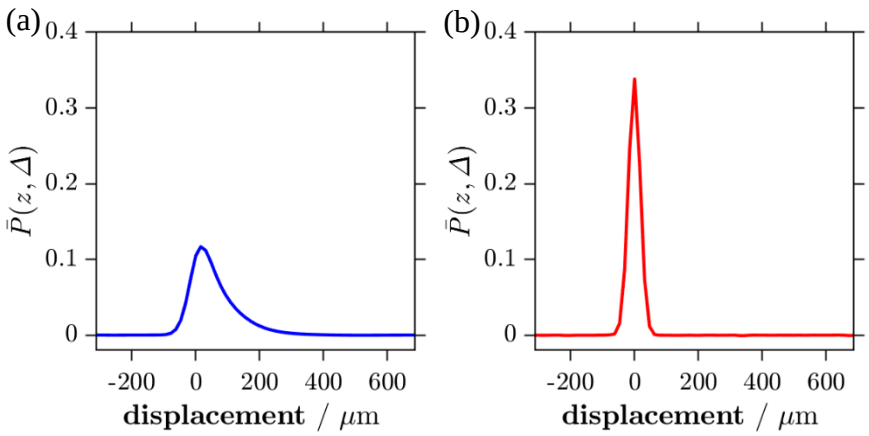

Figure 6-11: Total or global propagator of the water (a) and the oil (b) phase obtained from the summation of all the 3D local propagators acquired with the chemically-resolved APGSTE-RARE sequence in the ideal system of the bead holder with the vial filled with dodecane.

Secondly, the σ_{oil} for all the local propagators recorded inside the area of the vial were measured from Eq.(4-24) and the local D_{app} was measured by Eq.(4-26). The local D_{app} and its distribution are presented in Figure 6-12. The local D_{app} demonstrates an homogeneous distribution around a mean value of 0.85 10^{-9} m^2s^{-1} which is very close to the D_s of the oil. Increased D_{app} can be seen in the area close to the trapped air bubble as shown in Figure 6-12(a). The great agreement in these measurements shows that not only the global but also the local chemically-selective propagators have a quantitative meaning.

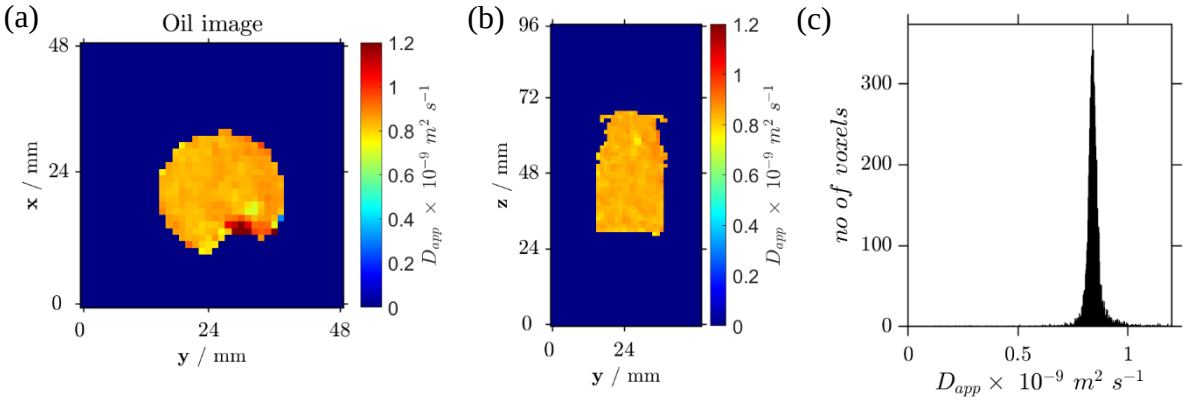

Figure 6-12: 2D x,y- (a) and z,y- (b) slice images and histogram (c) of the local apparent diffusion coefficient measured from the local propagator acquired with chemically-selective APGSTE-RARE sequence for the oil trapped in the vial.

Having confirmed the quantitative nature of the chemically-selective propagators, we moved into analysing for the first time some local propagators with interesting shapes. Figure 6-13 and Figure 6-14 present the z,y-slice of 3D image of the bead holder in parallel with the per voxel propagators coming from the oil and the water phase. The resolution of the intensity image was 3.2 times higher than the resolution of the propagator data. The white square represents the voxel location and its size was adjusted to the resolution of the propagator measurements. Figure 6-13(a) presents a Gaussian-shaped propagator shifted from zero by 58.1 ± 0.1 μm at the inlet of the bead holder. The Gaussian shape can also be confirmed by the very small value of γ_{water} equal to 0.2 ± 0.1 μm. In this voxel, Taylor dispersion was dominant and molecules were displaced to adjacent streamlines due to diffusion. Figure 6-13(b) shows a voxel in a high shear region adjacent to the interface with the vial. The local propagator was characterised by ζ_{water} = 75.8 ± 2.8 μm, σ_{water} = 84.3 ± 3.3 μm and γ_{water} = 1 ± 0.1 μm. The high positive skewness is a descriptor of significant flow dispersion added to molecular self-diffusion. As expected, the oil propagator is zero for all of these voxels. Close to the outlet of the bead holder, an interesting top-hat shaped propagator was identified and is presented in Figure 6-13(d). This propagator shape is typical of the laminar flow of a Newtonian fluid through a pipe. For this voxel, ζ_{water} = 128.4 ± 0.2 μm , σ_{water} = 82.2 ± 0.7 μm and γ_{water} is zero as expected for the uniform velocity profile of the tube.

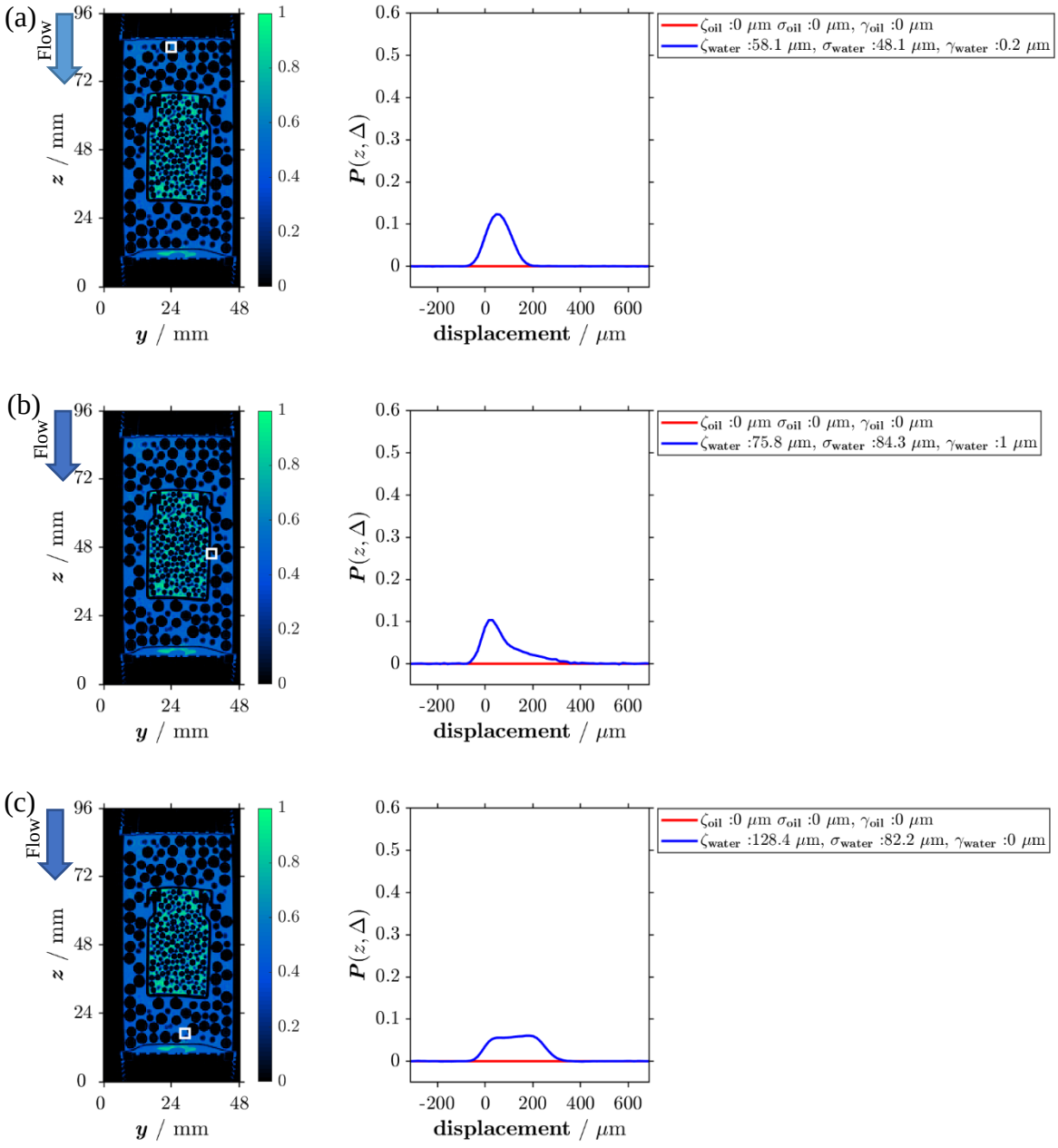

Figure 6-13: Chemically-selective propagators for water flow through the bead holder filled with 4 mm beads and a vial packed with 2 mm spheres and dodecane. For Δ = 200 ms, the local propagator and the the statistical metrics for each phase are shown at the inlet(a), the middle(b) and the outlet(c) of the sample.

Figure 6-14(a) demonstrates a voxel inside the vial, where only the oil phase is present and stagnant. The Gaussian-shaped propagator had a σ_{oil} of 18.3 ± 0.6 μm which is translated into a D_{app} of 0.84 ± 0.05 10^{-9} m^2s^{-1}. Since ζ_{oil} was near zero and D_{app} close to the D_s the mechanism of Brownian motion due to diffusion is confirmed for the area inside the vial. Figure 6-14(b) presents a voxel where both the water and the oil phase are present. The oil phase exhibited the Gaussian-shaped propagator curve around zero with an σ_{oil} of 18.5 ± 1.3 μm as expected. On the contrary, the mobile water phase experienced high shear stress on the vial interface which was combined with high dispersive flow. The statistical metrics of the water propagator

curve were calculated as ζ_{water} = 70.9 ± 1.2 µm, σ_{water} = 68.6 ± 2.2 µm and γ_{water} = 0.6 ± 0.3 µm.

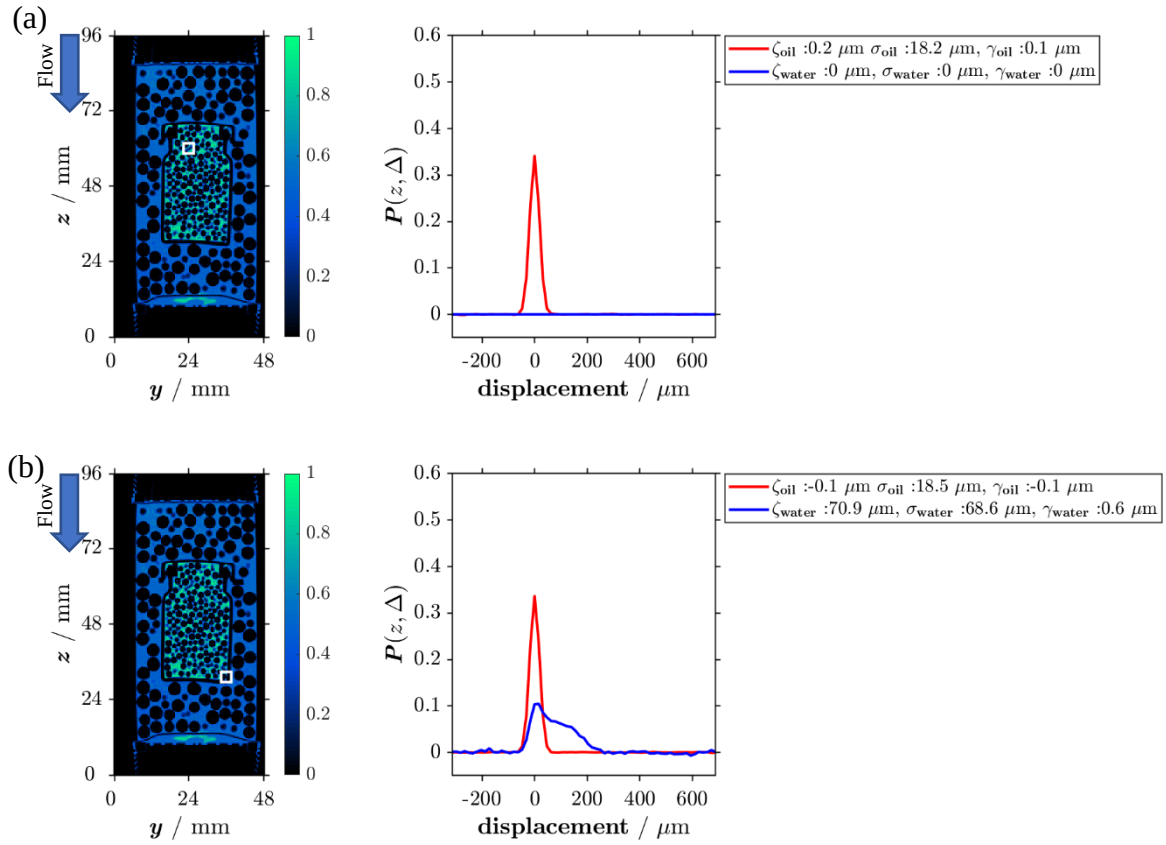

Figure 6-14: Chemically-selective propagators for water flow through the bead holder filled with 4 mm beads and a vial packed with 2 mm spheres and dodecane. For Δ = 200 ms, the local propagator and the the statistical metrics for each phase are shown inside the vial (a) and at the edge of the vial where both phases coexist in the same voxel (b).

6.4.4 Chemical Selectivity of the Pulse-Acquire Sequence in Estaillades

Estaillades is a dual-porosity carbonate rock (studied in Chapter 5) and is a more complex system than the bead pack. The t_{RD} as well as the δ_h and τ_h of the WET suppression scheme presented in Figure 6-1 were optimised separately for this sample. From the multiple pulse-acquire experiments without chemical selectivity, a t_{RD} of 3 s was proved sufficient for the full magnetisation recovery. Then from the multiple pulse-acquire experiments with chemical selectivity, δ_h of 3 ms and τ_h of 1.08 ms were found as the optimum parameters of the WET scheme for that precise two-phase system in Estaillades.

6.4.4.1 Quantification of the Chemical Selectivity in the Spectra of Estaillades

Figure 6-15(a) presents the reference spectrum (black dashed line) in parallel with optimum areas of integration for the calculation of the I_w^{ref} and I_o^{ref}. Figure 6-15(c) shows the chemically-selective spectra in front of the dashed line of the reference spectrum. Figure 6-15(b) shows that the measured S_w^{ref} of 0.73 ± 0.01 and S_o^{ref} of 0.28 ± 0.01 were inside the error bandwidth of the S_w^{vol} equal to 0.66 ± 0.04 and the S_o^{vol}

equal to 0.34 ± 0.02. The small deviation in the S_w^{ref} and S_o^{ref} could be related to the overlap between the two peaks which is a result of the presence of the rock. Figure 6-15(d) shows that the measured S_w^{supp} of 0.68 ± 0.05 and S_o^{supp} of 0.32 ± 0.05 were even closer to the S_w^{vol} and S_o^{vol} values. It can be concluded that the chemically-selective spectra result in quantitative saturation measurements with better precision.

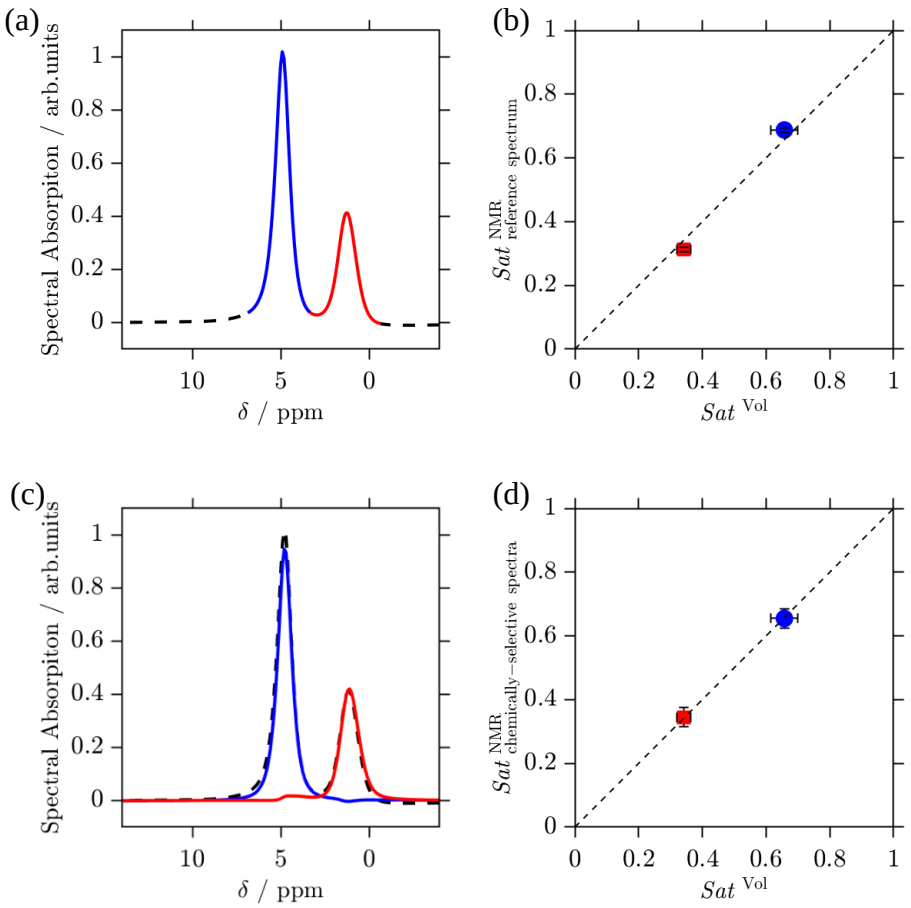

Figure 6-15: The reference spectrum is plotted in parallel with the optimum area of integration for the oil peak (red curve) and the water peak (water curve)(a) in the Estaillades rock. The relative saturation measured from each optimum area is compared to the relative saturation measured volumetrically from the effluent at the end of the brine injection process (b). The reference spectrum is plotted in parallel with the chemically-selective spectra acquired with the four pulses WET pulse-acquire sequence in the Estaillades rock (c). The relative saturation coming only from the chemically-selective spectra is compared to the relative saturation measured volumetrically (d).

6.4.4.2 Quantification of 1D CSI with Chemical Selection

The optimum parameters for the WET suppression scheme were implemented in the CSI pulse sequence encoded along with the axial position of the rock. The mean S_w and S_o coming CSI were measured as 0.69 ± 0.03 and 0.31 ± 0.03 respectively. Figure 6-16(a) shows the great agreement of these data with the volumetric measurements. The error analysis in the spatially-resolved spectra was the same as the method described in Section 6.4.1.3 for each spatial position. Then, the S_w and S_o profiles coming from the CSI were plotted in parallel with the S_w and S_o profiles coming from the 3D chemically-selective fully-sampled RARE images. The great agreement between these results is presented in Figure 6-16(b).

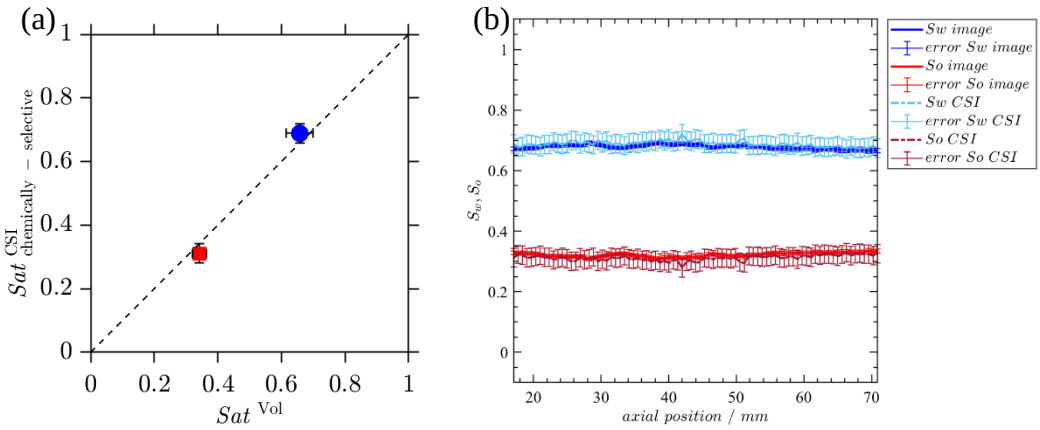

Figure 6-16: Comparison of the CSI and volumetric determinations of the relative saturation of the dodecane S_o (red squares) and water S_w (blue circles) from the CSI spectra using the chemically-selective pulse-acquire method (a). The 1D spatially-resolved S_w (light blue line) and S_o (dark red line) along the axial position of the Estaillades rock coming from the CSI are plotted in parallel with the results coming from the chemically-selective 3D fully-sampled RARE image.

The great agreement in all of these data proves the quantitative nature of the four pulses WET suppression scheme when combined with the CSI and the fully-sampled 3D RARE sequence.

6.4.5 Chemical Selectivity in the 3D CS-RARE Images of the Estaillades

6.4.5.1 Error Analysis of the 3D CS-RARE Images

The first error added in the I_w^{MRI} and I_o^{MRI} comes from ranging the limits of the optimum cut-off value derived from the automatic background thresholding method described in Section 3.5.2. Another error comes from the difference between the intensity of the reference image and the sum of the I_w^{MRI} and I_o^{MRI} coming from the chemically-selective images for each voxel. It was found that the intensity of the reference image was suppressed by 3.5 % on average. This result came from the images of 656.3 μm pixel^{-1} resolution. The same mean value of suppression was used in the per voxel error analysis of the images acquired with 437.5 μm pixel^{-1} resolution.

Last but not least, the effect of the CS in the measurement of the S_w^{MRI} and S_o^{MRI} should be assessed. Therefore, the fully-sampled and the reconstructed images acquired under the same parameters were compared and the difference in the measured I_w^{MRI} and I_o^{MRI} was integrated into the total error analysis of the CS images.

6.4.5.2 Quantification of the Chemical Selectivity in the 3D CS-RARE Images

The reconstructed under-sampled 3D RARE images following the Scheme B trajectory of **k**-space sampling with a resolution of 437.5 μm pixel^{-1} for the water and the oil phase are illustrated in Figure 6-17(a) and (b), respectively. The red arrows point at two regions of the rock where the water image seems to present a ‘cavity’. By observing these regions in the oil image, we can distinguish a significant amount of oil occupying the ‘cavity’ areas. The structural quality of the chemically-selective images after reconstruction is much better compared to Ramskill et al., (2018).

The S_w^{MRI} and S_o^{MRI} were estimated as 0.68 ± 0.02 and 0.32 ± 0.02, respectively. The relative saturations coming from the fully-sampled images were also measured. Figure 6-17(c) and (d) illustrate the great agreement between the volumetric measurements and the S_w^{MRI} and S_o^{MRI} coming from both the fully- and the reconstructed 3D images.

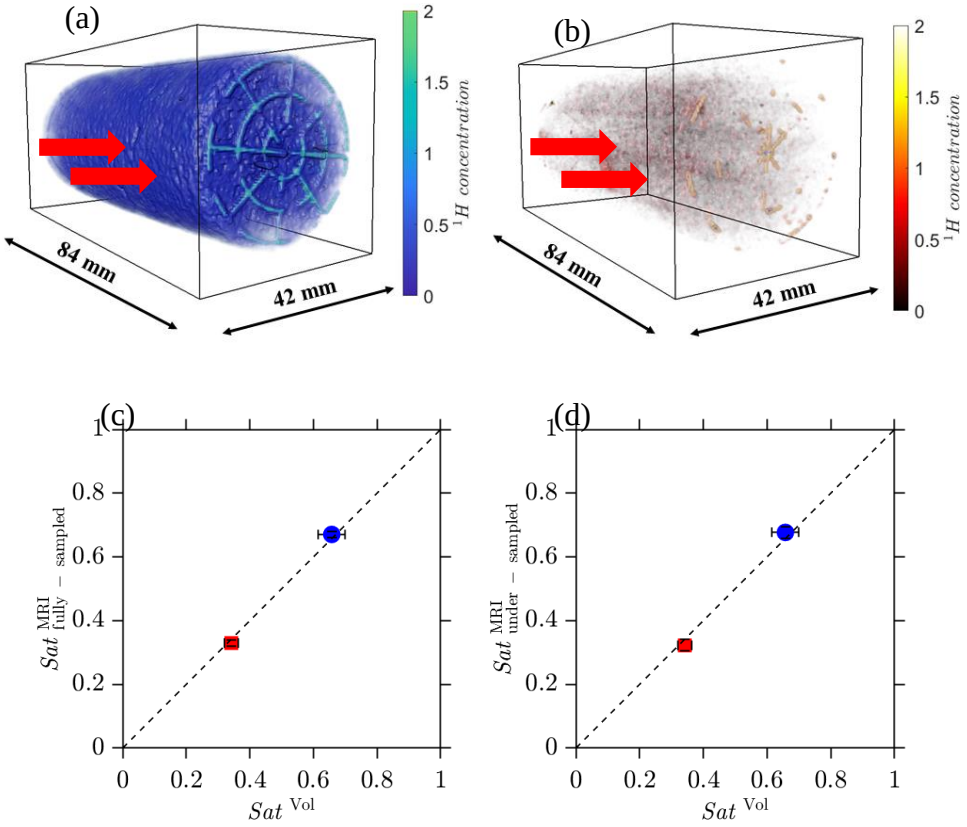

Figure 6-17: Reconstructed 3D RARE image of 437.5 μm pixel^{-1} resolution for the brine (a) and the dodecane (b) phase. The relative saturation of the dodecane S_o (red squares) and the brine S_w (blue circles) measured by the fully- sampled (c) and the reconstructed under-sampled (d) 3D RARE images using the four pulses WET scheme for suppression are compared to the volumetric measurement of the effluent.

The improvement in the image quality is the result of several parameters. Firstly, the sampling pattern and the reconstruction parameters were optimised following the method described in Section 3.4.1. Secondly, the masking of the background noise followed the method described in Section 3.5.2. Thirdly, the optimization of the four pulses WET scheme followed the method described in Section 6.4.4. All these improvements enabled the interesting structural observations mentioned above.

6.4.6 Chemically-Selective Propagators Following the APGSTE-RARE Sequence in the Estaillades

The results coming from the global propagator for the brine and the dodecane phase are presented in Figure 6-18. The $\langle\zeta\rangle_{water}$ from the water phase was measured as 94.9 ± 2 μm while the $\langle\zeta\rangle_0$ for the given Δ was 31.8 μm. The $\langle\zeta\rangle_{oil}$ was measured as 1.8 ± 2 μm which confirmed that the oil phase remained trapped in the porous medium.

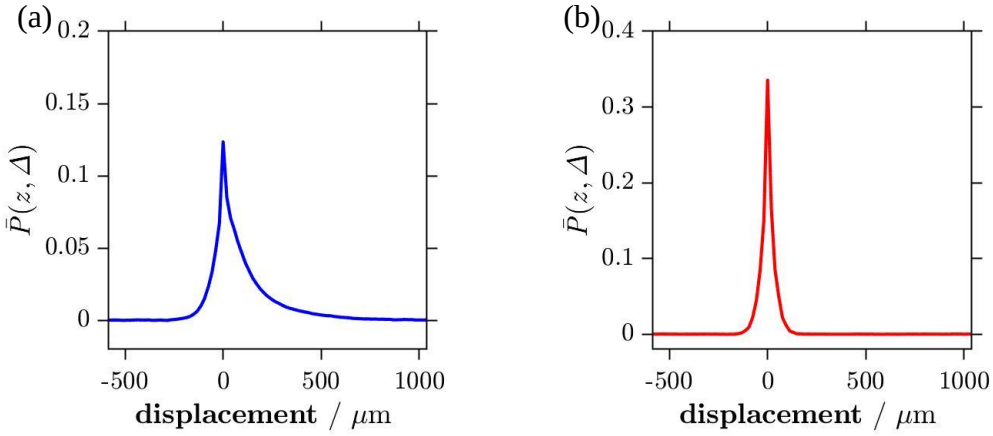

Figure 6-18: Total or global propagator of the water (a) and the oil (b) phase obtained from summation of all the 3D local propagators acquired with the chemically-resolved APGSTE-RARE sequence in the Estaillades rock.

The $\bar{P}(z,\Delta)$ of water is a positively skewed distribution characterised by a sharp peak near zero. This sharp peak is associated with dead zones in the flow field. The chosen Δ was longer than the longest T_1 leading to significant signal attenuation. This signal loss in addition to the surface relaxation led to $\langle\zeta\rangle_{water} > \langle\zeta\rangle_0$. It has been shown that the longer the Δ the larger the measured $\langle\zeta\rangle_{water}$ since slow-moving spins are not detected (Scheven et al., 2005a).

Analysing the local propagators for the oil phase, the D_{app} map in parallel with its distribution is presented in Figure 6-19. The D_{app} values were equally distributed are a mean of 0.37 10^{-9} m^2s^{-1}. Since there are no similar data in the literature the expected value of D_{app} was adjusted following the long-time approximation recommended by Latour et al. (1993). According to this approximation, for long Δ, D_{app} becomes equal to $D_s \times 1/\psi$, where ψ is the tortuosity of the porous medium. For the Estaillades core, a ψ of 4 is recommended in the literature (Yang et al., 2019). Therefore a D_{app} around 0.21 10^{-9} m^2s^{-1} would be expected. This expected value is not very far from the measured D_{app} value taking into account that ψ in that precise two-phase system of the Estaillades rock may be different than 4.

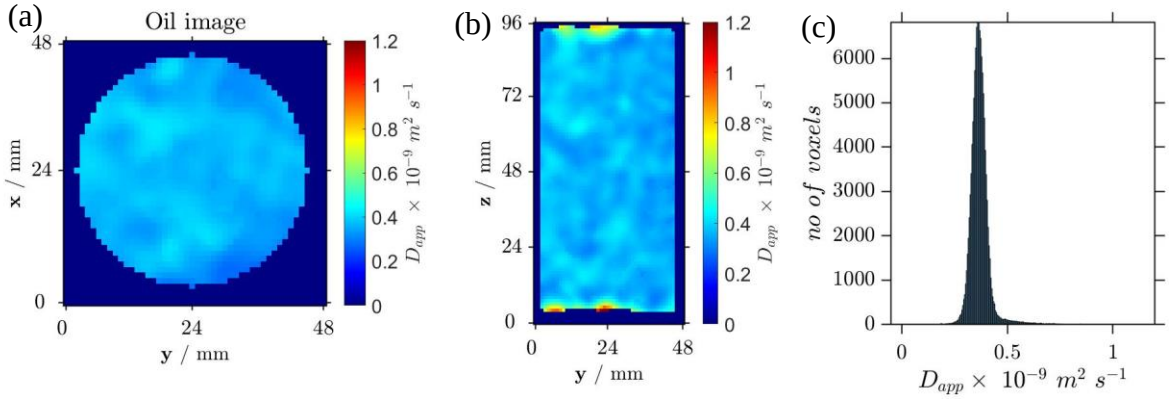

Figure 6-19: 2D x,y- (a) and z,y- (b) slice images and histogram (c) of the local apparent diffusion coefficient measured from the local propagator acquired with chemically-selective APGSTE-RARE sequence for the oil confined in the Estaillades pore structure.

This is the first time that the D_{app} of dodecane confined in a carbonate rock is measured locally in the presence of brine. Another interesting observation is that D_{app} is macroscopically uniform along the core even though the Estaillades has a bimodal pore structure.

Figure 6-20 illustrates three local propagators chemically-selective for the oil (red) and the brine (blue) phase along the flow direction. This is the first time that such data are presented in a rock system. Comparing the voxel at the inlet with the voxel in the middle of the core plug as shown in Figure 6-20(a) and (b), respectively, ζ_{water} present a small increase from 72.9 ± 4 μm up to 86.3 ± 3.1 μm. This increase in ζ_{water} is accompanied by an increase in σ_{water} from 130.2 ± 4.5 μm up to 147.1 ± 3.4 μm. This means that more molecules diffuse to streamlines of higher velocity increasing the broadness of the propagator curve. Moving closer to the outlet of the core in Figure 6-20(c), a decreased ζ_{water} of 30.45 ± 4.5 μm and a σ_{water} of 96.6 ± 10 μm were observed. The water propagator at this voxel approximates the shape of the oil propagator. One possible explanation is the existence of artefacts close to the outlet of the RCH since the recorded intensity in that area is lower compared to the fluid intensity at the inlet.

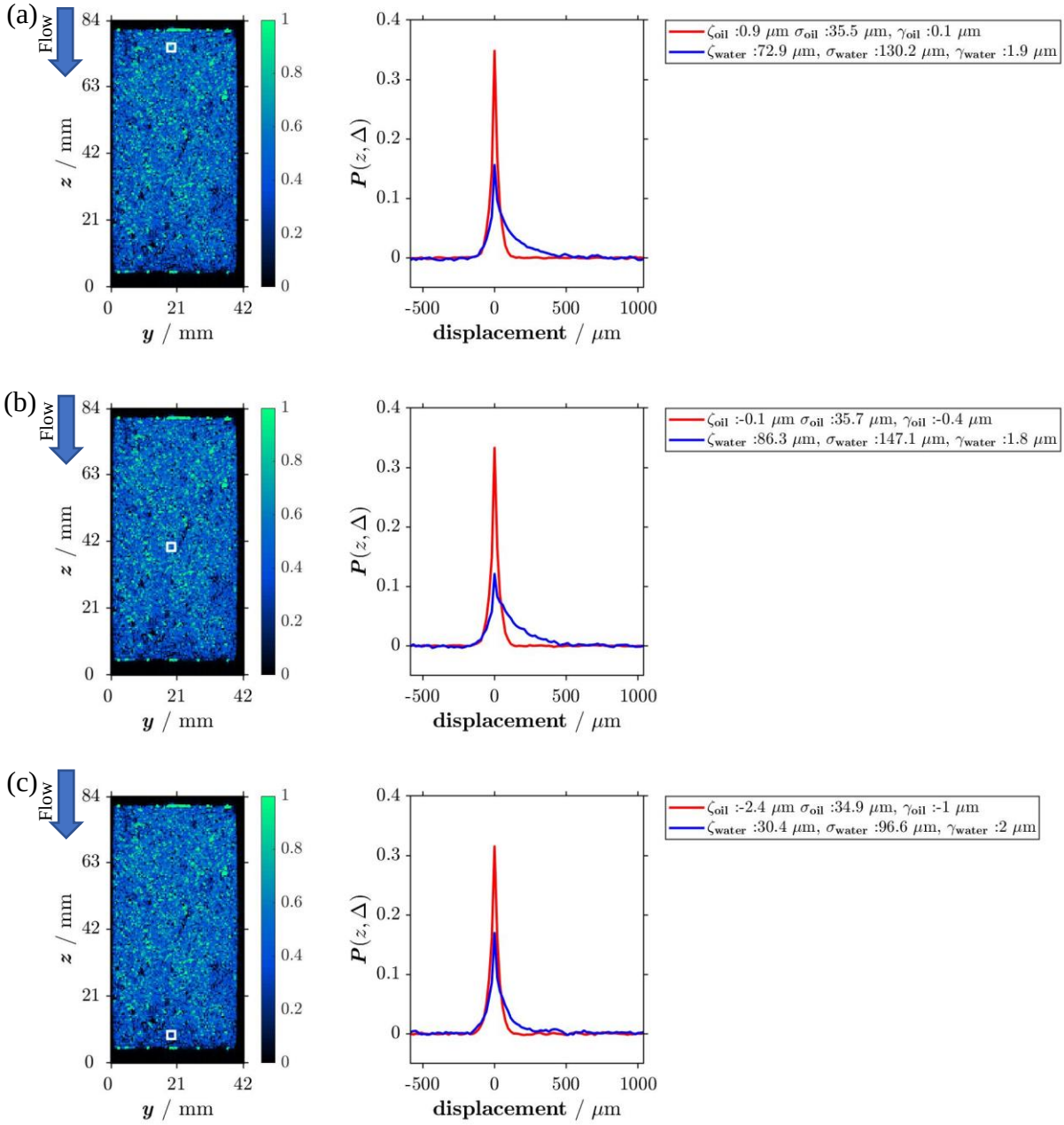

Figure 6-20: Chemically-selective propagators for water flow through an Estaillades core with S_w=0.68 and S_o=0.32. For an observation time Δ = 1.8 s, the local propagator and the statistical metrics for each phase are shown at the inlet(a), in the middle(b) and close to the outlet of the core plug(c).

6.5 Conclusions

In this work, a novel four pulses WET sequence was employed for the acquisition of quantitative bulk spectra, 1D spatially-resolved spectra, images and propagators in a bead pack and in a complex Estaillades core. Two-phase flow detection with NMR is achieved for the first time by combining this novel suppression scheme with the APGSTE-RARE sequence.

The four pulses WET scheme combined with the pulse-acquire sequence showed great agreement with the gravimetric measurements for the system of the bead pack and was proved more efficient than the single-pulse suppression scheme used previously (Ramskill et al., 2018). The effectiveness of the WET suppression in the APGSTE-RARE sequence was verified by the propagator measurements. Firstly, the measured $\langle \zeta \rangle_{water}$ from the water propagator was similar the $\langle \zeta \rangle_0$ implemented by the pump. Secondly, the D_{app} from oil propagators showed a great agreement with the D_s of dodecane, showing that the chemical selectivity combined with propagators can give quantitative results.

The chemically-selective bulk and 1D (CSI) spectra showed great agreement with the gravimetric measurements in the Estaillades sample as well. The novel suppression scheme in parallel with the improved reconstruction process described in Chapter 3, resulted in S_w^{MRI} and S_o^{MRI} of higher accuracy coming from the 3D CS-RARE sequence. The chemically-selective APGSTE-RARE presented interesting shapes for the water and the oil propagators in the rock system. The water phase which was the mobile phase presented skewed propagators with a large peak around zero as expected by the literature (Scheven et al., 2005a). The oil phase presented Gaussian-shaped propagators proving that oil was trapped in the porosity as the water was flowing through it. From the local oil propagators, a mean D_{app} was measured and the obtained value was not very far from the approximations found in the literature.

The MRI technique demonstrated herein is a useful tool for the study of spatially-resolved multiphase displacement processes inside complex porous media encountered in petrophysics. The chemically-selective CS-RARE sequence is used to monitor the imbibition and the polymer injection dynamic processes presented in Chapter 8. The multiphase propagator technique will also be used in the polymer injection stage to map the polymer and brine displacement through the rock.

Chapter 7 Primary Drainage in Estaillades Carbonate Rock

7.1 Introduction

Laboratory-scale displacements in rock core plugs are widely used to examine the mechanisms of oil recovery. There are several methods to prepare the cores and achieve reservoir representative saturation under laboratory conditions. The phenomenon of displacement of the non-wetting fluid within a porous medium by a wetting fluid is known as primary drainage. Monitoring the oil and water distribution during the primary drainage process in parallel with the pressure change in the sample leads to interesting observations regarding the capacity of the reservoir, the pore geometry (Lindquist, 2006) and the wetting characteristics (Anderson, 1986). All these characteristics are fundamental for the digitalisation of the reservoir which is the core of DR. Digitalisation is important to predict the relative saturation of the reservoir with depth.

NMR has already been used to monitor the primary drainage process. In log data, T_2 distributions have been used to map the pore space distribution and relate it to the P_{cap} (Volokitin et al., 2001). Several MRI techniques have also been used for the acquisition of saturation profiles during drainage (Cano Barrita et al., 2008; Spinler et al., 1999). Other techniques such as diffusion-weighted profiles (Sylta, 2010) and spatially resolved T_1-T_2 sequences have been employed to provide localised quantitative measurements for the hydrocarbon and the water phases (Bush, 2018b). Taking advantage of the chemical shift between the hydrocarbon and the brine peak confined in the pore space, a 1D spectra profile sequence has been implemented to quantify spatially and dynamically the presence of oil and water (Hall and Rajanayagam, 1987).

This chapter builds upon the use of the 1D spatially resolved CSI sequence in parallel with the dynamic pressure drop measurement during the slow injection of dodecane in a brine-saturated Estaillades rock. The 1D spatially-resolved CSI sequence is used to quantitively, spatially and dynamically monitor the primary drainage of a carbonate core with the porous plate technique maintaining a continuous injection of 0.3 ft d^{-1} until the entry pressure of the ceramic disc was reached. At this point, the injection was changed to constant pressure flow reaching a connate relative saturation. The relative saturation recorded in this experiment is the lowest water concentration mentioned in the literature for the drainage of carbonate rock. The aim of this study is to analyse the pore-filling mechanisms and the saturation profile within a dual-porosity carbonate rock.

7.2 Theoretical Background

7.2.1 Definition of Primary Drainage

Drainage refers to the displacement of a wetting fluid from a non-wetting fluid within a porous medium, initially fully saturated with the wetting phase. The word primary

indicates that this is the first time the non-wetting phase invades the pore network. One example of primary drainage is the injection of CO_2 into a saline aquifer. Another popular process of primary drainage is the Mercury Intrusion Porosimetry (MIP) used for the assessment of the pore size distribution. Another case of primary drainage in a natural system is the migration of the hydrocarbon phase from the source rock to a hydrocarbon reservoir. During this natural process, the oil or gas moves upwards under buoyancy until it faces a barrier to movement and it is then accumulated to form a reservoir. At this stage, the oil displaces the brine phase in the pore space driven by the buoyancy force caused by the density difference since the hydrocarbons are less dense than the brine (Blunt, 2017).

7.2.2 Techniques for Capillary Pressure Curves and Resistivity Index

MIP (Blunt, 2017), dynamic displacement, centrifuge and Porous Plate injection (PP) are routinely used in the oil industry (Kalam et al., 2006). The PP method is deliberately used in core analysis and involves the placement of a semi-permeable ceramic disc in capillary contact with the sample. Then a constant displacement pressure is imposed stepwise. More precisely, the displacing fluid is injected at different pressure stages and when capillary equilibrium is reached, an average water saturation, S_w, is calculated giving the P_{cap}-S_w curve(Dullien et al., 1986). Even though PP is reliable for measuring capillary pressure curves, it is time-consuming. As a result, a slightly altered technique known as Short-Wait Porous Plate (SWPP) method has been studied. In this method, the non-wetting phase is injected at ultra-slow flow rates constantly instead of stepwise. SWPP has given reliable S_w-Resistivity Index (RI) curves in short experimental time. Nevertheless, P_{cap}-S_w curves obtained with SWPP present deviations when compared to the ones obtained with MIP or PP (Kalam et al., 2006). An exponential model fitting of the SWPP results to the MICP or PP results has been recommended by Dernaika et al., (2016) as a solution to extract reliable P_{cap}-S_w curves from SWPP.

P_{cap} is defined as the pressure difference between the non-wetting and the wetting phase. The non-wetting phase invades the pore when P_{cap} is higher than zero. Primary drainage implementing the conventional PP method leads to the acquisition of throat size distributions for the rock. The measured P_{cap} is related to the throat size, r_t, as:

$$P_{cap} = \frac{2\,\sigma_\tau\, cos\theta_R}{r_t}, \tag{7-1}$$

where θ_R is the receding contact angle and is considered (Lenormand, 1990). In the SWPP method, there is a continuous injection of the non-wetting phase, therefore recorded pressure could be related to the narrow throats. However, information from the wider throats is lost since there is no equilibrium in the system and this method is not recommended for the acquisition of the throat size distributions.

7.2.3 Mechanisms of Immiscible Fluid Displacement

Two mechanisms control the displacement of one fluid by another non-immiscible fluid in a capillary tube, without any gravity effects. The first one is described by the

viscous pressure drop between the two fluids and the other by the capillarity. The effect of these two kinds of forces is quantified by the capillary number, Ca, given by:

$$Ca = \frac{u_D\, \mu_D}{\sigma_\tau}, \tag{7-2}$$

where u_D and μ_D are the Darcy interstitial velocity and the viscosity of the displacing phase, respectively, and σ_τ is the interfacial tension between the two fluids (Lenormand and Zarcone, 1989). Knowing that the Darcy velocity, for the flow of a displacing phase through a porous media is given by:

$$u_D = \frac{k\, k_{rD}}{\mu_D} \frac{\Delta P}{L}, \tag{7-3}$$

then combining Eq.(7-2) and Eq.(7-3) it can be derived that:

$$Ca = \frac{k\, k_{rD}}{\sigma_\tau} \frac{\Delta P}{L}, \tag{7-4}$$

where k is the absolute permeability of the rock, k_{rD} is the relative permeability of the displacing phase, ΔP is the pressure drop and $\Delta P/L$ is the pressure gradient along the flow direction. The relative permeability of a phase i is given by:

$$k_{ri} = {}^{k_i}/_{k} \text{ for } i\text{= phase } D, d, \tag{7-5}$$

where k_i is the effective permeability of the phase i. Ca represents the ratio of viscous to capillary forces. Another important parameter for describing the mechanism of displacement is the mobility ratio, M_R, defined as:

$$M_R = \frac{k_{rD}}{\mu_D} \Big/ \frac{k_{rd}}{\mu_d} = \frac{k_{rD}\, \mu_d}{k_{rd}\, \mu_D}, \tag{7-6}$$

where k_{rd} and μ_d are the relative permeability and the viscosity of the displaced phase. The viscosity component of Eq.(7-6) is usually dominant. Mobility is favourable when $M_R \leq 1$, whereas displacement is not efficient when $M_R > 1$ (Rellegadla et al., 2017; Wei et al., 2014). In primary drainage, the displacing phase is the non-wetting phase and the displaced phase is the wetting phase.

7.2.3.1 Mechanisms of Displacement in Primary Drainage

Lenormand et al. (1988) identified three main mechanisms of displacement in drainage. The first mechanism is called stable displacement and it is triggered by the viscosity of the injected fluid. The pattern of displacement looks like a piston with a flat front. The second is called unstable displacement or viscous fingering and it is controlled by the viscosity of the displaced fluid. The third mechanism is called capillary fingering and it occurs when the flow rate is slow, hence Ca is small. In this case, viscous forces are negligible and the displacement is governed by capillary forces. This mechanism has the pattern of fingers spread across a connected network

of pores in all directions. In more detail, as the non-wetting phase is injected, molecules advance along the flow direction forming loops which 'trap' the wetting phase until a flow channel reaches the outlet-end as shown in Figure 7-1.

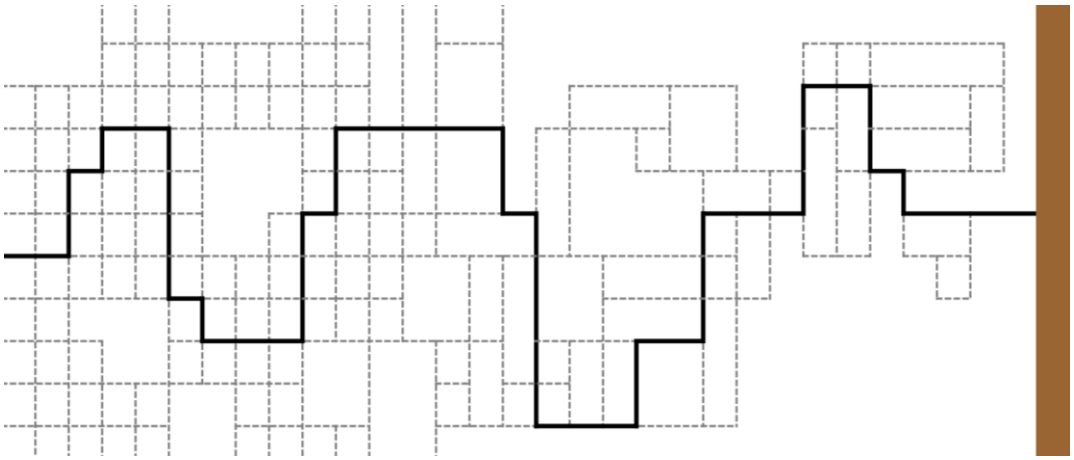

Figure 7-1: Illustration of the invasion percolation statistical simulation presenting the capillary fingering mechanism of displacement on a large network. Flow occurs from the left to the right. The black solid line represents the first path reaching the ceramic disc (outlet) while the dashed grey lines describe the fingers formed along the path due to capillarity. Adapted from Lenormand et al. (1988).

In the standard PP method, Ca is vanishingly small since the system is left to reach capillary equilibrium at each pressure stage. In the SWPP method, the flow rate is designed to keep $Ca < 10^{-4}$ maintaining low saturation rates (Dernaika et al., 2016). Consequently, the expected mechanism of displacement in the SWPP is capillary fingering. Figure 7-1 shows that more fingers are growing close to the inlet. Therefore, capillary fingering is characterised by the presence of a declining S_o profile from the inlet towards the ceramic disc.

7.2.3.2 Wetting Layers

Fingers are growing following the invasion percolation process. As the non-wetting phase invades a pore or moves through a throat, the wetting phase is not entirely expelled. Instead, the wetting phase is retained in the cracks, crevices and corners of the complex pore structure, leaving the non-wetting phase in the centre. These areas of the trapped wetting phase are called wetting layers. Wetting layers have a thickness of a few microns in reservoir rocks as illustrated in Figure 7-2.

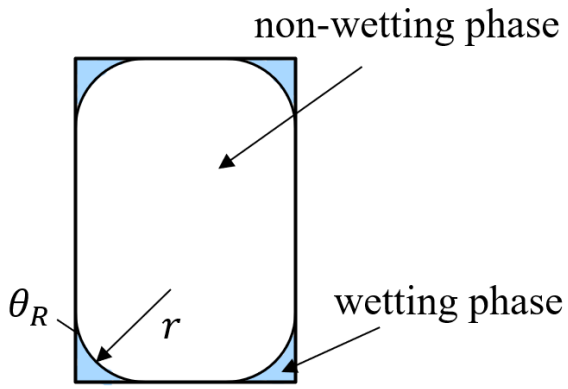

Figure 7-2: Cross-sectional area of a rectangular throat. The wetting phase (blue shaded area) is accumulated on the corners and the roughness of the pore space forming the wetting layers. The non-wetting phase resides in the centre of the pore. In capillary equilibrium, the interface between the two fluids has the form of an arc meniscus and does not interfere with the flow. The interface between the fluids has a radius r and a contact angle θ_R. Adapted from Lenormand et al., (1983).

In capillary equilibrium, there is a fixed radius of the arc menisci formed in the interface between the two fluids. As the pressure is increased, the wetting fluid gets squeezed to the corners. So at the end of the primary drainage, the non-wetting phase will reside on the solid surface directly, but some of the wetting fluid will always be present in the cracks at any finite P_{cap} (Blunt, 2017).

7.2.3.3 Irreducible Water Saturation

This finite minimum water concentration remaining at the end of the primary drainage process is called irreducible or connate water saturation, S_{wc} (Collins, 1975). In rock porous systems, the value of S_{wc} is higher compared to bead packs. This is happening because brine molecules are adsorbed by hydratable solids and they are accumulated in ultra fines throats or squeezed in the wetting layers (Dullien et al., 1986). The externally applied pressure cannot overcome the threshold capillary pressure, P_{cap}^{*}, needed to invade these small cavities. Therefore, the wetting phase will always be present in the system as happens in real reservoir conditions.

7.2.3.4 Wettability and Capillary Pressure in Real Reservoirs

In natural systems, primary oil migration takes place over geological time scales or millions of years. Sedimentary rocks consist of a variety of minerals that have different wettabilities (Abdallah et al., 2007). The non-wetting phase moves under the influence of gravity. Consequently, the wettability changes as a function of the reservoir depth, since the fluid pressure changes with depth. In this case, P_{cap} is given by:

$$P_{cap} = (\rho_w - \rho_{nw}) g_r \, h \tag{7-7}$$

where $\rho_w - \rho_{nw}$ is the density difference between the wetting and the non-wetting phases, g_r is the gravitational acceleration and h is the height above h_0. The h_0 is the datum depth where the pressure of the non-wetting and the wetting phases are equal

and is known as free water level. Figure 7-3 shows that P_{cap} is decreased as the depth of the reservoir is increased.

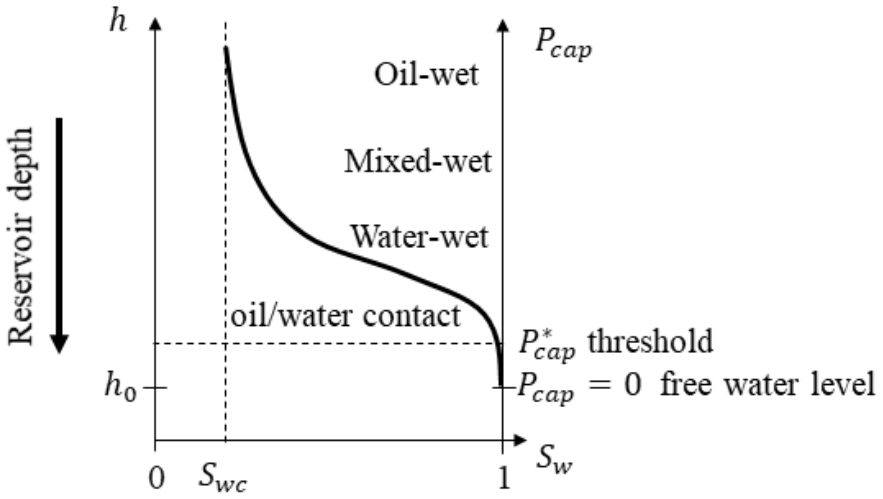

Figure 7-3: Illustration of the variation of the wettability, the relative water saturation, S_w, and the capillary pressure curve as a function of the height in a real reservoir.The nominal height h_0 is the free water level where the P_{cap} is zero. S_{wc} is the irreducible water saturation. The dashed horizontal line shows the oil/water contact represents the location of the capillary pressure threshold, P^*_{cap}, where a finite oil saturation is reached. Adapted from Blunt (2017) and Abdallah et al., (2007).

In low depth, P_{cap} is high enough to enable oil molecules to force the water out of the pore-throat system, making the reservoir more oil-wet. Moving deeper into the reservoir, P_{cap} decreases and the water wetting films become thicker. At this stage, the system is either oil-wet or water-wet. This inhomogeneous wetting of the reservoir rock is called 'mixed-wetting'. Close to the oil/water contact, the P_{cap} is known as threshold pressure. At this stage, the water phase is dominant and only a small finite amount of oil is present (Blunt, 2017).

Based on this analysis, we can now understand how the acquisition of P_{cap}-S_w curves under laboratory conditions can help us predict the reservoir wettability and S_w based on the depth. The ΔP recorded during the SWPP method deviates from the P_{cap} since no equilibrium is attained. The aim of this work is to implement the SWPP technique and identify the pattern of invasion through the acquisition of S_w and S_o profiles within a dual-porosity carbonate rock. For this purpose, ΔP was recorded in parallel with fast NMR acquisitions.

7.3 Materials and Methods

7.3.1 Material and Chemicals

The Estaillades rock (EST1_102) was used in this series of experiments and the process for measuring its porosity through saturation is described in Section 6.3.1.2. The ceramic disc was saturated following the exact same procedure. Estaillades' porosity was measured as 29.62 ± 0.67 %. In the current experiment, dodecane Dodecane (99%, Acros Organics) was used as the non-wetting fluid with a standard

viscosity of 1.36 cP and brine as the wetting phase with a viscosity of 0.89 cP (Liu et al., 2011).

7.3.2 Methods

7.3.2.1 Core-Flooding Protocol for the Primary Drainage

Following brine saturation, the core and the ceramic disc were enclosed in a layer of polytetrafluoroethylene (PTFE) heat-shrink tubing. The ceramic disc (ELE International) was rated to 1.5 MPa (217.5 psi) and the permeability provided by the supplier was 4.5 10^{-2} mD with 1.0 cm width and 0.32 porosity. Initially, PTFE heat shrink was used to enclose both the ceramic disc and the core plug. However, due to an increased confining pressure (6.3 ± 0.3 MPa), the use of the heat-shrink was impossible. Therefore, the brine saturated ceramic disc and the rock core were loaded in the Aflas sleeve without being enclosed in the heat shrink as shown in Figure 7-4. More precisely, the PEEK Rock Core Holder (RCH) flow cell (ErgoTech, Conwy, UK) was filled with brine and then the ceramic disc and the core were pushed inside to avoid the formation of air bubbles inside the porous network. No flow distributor plates were placed in the inlet or the outlet of the RCH flow cell. The inlet lines of the RCH were filled with brine to avoid capturing air bubbles and they were attached to the fixed end platen. The inner diameter of the tubes between the accumulator and the RCH was 1/16″ (1.6 mm), while close to the inlet of the RCH there were two high-pressure lines of 1/32″ inner diameter. Then, the adjustable platen was placed at the other end of the RCH and it was connected to the outlet line. The confining pressure was monitored and brine was injected with a constant flow rate of 0.071 mL min^{-1} (~ 1 ft d^{-1}) for 11.1 h until a quantity of 2 P.V. passed through the core. The step of brine injection at 1 ft d^{-1} was important to ensure the removal of air bubbles trapped within the porous system which could lead to signal loss.

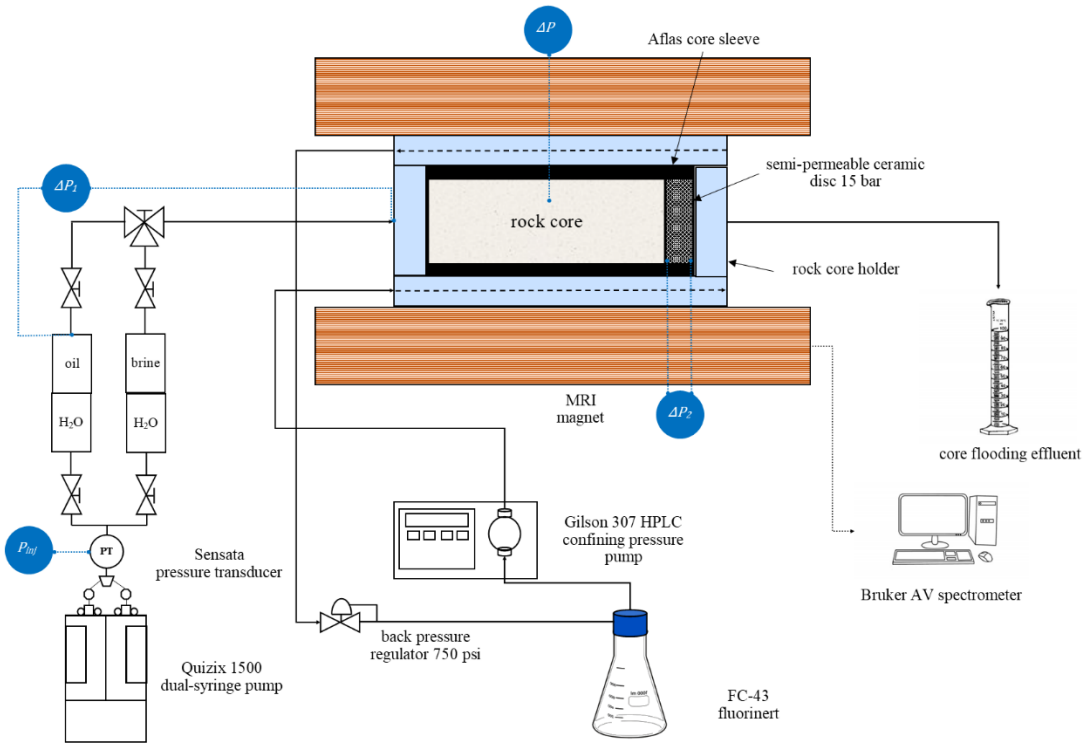

Figure 7-4: Schematic representation of the CFS set-up used during the primary drainage. ΔP_1 is the pressure drop across the pump and the CFS and ΔP_2 is the pressure drop across the ceramic disc. P_{inj} is the pressure recorded from the pressure transducer during the injection, while ΔP is the pressure drop along the sample.

Then, dodecane was injected with a constant flow rate of 0.02 mL min^{-1} (~ 0.3 ft d^{-1}) until a maximum pressure of 1.49 MPa (216 psi) was reached. This pressure threshold was chosen less than the pressure limit of the ceramic disc (217.5 psi) making sure that dodecane would not break through the disc. After 14.4 h of oil injection, the pressure threshold was reached. At this point, the injection mode changed to constant pressure injection which is described by a fluctuating Q as shown in Figure 7-5. Primary drainage of the core to S_{wc} was terminated after 249.7 h (10.4 d) of oil injection under constant pressure.

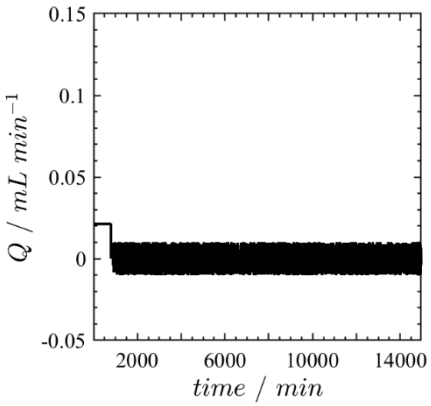

Figure 7-5: Flow rate of oil injection recorded by the pump pressure transducer during the whole duration of the primary drainage.

7.3.2.2 NMR Protocol for Monitoring the Primary Drainage

All NMR experiments were conducted at room temperature (20 ± 1°C) in a 2 T (85 MHz for ^{1}H nuclei) horizontal bore superconducting magnet, controlled by a Bruker AV spectrometer. A 63 mm inner diameter r.f. birdcage coil, tuned to 85.2 MHz was used for excitation and signal detection. Spatial resolution along the direction of superficial flow (z) was achieved using a magnetic field gradient, capable of a maximum gradient strength of 10.7 G cm^{-1}, along the z-direction. The primary drainage flood was dynamically monitored using 1D CSI along the flow direction of the core plug as illustrated in Figure 7-6. Before starting the injection, a series of reference spectra and low-resolution images were acquired to align the sample with B_1 and B_0 magnetic fields and to assess the reproducibility of the spectrum.

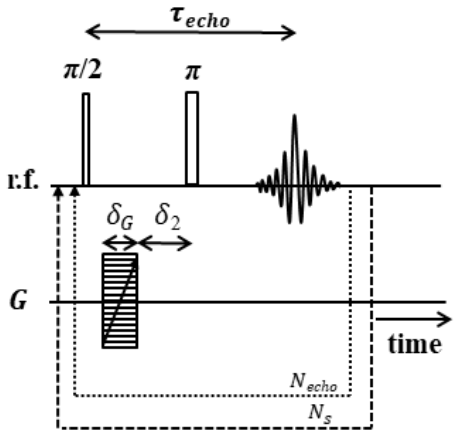

Figure 7-6: Schematic of the CSI pulse sequence.

7.3.2.3 NMR Experimental Parameters

A hard 90º pulse of 48.2 µs and a refocusing 180º pulse of 96.5 µs were used. After comparing several spectra with different t_{RD} values, the optimum t_{RD} was chosen as 1.12 × T_1. As explained in the theory chapter, t_{RD} affects the t_{exp}. In dynamic measurements, t_{RD} should be short enough to record dynamic changes and in parallel maintain an acceptable SNR. The duration of the phase gradient, δ_G, was 0.14 ms and

it was ramped to a maximum value of 0.102 T m^{-1} (95% g_{max}) in 128 evenly distributed increments. The gradient stabilisation time, δ_2, was 2 ms resulting in a FOV of 105 mm with a resolution of 0.82 mm pixel^{-1} along the z-direction. The acquisition time of one CSI experiment with 4 averages was 17.5 min and the total data acquisition lasted 112.3 h.

7.3.2.4 Pressure Drop Along the Core Plug

The injection pressure, P_{inj}, was monitored using the CFS injection pump in-built Sensata pressure transducer (0-20,000 psi range, ± 1.6 psi sensitivity) as shown in Figure 7-4. The pressure drop across the core plug was calculated as:

$$\Delta P = P_{inj} - \Delta P_1 - \Delta P_2 \,, \tag{7-8}$$

where ΔP_1 is the pressure drop across the accumulator and the entrance of the RCH and ΔP_2 is the pressure drop along the ceramic disc. The pressure drop between the pressure transducer and the accumulator was considered negligible. ΔP_1 was estimated using the Poiseuille law along the tube that connects the accumulator with the entrance of the RCH given by:

$$\Delta P_1 = \frac{Q\ L\ 8\ \mu_{eff}}{\pi\ r_{tube}^4}, \tag{7-9}$$

where μ_{eff} is the effective viscosity along the tube, r_{tube} is the radius and L the length of the tube. The L was calculated using the NMR data. Knowing that each 1D CSI experiment required 17.5 min, the length of the tube was adjusted based on the time and the volume of the injected oil until the first oil peak appeared in the spectrum. Dodecane was injected from the right towards the left side of the spectrum intensity presented in Figure 7-7. Figure 7-7(a) shows that the oil peak appeared at the inlet of the RCH after 175 min of oil injection. Since the flow rate was constant at 0.02 mL min^{-1}, the dead volume between the accumulator and the RCH was 3.7 mL. Figure 7-7(b) gives an insight into the oil propagator along the flow direction after 210 min of flow.

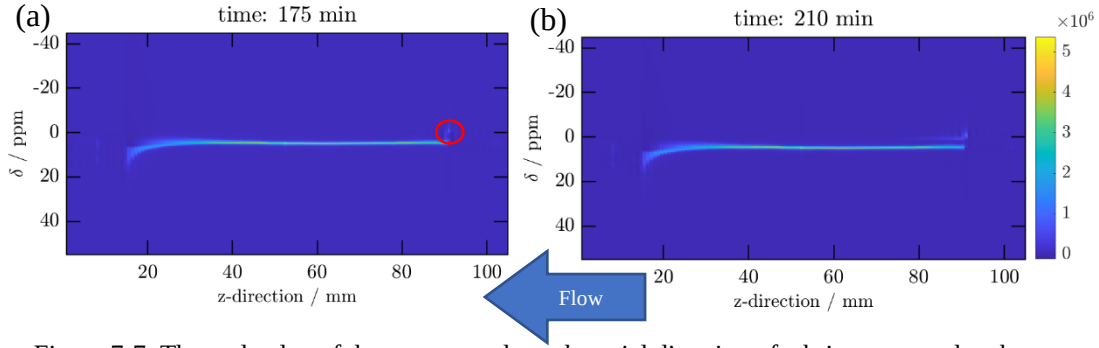

Figure 7-7: The real value of the spectrum along the axial direction of a brine saturated carbonate rock. (a) The oil peak became apparent at the inlet of the core after 2.9 h of oil injection. At this point, the interstitial flow rate was constant at 0.3 ft d^{-1}. (b) The oil peak was better distinguished when the oil propagated more after 4.1 h of injection.

Using Eq.(7-8), ΔP_1 was measured as 1.8×10^{-7} MPa (2.6 10^{-5} psi) during the period of constant flow rate and as 4.0 10^{-8} MPa during the period of injection under constant

pressure. Following Darcy's law described by Eq.(7-3) along the ceramic disc, ΔP_2 was measured as 0.2 MPa (29 psi) during the period of constant flow rate, while it fluctuated around 0 MPa during the period of injection under constant pressure.

7.4 NMR Data Processing

7.4.1 Methods for Measuring the Relative Saturations

Quantification of the spatially-resolved spectra was performed with two different methods. The first method is called the 'integration' method and was based on dividing the spectrum into two areas and integrating the peak within these areas. Optimising carefully the area around each peak, I_w and I_o at each axial position were measured. Using Eq.(6-1) and (6-2), the corresponding S_w and S_o were calculated. The second method is called the 'line shape' method and was based on the fitting of a Langragian curve to the obtained experimental data. Firstly, a Langragian curve was fitted to the brine peak which was the dominant component in the initial system. Then, a second curve similar to the first one but broader by 1.46 ppm and shifted by 3.5 ppm was simulated for the oil component. Both simulated curves were compared to the experimental data giving the final S_w and S_o measurements.

Both methods are affected by field distortions such as line broadening, deviation on the ppm axis, baseline offset and peak overlap due to the presence of the rock and the ceramic plate. These distortions and their effect on the spectrum are further analysed.

7.4.2 Broadening of the Line Width and Deviation on the ppm Axis

The first distortion in the spectrum was observed close to the outlet of the RCH, where the ceramic disc was placed. Figure 7-8 presents the 1D CSI results acquired after 16.6 h of oil injection. At this point, dodecane had reached the ceramic disc and both brine and oil peaks were present at each axial position.

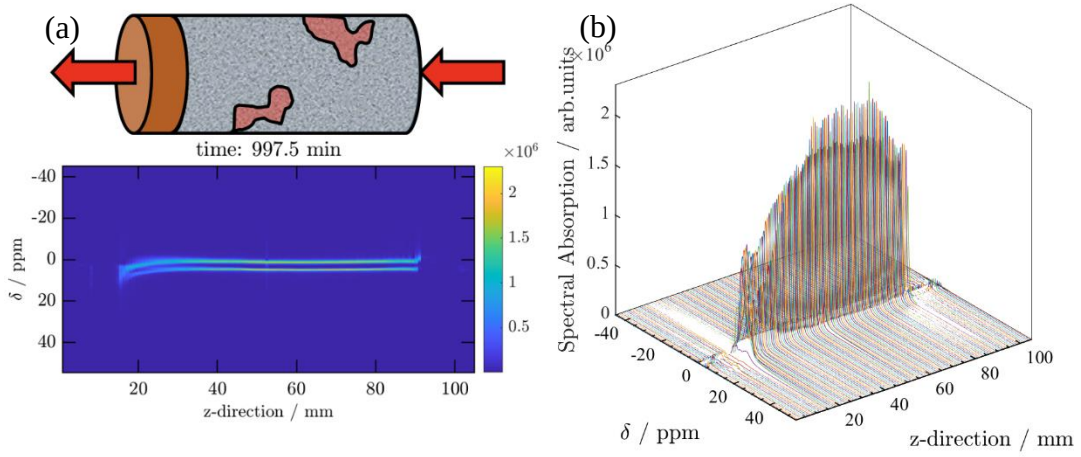

Figure 7-8: A schematical representation of the brine saturated Estaillades with the ceramic disc (brown cylinder) is plotted in parallel with the 2D magnitude of the spectrum acquired from the 1D CSI experiment after 997.5 min (16.6 h) of dodecane injection at 0.3 ft day^{-1} (a). The red arrows on the left and right sides of the core plug show the direction of the dodecane flow. The same data are presented in a 3D plot illustrating the spectrum in each axial position of the rock (b).

Figure 7-8(a) shows the magnitude of the brine and the oil peaks along the flow direction. The oil presence is described by the top line and is around δ = 1.3 ppm. The brine presence is displayed by the bottom line around δ = 4.8 ppm. The schematical representation of the core plug attached to the ceramic disc with the dodecane flow from the left to the right is plotted on the top for a better understanding of the injection system. It is noticeable that the two horizontal parallel lines were tilted towards the positive side of the y-axis (δ-axis). Broadening and distortion of the spectrum near the ceramic disk are also seen in the 3D plot of the spectrum presented in Figure 7-8(b).

Further analysis of this line broadening effect is apparent in Figure 7-9 where the spectrum at four axial positions is plotted. At a distance of 22.1 mm from the outlet of the RCH, the spectrum deviates a lot and the brine peak was shifted from 4.8 ppm to 6.3 ppm. At distances 24.6 and 27.9 mm, the brine peak was found at the expected 4.8 ppm. Nevertheless, both peaks were broader than expected showing significant overlap. Moving closer to the centre of the rock core at a distance of 59.9 mm, the oil and brine peaks can easily be distinguished. The distortion in the spectral shape affects both the 'integration' and the 'line shape' methods and is taken into account during the error analysis.

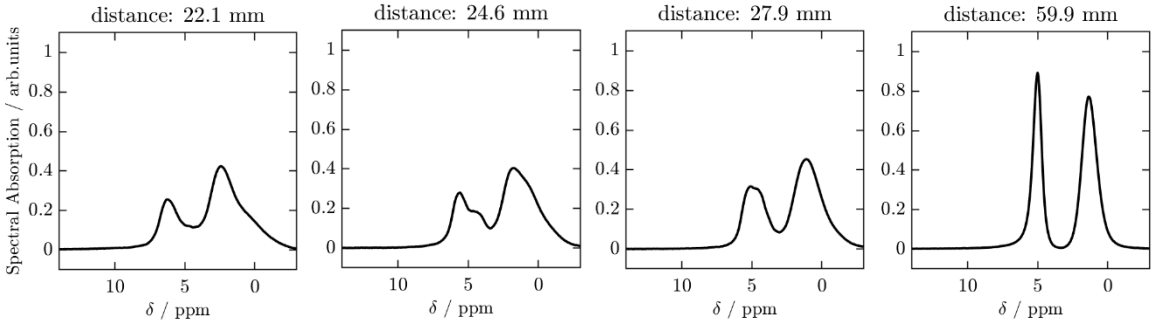

Figure 7-9: Spectrum at 22.1, 24.6, 27.9 and 59.9 mm from the outlet of the RCH. The distance is estimated starting from the left (outlet), where the ceramic disc was placed, to the right side (inlet) of the RCH.

7.4.3 Baseline Offset Error

Another distortion in the spectrum was observed at the centre of the FOV with a baseline offset. Figure 7-10(a) displays the experimental spectrum (solid black line) and the fitting coming from the 'line shape' method (dashed red line) at the position pointed by the yellow dashed line in Figure 7-10(b) for the same experiment shown in Figure 7-8. Even though the 'line shape' method seems insusceptible to the baseline deviation, the measured S_w is slightly higher than expected. More precisely, the S_w of the central point was measured as 0.46 which was higher than 0.44 measured in the other pixels close to the centre. This deviation in the values of S_w and S_o was included in the local error analysis.

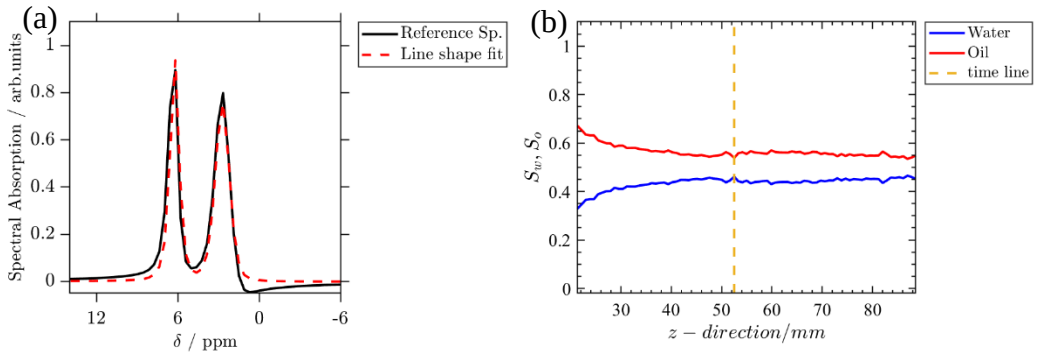

Figure 7-10: The reference spectrum is plotted in parallel with the spectrum measured using the 'line shape' method (a) at the central point of the sample pointed out by the yellow dashed line in (b). The solid blue and red lines along the axial direction of the core represent the value of S_w and S_o respectively (b), as it is measured from the spectrum using the 'line shape' method.

7.4.4 Effect of Artefacts in the 'Integration' Method

To understand better the effect of these distortions in the S_w and S_o obtained using the 'integration' method the experiment presented in Figure 7-8 is further analysed. Three axial positions were picked for analysis in Figure 7-11. The closest point to the ceramic disc was 22.1 mm from the outlet, the second position of interest was at 27.9 mm and the third point was at position 59.9 mm from the outlet. At each position, the reference spectrum (dashed black line) is presented in parallel with the optimum area of integration for each chemical component (red curve for dodecane and blue curve for water). The yellow dashed line points out the pixel of the spectrum along the core plug.

Figure 7-11(a) and (b) demonstrate that broadening and deviation on the ppm axis make difficult the optimisation of the integration area around the oil and brine peaks. More precisely, the appearance of a tail on the right side of the oil peak affects the choice of the optimum integration limits. Even though, the fitting follows the deviation on the ppm axis, the estimated values of S_w and S_o are different compared to the values acquired along the full length of the core where the oil and brine peaks were well separated and distinguished as shown in Figure 7-11(c).

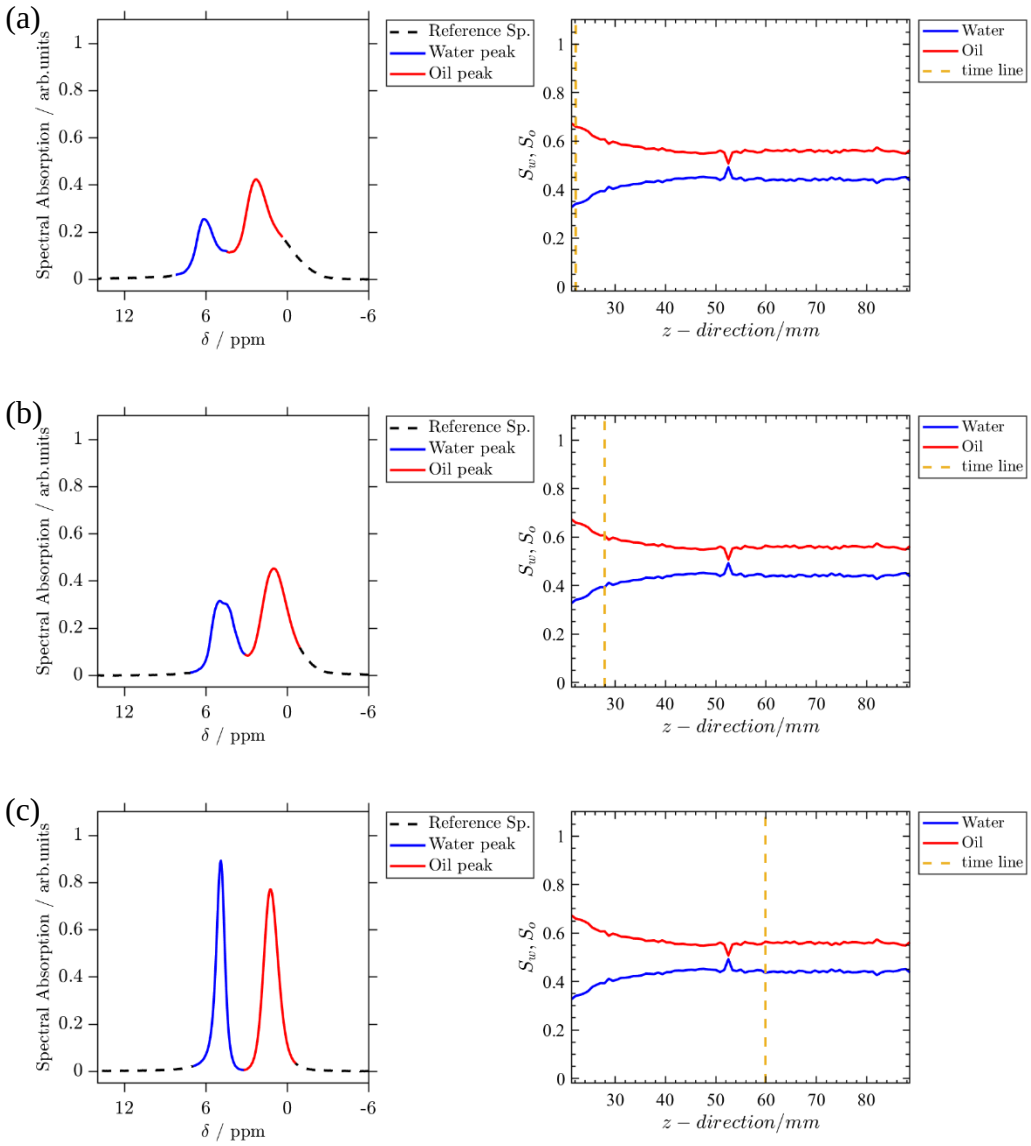

Figure 7-11: The reference spectrum (dashed black line) acquired with 1D CSI is plotted in parallel with the optimum area of integration adjusted using the 'integration' method for the water peak (blue curve) and the oil peak (red curve) at distance 22.1 (a), 27.9 (b) and 59.9 mm (c) from the outlet of the RCH. A ceramic disc was placed at the outlet of the RCH. The yellow dashed line points to the exact position along with the core where the reference spectrum was acquired and the values of S_o (red line) and S_w (blue line) along the core were measured using the optimum area of integration for each component.

The effect of peak broadening and overlap was further analysed by comparing the sum of I_w and I_o from the optimum area of integration (green line) to the total integral of the reference spectrum (black line) at all axial positions. Figure 7-12 proves that the 'integration' method leads to reliable results for the data obtained 16.6 h of oil injection. This difference between the sum of I_w and I_o and the total integral of the spectrum was taken into account for the total error analysis. Another important parameter to assess was the limits of the optimum area of integration. The limits of the integration area around each peak were varied. Then, the standard deviation among the measured I_w and I_o at each position was mesured. Last but not least, the

reproducibility of the spectra was also analysed and was added to the total error analysis for the final S_w and S_o measurements.

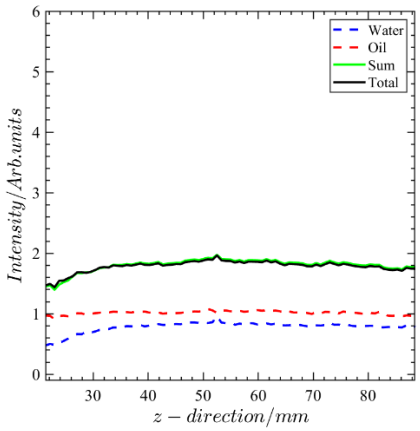

Figure 7-12: Analysis of the peak integration method along the axial direction of a carbonate rock core when both oil and brine peaks are present along with the core. The sum of the optimised oil and water integral (green line) is plotted in parallel with the integral derived from the whole reference spectrum (black line) along the axial dimension of the core after 997.5 min (16.6 h) of data acquisition. Water and oil integrals are shown by the dashed blue and red lines, respectively.

7.4.5 Effect of Artefacts in the 'Line Shape' Method

The same data were also analysed using the 'line shape' method. In Figure 7-13, the experimental spectrum (solid black line) is plotted in parallel with the simulated spectrum (red dashed line) at the same three axial positions as in Figure 7-11. Each position is pointed out by the yellow dashed line. The spectrum was normalised to the highest intensity point of all the spectra acquired along with the axial position. It can be seen that the simulated spectrum follows the deviation and the broadening of the reference spectrum at 22.1 and 27.9 mm from the outlet of the RCH.

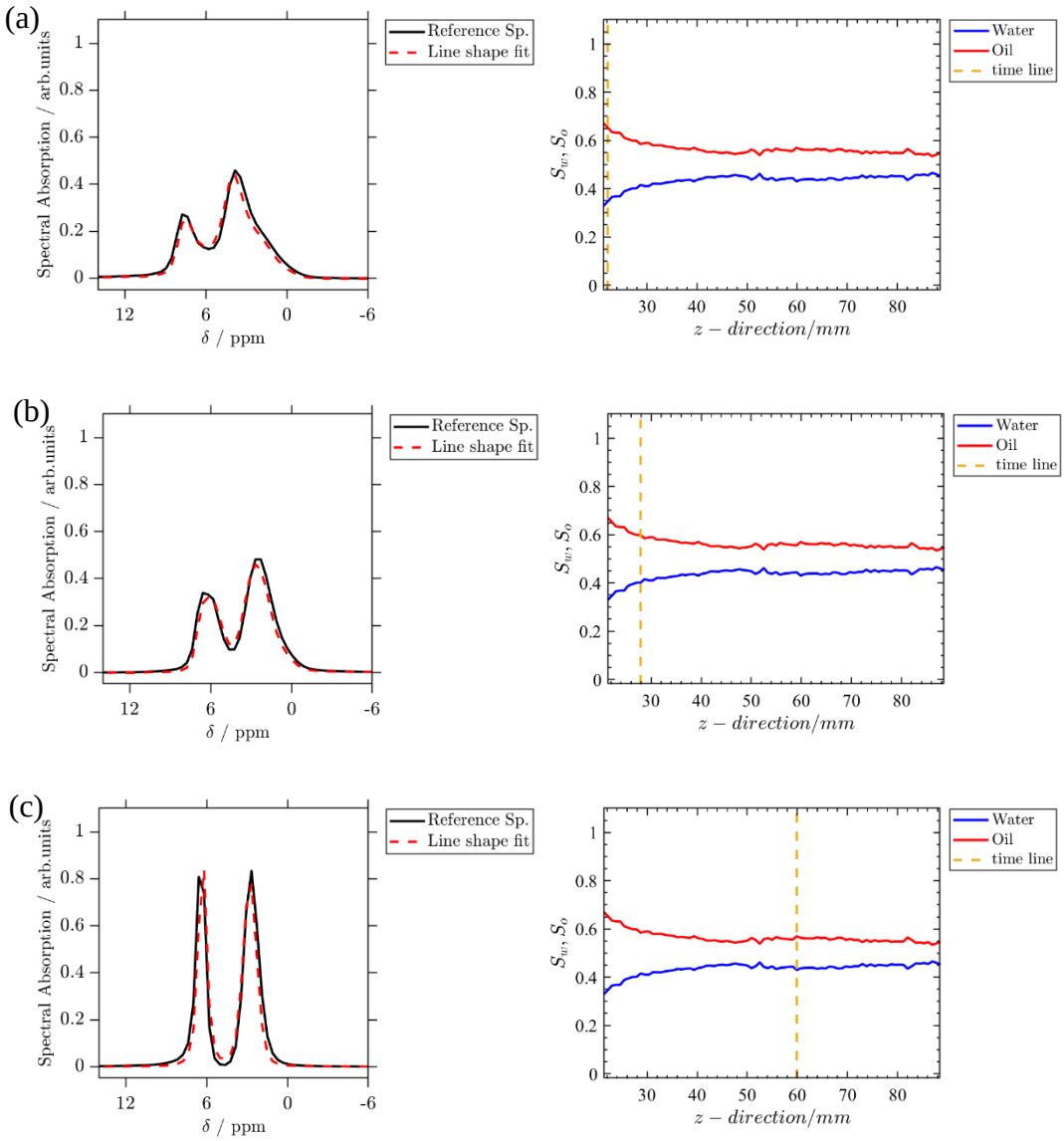

Figure 7-13: The reference spectrum (solid black line) acquired with 1D CSI is plotted in parallel with the simulated spectrum using the 'line shape' method (red dashed line) for the water and the oil peak at a distance of 22.1 (a), 27.9 (b) and 59.9 mm (c) from the outlet of the RCH. A ceramic disc was placed at the outlet of the RCH. The yellow dashed line points to the exact position along with the core where the reference spectrum was acquired and the values of S_o (red line) and S_w (blue line) along the core were calculated by analysing the line shape fitting (red dashed line).

The total error in the calculation of S_w and S_o using the 'line shape' method is divided into two parameters; the reproducibility of the spectrum and the difference between the reference and the fitted curve at each axial position.

7.4.6 Conclusions Driven by Comparing 'Integration' and 'Line shape' Methods

Both the 'integration' and the 'line shape' methods derive quantitative results for the S_w and S_o profiles. The 'line shape' method gave more robust measurements at the initial stage of the drainage when the oil had not reached the ceramic disc since it is

less sensitive to the broadening of the linewidth. The 'integration' method presented better accuracy in the measurement of the S_w and S_o , when S_o reached 0.20 in the area close to the ceramic disc.

7.5 Results

Figure 7-14 presents the ΔP as a function of the mean saturation of the wetting phase, $\bar{S}_w$. $\bar{S}_w$ comes from the mean value of the local S_w measured along the flow direction using both the 'line shape' (solid black) and the 'integration' (dashed black) methods. It can be seen that ΔP is a monotonically decreasing function of the $\bar{S}_w$. Eight different zones have been identified and highlighted with dashed lines of various colours on the ΔP-$\bar{S}_w$ curve. The S_w and S_o profiles obtained in each of these zones are further analysed below. The goal is to identify the pattern of the brine displacement.

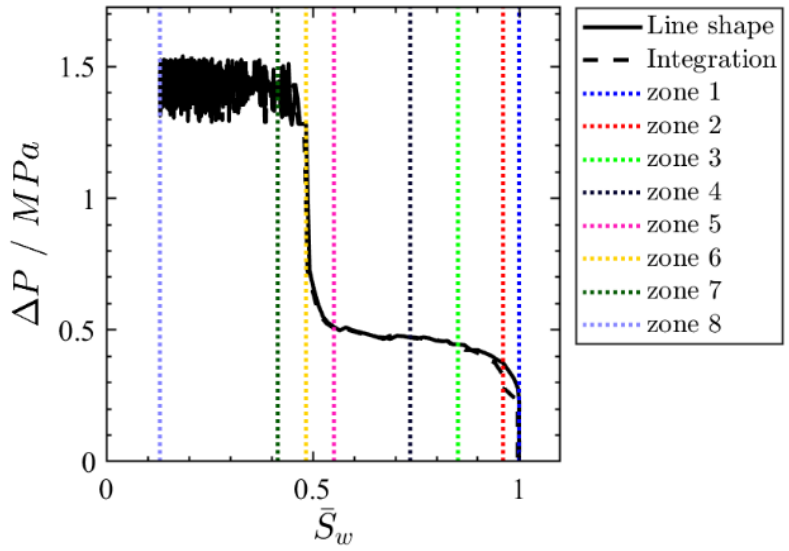

Figure 7-14: ΔP as a function of the $\bar{S}_w$ during the injection of dodecane into an initially brine-saturated Estaillades carbonate core. Primary drainage was conducted using the porous plate method, with continuous injection at Q equal to 0.3 ft d^{-1} until the maximum pressure threshold of the ceramic disc (1.5 MPa) was reached. Then the Q was reduced keeping the pressure constant while the $\bar{S}_w$ was further reduced until a reservoir-representative S_{wc} was achieved. Dotted coloured lines indicate eight zones of interesting dodecane-brine equilibrium.

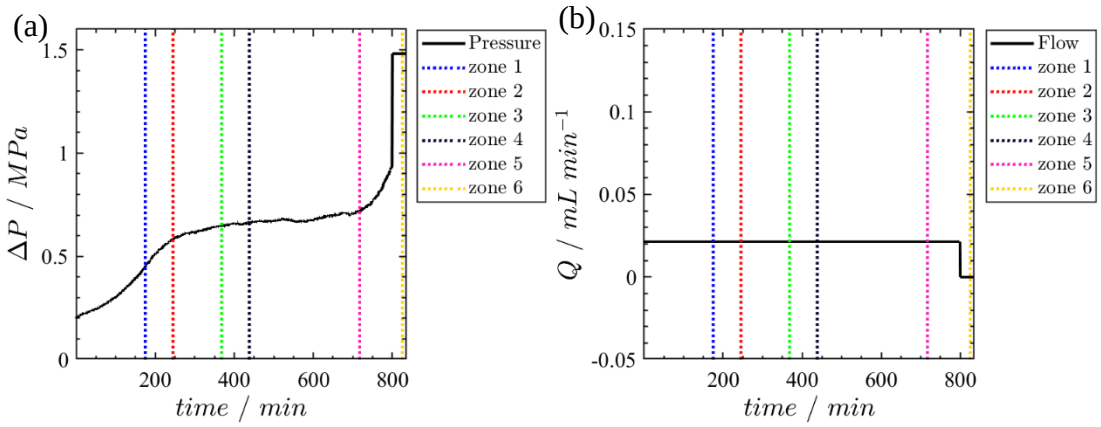

Figure 7-15: ΔP(a) and Q(b) change with time while dodecane was injected into the brine saturated Estaillades rock for the first six zones of interest presented in Figure 7-14.

Figure 7-15 presents the ΔP and the Q change with time for the first six zones highlighted in Figure 7-14. It can be seen that Q was switched to zero when ΔP reached the threshold. The S_w and S_o profiles for each zone are analysed in Figure 7-16.

Figure 7-16(a) until (d) are results of the 'line shape' method, while Figure 7-16(e) and (f) are results of the 'integration' method. The Ca measured from the constant oil injection was at the order of ~ 2.7×10^{-8}, hence capillary forces were expected to control the process of oil invasion into connected pores and throats.

Initially, the recorded P_{inj} following the brine injection was 0.21 MPa (31 psi). Oil was injected at a constant Q of 0.02 mL min^{-1} oil reached the inlet of the RCH. ΔP started to increase linearly until it reached the value of 0.23 ± 0.01 MPa after 175 min. This ΔP is better presented in Figure 7-15(a) with the dotted blue colour and can be related to the oil-water contact since a measurable quantity of the brine was displaced from the system and not only from a single pore. The S_w close to the inlet of the RCH was measured as 0.99 ± 0.003 and is illustrated in Figure 7-16(a).

As more oil was injected, the value of $\bar{S}_w$ started to significantly deviate from one while the ΔP presented a large increase. In zone 2, oil has invaded the throats adjacent to the inlet of the sample as projected in Figure 7-16(b). After 245 min of injection, dodecane has filled the available flow paths until a distance of 29 mm from the inlet. ΔP was calculated as 0.37 ± 0.01 MPa and is better seen in Figure 7-15(a) with the dotted red line. A small difference between the $\bar{S}_w$ measured from the 'line shape' (0.96 ± 0.003) and the 'integration' method (0.94 ± 0.008) was observed in Figure 7-14. As we discussed in Section 7.4.6, the 'line shape method's result is considered more robust at this stage.

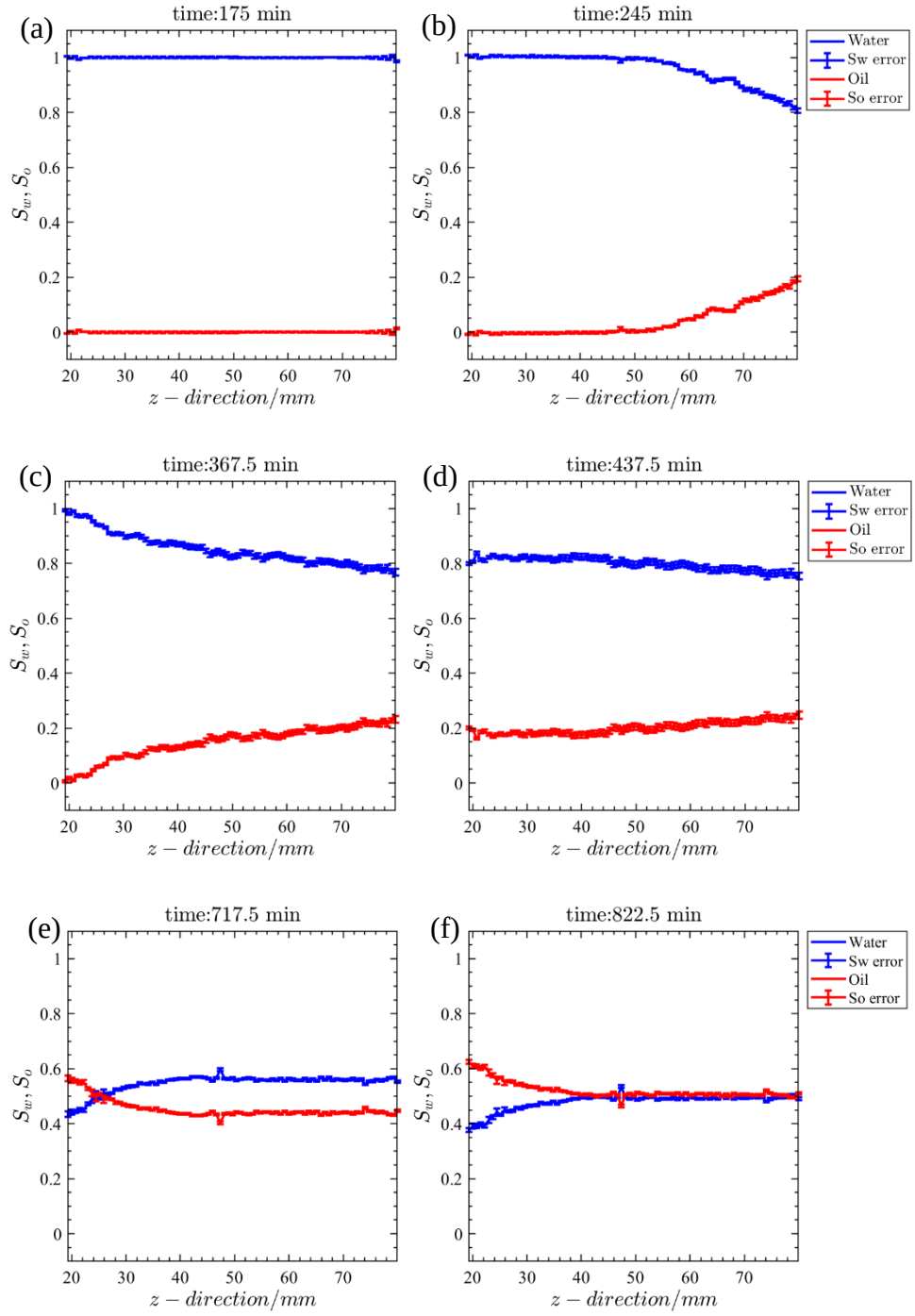

Figure 7-16: 1D spatially resolved relative saturation for the brine (S_w, blue) and the dodecane (S_o, red) related to zone 1(a), zone 2(b), zone 3(c), zone 4(d), zone 5(e) and zone 6(f) presented in Figure 7-14 and Figure 7-15. Oil was injected from the right to the left side of the core plug.

As more oil was injected, S_w and S_o profiles continued to present this uniform shape with slightly higher values of S_o close to the ceramic disc as illustrated in Figure 7-16(e). ΔP presented a slight increased from 0.47 up to 0.51 ± 0.01 MPa as seen in Figure 7-15(a) between the dotted black and the dotted pink lines. However, $\bar{S}_w$ presented a significant decrease from 0.80 ± 0.005 (zone 4) down to 0.54 ± 0.004 (zone 5) as shown in Figure 7-14. More injection of oil resulted in an abrupt increase

of ΔP from 0.51 (zone 5) to 1.28 ± 0.01 MPa (zone 6) as seen in Figure 7-15(a) between the dotted pink and the dotted yellow lines. At this stage, Q turned from constant to zero as seen in Figure 7-15(b) by the same dotted lines. $\bar{S}_w$ was decreased from 0.54 down to 0.48 ± 0.004. Analysing the S_w profile in Figure 7-16(f), a uniform decrease along the axial position is observed. After 825 min of injection, the presence of oil and brine was equal along the full length of the core, with a slightly higher presence of oil close to the ceramic disc.

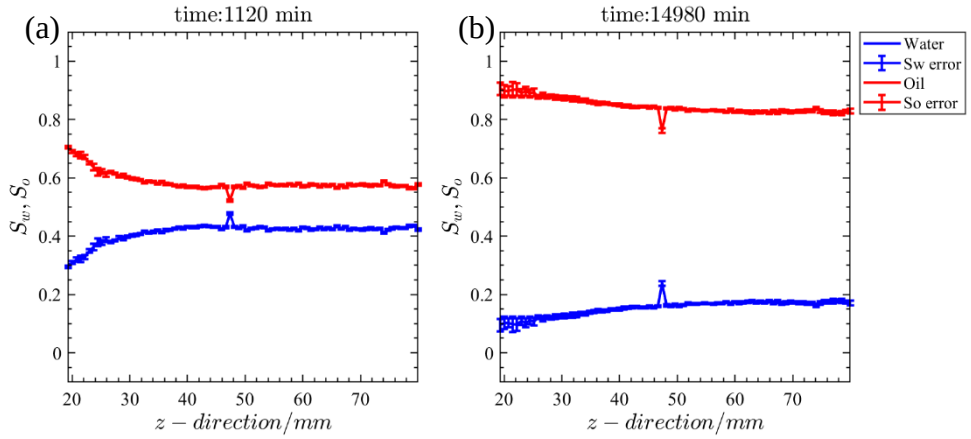

Figure 7-17: 1D spatially resolved relative saturation for the brine (S_w, blue) and the dodecane (S_o, red) related to zone 7(a) and zone 8(b) presented in Figure 7-14. Oil was injected from the right to the left side of the core plug.

Right before zone 6 (822.5 min), ΔP reached the ceramic disc pressure threshold of 1.49 MPa. The injection continues under constant pressure conditions. Figure 7-17 demonstrates that the S_w and S_o profiles related to zone 7(a) and zone 8(b) in Figure 7-14 continue to change following the same uniform profile seen in Figure 7-16(e) and (f). Figure 7-17(a) presents the small increase of S_o close to the ceramic disc. At this stage, $\bar{S}_w$ presented a decrease from 0.48 (zone 6) down to 0.41 ± 0.004 (zone 7). Figure 7-17(b) indicates the S_w and S_o profiles at the end of the imbibition process after 10 d (14,980 min). The uniform S_w is the result of the hydraulic conductivity between the wetting layers along the whole volume of the core plug. At zone 8, the measured $\bar{S}_w$ was defined as the S_{wc} and was equal to 0.15 ± 0.007. This is the lowest S_{wc} ever recorded in laboratory drainage for a dual-porosity carbonate rock.

7.6 Discussion

The 1D CSI sequence employed in this research required 17.5 min. During one acquisition 0.37 mL of oil which is equivalent to 1.6 % of the total P.V. of the rock had been injected. This very small change in the saturation of the system enabled the dynamic monitoring of the process of drainage. Combining Figure 7-14 with Figure 7-15 and Figure 7-16, interesting observations can be made. The S_w and S_o profiles presented in Figure 7-16(a), (b) and (c) suggest that the main mechanism of displacement at this stage was the capillary fingering. The larger values of S_o close to the inlet could be related to the finger growth formed perpendicular to the flow direction as discussed in Section 7.2.3.1. As illustrated from the profiles, brine was trapped as oil was propagated towards the ceramic disc.

As more oil entered the system and more oil channels reached the ceramic disc, a uniform S_w and S_o profile was created as illustrated in Figure 7-16(d). The transition from zone 3 to zone 4 is analysed in Figure 7-18 by presenting the S_w and S_o profiles between these two areas of interest. Gradually declining values of S_w close to the ceramic disc could be related to the growth of small oil fingers in that area. This mechanism of finger growth close to the ceramic disc has been demonstrated by Lenormand et al., (1983) for flow through a 2D duct model with a ceramic disc placed at the outlet. This model showed that fingers close to the area of the obstacle expanded faster than fingers already formed along the main paths of flow. This gives a potential explanation for the slightly higher values of S_o in the area close to the ceramic disc as observed in Figure 7-16(e) and (f). However, the broadness of the spectrum line in parallel with the other artefacts discussed in Section 7.4, adds significant experimental noise to our measurements for that area of the sample.

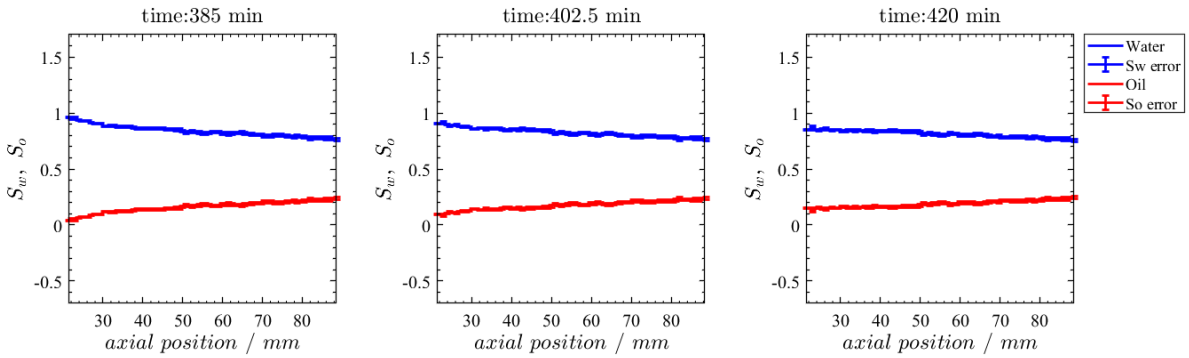

Figure 7-18: Spatial distribution of the relative saturation along the axial direction of the Estaillades rock for the pore-filling mechanism after 385, 402.5 and 420 min of oil injection with flow direction from the right to the left. These periods appear between zone 3 when oil reached the ceramic plate, and zone 4 when a uniform distribution along the core was reached, in Figure 7-14.

The data acquired during the constant pressure regime, therefore between zone 6 and 8, are probably related to the Haines jump mechanism of throat invasion. During this mechanism, oil molecules already injected into the system are moving to regions of lower pressure and therefore towards larger pores and throats located along the fingers already formed. This displacement of the oil molecules will bring a decline in the overall recorded ΔP. Then, a very small quantity of oil should be injected reaching again the ΔP threshold. These continuous displacements and injections are the possible explanation for the fluctuations recorded in the ΔP in Figure 7-14. The hydraulic conductance due to the residual water trapped within the calcite grains was responsible for the uniform S_w along the core and for the continuous production of the wetting phase under the constant pressure regime (Dullien et al., 1986). Due to limited experimental time, the process was stopped after 10 days reaching a S_{wc} of 0.15 which is the lowest value ever recorded in a dual-porosity carbonate rock.

Analysing the recorded ΔP, some extra observations can be made. It is known that P_{cap} describes a single pore-filling phenomenon and in the case of Estaillades core, the P_{cap}- S_w curve presents two stages of invasion as seen in the literature (Blunt, 2017). The first stage of pore-filling is related to the macro-, while the second stage is

related to the micro-porosity. In contrast, the ΔP- S_w curve shown in Figure 7-14 is monotonical, proving that under continuous injection both macro- and micro-pores were invaded. Using ΔP instead of P_{cap} in Eq.(7-1) and assuming that Estaillades is a system of cylindrical capillary bundles, an approximate for the size of the penetrated throat can be made. In the current experiment, σ_τ between water and dodecane can be assumed as 53.7 mN m^{-1} (Goebel and Lunkenheimer, 1997) and θ_R as zero (Demond and Roberts, 1991; Lenormand, 1990).The r_t was found between 0.042 and 0.23 μm for the measurements between zones 1 and 5. This r_t range is within the limits of the micro-pore distribution as mentioned in the literature for several Estaillades samples (Blunt, 2017; Dautriat et al., 2011; Mitchell and Fordham, 2014).

The continuous injection model in the SWPP does not allow the restoration of capillary equilibrium. Therefore, information coming from the macro-pores was lost in the recorded ΔP. However, ΔP seems to derive good estimates for the size of the throats invaded at each stage. At the oil/water contact point (zone 2), ΔP was 0.23 MPa which is related to an r_t of 0.23 μm. Between zone 2 and zone 5, ΔP was almost stable which means that throats between 0.11 and 0.14 μm located in the newly formed fingers were invaded by oil. Even though the SWPP technique cannot be used to obtain a representative pore-throat size distribution for the sample, it can give a good estimate of the size of the smallest throats located along the formed oil channels.

7.7 Conclusion

In this chapter, the SWPP technique was chosen for the primary drainage of an Estaillades core plug to prepare the rock in a real reservoir S_{wc} before the stage of forced imbibition and polymer injection. The dodecane injection was monitored using 1D spatially resolved CSI and the pressure change was recorded along with the injection rate. The aim of this study was to identify the mechanisms of brine displacement from the dodecane phase in a dual-porosity carbonate rock.

The acquired data were treated with the newly developed 'integration' and 'line shape' methods. The 'line shape' method presented a smaller error when the quantity of oil inside the sample was small. When the oil reached the ceramic disc, the 'integration' started to give more accurate results compared to the 'line shape' method. Both methods are suitable for the accurate analysis of 1D spectra and provide similar S_w and S_o profiles. Both techniques were used in the S_w and S_o profile analysis in parallel with the ΔP and Q change with time. Combining these results with the ΔP-$\bar{S}_w$ curve was important for the identification of the displacement pattern. The main key points can be summarised below:

- The S_w and S_o profiles along with the ΔP enabled the allocation of the oil-water contact point. Even though this point could not be observed in ΔP-$\bar{S}_w$ curve since $\bar{S}_w$ did not deviate from one, the S_w and S_o profiles enabled its identification. At the oil-water contact, ΔP was measured as 0.23 MPa.
- The profile analysis between zone 1 and zone 4 was in agreement with the invasion percolation pattern. Brine was trapped in several areas close to the inlet while oil propagated towards the outlet. When the oil reached the ceramic disc, a homogeneous distribution was established.

- Haines jump was identified as the most possible mechanism of pore-filling during the constant pressure injection, explaining the fluctuations in the recorded Q and ΔP and the decrease in the measured $\bar{S}_w$.

The recorded ΔP was proved to give a good estimate for the r_t of the micro-porosity of the Estaillades invaded as each stage. This means that ΔP recorded during the SWPP method of drainage could potentially be used for the assessment of the micro-porosity in an unknown rock sample. This is a useful observation for the determination of the complexity of a system knowing that the SWPP method cannot produce a representative pore-throat distribution.

Finally, a reservoir representative S_{wc} of 0.15 was achieved by switching the injection mode from constant Q to constant pressure. This is the smallest ever recorded S_{wc} in a carbonate rock using the SWPP. The reservoir-representative S_{wc} is very important for the quantification of the oil recovery during the imbibition and the polymer injection experiments presented in Chapter 8.

Chapter 8 Imbibition and Xanthan Gum Injection in the Estaillades Carbonate Rock

8.1 Introduction

Since the early 1960s, chemical EOR techniques were employed after the secondary imbibition step to improve oil production. Polymer flooding is currently considered one of the most promising technologies in EOR due to its commercial and technical feasibility. However, the mechanisms of displacement are still debatable. Simulations (Seybold et al., 2021; Sullivan et al., 2007), as well as flow-through transparent model systems (Demin et al., 2000; Lenormand et al., 1983; Lenormand and Zarcone, 1989), have been implemented for the understanding of the displacement mechanisms. Non-invasive techniques such as NMR (Clarke et al., 2015; Li et al., 2016; Mitchell et al., 2016) and μCT (Celauro et al., 2014; Tapias Hernández and Moreno, 2020; Van Batenburg et al., 2015; X. Wang et al., 2019) have also been used to measure the apparent viscosity and relative saturation after polymer injection through bead packs and sandstones. Nevertheless, most of these data have been acquired under no-flow conditions. These stop-acquire experiments cannot fully describe the mechanisms of displacements, especially in the process of polymer injection since the dynamics of the system are different. In addition, the homogeneous pore structure of bead packs and sandstones cannot fully describe the brine and polymer flow through complex pore structures such as carbonate rocks. More than 60% of the world's oil is trapped in carbonates (Zaeri et al., 2018). One of the aims of DR is to predict multi-phase displacements at the pore-scale and then run flow simulations at the macro-scale (Andersen, 2014). Micro-scale imaging of displacement has been achieved with time-resolved synchrotron μCT. This technique was used to monitor the evolution of drainage and imbibition in a carbonate sample with relatively large pores (>100 μm, Ketton) (Singh et al., 2018).

This chapter employs various NMR techniques to dynamically map the oil displacement during brine and then polymer injection at a macro-scale. Chemically-selective snapshot images, pulse-acquire and CSI experiments in parallel with pressure logging were employed to continuously monitor the brine and xanthan gum flood through Estaillades. Moreover, the chemically-selective APGSTE-RARE sequence developed in Chapter 6 was employed under steady-state conditions for the brine and the polymer flood separately. This is the first time that spatially-resolved propagators of Low-Salinity Brine (LSB) and xanthan gum are obtained and compared. The aim of this study is to identify the pattern of imbibition and the mechanisms of oil displacement during the injection of a biopolymer.

8.2 Theoretical Background

8.2.1 Waterflooding and Oil Recovery

Imbibition is the inverse process of drainage when the wetting phase is entering the pore space displacing the non-wetting phase. Secondary imbibition is the invasion of a pore structure when the wetting phase is already trapped in it in narrow areas such as crevices and roughness. Oil recovery from real reservoirs is a secondary imbibition process since the wetting phase is present in all the depths (Figure 7-3) (Blunt, 2017). Waterflooding is a relatively cheap secondary imbibition process used in oil recovery since seawater is used as the wetting phase. The efficiency of the oil recovery depends on two factors; the macroscopic sweep efficiency described by the M_R and the microscopic sweep efficiency described by the Ca. Figure 8-1 illustrates the difference between these two factors.

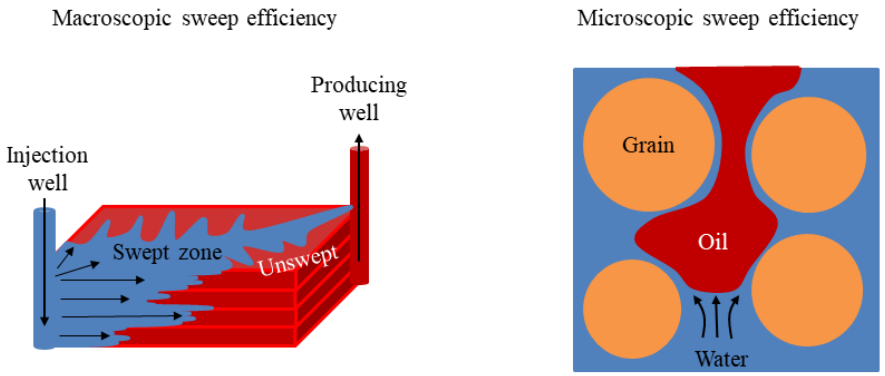

Figure 8-1: Illustration of the macroscopic and the microscopic sweep efficiency during water flooding in a real reservoir. Adapted from Lake, (1989).

The macroscopic sweep efficiency depends mainly on the spatial heterogeneity of the reservoir. Brine flows through the higher permeability channels bypassing oil confined in the lower permeability regions (Shende et al., 2021). The microscopic efficiency depends on the u_D of the injected phase at a distance from the well, the viscosity difference and the σ_τ between the two phases (Muggeridge et al., 2014; Rellegadla et al., 2017).

8.2.2 Pore-Filling Mechanisms in Imbibition

The microscopic efficiency depends on the pore-filling mechanisms. There are two distinct mechanisms to describe the displacement of the non-wetting phase; the snap-off and the piston-like mechanism. An example of how these pore-filling mechanisms act on a water-wet pore-throat is given in Figure 8-2. At very low u_D, the wetting phase advances from pore to throat with piston-like displacement as shown in Figure 8-2(a). When the brine-oil interface (dashed line) meets the large water-wet pore, the brine starts to travel through the wetting layers. The adjacent throat starts to swell and the thickness of the brine layer reaches a r_{crit} which triggers the snap-off mechanism of pore-filling as shown in Figure 8-2(b). At this stage, the oil phase in the large pore is disconnected and remains in the system in the form of a trapped ganglion. The capillary pressure of the oil ganglion remains constant as more brine is injected into the system with the same u_D. These mechanisms have been imaged in a square lattice

network of varying throat sizes (Lenormand et al., 1983) and in a Ketton limestone (Singh et al., 2017).

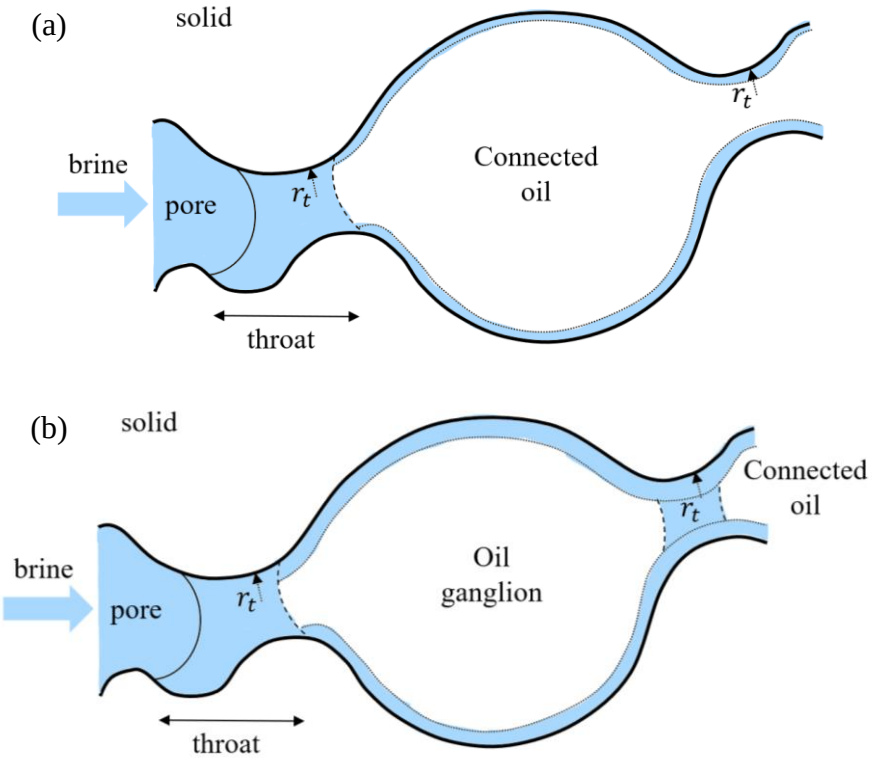

Figure 8-2: An illustration of the pore-filling mechanisms during imbibition at a low capillary number in a water-wet pore-throat system. The brine-oil interface (dashed line) propagates with a piston-line mechanism from the first pore to the throat of similar size (a). Then, the brine flows through the wetting layers of the large pore initiating the swelling of the adjacent throat (b). When the thickness of the layer at the second throat reaches a critical radius, snap-off occurs forming two terminal menisci and trapping the oil under the form of an oil ganglion.

8.2.3 Displacement Patterns of Imbibition at Macro-Scale

There are four generic displacement patterns simulated on a square lattice network of pores and throats as presented in Figure 8-3 (Blunt and Scher, 1995; Chandler et al., 1982; Lenormand and Zarcone, 1984; Vidales et al., 1998). These patterns can be described as:

Cluster growth: At very slow flow rates ($Ca \sim 10^{-9}$), the snap-off mechanism triggers the growth of the wetting layers and patches of water in the form of clusters as shown in Figure 8-3(d). Very little or no trapping of the oil phase is observed.

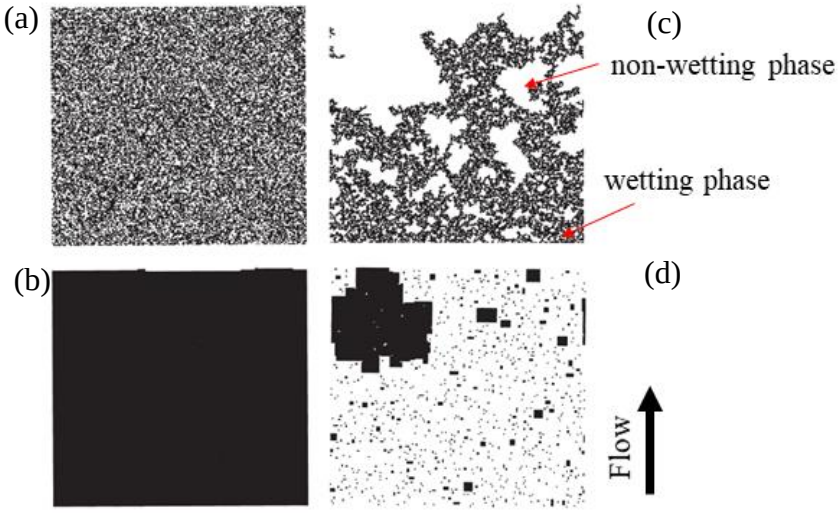

Figure 8-3: Illustration of the four patterns of imbibition resulting after simulation at a 200×200 square network. (a) is the percolation with cluster growth pattern. The injected fluid is represented by the black colour and travels through the crevices triggering the snap-off mechanism. (b) is the flat frontal advance where the fluid advances as a uniform front. (c) is the invasion percolation pattern where only the connected pores are filled and there is no crevice flow. (d) is the cluster growth mechanism where the wetting phase travels through the layers allowing pores and throats to be filled anywhere. The largest clusters will continue to grow filling the whole system. Reproduced from Blunt and Scher, (1995).

Percolation with trapping: At a slightly higher flow rate ($Ca \sim 10^{-7}$), the snap-off mechanism is again triggering the filling process. More precisely, the injected fluid invades the pores with a piston-like mechanism but it also moves through the connected wetting layers triggering the snap-off phenomenon as presented in Figure 8-2. The process is called percolation and significant trapping of the oil phase is observed. The oil phase can escape if it has access to a connected pathway to the outlet. Figure 8-3(a) shows the pattern of a dendritic front with discontinuous clusters. This pattern is deliberately seen in real reservoir settings.

Invasion percolation with trapping: Increasing further the flow rate ($Ca \sim 10^{-5}$) and considering that there is no connectivity among the wetting layers, the water phase advances across the system with a piston-like mechanism. Figure 8-3(c) illustrates that in invasion percolation the oil phase is trapped among the wetting fingers creating a fractal pattern.

Frontal advance: Further increase in the flow rate ($Ca \sim 10^{-4}$) leads to a frontal advance pattern as presented in Figure 8-3(b). The injected phase advances with piston-like filling from the inlet to the outlet establishing a uniform front. Therefore, no trapping of the oil phase is observed.

Trapping is controlled by both the pore-throat structure and the wettability of the reservoir resulting in poor efficiency of the oil recovery (Gao et al., 2021). In water-wet reservoirs, waterfloods lead to an approximate recovery of 40% of the OOIP since the largest portion of the oil is trapped under capillary effects (Haugen et al., 2014).

8.2.4 Mechanical Behaviour of Polymers in EOR

To increase the oil extraction, waterflooding is followed by a tertiary recovery stage known as EOR. This research focuses on the chemical EOR and in particularly in the polymer injection. More information regarding the different EOR methods (Gbadamosi et al., 2019; Rellegadla et al., 2017; Terry, 2001) and the criteria for the polymer selection can be found in the literature (Mohamid et al., 2015; Rellegadla et al., 2017). The most common polymers used in oil field applications are hydrolysed polyacrylamides (HPAM) and xanthan gums (Al-Shakry et al., 2019). This research focuses on the use of xanthan gum. To better understand the mechanisms of displacement, it is important to analyse the mechanical behaviour of this biopolymer. The shear and elongational stresses exerted on the molecule during its flow, influence the apparent viscosity, μ_{app}, of the aqueous solution.

Xanthan gum is a semi-flexible polymer with less-known characteristics. In an aqueous solution at rest, xanthan gum presents a semi-rigid molecular structure as illustrated in Figure 8-4. Hydrogen and ionic bonds are formed among the rigid rods, while a ratio of entanglement between the macromolecules is also expected. These intermolecular bonds are easier to break than the intramolecular associations of the random coil-conformation of the HPAM. Hence, xanthan gum solutions are easier to flow compared to HPAM. At low shear rates, $\dot{\gamma}$, the initial bonds and entanglements are fractured and get replaced by new intermolecular bonds among the aligned rigid rods (dotted red lines). At this stage, there is no reduction in the μ_{app} since the number of fractured bonds is equal to the number of newly formed bonds and the polymer exhibits Newtonian behaviour. The 'onset' of the power-law (shear-thinning) regime occurs when the externally imposed movement becomes faster than the rate of formation of new entanglements and molecules start to slide over each other. Xanthan gum has presented an extension-thickening behaviour when flowing through a core under high $\dot{\gamma}$. This thickening behaviour has been related to the generation of new transient entanglements due to the continuous expansions and contractions and the presence of stagnation points. The onset $\dot{\gamma}$ is decreased as the polymer concentration is increased (González et al., 2005; Morris et al., 1981; Urlacher and Noble, 1997). Xanthan gum is less sensitive to salinity changes compared to HPAM (Kohler and Chauveteau, 1981). High salinity decreases its viscosity mainly in the Newtonian regime (Martel et al., 1998).

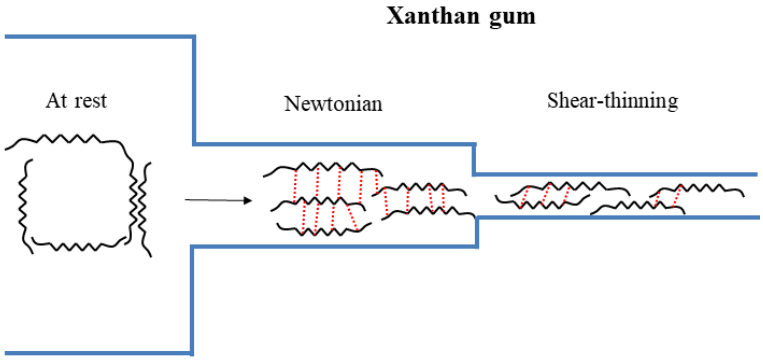

Figure 8-4: Schematical representation of the xanthan gum macromolecules at rest and when flowing through a narrow throat under the effect of shear stress. The red dotted lines represent the intermolecular interactions and the black dots the associations. Adapted from Zaitoun et al., (2012) and Urlacher and Noble, (1997).

8.2.5 Mechanisms of Oil Displacement in Polymer Flooding

Polymer injection enhances the oil mobility through a combination of mechanisms which were first summarised by Wei et al., (2014) and Gbadamosi et al., (2019). The two most important mechanisms of displacement can be summarised as:

Mobility control: In simple waterflooding, brine is usually less viscous, hence more mobile than oil, $M_R > 1$, creating a pattern of viscous fingering towards the production well. This fingering effect leaves regions of unswept oil as shown in Figure 8-5(a) (Abidin et al., 2012; Homsy, 1987). When a polymer is dissolved in the injected phase, the μ_D is increased. Therefore $M_R \leq 1$, resulting in a stable front of injected phase as presented in Figure 8-5(b).

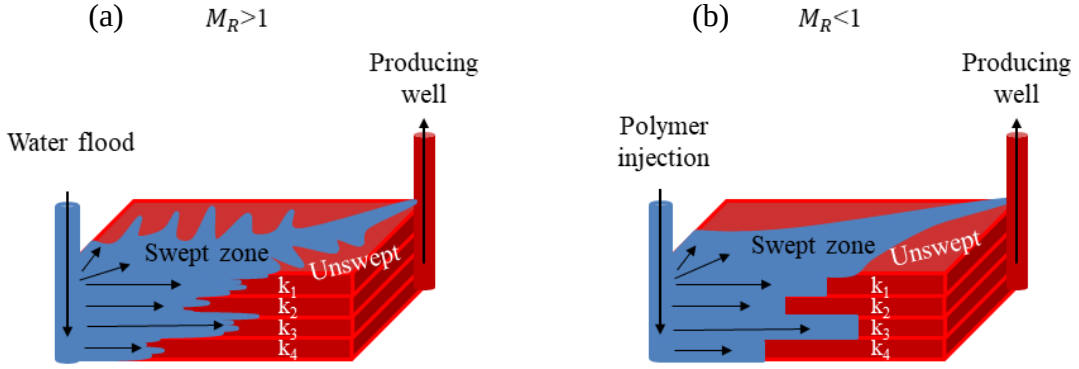

Figure 8-5: Illustration of the macroscopic sweep efficiency when viscous fingering occurs for M_R>1(a) and when the piston-like mechanism is employed for M_R<1(b). Adapted from Lake, (1989) and Gbadamosi et al., (2019).

Disproportionate Permeability Reduction (DPR): The spatial heterogeneity met in real reservoirs is expressed by regions of different porosity and permeability. For simplicity, this spatial heterogeneity is illustrated by four layers of different k_1, k_2, k_3 and k_4 as shown in Figure 8-5. In waterflooding, the brine will flow faster through the higher permeability layers such as k_1 and k_3 until it reaches the production well. As more brine is injected, it follows the already formed paths towards the production well. Consequently, oil remains trapped in the low permeability regions of k_2 and k_4.

When polymer is injected into the reservoir, it initially invades the high permeability zones previously swept by the brine phase. Polymeric molecules are retained in the pore wall reducing the k_r. There are three types of polymer retention; polymer adsorption on the grain surface (Mishra et al., 2014), mechanical entrapment in narrow throats and hydrodynamic retention in stagnant zones (Agi et al., 2018). The newly injected brine after the polymer retention is diverted to other unswept areas resulting in oil production.

Having analysed the displacement patterns and the mechanical behaviour of the polymeric molecules, imbibition and xanthan gum injection through the Estaillades rock after the primary drainage step is studied. Chemically-selective images and 3D spatially-resolved propagators in parallel with pressure monitoring have been employed to visually and quantitatively analyse these mechanisms.

8.3 Materials and Methods

8.3.1 Materials and Chemicals

The Estaillades core and the LSB used in this EOR study have been described in Chapter 7. Following primary drainage, 87 ± 2% of the core was filled with dodecane and 13 ± 2% was filled with brine. The xanthan gum (Sigma LifeScience, from Xanthomonas campestris) powder was dissolved in the LSB with mechanical stirring for 48 h at a concentration of 3000 mg/L at 20 ºC. The solution was then filtered through a 3 μm and subsequently through a 1.2 μm filter (Millipore) (Mahani et al., 2017). Out of this high in concentration solution, eight samples of varying concentrations were prepared. The rheological behaviour of these samples was analysed and the optimum concentration for the current system was picked. Then, a large portion of the polymeric solution was prepared and its pH was calibrated at ~ 8.3 by adding a buffer of diethanolamine (provided by STCH) to avoid any dissolution of the carbonate rock (Mahani et al., 2015).

8.3.2 EOR Polymer Concentration

8.3.2.1 Method for Defining the Optimum Polymer Concentration

To choose the optimum xanthan gum concentration, a better understanding of the range of $\dot{\gamma}$ exerted during flow through the pore-throat system of the rock is necessary. For that purpose, a profile of laminar Newtonian flow within a throat of cylindrical shape is assumed. Therefore, the velocity profile is expected to be parabolic, having the maximum velocity along the axis and zero velocity at the pore wall (Lovell, 1989). The effective maximum shear rate, $\dot{\gamma}_{eff,max}$, is met at the pore wall and depends on the A_c, the average pore diameter, $2r_p$, and the amount of liquid, V, at time t according to:

$$\dot{\gamma}_{eff,max} = \frac{4}{A_c\, r_p}\,\frac{V}{t}. \tag{8-1}$$

The amount of liquid V at time t that passes through the cylindrical throat is equal Q. The Darcy velocity is also written as:

$$u_D = \frac{Q}{\phi A_c}. \quad (8\text{-}2)$$

According to the capillary bundle approach, the rock is simulated as a sum of capillary tubes of varying diameters. After Eq.(8-1) and Eq.(8-2):

$$\dot{\gamma}_{app,max} = \frac{4\,u_D}{r_p}. \quad (8\text{-}3)$$

The pore structure in a carbonate rock is very heterogeneous, hence u_D presents spatial variation. More precisely, the difference between the r_t and the r_p has an impact on the particle acceleration which is different in each porous system. Knowing the expected u_D met in the system, we can define a range of expected $\dot{\gamma}$ for the flow inside a rock. Xanthan gum is a non-Newtonian fluid, hence its viscosity changes with $\dot{\gamma}$ following the fully developed Carreau model given by:

$$\mu_{app}(\dot{\gamma}) = \mu_{inf} + (\mu_0 - \mu_{inf})[1 + (\lambda\,\dot{\gamma})^{\alpha}]^{\frac{n_1-1}{\alpha}}, \quad (8\text{-}4)$$

where μ_{inf} is the Newtonian viscosity at an infinite shear rate and is usually defined as 1 cP, μ_0 Newtonian viscosity at zero shear rate, n_1 and a are the fitting constants, $1/\lambda$ is the critical shear rate which defines the onset from Newtonian to power-law rheological behaviour. Knowing that an μ_{app} of ~10 cP inside the rock is desired, the optimum concentration is defined based on the rheological behaviour of the solution and the $\dot{\gamma}_{app,max}$ inside the pore structure.

8.3.2.2 Optimum Polymer Concentration

The xanthan gum solutions of different concentrations were subjected to a range of $\dot{\gamma}$ between 500 s^{-1} and 0.1 s^{-1} in a controlled strain rheometer (Rheometric Scientific ARES 320). This range of $\dot{\gamma}$ is representative of field conditions. The chosen concentrations were 300 ± 10, 600 ± 10, 900 ± 10, 1200 ± 10, 1500 ± 10, 1800 ± 10, 2100 ± 10 and 3000 ± 10 mg l^{-1}. The rheological behaviour of these solutions at 20°C is illustrated in Figure 8-6.

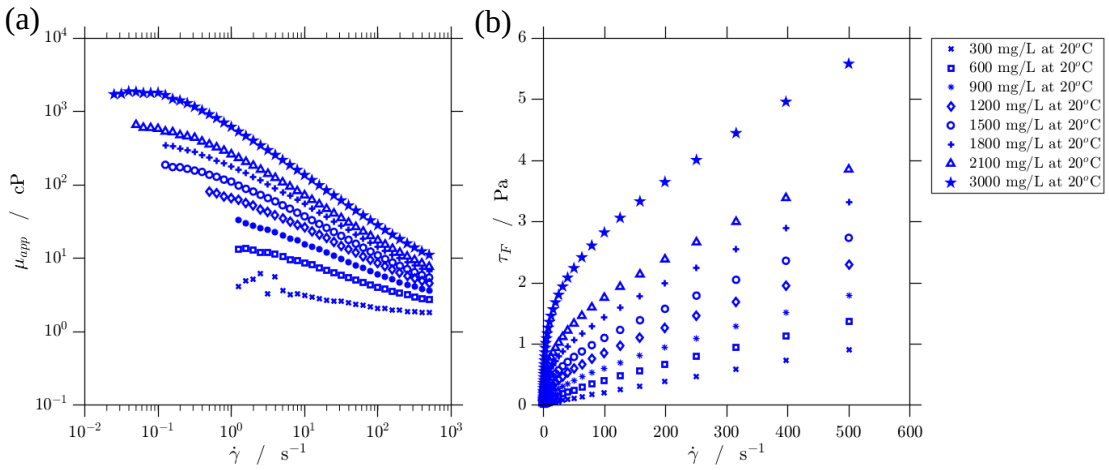

Figure 8-6: The effect of shear rate, $\dot{\gamma}$, on the apparent viscosity ,μ_{app}, (a) and on shear stress (b) of xanthan polymer solutions prepared to different concentrations in low-salinity brine.

It can be observed that at higher concentrations, the 'onset' of the shear-thinning regime occurs at lower $\dot{\gamma}$. The particle acceleration inside the Estaillades rock can lead to a u_{max} of 384 ft d^{-1} as proven by simulation (Zamani et al., 2017). Since the r_t distribution for most Estaillades rocks studied in the literature present a large peak around 10 µm and a smaller peak around 0.2 µm (Dautriat et al., 2011; Mitchell and Fordham, 2014), $\dot{\gamma}_{app,max}$ was estimated between 2.8 s^{-1} and 1,092 s^{-1} in the large throats and between 113 s^{-1} and 43,688 s^{-1} in the smaller throats. Since the rheometer reaches a maximum $\dot{\gamma}$ of 500 s^{-1}, the rheological behaviour of the fluid inside the porous medium cannot fully be described. Figure 8-6 shows that at 500 s^{-1} only the solution with a concentration of 3000 ± 10 mg l^{-1} is above 10 cP. This was chosen as the optimum concentration for the current experiment. Figure 8-7 shows the Carreau model fit (Eq.(8-4)) for the chosen xanthan gum solution.

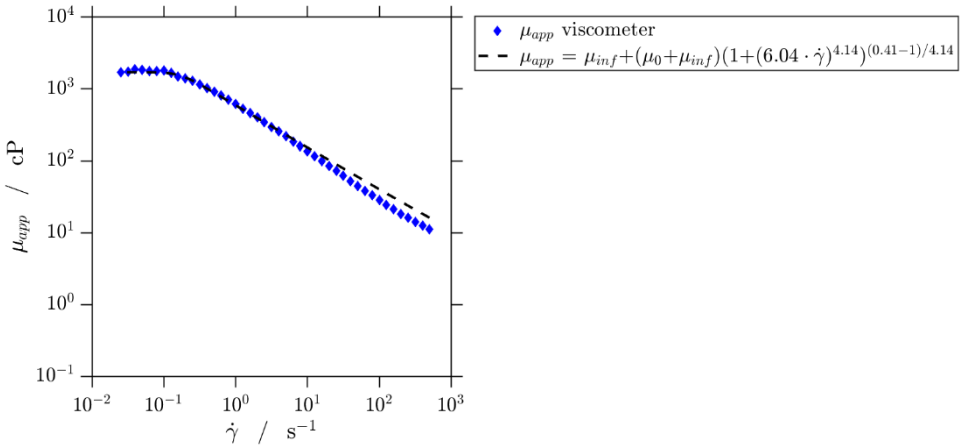

Figure 8-7:Fully developed Carreau model for xanthan gum polymer prepared to a concentration of 3 g L^{-1} at 20 ºC in low-salinity brine of 3.0 ± 0.1 g NaCl l^{-1}.

8.3.3 Methods

8.3.3.1 Core Flooding and NMR Protocol for Imbibition and Polymer Injection

The core flood was conducted using a different flooding system. A syringe pump (Quizix QX-1500HC dual-cylinder syringe pump, Chandler Engineering, Oklahoma, USA) and pressurised-air accumulator were employed as illustrated in Figure 8-8. The ceramic disc was detached from the RCH. The rock was placed back in the RCH and was confined under a pressure of 6.3 MPa. LSB was stored in a beaker and the polymeric solution in the accumulator under pressure. The cylindrical tube between the pump and the RCH had a 30.3 m length and 1/16″ (1.6 mm) inner diameter. ΔP_1 was the pressure drop across the inlet tube. Then, brine and subsequently polymer were injected at different flow rates. The P_{inj} was monitored using the pump in-built Sensata pressure transducer of this syringe pump.

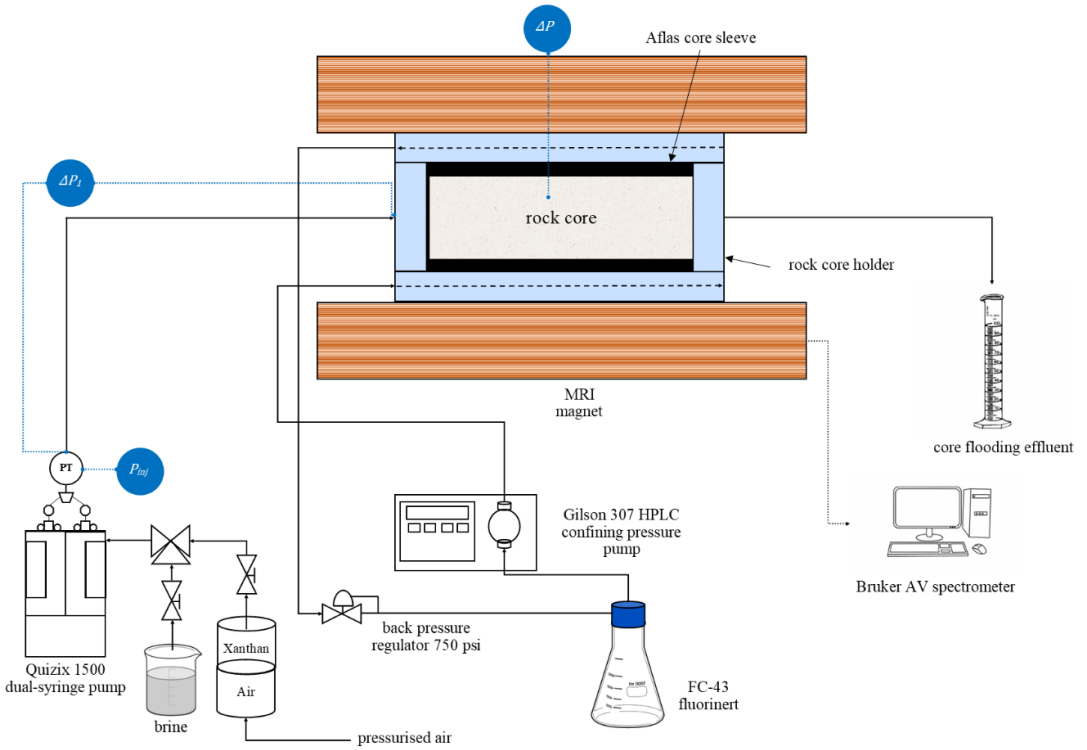

Figure 8-8: Schematic representation of the CFS set-up used during the imbibition and the polymer injection. Xanthan gum (polymer) was stored in an accumulator and was pushed out using compressed air, while the brine was stored in a beaker.

The imbibition and polymer injection in parallel with the NMR techniques employed in this chapter were as follows:

1. *Secondary imbibition*: The Estaillades rock reached an S_{wir} of 0.15 at the end of primary drainage. The ceramic disc was detached and the sample was confined in the same RCH. Then, 3 g l^{-1} NaCl/H_2O brine was injected at 0.15 ft d^{-1} (0.011 mL min^{-1}) until a quantity equal to 2.1 P.V. filled the system. The effluent was collected in a volumetric cylinder and the process was monitored in-situ using chemically selective spectra and snapshot imaging.
2. *1st brine injection*: Then brine was initially injected at 8.4 ft d^{-1} (0.6 mL min^{-1}) to remove the oil ganglia trapped in the system and the process was monitored

with bulk spectra for ~ 30 min. Then velocity was increased even up to 15 ft d^{-1} and no further recovery of oil was seen. 3D spatially-resolved propagators with CS for the oil and the water phase were acquired at 1 ft d^{-1}.

3. *1st polymer injection*: the viscous solution was injected into the core at 0.15 ft d^{-1}. The process was monitored with chemically selective spectra and snapshot images.
4. *2nd polymer injection*: xanthan gum was injected at 1 ft d^{-1} (0.071mL min^{-1}). This process was initially monitored with chemically selective spectra and snap-shot images and then with 3D chemically-selective propagators.
5. *2nd brine injection*: LSB was injected at a velocity of 3 ft d^{-1} (0.21 mL min^{-1}). The dynamic stage of displacement was monitored with 1D CSI and the steady-state with 3D chemically-selective propagators.
6. *3rd polymer injection*: xanthan gum was injected at 3 ft d^{-1}. 1D CSI and 3D chemically selective propagators were acquired.
7. *3rd brine injection*: LSB was injected at 6 ft d^{-1}. The dynamic stage was monitored with chemically-selective spectra and when there was no further removal of oil spatially and chemically-resolved propagators were obtained.
8. *4th polymer injection*: xanthan gum solution was injected at 6 ft d^{-1} and the dynamic stage was monitored with 1D CSI. The propagator acquisition was interrupted due to plugging which caused an abrupt increase in the pressure.

Step 2 aimed to remove the trapped oil ganglia by changing abruptly the ΔP. Consequently, we could study only the effect of the DPR mechanism on oil displacement. All the steps are summarised in Figure 8-9.

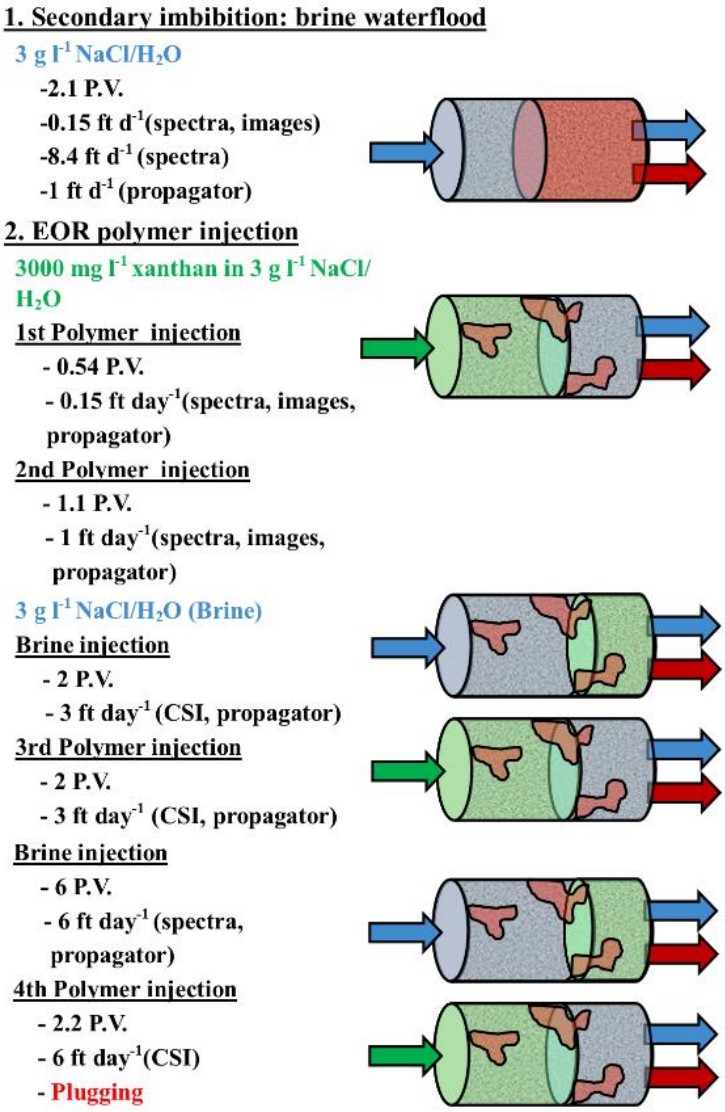

Figure 8-9: Schematic illustration of the EOR core-flooding and the NMR protocol.

8.3.3.2 Pressure Drop Along the Inlet Line in the CFS system

Knowing the r_{tube}, the u_D for each externally applied Q can be estimated. Using Eq.(8-3), the $\dot{\gamma}$ profile along the tube can be measured. Then, the μ_{app} profile is calculated using the Carreau model. According to the average viscosity approach (Eberhard et al., 2019), the mean value of the μ_{app} profile is a good approximate for the μ_{eff} of the polymer. ΔP_1 was calculated using Poiseuille law (Eq.(7-9)). Subtracting this value from the recorded P_{inj}, an estimate of ΔP across the rock was defined.

8.3.3.3 Operational Errors in Core Flooding

Following the primary drainage step, the RCH was opened to the air and the ceramic disc was removed from the system. At the same time, the CFS was changed to the system described in Section 8.3.3.1. The inlet lines of the RCH were filled with brine to limit the trapped air and the rock was confined again in the RCH without the ceramic disc. Then two chemically-selective snapshot images were obtained and the bulk S_w and S_o were measured as 0.18 ± 0.01 and 0.82 ± 0.01. These values deviated

from the 0.12 ± 0.02 and 0.88 ± 0.02, respectively, measured at the final stage of drainage, as shown in Figure 8-10(a). Analysis of the S_w and S_o profiles in Figure 8-10(b) demonstrates a decline in the S_o on the right side (inlet). This proves that brine from the inlet tubing invaded the inlet of the RCH. Moreover, a decline in the S_o on the left side indicates that an amount of oil close to the outlet was removed when the confining pressure was applied to the rock due to pressure change.

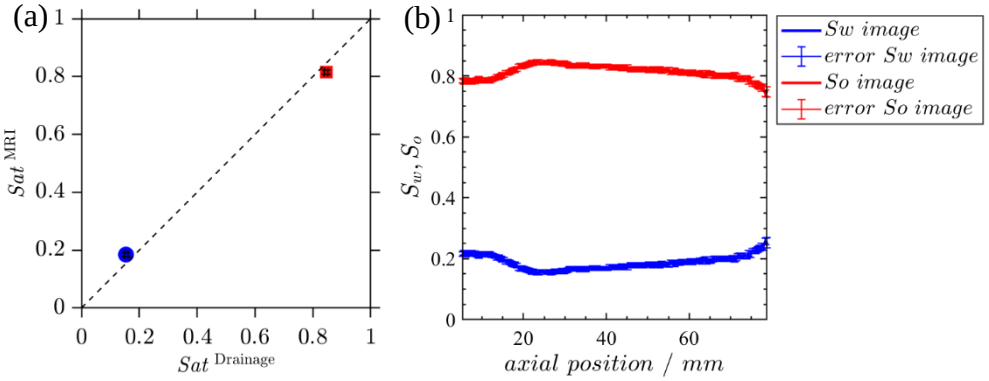

Figure 8-10: Comparison of the relative saturation of the dodecane S_o (red square) and the water S_w (blue circles) coming from the first chemically-selective MRI images with 437.5 µm pixel^{-1} resolution at the beginning of imbibition and the final 1D CSI experiment of drainage(a). The result of the MRI images is further analysed by projecting the profile of S_w and S_o where the inlet is on the right side and the outlet on the left side(b).

These operational errors due to the change of the CFS and the detachment of the ceramic disc do not impact the monitoring of the saturation during the imbibition and polymer injection processes. They are accounted as the initial state of the core plug for the measurement of the total oil recovery.

8.3.3.4 NMR Experimental Parameters

The imbibition was monitored with a reference spectrum and two chemically-selective spectra. The t_{RD} was 3 s and the 90º pulse 40.7 µs. A full phase cycle required 8 averages and 2 dummy scans were also employed. The flip angles for the selective pulses were manually calibrated as 68º, 84.7º, 91.8º and 103º for a duration of 8192 µs. The duration of δ_h and τ_h were calibrated as 3 ms and 1 ms, respectively. 3D RARE images were acquired for a FOV of 84 mm in the $\mathbf{k}_{read}$ dimension and 42 mm in both $\mathbf{k}_{phase}$ dimensions. The under-sampling rate was 25% for N_{echo} equal to 32. The N_{read} was 192 and the N_{phase1}, N_{phase2} were 96 giving an isotropic spatial resolution of 437.5 µm pixel^{-1}. The t_{RD} was 3 s using 4 scans and 2 dummy scans. The pulse-acquire experiments employed during the increase of the brine flow rate used a 90º pulse of 40.7 µs, 4 scans and a t_{RD} of 3 s.

In the polymer injection, the dynamic and the steady-state (no oil was recovered) stages were monitored with different NMR experiments. During the dynamic stage, the spectra and the chemically-selective images were acquired with the same parameters as in the imbibition process and the results are presented in Section 8.4.3. The 1D CSI experiments were acquired with a t_{RD} of 3 s and a δ_G of 0.18 ms and it was ramped to a maximum of 95% g_{max} in 128 evenly distributed increments. The FOV was 84 mm with a resolution of 656.3 µm pixel^{-1} along the z-direction and δ_2 was 1.7 ms. The acquisition time of one CSI experiment for 4 averages was 28 min.

The 3D propagators obtained during the steady-state stage are presented in Sections 8.4.5 and 0. They were acquired with the same suppression scheme as the one used for the snapshot images. For all propagators, the duration of the homospoil during the t_{store} time interval was 10 ms while its amplitude was set at 30% of the g_{max}. A gradient stabilisation delay of 2 ms was placed before and after the homospoil. The FOV along the three dimensions was maintained the same as in the images while the N_{read} was chosen as 96 and the N_{phase1}, N_{phase2} were 48 giving an isotropic spatial resolution of 875 μm pixel^{-1}. The 90º pulses were 41.9 μs, 180º pulses 83.4 μs, the N_{echo} 32 and the under-sampling rate was 23%. Two dummy scans and 8 averages were employed for a total acquisition time of ~18 h. The oil, brine and polymer propagators at 1 ft d^{-1} were acquired with a t_{RD} of 5.5 s, a Δ of 1100 ms and a δ_G of 1.1 ms. A total of 33 **q**-points were sampled by applying flow encoding gradients between - 9.2 ×10^{-2} and 9.2 ×10^{-2} Tm^{-1} (86% of g_{max}) in equidistant steps. The brine and polymer propagators at 3 ft d^{-1} were acquired with a t_{RD} of 4.5 s, a Δ of 600 ms and a δ_G of 1.8 ms for a total of 49 **q**-points with the same amplitude. The brine propagator at 6 ft d^{-1} was acquired with a t_{RD} of 5.5 s, a Δ of 500 ms and a δ_G of 2.4 ms for a total of 87 **q**-points with the same amplitude. The same mask was applied to all the propagator data.

8.4 Results

8.4.1 Dynamic Monitoring of the Imbibition

The process of imbibition was monitored with spectra and snapshot images while brine was injected at 0.011 mL min^{-1}. Each image required 16 min, so there is an increase in the brine volume by 0.18 mL between the consecutive images. This increase in the brine volume was taken into account for the error analysis of the S_w and S_o. The error analysis for the pulse acquire experiments with chemical selection is described in Section 6.4.4 and for the CS-RARE images in Section 6.4.5. Seven stages during the imbibition process were picked and are presented in Figure 8-11. More precisely, Figure 8-11 shows the time evolution of the imbition process in parallel with the images and the S_w and S_o profiles.

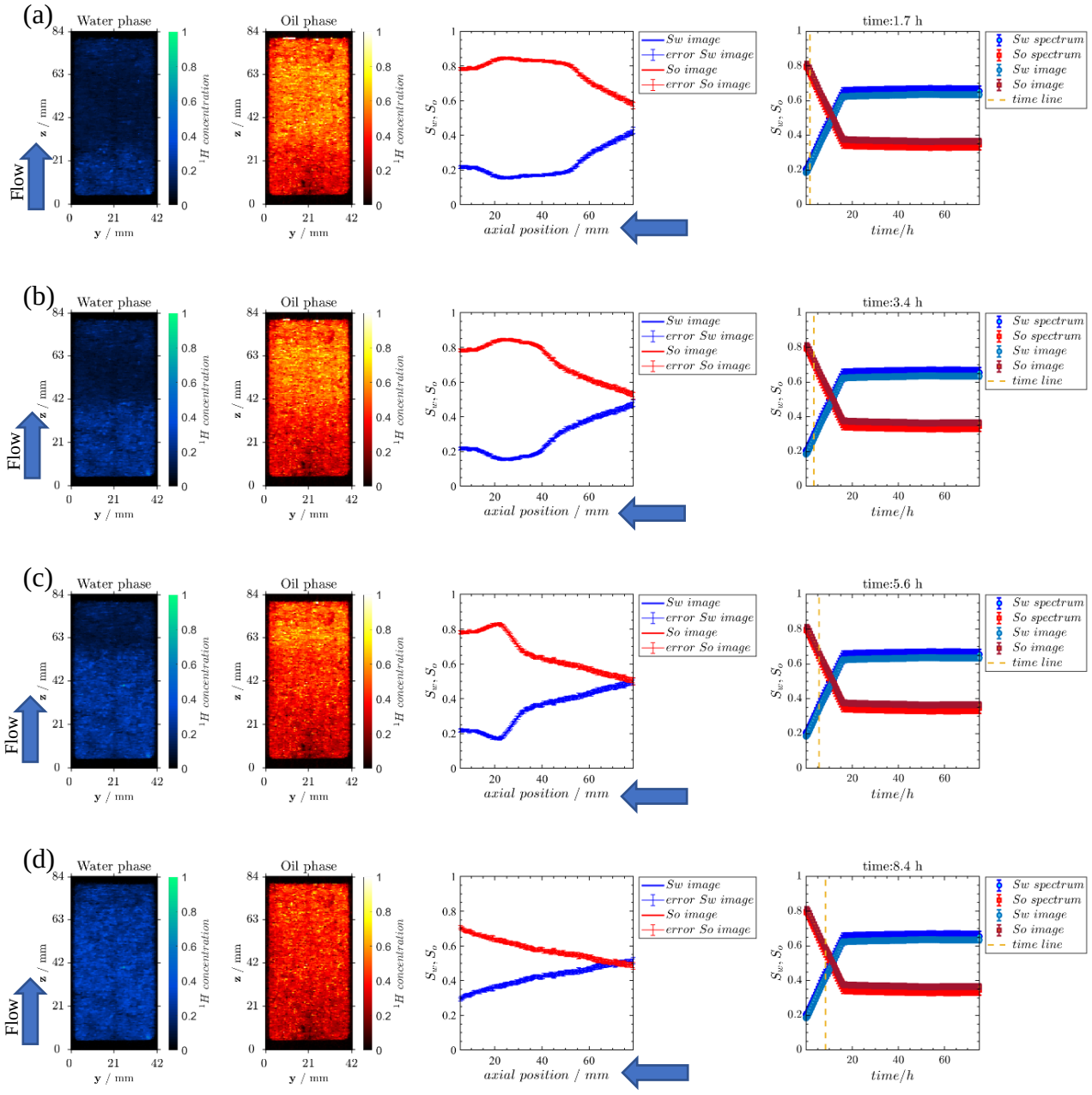

Figure 8-11: 2D slices coming from the 3D CS-RARE images with chemical selection in parallel with the profile of S_w and S_o along the flow direction and the mean values of S_w and S_o coming the whole images (light blue for brine and dark red for oil) and from the chemically-selective spectra (blue for brine and red for oil) along with the time of brine injection. The time for the acquisition of each set of experiments is demonstrated by the dashed yellow line and the results obtained after 1.7(a), 3.4(b), 5.6(c), 8.4 h(d) of injection are shown. The flow direction in images is from bottom to top and in the S_w and S_o profiles from the right side to the left.

Better visualisation of the displacement pattern is given by 3D images in Figure 8-12. The 3D images were treated with Avizo 9.5.0 (FEI Visualisation Sciences Group, USA). The mechanism of displacement presents similarities with the mechanism of invasion percolation with cluster growth demonstrated by Lenormand and Zarcone, (1984). As the brine propagates along the core a dendritic front seems to be formed. creating discontinuous areas at the lateral edges (clusters). However, more statistical analysis which is out of the scope of this thesis is required to support this theory.

After 5.6 h of injection, the S_o profile decreased in the middle area from ~ 0.83 down to ~ 0.62 as shown in Figure 8-11(c). At the same time a small change at the inlet from ~ 0.55 down to ~ 0.51 was recorded. This change at the inlet is an indication of new flow paths formed due to snap-off events while brine was injected. The brine reached the outlet of the core in Figure 8-11(d). When the first brine flow paths reached the outlet, large portions of oil were either unswept or trapped along the flow direction as illustrated in Figure 8-12(d).

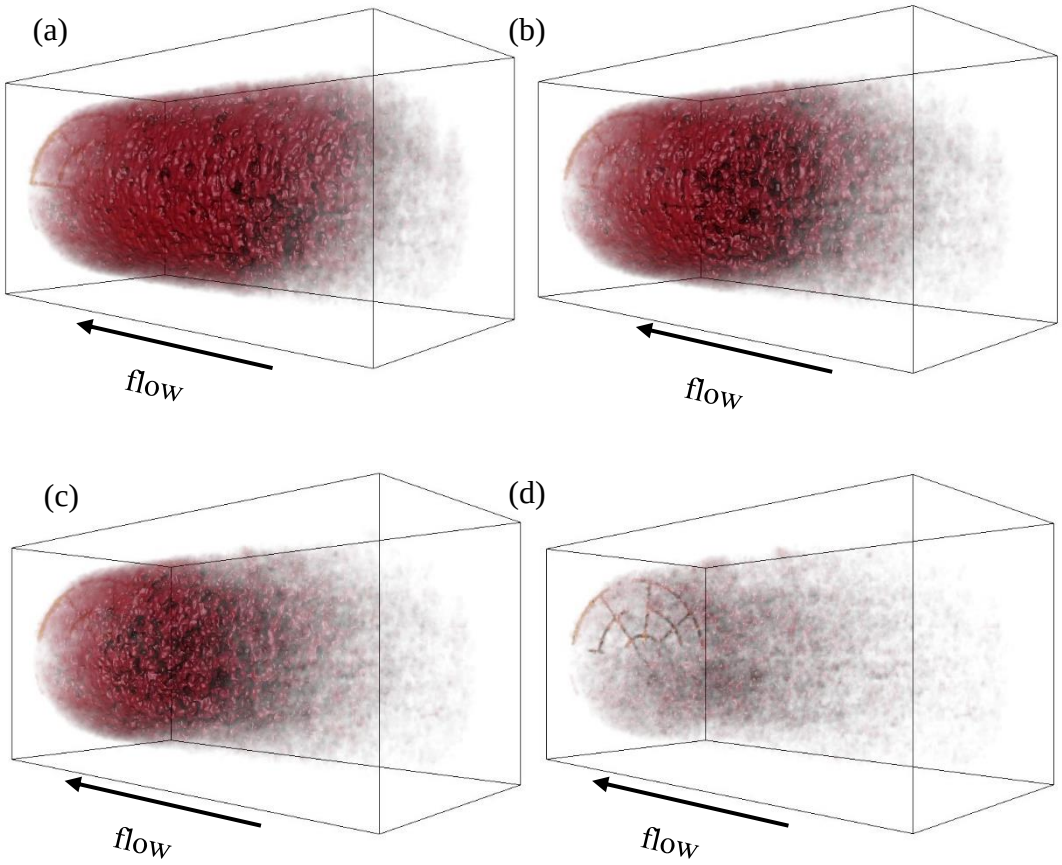

Figure 8-12: 3D reconstructed images of the oil phase for the imbibition process after 1.7(a), 3.4(b), 5.6(c), 8.4 h(d) of brine injection at 0.15 ft d^{-1}. Each (a), (b), (c) and (d) 3D image is associated to the (a), (b), (c) and (d) time evolution of Figure 8-11. The red area represents the oil phase which is decreased as more water is injected following the direction indicated by the arrow. The water phase is located at the transparent area of the ROI. The black areas comes from the 3D shadowing effect created in Avizo 9.5.0 and they do not have any physical meaning. The red ring seen at the outlet-end of the sample was due to oil trapped at the formation of the adjustable platen.

As more brine was injected into the system, oil was produced in parallel with brine. In Figure 8-13(a), the mean S_w was equal to the mean S_o. However, the water oil concentration close to the outlet was higher. As more brine was injected into the system, new flow paths were created displacing the previously bypassed oil. The S_o profile presented a larger decrease in the middle and the outlet area as illustrated in Figure 8-13(b). The swept zone continued to expand as more brine was injected until a steady-state was reached in Figure 8-13(c). After this stage, there was no more oil production and only brine was collected at the effluent. Brine injection continued for 58.8 h and the final S_w and S_o were compared with the volumetric measurements of the effluent in Figure 8-14 presenting a great agreement. During the secondary imbibition in Estaillades, 55.2% of the OOIP was recovered.

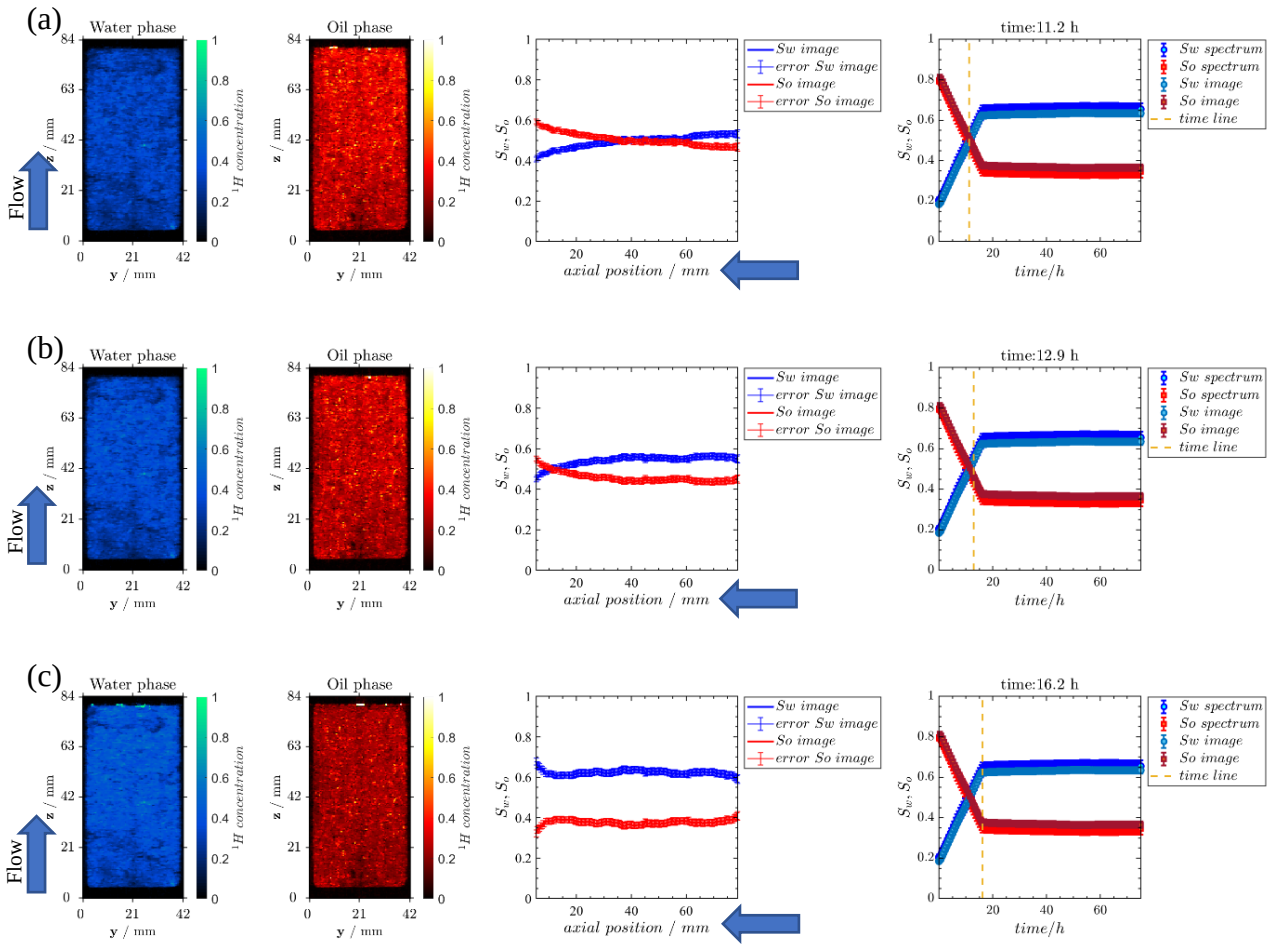

Figure 8-13: 2D slices coming from the 3D CS-RARE images with chemical selection in parallel with the profile of S_w and S_o along the flow direction and the mean values of S_w and S_o coming the whole images (light blue for brine and dark red for oil) and from the chemically-selective spectra (blue for brine and red for oil) along with the time of brine injection. The time for the acquisition of each set of experiments is demonstrated by the dashed yellow line and the results obtained after 11.2(a), 12.9(b) and 16.2 h(c) of injection are shown. The flow direction in images is from bottom to top and in the S_w and S_o profiles from the right side to the left.

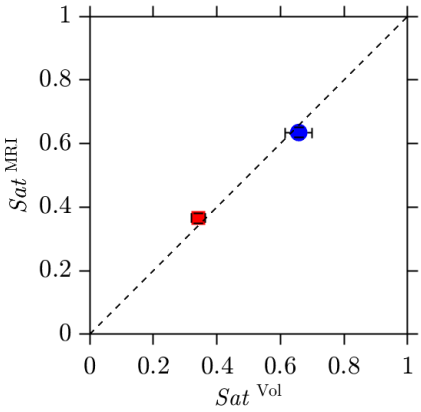

Figure 8-14: Comparison of the MRI and the volumetric determination of the relative saturation of the dodecane S_o (red square) and the water S_w (blue circles) from the 3D CS- images acquired with the four pulses WET RARE experiment.

8.4.2 Removal of the Oil Ganglia

Removal of the oil ganglia was important since Chapter 8 focuses on the study of the DPR mechanism. Increasing the velocity from 0.15 up to 8.4 ft d^{-1}, an abrupt increase in the ΔP led to an abrupt change in S_w. This abrupt change was monitored with multiple spectra for 30 min. Oil was displaced in less than 22 s after the initiation of the pump without allowing the spectra to map dynamically this change. More precise, S_o was decreased from 0.37 ± 0.02 down to 0.33 ± 0.01 after the pump initiation and no further change in S_o was observed for the rest of the acquisition as shown in Figure 8-15.

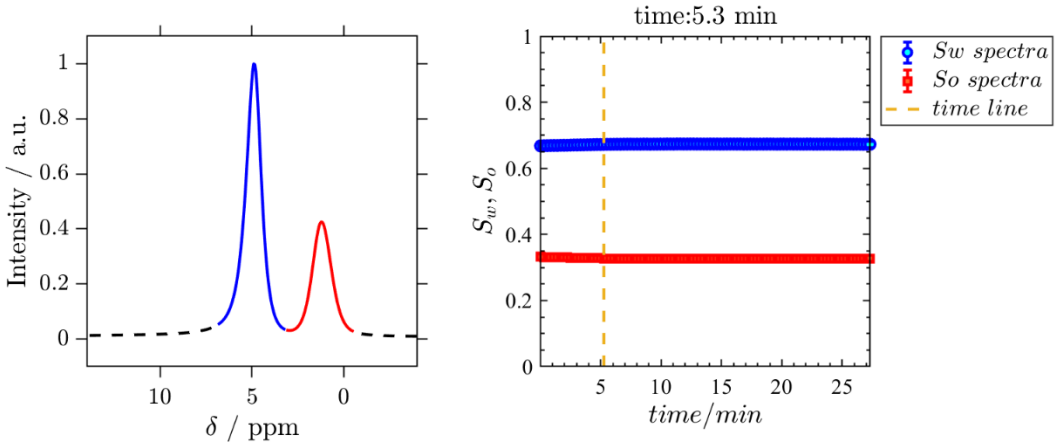

Figure 8-15: Spectrum and optimum areas of integration for the brine (blue) and the oil (red) phase after 5.3 min of brine injection at 8.4 ft d^{-1} in parallel with the S_w and S_o change during 30 min of injection at the same flow rate.

8.4.3 Dynamic Monitoring of Polymer and Brine Injections

Xanthan gum was initially injected at 0.15 ft d^{-1}, the same velocity used in the imbibition process. Even though, M_R was decreased due to an increase in μ_D, no more oil was displaced. The S_o before the injection was 0.33 ± 0.02 and after the injection was 0.32 ± 0.02. Figure 8-16 presents the S_w and S_o profiles coming from the image

after 7.7 h of polymer injection in parallel with the time evolution of the bulk S_w and S_o and the measured ΔP per injected quantity of polymer measured in P.V.. The data acquisition was interrupted after 7.7 h due to coil overheating while the polymer injection continued for 27.7 h until 0.75 P.V. had been injected.

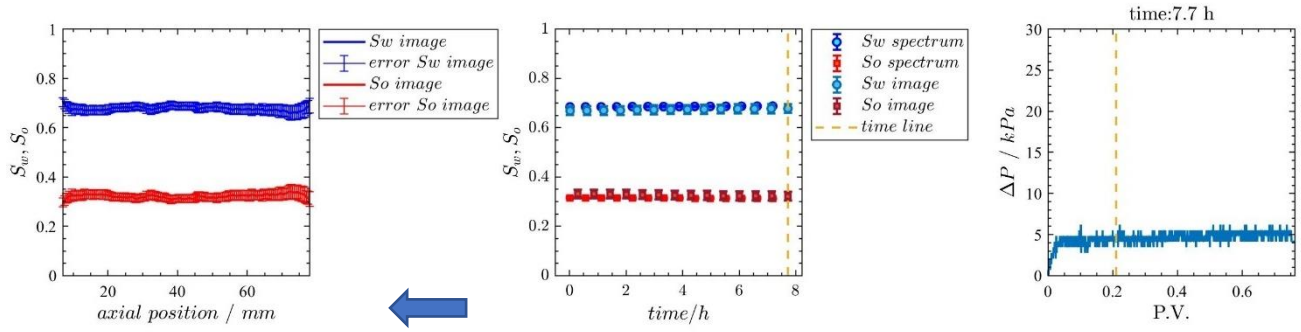

Figure 8-16: S_w and S_o profiles coming from the 3D reconstructed images at the time shown by the yellow dashed line and time evolution of the mean values of S_w and S_o coming the whole images (light blue for brine and dark red for oil) and from the chemically-selective spectra (blue for brine and red for oil) along with the time evolution of the pressure drop along the sample for xanthan gum injection at 0.15 ft d^{-1}.

Then, the velocity was increased up to 1 ft d^{-1} without any extraction of oil. However, interesting fluctuations in the measured ΔP were recorded as shown in Figure 8-17. The data acquisition was again interrupted due to coil overheating after ~ 6 h. At this stage, a polymer quantity equal to 1.1 P.V. had been injected. Xanthan gum injection continued for ~ 18 h to obtain a 3D propagator. As mentioned in Section 8.3.3.4, t_{RD} was increased from 3 up to 5.5 s to avoid coil overheating and acquire a representative flow map.

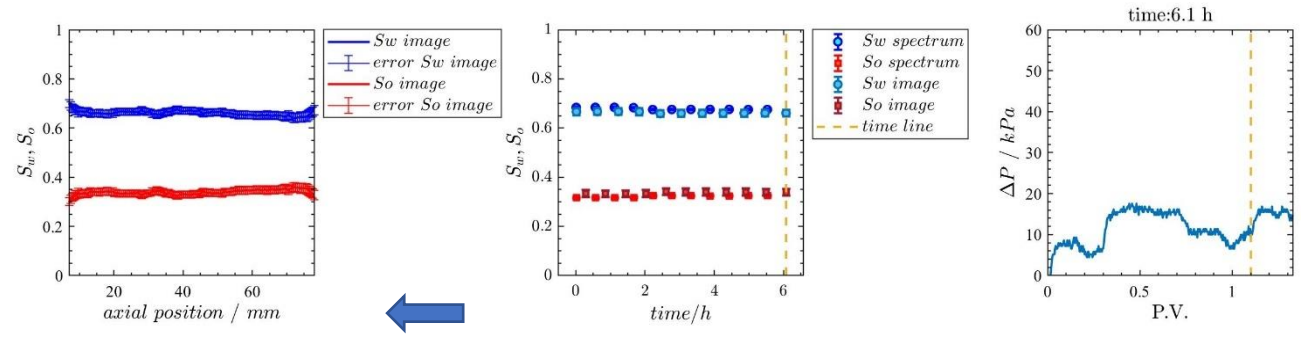

Figure 8-17: S_w and S_o profiles coming from the 3D reconstructed images at the time shown by the yellow dashed line and time evolution of the mean values of S_w and S_o coming the whole images (light blue for brine and dark red for oil) and from the chemically-selective spectra (blue for brine and red for oil) along with the time evolution of the pressure drop along the sample for xanthan gum injection at 1 ft d^{-1}.

After the results in Figure 8-17, brine was injected at 3 ft d^{-1} leading to extra oil recovery. Figure 8-18 presents the saturation profiles, the $\bar{S}_o$ and $\bar{S}_w$ coming from the 1D CSI sequence as well as the recorded pressure change. After 0.5 h, the S_o profile presented a greater decrease close to the inlet while the $\bar{S}_o$ decreased from 0.33 ± 0.01 down to 0.30 ± 0.01. The S_o profile continues to decrease from the inlet towards the

outlet after 0.9 h. After 3.8 h, a quantity of brine equal to 2 P.V. had been injected giving a homogenous profile with a $\bar{S}_o$ decrease from 0.30 ± 0.01 down to 0.28 ± 0.01. During this stage, an extra 18.2% of OOIP was extracted. ΔP presented a gradual increase until it started to decline after 5.5 h of injection. The ΔP fluctuations are further discusses in Section 8.4.4.

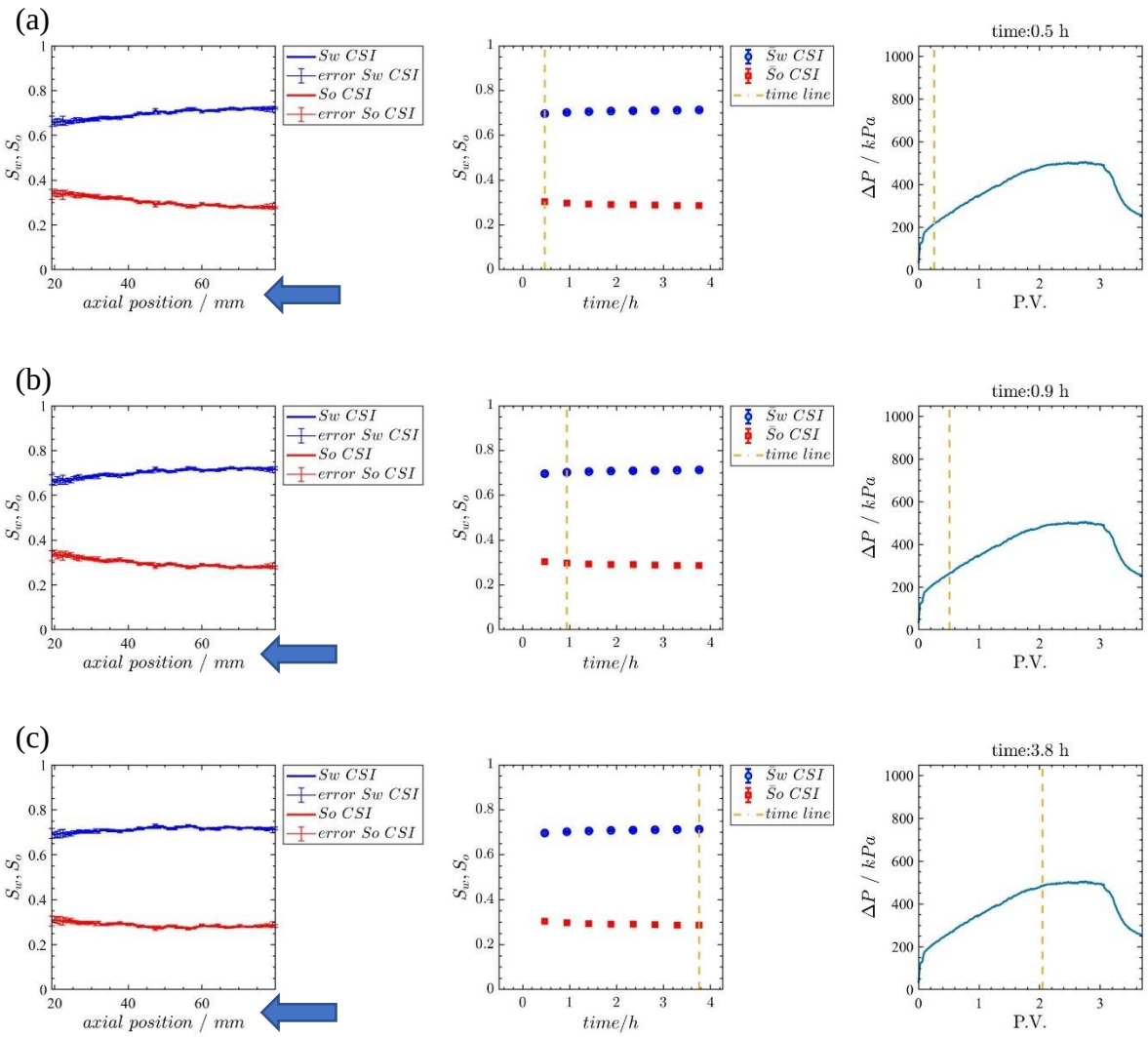

Figure 8-18: S_w and S_o profiles coming from the 1D CSI sequence at the times 0.5 (a), 0.9 (b) and 3.8 h (c) after injection are shown by the yellow dashed line in parallel with the time evolution of the $\bar{S}_w$ and $\bar{S}_o$ coming the CSI and the pressure drop across the sample during brine injection at 3 ft d^{-1} after xanthan gum injection at 1 ft d^{-1}.

Brine injection continued for 18 h to obtain a 3D propagator. Then a quantity of 2 P.V. of Xanthan gum was injected at ~ 3 ft d^{-1}. Unfortunately, the pressure was not recorded during this stage. The $\bar{S}_o$ remained the same during the whole polymer injection as shown in Figure 8-19. Polymer injection continued for the acquisition of a 3D propagator.

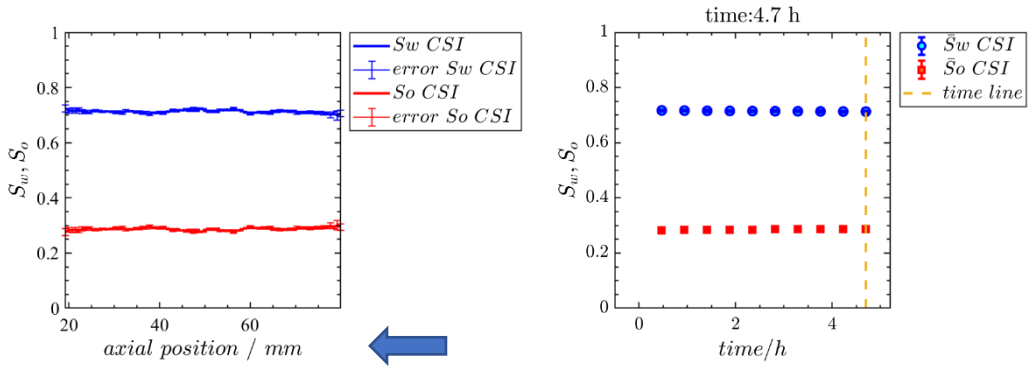

Figure 8-19: S_w and S_o profiles coming from the 1D CSI sequence after 4.7 h of injection shown by the yellow dashed line in parallel with the time evolution of the $\bar{S}_w$ and $\bar{S}_o$ coming the CSI during xanthan gum injection at 3 ft d^{-1} after brine injection at 3 ft d^{-1}.

Brine was then injected at a higher 6 ft d^{-1} velocity. The decrease of $\bar{S}_o$ was abrupt from 0.28 ± 0.01 recorded at the end of the polymer injection down to 0.26 ± 0.01 recorded at the beginning of the brine injection. A homogeneous change the S_o profile occurred at this stage and an extra 8.5% of OOIP was extracted. The measured ΔP presented a gradual decrease until reaching a steady value for ~ 2 h and then fluctuations with time. The dynamic process was monitored for ~ 6 h during which 6 P.V. of brine had been injected. Brine injection continued for the acquisition of a 3D propagator.

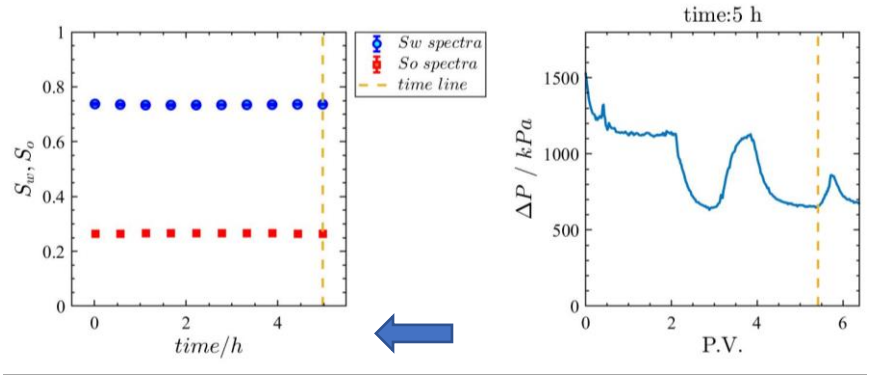

Figure 8-20: Time evolution of the S_w and S_o coming from the chemically selective spectra in parallel with the time evolution of the pressure drop across the sample for brine injection at 6 ft d^{-1} after xanthan gum injection at 3 ft d^{-1}.

Xanthan gum was finally injected at 6 ft d^{-1}. No further change in the S_o profile was recorded as presented in Figure 8-21. Plugging occurred after almost 10 h of polymer injection interrupting the propagator acquisition. Figure 8-21 shows a small peak in the ΔP after 1.2 h of injection and then a smooth decrease.

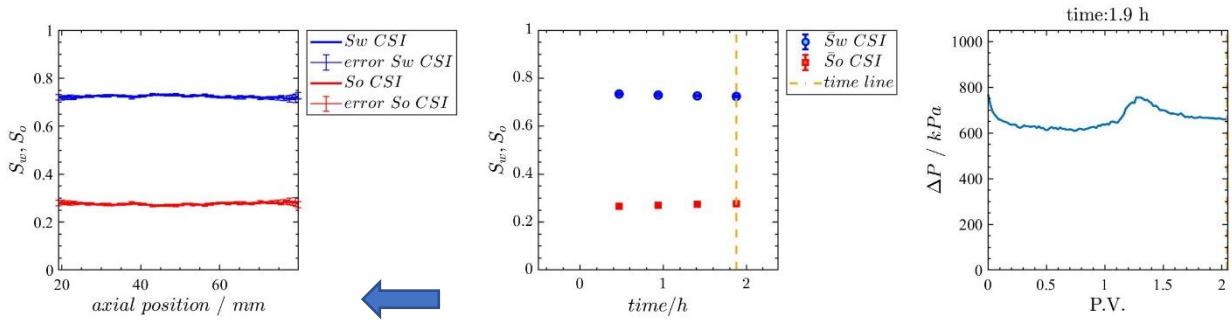

Figure 8-21: S_w and S_o profiles coming from the 1D CSI sequence after 1.9 h of injection shown by the yellow dashed line in parallel with the time evolution of the $\bar{S}_w$ and $\bar{S}_o$ coming the CSI and the pressure drop across the sample during xanthan gum injection at 6 ft d^{-1} after brine injection at 6 ft d^{-1}.

The oil distribution across the core at the end of each recovery stage is further analysed by projecting the 3D images. The DPR mechanism can be mapped by visually analysing the areas of trapped oil. Figure 8-22(a) indicates the areas of trapped oil after the removal of the oil ganglia by injecting brine at 8.4 ft d^{-1}. At this stage, the $\bar{S}_o$ was 0.33 ± 0.01. Then polymer was injected at 0.15 and 1 ft d^{-1}. Figure 8-22(b) shows that the brine injected at 3 ft d^{-1} right after the polymer injection created new flow paths removing the bypassed oil from several regions across the core plug. This shows that the previously injected polymer reduced the relative permeability of the high permeability swept areas. Then the newly injected brine invaded new regions where oil was trapped, leading to a reduced $\bar{S}_o$ of 0.29 ± 0.01. Injecting more polymer led to the blockage of these newly formed brine flow paths. Figure 8-22(c) demonstrates that brine injection at 6 ft d^{-1} right after polymer injection at 3 ft d^{-1} created new flow paths. Oil was extracted from several previously unswept areas. Even the large blocks of confined oil presented smaller intensity, hence smaller oil concentration. The final measured $\bar{S}_o$ was 0.26 ± 0.01.

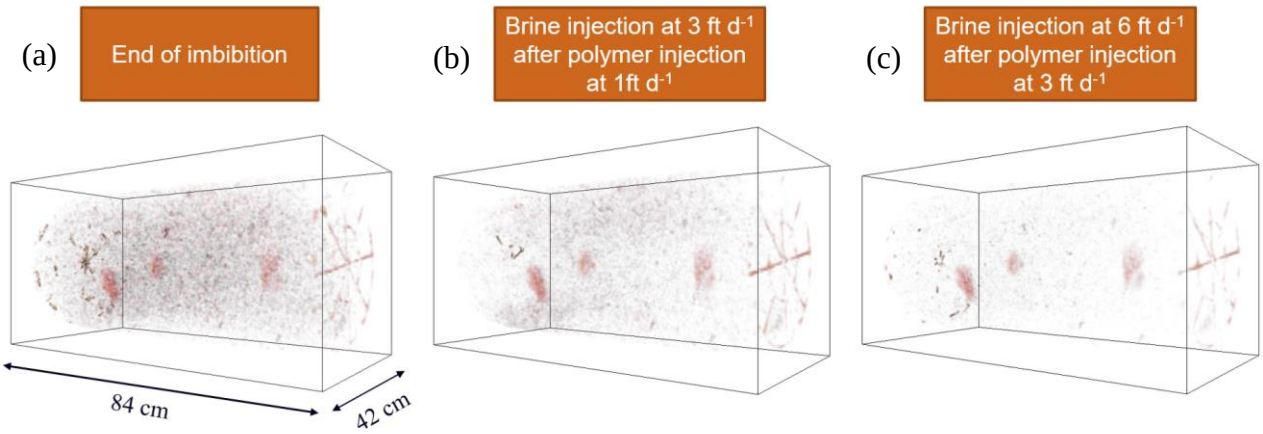

Figure 8-22: 3D fully-sampled images acquired with Scheme B for the oil phase at the end of the imbibition process after the removal of trapped oil ganglia (a), at the end of the brine injection at 3 ft d^{-1} after polymer injection at 1 ft d^{-1} (b) and at the end of the brine injection at 6 ft d^{-1} after polymer injection at 3 ft d^{-1}(c).

The whole waterflooding and xanthan gum injection led to a total recovery of 68.3% of OOIP out of which 4.6% came from the removal of the oil ganglia and 8.5% from the DPR mechanism due to polymer injection.

8.4.4 Time-Dependence of the Recorded Pressure Drop

At 0.15 ft d^{-1} the recorded ΔP in Figure 8-23(a) was constant. This is potentially related to the Newtonian behaviour of the polymer at ultra-slow u_D (Al-Shakry et al., 2019; Eberhard et al., 2019). The fluctuations observed in Figure 8-23(b) and (c) for higher Q are time-dependent and are related to the shear-thinning behaviour of the polymer.

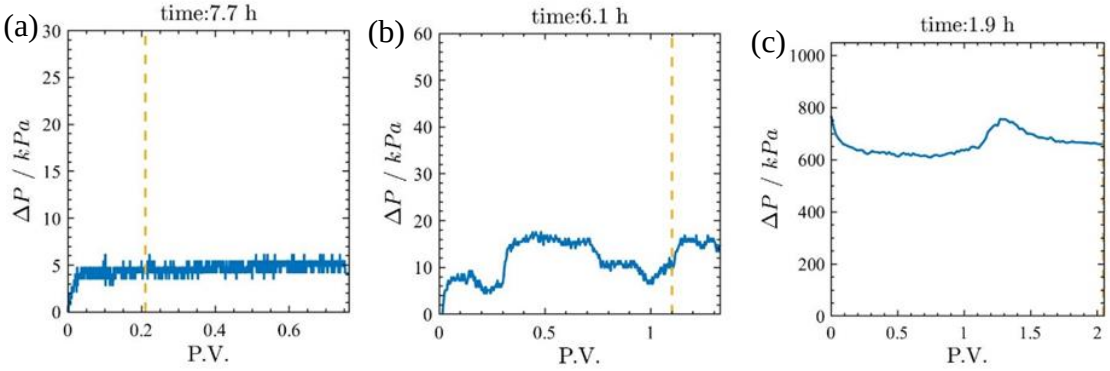

Figure 8-23: Pressure drop along the core with time for xanthan gum injection at 0.15(a), 1(b) and 6 ft d^{-1}(c) through Estaillades core. The dashed yellow line shows the end of data acquisition.

A potential explanation of these ΔP fluctuation can be derived from the analysis of the disentanglements among the polymeric rods. Figure 8-23(b) shows an initial increase in ΔP which comes from the increase in u_D from 0.15 up to 1 ft d^{-1}. A relatively constant ΔP was maintained for 2 h. At 0.36 P.V., a large increase in ΔP was seen. This increase can be related to the formation of large aggregates along the core. From these two stages of injection, a quantity of polymer equal to 1.1 P.V. had been injected. This means that polymer molecules had travelled across the whole P.V. of the rock. When more polymeric molecules entered the core, the 'newer' molecules experienced deformation due to the $\dot{\gamma}$ and then they collided with the 'older' molecules already placed in areas of large permeability. Out of these collisions, new entanglements were formed reducing gradually the permeability of these areas. ΔP remained constant at this higher value for 2 h when a gradual decrease was noticed. This gradual decrease could be associated with the dissociation of the aggregates and lasted for 2 h. After injecting a total quantity of 1.1 P.V. at 1 ft d^{-1}, the injection stopped. In the absence of flow, the dissociation stopped and the formation of new entanglements caused a new increase in ΔP.

Figure 8-23(c) presents the ΔP change during the polymer injection at 6 ft d^{-1} after brine injection. At this stage, the polymer was located at several positions along the core. ΔP showed an initial small decrease. This could be related to the fast rate of fission of the covalent bonds due to the externally applied pressure. Then a constant ΔP was observed until a 1.1 P.V. had been injected. During this constant ΔP the rate of dissociation is equal to the rate of formation of new entanglements. At this point,

an abrupt increase in ΔP which lasted for only 18 min followed by a fast decrease was recorded.

The recorded ΔP during the brine injection is also analysed. Figure 8-24(a) presents the gradual increase of ΔP as brine was flowing at 3 ft d^{-1} displacing the unswept oil from the low permeability regions due to DPR from the polymer. Oil was produced along with small quantities of xanthan gum. After 3.8 h, a quantity of brine equal to 2 P.V. had been injected and no more oil was produced. The increase in ΔP could be related to the formation of entaglements as polymeric molecules were displaced inside the pore structure. ΔP remained constant for a short time and started to rapidly decrease after 3 P.V.. At this point, a large amount of polymer had been displaced out of the system and the degree of bond dissociation was high.

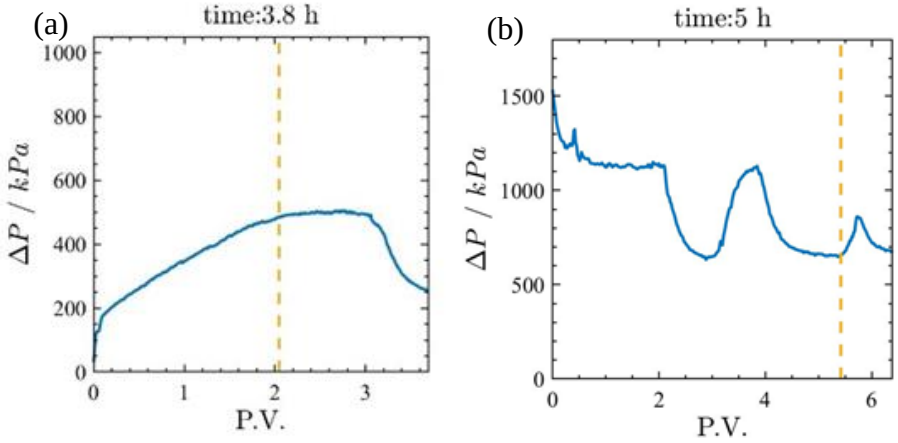

Figure 8-24: Pressure drop along the core with time for brine injection at 3(a), 6 ft d^{-1}(b) through Estaillades core after the polymer injection. The dashed yellow line shows the end of data acquisition.

Figure 8-24(b) exhibits the ΔP fluctuations as brine was flowing at 6 ft d^{-1}. In this experiment, the oil was extracted abruptly. This is why ΔP presented its highest value at the start of the data acquisition since brine started to flow through the lowest permeability areas displacing the unswept oil. As more brine was injected, there was no more oil recovery and large quantities of xanthan were pushed out of the rock. After 2 h (~2 P.V.), a large decrease in ΔP was recorded followed by a subsequent increase. These fluctuations in the ΔP could be related to the formation and dissociation of entanglements as the polymeric molecules were displaced from high and low permeability areas of the pore structure.

8.4.5 Comparing Propagator Data for Polymer and Brine Flow

The data coming from the 3D spatially and chemically-resolved propagators for a velocity of 1 and 3 ft d^{-1} are compared to detect the changes in the flow behaviour of the two fluids. For the 1 ft d^{-1}, $\langle\zeta\rangle_0$ was 3.9 μm while l_D was 69.7 μm, while for the 3 ft d^{-1}, $\langle\zeta\rangle_0$ was 6.4 μm and l_D was 51.5 μm. Since l_D was higher than $\langle\zeta\rangle_0$ in both cases, mixing between stagnant and flowing populations was expected to affect the fluids' behaviour. The mean volumetric velocity was calculated as described in Section 4.3.2.7 and is presented in Figure 8-25.

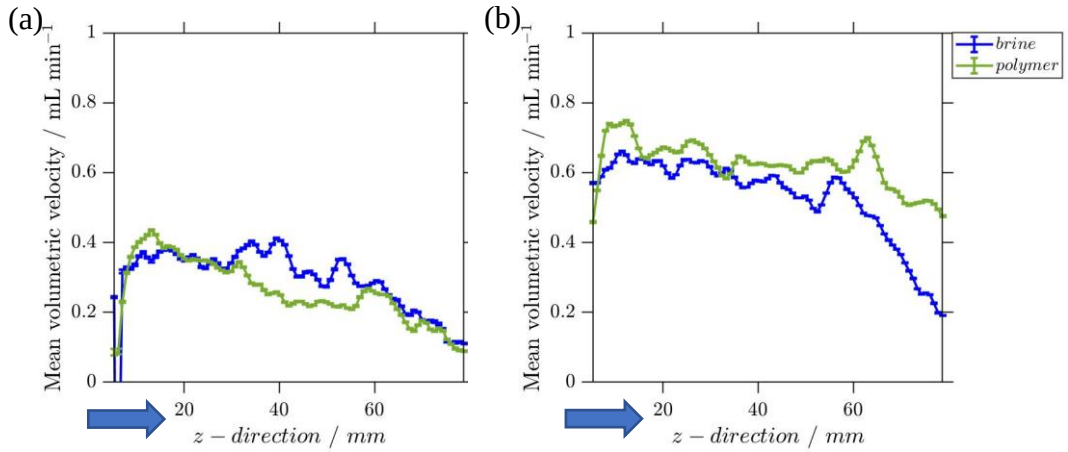

Figure 8-25: Flow rate profile for the brine (blue) and the polymer (green) phase coming from the APGSTE-RARE sequence with chemical selection in parallel with the flow rate set by the pump (yellow dashed line) for 1(a) and 3 ft d^{-1}(b).

Figure 8-25 shows that for 1 and 3 ft d^{-1} both brine and polymer presented a declining and fluctuating profile in the measured mean volumetric velocity. In the 1 ft d^{-1}, the polymer velocity profile presents a higher decline compared to the brine. In the 3 ft d^{-1}, the polymer velocity profile presents a smaller decline and overall higher mean volumetric velocities compared to the brine phase. The declining profile close to the outlet is probably related to errors that have not been accounted for. There is the possibility that the magnetic field pesented distortions close to the outlet area of the RCH. There is also the possibility that ΔP did not remain constant during this stage of injection. In this case, the measurements were not obtained under steady-state conditions which explains the noise imported in the measurements close to the outlet. It should be pointed out that fluctuations in the ΔP were recorded even when oil was not extracted. ΔP was not recorded during the propagator measurements. However, detecting the displacement of both the brine and polymeric molecules at these ultra-slow flows was important. Higher mean volymetric velocities were recorded for the polymer phase showing the effect of the shear-thinning even when the externally applied velocities are the same.

8.4.6 Comparing Brine Propagators Before and After Polymer Injection

The goal of this comparison is to identify the change in the brine flow paths due to the polymer injection and the DPR effect. Figure 8-26(a) presents the per voxel brine displacement for 1 ft d^{-1}(before) and 3 ft d^{-1}(after), while Figure 8-26(b) indicates the per voxel brine displacement for 3 ft d^{-1}(before) and 6 ft d^{-1}(after). In Figure 8-26(a), a large number of voxels is included inside the red cycle showing that many voxels exhibit larger displacements for the 1 ft d^{-1} compared to the 3 ft d^{-1}. This means that the initially formed flow paths invaded by the brine were blocked by the polymer injection at 0.15 and 1 ft d^{-1}. Therefore, when the new brine was injected at 3 ft d^{-1}, the molecules searched for other areas of higher relative permeability. Moreover, even though the same mask was applied to all the data, there is a large number of voxels that present displacement for 1 ft d^{-1} but they are stagnant for 3 ft d^{-1} and the opposite. This is a clear effect of the DPR phenomenon. Similarly in Figure 8-26(b), there are

many voxels of high displacement at 3 ft d^{-1} which presented smaller displacements in the 6 ft d^{-1} regime. In Figure 8-26(a), the number of voxels is equally distributed around the diagonal showing that even though the externally imposed velocity by the pump is higher, the detected displacements in the 3 ft d^{-1} regime are not higher. In contrast, Figure 8-26(b) demonstrates that for the 6 ft d^{-1} regime most voxels present higher displacements.

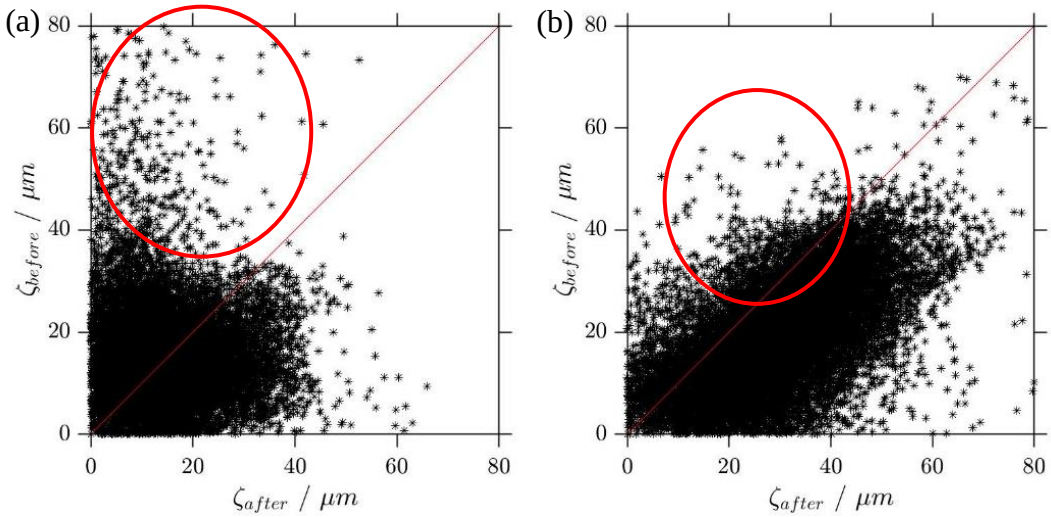

Figure 8-26:Voxel-per-voxel comparison of the displacement coming from the local propagators of the brine phase across the whole Estaillades core for 1 ft d^{-1}(before) and 3 ft d^{-1}(after polymer injection) (a) and for 3 ft d^{-1}(before) and 6 ft d^{-1}(after polymer injection) (b).

8.5 Discussion

The Estaillades core plug employed in this study can be considered as a reservoir representative sample giving an understanding of the macroscopic imbibition in a real reservoir. The imbibition took place with a flow rate of 0.011 mL min^{-1}, hence a Ca of ~ 8.8 10^{-9}. According to Section 8.2.3, the brine was expected to advance across the core following the pattern of invasion percolation with cluster growth. The expected dendritic front and the cluster growth in different areas within the sample are illustrated in Figure 8-12. Trapping of large quantities of oil due to the formation of these clusters is seen along the whole volume. This is the first time that the mechanism of displacement is imaged in a 1.5″ carbonate core plug. As more brine was injected, new flow paths were created displacing the previously bypassed oil until a uniform oil distribution was established. After 16.2 h of injection, no more oil was observed in the effluent. At this stage, 55.2 % of the OOIP was recovered.

Oil was trapped in the bypassed areas but also in the form of oil ganglia at different areas along the core due to the snap-off mechanism. The snap-off mechanism has been imaged at pore-scale resolution in a Ketton limestone (carbonate) using time-resolved synchrotron X-ray μCT imaging (Singh, 2018). In the current thesis, oil ganglia were removed from the system by increasing abruptly the brine injection from 0.15 up to 15 ft d^{-1} achieving an extra recovery of 4.6% OOIP. In order to increase the oil recovery during the chemical EOR stage, a xanthan gum concentration of 3000 ±

10 mg l^{-1} was chosen. According to Figure 8-6, the polymeric solution is expected to present a μ_{app} above 10 cP when flow through the porous network.

Oil occupied 33% of the P.V. before the EOR stage. The polymer was injected at 0.15 ft d^{-1} and presented a constant ΔP confirming the expected Newtonian behaviour. When the polymer injection was increased up to 1 ft d^{-1}, fluctuations in ΔP were recorded. At this stage, the polymeric solution was expected in the shear-thinning regime. These fluctuations were related to the formation and dissociation of entanglements as more polymeric molecules were entering the pore structure (Morris et al., 1981). Time-dependent phenomena for xanthan gum have also been reported by Dupuis et al., (1994). Increase in the μ_{app} of the xanthan gum solution has been recorded in the literature for flow through rocks at $\dot{\gamma}$ >1000 s^{-1} (González et al., 2005). No more oil was extracted during the injection of polymer. This is the first time that ΔP fluctuations were recorded for a biopolymer flow through a carbonate rock. Oil recovery was recorded when brine was injected at 3 ft d^{-1}. As illustrated in the 3D images in Figure 8-22, brine invaded new areas where oil was trapped. This oil recovery is a result of the DPR mechanism described in Section 8.2.5. Polymeric molecules injected at 0.15 and 1 ft d^{-1} were attained to the pore wall reducing the k_r of the previously swept areas. The newly injected brine at 3 ft d^{-1} entered new unswept areas where oil was present. The DPR mechanism was also confirmed by the per voxel comparison of the displacement before and after the polymer injection in Figure 8-26.

8.6 Conclusions

In this chapter, the imbibition of the Estaillades core plug was followed by xanthan gum injection and various NMR techniques were used to map the structural and flow changes. The aim of this study was to identify initially the pattern of oil displacement from brine and then identify the DPR mechanism during the biopolymer injection through a bimodal rock.

The improved WET suppression scheme enabled us to map visually and quantitatively the oil extraction during the imbibition process by acquiring fast images. This is the first time that the mechanism of displacement was imaged in a carbonate rock during continuous flow. The imbibition at 0.15 ft d^{-1} resulted in a recovery of 55.2% of the OOIP.

Trapped oil ganglia were then removed by increasing the externally applied velocity up to 15 ft d^{-1}. An extra 4.6% of OOIP was recovered during this stage. Then polymer was injected at 0.15 ft d^{-1} presenting a constant ΔP. When the velocity was increased up to 1 ft d^{-1}, fluctuations in the recorded ΔP were observed. This is the first time that time-dependent phenomena are recorded for xanthan gum flow through a carbonate rock. According to the theory, the polymer is expected to present a Newtonian behaviour at 0.15 ft d^{-1}, whereas at 1 ft d^{-1} the polymer is expected to be in the shear-thinning regime. Nevertheless, the simulation cannot fully predict fluid's behaviour in the rock pore structure which is full of contractions and expansions. No more oil was extracted during polymer injection proving that the polymeric molecules entered the same flow paths swept by the brine phase during imbibition. Oil was recovered when

brine was injected at 3 ft d^{-1} after the polymer injection. This shows that the previously swept areas were blocked by the polymeric molecules and the newly injected brine was forced to invade new flow paths pushing out the trapped oil. This diversion of the flow due to the DPR mechanism was also proved by the per voxel comparison of the displacement before and after the polymer injection. Fluctuations in the ΔP were also observed during the polymer flow at 3 ft d^{-1}. Fluctuations were related to the formation and dissociation of aggregates as more polymer was injected. Oil was recovered during the brine injection at 6 ft d^{-1} following this polymer injection. From this series of consecutive brine and polymer injections, an extra 8.5% of OOIP was extracted. Imbibition and polymer injection led to a total recovery of 68.3% of OOIP.

The different behaviour exhibited by the brine and the polymeric phase when flowing at 1, 3 and 6 ft d^{-1} show how important is the development of the novel ultra-slow flow measurements technique presented in Chapter 4 and Chapter 5. This technique offers the potential to further study and compare brine and polymer flow in various complex pore structures in two-phase systems.

Chapter 9 Summary of Conclusions and Future Work

9.1 Summary of Conclusions

In this thesis, two novel techniques were developed for the characterisation of the flow through complex pore structures. The first technique enabled the detection of ultra-slow interstitial velocities through a bead pack and then through low permeability cores. The second technique improved the detection of two different phases by efficiently suppressing one phase in each acquisition. The technique quantitatively measured the relative saturation of oil and water inside a bead pack and a carbonate rock. Moreover, the suppression technique was combined for the first time with the spatially-resolved MRI flow propagator sequence enabling the detection of two-phase flow. This novel technique enabled the identification of the mechanisms of displacement during imbibition and EOR under reservoir-representative conditions. The main conclusions of the research undertaken are given below.

Chapter 1 introduced the EOR steps and the importance of DR in the oil and gas industry. It also introduced how NMR can contribute to the development of the DPR and the optimisation of the EOR strategies. Chapter 2 introduced the basic principles of NMR and MRI in structural imaging and translational motion. Chapter 3 described the novel **k**-space under-sampling strategy, the method for choosing the optimum reconstruction parameters and the denoising methods for all the reconstructed data.

In Chapter 4, a novel multi-objective optimisation toolbox which identifies the optimum experimental parameters for phase-contrast imaging based on the complexity of the system was reported. More precisely, the optimisation toolbox assesses the T_1, T_2 and D_{app} of the system to derive the optimum Δ, δ_G and g used in the APGSTE-RARE sequence for phase-contrast imaging. The optimum parameters were tested for flow through the ideal system of a bead pack filled with water and 4 mm beads. The experimental time was reduced from 4 h down to 56 min using CS and velocities as low as 1 ft d^{-1} (3.5 μm s^{-1}) were detected for the first time. Phase-contrast images with pore-scale resolution and 3D propagators without pore-scale resolution were obtained for 1, 3, 6, 10 and 15 ft d^{-1}. Error analysis proved that the local velocities were measured with good accuracy. Combining these data, it was concluded that self-diffusion was the main mechanism for displacement for 1 and 3 ft d^{-1}. Increasing the velocity at 6 ft d^{-1} or higher, the $D_{//}$ coming from propagators showed that mechanical mixing became the dominant mechanism of displacement. This is the first time that MRI achieved to detect ultra slow velocities for water flow through a bead pack.

Chapter 5 presented the implementation of the novel phase-contrast imaging with optimised experimental parameters for flow through a Bentheimer, an Estaillades and two Indiana limestone core plugs. Phase-contrast images and 3D propagators of the lower resolution were obtained for 6, 10 and 15 ft d^{-1}. All the measurements were obtained in less than 40 min. Error analysis showed that local velocities were

measured accurately, even though the fast T_2 relaxation and the presence of internal gradients decreased the SNR. Velocity maps derived from both of these methods in combination with the flow paths coming from the phase-contrast images obtained along x, y and z indicated different flow behaviours for each rock. Bentheimer is a homogeneous sandstone with long T_1 and T_2 relaxations which are related to a unimodal system of pores and higher SNR. This higher SNR results in a small error in the measured local velocities. Estaillades also presented a homogeneous distribution in the velocity field obtained using both the phase-contrast and propagator sequences. The flow paths formed for the 15 ft d^{-1} regime for the Bentheimer core plug presented long and straight line proving the good connectibity of the pore-throat channels. These long lines became more tortuous in the case of the Estaillades core plug, showing that the water behaved differently in this dual-porosity network. $IND4_33$ and $COR1_7$ presented very fast T_2 relaxation times which resulted in areas of low SNR. For $IND4_33$ the phase-contrast images of higher resolution detected voxels of higher velocity, whereas the propagator measurements of low-resolution presented a homogeneous distribution of velocities around zero for all the flow velocities. Phase-contrast imaging was considered as the best velocity mapping technique for this rock and the analysis of the formed flow paths proved that the pore network is dominated by dead ends and unconnected flow paths. $COR1_7$ is the first ultra-low permeability rock studied at ultra-slow flow regimes. In this rock, the areas of higher velocities were mapped by both the phase-contrast and the propagator sequence. Phase-contrast imaging appeared less sensitive to the low SNR. The formed flow paths proved that this rock is also governed by unconnected pores. In contrast to $IND4_33$, an area of well connected paths and high velocities was identified on the z-y slice of the velocity maps. This is the first time that velocity maps and flow paths between four different rocks under ultra-slow flow conditions have been recorded and compared.

Chapter 6 described the development and the calibration of the novel four-pulses suppression scheme. The so-called WET scheme was combined with the pulse-acquire, the CSI, the RARE and for the first time the APGSTE-RARE sequence and was implemented in an ideal bead pack and a two-phase Estaillades rock. The four-pulses scheme was compared with the single-pulse scheme and the two chemically-selective spectra were compared for the system of the bead pack, showing the better performance of the novel technique. The S_w and S_o coming from the chemically-selective spectra, 1D spectra and images were compared with the volumetric measurements in both tested samples, presenting a great agreement. Moreover, this is the first time that chemically-selective propagators obtained with the APGSTE-RARE sequence were obtained. The D_{app} map coming from the propagator of the stagnant dodecane phase trapped inside the vial was in great agreement with the D_s of dodecane. Using the same technique in the rock system, a D_{app} map of the trapped dodecane inside Estaillades was calculated. However, there are no literature data for dodecane trapped in Estaialldes to prove the measured values. Water propagators obtained along the whole volume of the bead pack presented interesting shapes showing different flow behaviours inside the same system. Similarly, the skewness and the broadness of the local water propagators obtained in the Estaillades rock varied along the direction of flow.

In Chapter 7, the process of primary drainage in a dual-porosity Estaillades core was described. Dodecane was injected into the water saturation rock following the SWPP protocol, while S_w and ΔP were continuously recorded. The 1D CSI method was used for the acquisition of the saturation profiles. Combining the ΔP-$\bar{S}_w$ curve along with the S_w and S_o profiles showed that invasion percolation was the main mechanism of water displacement during the step of injection under a constant flow rate of 0.02 mL min^{-1}. After reaching the pressure threshold of 1.49 MPa of the ceramic disc, oil injection continued under constant pressure. During this step of constant pressure, oil was injected following the Haines jump mechanism. At the end of the drainage process, a S_{wc} of 0.15 was achieved. This is the lowest value ever recorded in dual-porosity carbonate rock and is a reservoir representative residual oil recovery. Accurate pore-throat size distribution is not possible using the SWPP method of filling since equilibrium is not established at any stage of injection. However, it was found that a good approximate of the narrowest r_t invaded at each stage of the injection can be made from the measured ΔP.

In Chapter 8, the process of imbibition and polymer injection through the Estaillades rock filled by 85% with dodecane is described. Chemically-selective spectra, 1D CSI, 3D RARE images and 3D propagators were employed to identify the mechanisms of displacement. The water injection in the step of imbibition occurred at 0.15 ft d^{-1} and resulted in a recovery of 55.2% of the OOIP. The pattern of invasion percolation with cluster growth was imaged for the first time using the 3D CSRARE sequence with the improved four pulses WET scheme. An extra 4.6% of OOIP was recovered by removing the oil ganglia through an abrupt increase in the flow velocity up to 15 ft d^{-1}. Then, the polymer was injected at 0.15 ft d^{-1}, presenting a constant ΔP. The measured ΔP was constant. This was related to the Newtonian behaviour of Xanthan gum when flowing through the wider throats of Estaillades as proved by the average viscosity simulation model. Increasing the velocity up to 1 ft d^{-1}, the recorded ΔP presented fluctuations. These fluctuations in ΔP were related to the shear-thinning regime and the formation and dissociation of entanglements. During this polymer injection, no more oil was recovered proving that the polymeric molecules entered the same flow paths swept by the brine phase during imbibition. Oil recovery was recorded when brine was injected at 3 ft d^{-1} after the polymer injection at 1 ft d^{-1}. This is an indication that the previously swept areas were blocked by the polymeric molecules. Consequently, the newly injected brine invaded new flow paths displacing the trapped oil. The per voxel comparison of the displacement derived from the propagator measurements before and after the polymer injection also proved this diversion of the flow due to the DPR mechanism. Oil was recovered also during the brine injection at 6 ft d^{-1} following the polymer injection at 3 ft d^{-1}. From these consecutive brine and polymer injections, an extra 8.5% of OOIP was extracted. The overall imbibition and polymer injection led to a total recovery of 68.3% of OOIP. This is the first time that the DPR mechanism was monitored and identified through ΔP and NMR measurements during EOR under real reservoir conditions.

9.2 Suggestions for Future Work

9.2.1 Systemic Study of Single-Phase Ultra-Slow Flow in Rocks

Chapter 5 demonstrated the velocity maps, the formed flow paths and the propagator measurements for 6, 10 and 15 ft d^{-1} obtained in one sandstone and four carbonate core plugs. The study could be expanded to more core plugs to create a library of rocks studied and identify similarities and differences in the mechanisms of displacement of water through these different rocks. These flow studies could serve to validate and calibrate the flow behaviour derived from DR simulations and machine learning algorithms. Moreover, flow velocities lower than 6 ft d^{-1} could be detected in rocks with relatively long T_1 and T_2 relaxations, hence higher SNR such as the Bentheimer sandstone studied in Chapter 5. Studying the flow behaviour of water in velocities lower than 6 ft d^{-1} could lead to new interesting observations. Ultra-slow flow studies are in a primary stage. There are few experimental (L. Wang et al., 2019; Zeng et al., 2011) and simulation studies (Dou et al., 2014; Wang and Sheng, 2017) investigating this regime. However, MRI techniques can give interesting insights into the mechanisms of flow that dominate each porous system.

9.2.2 Dynamic Monitoring of Single-Phase Polymer Core Floods

As explained in Chapter 8, it is important to understand the flow behaviour of polymers at ultra-slow velocities to explain the mechanism of oil recovery in EOR. HPAM, xanthan gum and Scleroglucan are three polymers of high interest for the EOR (Abidin et al., 2012; Agi et al., 2018). The injection of these polymers at ultra-slow velocities can dynamically be monitored with the MRI methods developed in Chapter 4. Phase-contrast images and low-resolution 3D propagators acquired in parallel with ΔP recorded by a differential pressure transducer connected directly to the RCH can relate the pressure changes with the flow behaviour of each polymer at each different flow rate. A differential pressure transducer (Wet/Wet Differential Pressure Model PXM409-WWDIFF, Omega, UK) with a ΔP range of 0-35 bar has been bought and the LabVIEW script for the data acquisition has been written enabling the beginning of such experiments. The concentration of the polymer in the formed polymeric solutions can vary and the same solution can be tested in different flow velocities and different porous systems. In addition to that, the brine concentration in each polymeric solution can vary and the same flow velocities and systems can be studied showing the effect of the salinity on the flow behaviour.

9.2.3 Dynamic Monitoring of Multi-Phase Polymer Core Floods

As discussed in Chapter 8, ultra-slow flow in two-phase systems presents higher resistance to flow (Hao et al., 2008). The novel four pulses WET scheme works efficiently in rocks with narrow spectral width. This is why the Estaillades rock was chosen for the complete EOR experiment described in Chapter 8. Another interesting rock with narrow spectral width when saturated with water is the Fontainebleau core plug. Identifying cores with narrow spectral widths which allow the separation of the oil from the water peak is crucial for the study of multiple two-phase systems. Conducting complete EOR core floods in these rocks and monitoring each stage with

the fast velocity maps for ultra-slow flow described in Chapter 4 can give valuable insights into the polymer injection and the oil recovery mechanisms.

References

Abdallah, W., Buckley, J.S., Carnegie, A., Edwards, J., Herold, B., Fordham, E., Graue, A., Habashy, T., Seleznev, N., Signer, C., Hussain, H., Montaron, B., Ziauddin, M., 2007. Fundamentals of Wettability. Oilf. Rev. 19, 44–61.

Abidin, A.Z., Puspasari, T., Nugroho, W.A., 2012. Polymers for Enhanced Oil Recovery Technology. Procedia Chem. 4, 11–16. https://doi.org/10.1016/j.proche.2012.06.002

Agi, A., Junin, R., Gbonhinbor, J., Onyekonwu, M., 2018. Natural Polymer Flow Behaviour in Porous Media for Enhanced Oil Recovery Applications: a Review. J. Pet. Explor. Prod. Technol. 8, 1349–1362. https://doi.org/10.1007/s13202-018-0434-7

Aja-Fernández, S., Alberola-López, C., Westin, C.F., 2008. Noise and Signal Estimation in Magnitude MRI and Rician Distributed Images: A LMMSE Approach. IEEE Trans. Image Process. 17, 1383–1398. https://doi.org/10.1109/TIP.2008.925382

Aja-Fernandez, S., Tristan-Vega, A., 2013. A Review on Statistical Noise Models for Magnetic Resonance Imaging.

Al-Mjeni, R., Arora, S., Cherukupalli, P., van Wunnik, J., Edwards, J., Felber, B., Gurpinar, O., Hirasaki, G.J., Miller, C. a, Jackson, C., Kristensen, M., Lim, F., Ramamoorthy, R., 2010. Has the time come for EOR? Oilf. Rev. 6, 16–35.

Al-Shakry, B., Skauge, T., Shiran, B.S., Skauge, A., 2019. Polymer injectivity: Investigation of Mechanical Degradation of Enhanced Oil Recovery Polymers Using In-Situ Rheology. Energies 12. https://doi.org/10.3390/en12010049

Amin, N., Claridge, T., 2017. Quantitative NMR Spectroscopy, University of Oxford. https://doi.org/10.1081/AL-100107290

Andersen, M.A., 2014. Digital core flow simulations accelerate evaluation of multiple recovery scenarios. World Oil 235, 50–56.

Anderson, W.G., 1986. Wettability Literature Survey-Part 3: The Effects of Wettability on the Electrical Properties of Porous Media. J. Pet. Technol. 38, 1371–1378. https://doi.org/10.2118/13934-PA

Andris, P., Frollo, I., 2016. Noise and Interference in Measured NMR Images. Meas. J. Int. Meas. Confed. 77, 29–33. https://doi.org/10.1016/j.measurement.2015.09.003

Appel, M., 2004. Nuclear Magnetic Resonance and Formation Porosity. Petrophysics 45, 296–307.

Arns, C.H., 2004. A comparison of pore size distributions derived by NMR and X-ray-CT techniques. Phys. A Stat. Mech. its Appl. 339, 159–165. https://doi.org/10.1016/j.physa.2004.03.033

Arns, C.H., Knackstedt, M.A., Martys, N.S., 2005. Cross-property correlations and permeability estimation in sandstone. Phys. Rev. E - Stat. Nonlinear, Soft Matter Phys. 72, 1–12. https://doi.org/10.1103/PhysRevE.72.046304

Benning, M., Gladden, L., Holland, D., Schönlieb, C.B., Valkonen, T., 2014. Phase Reconstruction From Velocity-Encoded MRI Measurements - A Survey of Sparsity-Promoting Variational Approaches. J. Magn. Reson. 238, 26–43. https://doi.org/10.1016/j.jmr.2013.10.003

Bernin, D., Topgaard, D., 2013. NMR Diffusion and Relaxation Correlation Methods: New Insights in Heterogeneous Materials. Curr. Opin. Colloid Interface Sci. 18, 166–172. https://doi.org/10.1016/j.cocis.2013.03.007

Bernstein, M., King, K., Zhuo, X., 2004. Handbook of MRI Pulse Sequence, Elsevier A. ed.

Bernstein, M.A., King, K.F., Zhou, X.J., 2004. Basic Pulse Sequences, in: Handbook of MRI Pulse Sequences. pp. 579–647. https://doi.org/http://dx.doi.org/10.1016/B978-012092861-3/50021-2

Bijeljic, B., Mostaghimi, P., Blunt, M.J., 2013. Insights into Non-Fickian Solute Transport in Carbonates. Water Resour. Res. 49, 2714–2728. https://doi.org/10.1002/wrcr.20238

Bird, R.B., Armstrong, R.C., Hassager, O., 1987. Dynamics of Polymeric Liquids, 2nd ed. John Wiley & Sons, United States of America.

Bloembergen, N., Purcell, E.M., Pound, R. V., 1948. Relaxation Effects in Nuclear Magnetic Resonance Absorption. Phys. Rev. 73, 679–712. https://doi.org/10.1103/PhysRev.73.679

Blumich, B., 2000. NMR imaging of materials. Oxford science publications, Aachen.

Blunt, M., 2017. Multiphase Flow in Permeable Media: A Pore-Scale Perspective.

Blunt, M.J., Scher, H., 1995. Pore-level Modelling of Wetting. Phys. Rev. 52, 6387–6403.

Bottomley, P., 1982. Selective Volume Method for Performing Localized NMR Spectroscopy.

Brummer, M.E., Mersereau, R.M., Eisner, R.L., Lewine, R.R.J., 1993. Automatic Detection of Brain Contours in MRI Data Sets. IEEE Trans. Med. Imaging 12, 153–165. https://doi.org/10.1007/BFb0033753

Bush, I., 2018a. NMR Studies of Enhanced Oil Recovery Core Floods and Core Analysis Protocols. University of Cambridge.

Bush, I., 2018b. NMR Studies of Enhanced Oil Recovery Core Floods and Core Analysis Protocols 203.

Callaghan, P., 2011. Translational Dynamics and Magnetic Resonance : Principles of Pulsed Gradient Spin Echo Nuclear Magnetic Resonance Paul. Oxford University Press.

Callaghan, P.T., 2014. Translational dynamics and magnetic resonance : principles of pulsed gradient spin echo NMR, 1st ed. Oxford University Press, Oxford.

Callaghan, P.T., 1991. Principles of Nuclear Magnetic Resonance. Clarendon Press, Bath.

Callaghan, P.T., Eccles, C.D., Xia, Y., 1988. NMR Microscopy of Dynamic Displacements: K-Space and Q-Space Imaging. J. Phys. E. 21, 820–822. https://doi.org/10.1088/0022-3735/21/8/017

Callaghan, P.T., Godefroy, S., Ryland, B.N., 2003. Diffusion-Relaxation Correlation in Simple Pore Structures. J. Magn. Reson. 162, 320–327. https://doi.org/10.1016/S1090-7807(03)00056-9

Callaghan, P.T., Trotter, C.M., Jolley, K.W., 1980. A Pulsed Field Gradient System for a Fourier Transform Spectrometer. J. Magn. Reson. 37, 247–259.

Canadian Society for Unconventional Resources, 2012. Understanding tight oil. Can. Soc. Unconv. Resour. 19. https://doi.org/10.2118/79914-MS

Cano Barrita, P.F. d. J., Balcom, B.J., McAloon, M.J., Green, D.P., Dick, J., 2008. Capillary Pressure Measurement on Cores by MRI. JPT, J. Pet. Technol. 60. https://doi.org/10.2118/0808-0063-jpt

Carr, H., Purcell, E., 1954. Effects of diffusion on free precession in Nuclear Magnetic Resonance experiments. Phys. Rev. 94, 630–638. https://doi.org/10.1103/PhysRev.94.630

Celauro, J.G., Torrealba, V.A., Karpyn, Z.T., Klise, K.A., Mckenna, S.A., 2014. Pore-scale Multiphase Flow Experiments in Bead Packs of Variable Eettability. Geofluids 14, 95–105. https://doi.org/10.1111/gfl.12045

Chandler, R., Koplik, J., Lerman, K., Willemsen, J.F., 1982. Capillary Displacement and Percolation in Porous Media. J. Fluid Mech. 119, 249–267. https://doi.org/10.1017/S0022112082001335

Chang, C.T.P., Watson, A.T., 1999. NMR Imaging of Flow Velocity in Porous Media. AIChE J. 45, 437–444. https://doi.org/10.1002/aic.690450302

Chang, D., Vinegar, H., Morriss, C., 1994. Effective Porosity, Producible Fluid and Permeability in Carbonates from NMR logging. SPWLA 35th Annu. Logging Symp. 1–21.

Clarke, A., Howe, A.M., Mitchell, J., Staniland, J., Hawkes, L., Leeper, K., 2015. Mechanism of Anomalously Increased Oil Displacement with Aqueous Viscoelastic Polymer Solutions. Soft Matter 11, 3536–3541. https://doi.org/10.1039/c5sm00064e

Colbourne, A.A., Sederman, A.J., Mantle, M.D., Gladden, L.F., 2016. Accelerating Flow Propagator Measurements for the Investigation of Reactive Transport in Porous Media. J. Magn. Reson. 272, 68–72. https://doi.org/10.1016/j.jmr.2016.08.018

Collins, A.G., 1975. Geochemistry of oilfield waters, Elsevier Scient.Publ. https://doi.org/10.1016/0012-8252(77)90073-3

Cotts, R.M., Hoch, M.J.R., Sun, T., Markert, J.T., 1989. Pulsed Field Gradient Stimulated Echo Methods for Improved NMR Diffusion Measurements in Heterogeneous Systems. J. Magn. Reson. 83, 252–266. https://doi.org/10.1016/0022-2364(89)90189-3

Coupé, P., Manjón, J. V., Gedamu, E., Arnold, D., Robles, M., Collins, D.L., 2010.

Robust Rician noise estimation for MR images. Med. Image Anal. 14, 483–493. https://doi.org/10.1016/j.media.2010.03.001

Daigle, H., Johnson, A., Gips, J.P., Sharma, M., 2014. Porosity Evaluation of Shales using NMR Secular Relaxation. Proc. 2nd Unconv. Resour. Technol. Conf. 1205–1216. https://doi.org/10.15530/urtec-2014-1905272

Darcy, H., 1856. Les fontaines publiques de la ville de Dijon, Exposition et application des principes a suivre et des formules a employer dans les questions de distribution d'eau; ouvrage terminé par un appendice relatif aux fournitures d'eau de plusieurs villes au filtrage des eaux et a la fabrication des tuyaux de fonte, de plomb, de tole et de bitume - Google Play Books [WWW Document]. URL https://play.google.com/books/reader?id=-FxYAAAAYAAJ&pg=GBS.PA10&hl=en_GB (accessed 12.24.21).

Dautriat, J., Gland, N., Dimanov, A., Raphanel, J., 2011. Hydromechanical Behavior of Heterogeneous Carbonate Rock under Proportional Triaxial Loadings. J. Geophys. Res. Solid Earth 116. https://doi.org/10.1029/2009JB000830

Davletbaev, A.Y., Ivaschenko, D.S., 2014. Non-Darcy flow Numerical Simulation and Pressure/Rate Transient Analysis for Ultra-Low Permeable Reservoirs. Soc. Pet. Eng. - SPE Russ. Oil Gas Explor. Prod. Tech. Conf. Exhib. 2014, RO G 2014 - Sustain. Optimising Prod. Challenging Limits with Technol. 1, 301–308. https://doi.org/10.2118/171174-ms

de Kort, D.W., Hertel, S.A., Appel, M., de Jong, H., Mantle, M.D., Sederman, A.J., Gladden, L.F., 2018a. Under-Sampling and Compressed Sensing of 3D Spatially-Resolved Displacement Propagators in Porous Media Using APGSTE-RARE MRI. Magn. Reson. Imaging 1–8. https://doi.org/10.1016/j.mri.2018.08.014

de Kort, D.W., Reci, A., Ramskill, N.P., Appel, M., de Jong, H., Mantle, M.D., Sederman, A.J., Gladden, L.F., 2018b. Acquisition of Spatially-Resolved Displacement Propagators using Compressed Sensing APGSTE-RARE MRI. J. Magn. Reson. 295, 45–56. https://doi.org/10.1016/j.jmr.2018.07.012

Demond, A.H., Roberts, P. V., 1991. Effect of Interfacial Forces on Two-Phase Capillary Pressure—Saturation Relationships. Water Resour. Res. 27, 423–437. https://doi.org/10.1029/90WR02408

Dernaika, M., Bjorn Wilson, O., M. Skjæveland, S., 2016. Drainage Capillary Pressure and Resistivity Index from Short-Wait Porous Plate Experiments 57, 369–376. https://doi.org/10.3997/2214-4609-pdb.248.224

DeSorcy, G. (Gerry), Warne, G.A., Lang, R.V. (Bob), S, J.G.R., Ashton, B.R., Campbell, G.R., Collyer, D.R., Dury, J., Robertson, W.D., Tutt, D.W., 1994. Determination of oil and gas reserves.

Dijk, P., Berkowitz, B., Bendel, P., 1999. Investigation of Flow in Water-Saturated Rock Fractures Using Nuclear Magnetic Resonance Imaging (NMRI). Water Resour. Res. 35, 347–360. https://doi.org/10.1029/1998WR900044

Diwu, P., Liu, T., You, Z., Jiang, B., Zhou, J., 2018. Effect of Low Velocity Non-Darcy Flow on Pressure Response in Shale and Tight Oil Reservoirs. Fuel 216, 398–406. https://doi.org/10.1016/j.fuel.2017.11.041

Donoho, D.L., 2006. Compressed sensing. IEEE Trans. Inf. Theory 52, 1289–1306. https://doi.org/Doi 10.1109/Tit.2006.871582

Dou, H.E., Ma, S.Y., Zou, C.Y., Yao, S.L., 2014. Threshold Pressure Gradient of Fluid Flow Through Multi-Porous Media in Low and Extra-low Permeability Reservoirs. Sci. China Earth Sci. 57, 2808–2818. https://doi.org/10.1007/s11430-014-4933-1

Doughty, D.A., Tomutsa, L., 1997. Imaging pore structure and connectivity by high resolution NMR microscopy. Int. J. rock Mech. Min. Sci. Geomech. Abstr. 34, 713. https://doi.org/10.1016/S1365-1609(97)00097-X

Dullien, F.A.L., Lai, F.S.Y., MacDonald, I.F., 1986. Hydraulic Continuity of Residual Wetting Phase in Porous Media. J. Colloid Interface Sci. 109, 201–218. https://doi.org/10.1016/0021-9797(86)90295-X

Dupuis, D., Lewandowski, F.Y., Steiert, P., Wolff, C., 1994. Shear Thickening and Time-Dependent Phenomena: The Case of Polyacrylamide Solutions. J. Nonnewton. Fluid Mech. 54, 11–32. https://doi.org/10.1016/0377-0257(94)80013-8

Eberhard, U., Seybold, H.J., Floriancic, M., Bertsch, P., Jiménez-Martínez, J., Andrade, J.S., Holzner, M., 2019. Determination of the Effective Viscosity of non-Newtonian Fluids Flowing Through Porous Media. Front. Phys. 7, 1–9. https://doi.org/10.3389/fphy.2019.00071

Edelstein, W.A., Glover, G.H., Hardy, C.J., Redington, R.W., 1986. The Intrinsic Signal-to-Noise Ratio in NMR Imaging. Magn. Reson. Med. 3, 604–618. https://doi.org/10.1002/mrm.1910030413

Farrar, T.C., Becker, E.D., 1971. Pulse and Fourier Transform NMR: Introduction to Theory and Methods. Academic Press. https://doi.org/10.1016/B978-0-08-091812-9.50008-9

Fayed, M.E., Otten, L., 1984. Fluidization Phenomena and Fluidized Bed Technology, Handbook of Powder Science and Technology.

Ferréol, B., Rothman, D.H., 1995. Lattice-Boltzmann simulations of flow through Fontainebleau sandstone. Transp. Porous Media 20, 3–20. https://doi.org/10.1007/BF00616923

Frahm, J., Merboldt, K.D., Hänicke, W., 1987. Localized Proton Spectroscopy using Stimulated Echoes. J. Magn. Reson. 72, 502–508. https://doi.org/10.1016/0022-2364(87)90154-5

Fredrich, J.T., Lakshtanov, D.L., Lane, N.M., Liu, E.B., Natarajan, C.S., Ni, D.M., Toms, J.J., 2014. Digital Rocks : Developing an emerging technology through to a proven capability deployed in the business. SPE Annu. Tech. Conf. Exhib. https://doi.org/10.2118/170752-MS

Gao, H., Wang, Y., Xie, Y., Ni, J., Li, T., Wang, C., Xue, J., 2021. Imbibition and Oil Recovery Mechanism of Fracturing Fluids in Tight Sandstone Reservoirs. ACS Omega 6, 1991–2000. https://doi.org/10.1021/acsomega.0c04945

Gbadamosi, A.O., Junin, R., Manan, M.A., Agi, A., Yusuff, A.S., 2019. An Overview of Chemical Enhanced Oil Recovery: Recent Advances and Prospects,

International Nano Letters. Springer Berlin Heidelberg. https://doi.org/10.1007/s40089-019-0272-8

Ghiselin, D., 2014. Integrated rock and fluid analysis services aim to improve enhanced oil recovery - Offshore [WWW Document]. Offshore Digit. Mag. URL https://www.offshore-mag.com/articles/print/volume-74/issue-1/departments/drilling-production/integrated-rock-and-fluid-analysis-services-aim-to-improve-enhanced-oil-recovery.html (accessed 4.21.18).

Gladden, L.F., 1994. Nuclear Magnetic Resonance in Chemical Engineering: Principles and Applications. Chem. Eng. Sci. 49, 3339–3408. https://doi.org/10.1016/0009-2509(94)00129-4

Glover, P., Mansfield, S.P., 2002. Limits to Magnetic Resonance Microscopy. Reports Prog. Phys. 65, 1489–1511. https://doi.org/10.1088/0034-4885/65/10/203

Goebel, A., Lunkenheimer, K., 1997. Interfacial Tension of the Water/n-Alkane Interface. Langmuir 13, 369–372. https://doi.org/10.1021/la960800g

González, J.M., Müller, A.J., Torres, M.F., Sáez, A.E., 2005. The Role of Shear and Elongation in the Flow of Solutions of Semi-Flexible Polymers Through Porous Media. Rheol. Acta. https://doi.org/10.1007/s00397-004-0421-4

Gudbjartsson, H., Patz, S., 1995. The Rician Distribution of Noisy MRI Data. J. Exp. Psychol. Gen. 910–914.

Gullion, T., Baker, D.B., Conradi, M.S., 1990. New, Compensated Carr-Purcell Sequences. J. Magn. Reson. 89, 479–484. https://doi.org/10.1016/0022-2364(90)90331-3

Gunther, H., 2013. NMR Spectroscopy: Basic Principles, Concepts and Applications in Chemistry.

Hahn, E.L., 1950. Spin echoes. Phys. Rev. 80, 580–594. https://doi.org/10.1103/PhysRev.80.580

Hall, L.D., Rajanayagam, V., 1987. Thin-slice, chemical-shift imaging of oil and water in sandstone rock at 80 MHz. J. Magn. Reson. 74, 139–146. https://doi.org/10.1016/0022-2364(87)90087-4

Hao, F., Cheng, L.S., Hassan, O., Hou, J., Liu, C.Z., Feng, J.D., 2008. Threshold Pressure Gradient in Ultra-Low Permeability Reservoirs. Pet. Sci. Technol. 26, 1024–1035. https://doi.org/10.1080/10916460701675033

Harris, F.J., 1978. On the Use of Windows for Harmonic Analysis with the Discrete Fourier Transform. Proc. IEEE 66, 51–83. https://doi.org/10.1109/PROC.1978.10837

Haugen, Å., Mani, N., Svenningsen, S., Brattekås, B., Graue, A., Ersland, G., Fernø, M.A., 2014. Miscible and Immiscible Foam Injection for Mobility Control and EOR in Fractured Oil-Wet Carbonate Rocks. Transp. Porous Media 104, 109–131. https://doi.org/10.1007/s11242-014-0323-6

Hennig, J., 1999. K-space Sampling Strategies. Eur. Radiol. 9, 1020–1031. https://doi.org/10.1007/s003300050788

Hennig, J., Nauerth, A., Friedburg, H., 1986. RARE Imaging : A Fast Imaging Method for Clinical MR 833, 823–833. https://doi.org/10.1002/mrm.1910030602

Holland, D.J., Malioutov, D.M., Blake, A., Sederman, A.J., Gladden, L.F., 2010. Reducing Data Acquisition Times in Phase-Encoded Velocity Imaging using Compressed Sensing. J. Magn. Reson. 203, 236–246. https://doi.org/10.1016/j.jmr.2010.01.001

Homsy, G.., 1987. Viscous Fingering in Porous Media. Annu. Rev. Fluid Mech. 19, 271–311. https://doi.org/0066-4189/87/01 1 5-027 1

Hoult, D.I., Richards, R.E., 1975. Critical Factors in the Design of Sensitive High Resolution Nuclear Magnetic Resonance Spectrometers. Proc. R. Soc. London. Ser. A, Math. Phys. Sci. 344, 311–340. https://doi.org/10.1098/rspa.1975.0104

Huang, L., Mikolajczyk, G., Küstermann, E., Wilhelm, M., Odenbach, S., Dreher, W., 2017. Adapted MR Velocimetry of Slow Liquid Flow in Porous Media. J. Magn. Reson. 276, 103–112. https://doi.org/10.1016/j.jmr.2017.01.017

Hübner, W., 2014. Studying the pore space of cuttings by NMR and μCT. J. Appl. Geophys. 104, 97–105. https://doi.org/10.1016/j.jappgeo.2014.02.016

Hürlimann, M.D., Venkataramanan, L., 2002. Quantitative Measurement of Two-Dimensional Distribution Functions of Diffusion and Relaxation in Grossly Inhomogeneous Fields. J. Magn. Reson. 157, 31–42. https://doi.org/10.1006/jmre.2002.2567

Ji, Y., Baud, P., Vajdova, V., Wong, T.F., 2012. Characterization of Pore Geometry of Indiana Limestone in Relation to Mechanical Compaction. Oil Gas Sci. Technol. 67, 753–775. https://doi.org/10.2516/ogst/2012051

Kalam, M.Z., 2012. Digital Rock Physics for fast and accurate special core analysis in carbonates. New Technol. Oil Gas Ind. https://doi.org/10.5772/3216

Kalam, M.Z., Hammadi, K. Al, Wilson, O.B., Dernaika, M., Samosir, H., 2006. Importance of Porous Plate Measurements on Carbonates At Pseudo Reservoir. Advances 1–12.

Karger, J., Pfeifer, H., Heink, W., 1988. Principles and Application of Self-Diffusion Measurements by Nuclear Magnetic Resonance. Adv. Magn. Opt. Reson. 12, 1–89. https://doi.org/10.1016/B978-0-12-025512-2.50004-X

Karlsons, K., de Kort, D.W., Sederman, A.J., Mantle, M.D., de Jong, H., Appel, M., Gladden, L.F., 2019. Identification of Sampling Patterns for High-Resolution Compressed Sensing MRI of Porous Materials: 'Learning' from X-Ray Microcomputed Tomography Data. J. Microsc. https://doi.org/10.1111/jmi.12837

Kleinberg, R.L., Straley, C., Kenyon, W.E., Akkurt, R., Farooqui, S.A., 1993. Nuclear Magnetic Resonance of rocks: T1 vs T2. SPE Annu. Tech. Conf. Exhib. 553–563. https://doi.org/10.2118/26470-MS

Kohler, N., Chauveteau, G., 1981. Xanthan Polysaccharide Plugging Behavior in Porous Media - Preferential Use of Fermentation Broth. JPT, J. Pet. Technol. 33, 349–358. https://doi.org/10.2118/7425-PA

Koroteev, D., Dinariev, O., Evseev, N., Klemin, D., Nadeev, A., Safonov, S., Gurpinar, O., Berg, S., Kruijsdijk, C. van, Armstrong, R., Myers, M.T., Hathon, L., Jong, H. de, 2014. Direct hydrodynamic simulation of multiphase flow in porous rock. Int. Symp. Soc. Core Anal. 55, 1–12. https://doi.org/SCA2013-014

Koroteev, D., Dinariev, O., Evseev, N., Klemin, D., Safonov, S., Gurpinar, O., Berg, S., VanKruijsdijk, C., Myers, M., Hathon, L., de Jong, H., Armstrong, R., 2013. Application of Digital Rock technology for chemical EOR screening. SPE Enhanc. Oil Recover. Conf. 12. https://doi.org/10.2118/165258-MS

Kutsovsky, Y.E., Scriven, L.E., Davis, H.T., Hammer, B.E., Kutsovsky, Y.E., Scriven, L.E., Davis, H.T., 1996. NMR Imaging of Velocity Profiles and Velocity Distributions in Bead Packs 863. https://doi.org/10.1063/1.868867

Lake, L.W., 1989. Enhanced Oil Recovery. Prentice Hall.

Latour, L.L., Mitra, P.P., Kleinberg, R.L., Sotak, C.H., 1993. Time-Dependent Diffusion Coefficient of Fluids in Porous Media as a Probe of Surface-to-Volume Ratio. J. Magn. Reson. - Ser. A 101, 342–346. https://doi.org/10.1006/jmra.1993.1056

Lauterbur, P.., 1973. Image Formation by Induced Local Interactions: Examples Employing Nuclear Magnetic Resonance. Nat. Phys. Sci. 22, 190–191.

Lebon, L., Leblond, J., Hulin, J.P., 1997. Experimental Measurement of Dispersion Processes at Short Times Using a Pulsed Field Gradient NMR Technique. Phys. Fluids 9, 481–490. https://doi.org/10.1063/1.869208

Lenormand, R., 1990. Liquids in Porous Media. J. Phys. Condens. Matter 2. https://doi.org/10.1088/0953-8984/2/S/008

Lenormand, R., Touboul, E., Zarcone, C., 1988. Numerical Models and Experiments on Immiscible Displacements in Porous Media. J. Fluid Mech. 189, 165–187. https://doi.org/10.1017/S0022112088000953

Lenormand, R., Zarcone, C., 1989. Capillary Fingering: Percolation and Fractal Dimension. Transp. Porous Media 4, 599–612. https://doi.org/10.1007/BF00223630

Lenormand, R., Zarcone, C., 1984. Role of Roughness and Edges During Imbibition in Square Capillaries. Proc. - SPE Annu. Tech. Conf. Exhib. 1984-Septe. https://doi.org/10.2523/13264-ms

Lenormand, R., Zarcone, C., Sarr, A., 1983. Mechanisms of the Displacement of one Fluid by Another in a Network of Capillary Ducts. J. Fluid Mech. 135, 337–353. https://doi.org/10.1017/S0022112083003110

Levitt, M.., 2000. Spin Dynamics: Basics of Nuclear Magnetic Resonance, John Wiley & Sons Ltd. https://doi.org/10.1002/cmr.a.20130

Li, L., Chen, Q., Marble, A.E., Romero-Zerón, L., Newling, B., Balcom, B.J., 2009. Flow Imaging of Fluids in Porous Media by MagnetizationPrepared Centric-Scan SPRITE. J. Magn. Reson. 197, 1–8. https://doi.org/10.1016/j.jmr.2008.10.020

Li, M., Xiao, D., Shakerian, M., Afrough, A., Goora, F., 2016. Magnetic Resonance

Imaging of Core Flooding in a Metal Core Holder 1–12.

Lin, Q., Bijeljic, B., Rieke, H., Blunt, M.J., 2018. Visualization and Quantification of Capillary Drainage in Pore Space of Laminated Sandstone by a Porous Plate Method Using Differential Imaging X-Ray Micro-Tomography 4, 244–253.

Lindquist, W.B., 2006. The geometry of primary drainage. J. Colloid Interface Sci. 296, 655–668. https://doi.org/10.1016/j.jcis.2005.09.041

Liu, M., Mao, X., Ye, C., Huang, H., Nicholson, J.K., Lindon, J.C., 1998. Improved WATERGATE Pulse Sequence for Solvent Suppression in NMR Spectroscopy. J. Magn. Reson. 132, 125–129.

Liu, Y., Difoggio, R., Sanderlin, K., Perez, L., Zhao, J., 2011. Measurement of density and viscosity of dodecane and decane with a piezoelectric tuning fork over 298-448 K and 0.1-137.9 MPa. Sensors Actuators, A Phys. 167, 347–353. https://doi.org/10.1016/j.sna.2011.03.017

Lovell, P.A., 1989. Dilute Solution Viscometry. Compr. Polym. Sci. Suppl. 173–197. https://doi.org/10.1016/b978-0-08-096701-1.00009-4

Luo, E., Wang, X., Hu, Y., Wang, J., Liu, L., 2019. Analytical Solutions for Non-Darcy Transient Flow With the Threshold Pressure Gradient in Multiple-Porosity Media. Math. Probl. Eng. 2019. https://doi.org/10.1155/2019/2618254

Lustig, M., Donoho, D., Pauly, J.M., 2007. Sparse MRI: The Application of Compressed Sensing for Rapid MR Imaging. Magn. Reson. Med. 58, 1182–1195. https://doi.org/10.1002/mrm.21391

Lustig, M., Donoho, D.L., Santos, J.M., Pauly, J.M., 2008. Compressed sensing MRI: A look at how CS can improve on current imaging techniques. IEEE Signal Process. Mag. 25, 72–82. https://doi.org/10.1109/MSP.2007.914728

Macovski, A., 1996. Noise in MRI. Magn. Reson. Med. 36, 494–497.

Magdoom, K.N., Zeinomar, A., Lonser, R.R., Sarntinoranont, M., Mareci, T.H., 2019. Phase Contrast MRI of Creeping Flows Using Stimulated Echo. J. Magn. Reson. 299, 49–58. https://doi.org/10.1016/j.jmr.2018.12.009

Mahani, H., Keya, A.L., Berg, S., Bartels, W.B., Nasralla, R., Rossen, W., 2015. Driving Mechanism of Low Salinity Flooding in Carbonate Rocks. Eur. 2015 210–236. https://doi.org/10.2118/174300-ms

Mahani, H., Menezes, R., Berg, S., Fadili, A., Nasralla, R., Voskov, D., Joekar-Niasar, V., 2017. Insights into the Impact of Temperature on the Wettability Alteration by Low Salinity in Carbonate Rocks. Energy and Fuels 31, 7839–7853. https://doi.org/10.1021/acs.energyfuels.7b00776

Mansfield, P., Grannell, P.K., 1973. NMR Diffraction in Solids. Solid State Phys. 6, 422–426.

Manz, B., Alexander, P., Gladden, L.F., 1999a. Correlations Between Dispersion and Structure in Porous Media Probed by Nuclear Magnetic Resonance. Phys. Fluids 11, 259–267. https://doi.org/10.1063/1.869876

Manz, B., Gladden, L.F., Warren, P.B., 1999b. Flow and Dispersion in Porous Media:

Lattice-Boltzmann and NMR Studies. AIChE J. 45, 1845–1854. https://doi.org/10.1002/aic.690450902

Marbach, W., Hertz, H.G., 1996. Self- and Mutual Diffusion Coefficients of Some n-Alkanes at Elevated Temperatures and Pressures. Zeitschrift fur Phys. Chemie 193, 19–40. https://doi.org/10.1524/zpch.1996.193.part_1_2.019

Martel, K.E., Martel, R., Lefebvre, R., Gélinas, P.J., 1998. Laboratory Study of Polymer Solutions Used for Mobility Control during in Situ NAPL Recovery. Gr. Water Monit. Remediat. https://doi.org/10.1111/j.1745-6592.1998.tb00734.x

Meiboom, S., Gill, D., 1958. Modified Spin-Echo Method for Measuring Nuclear Relaxation Times. Rev. Sci. Instrum. 29, 688–691. https://doi.org/10.1063/1.1716296

Mishra, S., Bera, A., Mandal, A., 2014. Effect of Polymer Adsorption on Permeability Reduction in Enhanced Oil Recovery. J. Pet. Eng. 2014, 1–9. https://doi.org/10.1155/2014/395857

Mitchell, J., 2014. Rapid Measurements of Heterogeneity in Sandstones using Low-Field Nuclear Magnetic Resonance. J. Magn. Reson. 240, 52–60. https://doi.org/10.1016/j.jmr.2014.01.006

Mitchell, J., Chandrasekera, T.C., Gladden, L.F., 2012. Numerical Estimation of Relaxation and Diffusion Distributions in Two Dimensions. Prog. Nucl. Magn. Reson. Spectrosc. 62, 34–50. https://doi.org/10.1016/j.pnmrs.2011.07.002

Mitchell, J., Chandrasekera, T.C., Gladden, L.F., 2010a. Obtaining True Transverse Relaxation Time Distributions in High-Field NMR Measurements of Saturated Porous Media: Removing the Influence of Internal Gradients. J. Chem. Phys. 132. https://doi.org/10.1063/1.3446805

Mitchell, J., Chandrasekera, T.C., Holland, D.J., Gladden, L.F., Fordham, E.J., 2013a. Magnetic Resonance Imaging in Laboratory Petrophysical Core Analysis. Phys. Rep. 526, 165–225. https://doi.org/10.1016/j.physrep.2013.01.003

Mitchell, J., Fordham, E.J., 2014. Contributed Review : Nuclear magnetic resonance core analysis at 0.3 T 85, 0–17. https://doi.org/10.1063/1.4902093

Mitchell, J., Gladden, L.F., Chandrasekera, T.C., Fordham, E.J., 2014. Low-Field Permanent Magnets for Industrial Process and Quality Control. Prog. Nucl. Magn. Reson. Spectrosc. 76, 1–60. https://doi.org/10.1016/j.pnmrs.2013.09.001

Mitchell, J., Johns, M.L., Gladden, L.F., Fordham, E.J., 2010b. Nuclear Magnetic Resonance Relaxation and Diffusion in the Presence of Internal Gradients: The Effect of Magnetic Field Strength. Phys. Rev. E - Stat. Nonlinear, Soft Matter Phys. 81, 1–19. https://doi.org/10.1103/PhysRevE.81.026101

Mitchell, J., Lyons, K., Howe, A.M., Clarke, A., 2016. Viscoelastic Polymer Flows and Elastic Turbulence in Three-Dimensional Porous Structures. Soft Matter 12, 460–468. https://doi.org/10.1039/c5sm01749a

Mitchell, Jonathan, Staniland, J., Chassagne, R., Fordham, E.J., 2012. Quantitative In Situ Enhanced Oil Recovery Monitoring Using Nuclear Magnetic Resonance. Transp. Porous Media 94, 683–706. https://doi.org/10.1007/s11242-012-0019-8

Mitchell, J., Staniland, J., Chassagne, R., Mogensen, K., Frank, S., Fordham, E.J., 2013b. Mapping Oil Saturation Distribution in a Limestone Plug with Low-Field Magnetic Resonance. J. Pet. Sci. Eng. 108, 1–8. https://doi.org/10.1016/j.petrol.2013.04.008

Mohamid, S., Quadri, R., Shoaib, M., Alsumaiti, A.M., Alhassan, S.M., Petroleum, T., 2015. Screening of Polymers for EOR in High Temperature , High Salinity and Carbonate Reservoir Conditions. Int. Pet. Technol. Conf. https://doi.org/https://doi.org/10.2523/IPTC-18436-MS

Morozov, V.A., 1965. Regularization of Incorrectly posed problems and the Choice of Regularization Parameter 242–251.

Morris, E.R., Cutler, A.N., Ross-Murphy, S.B., Rees, D.A., Price, J., 1981. Concentration and shear rate dependence of viscosity in random coil polysaccharide solutions. Carbohydr. Polym. 1, 5–21. https://doi.org/10.1016/0144-8617(81)90011-4

Muggeridge, A., Cockin, A., Webb, K., Frampton, H., Collins, I., Moulds, T., Salino, P., 2014. Recovery Rates, Enhanced oil Recovery and Technological Limits. Philos. Trans. R. Soc. A Math. Phys. Eng. Sci. 372. https://doi.org/10.1098/rsta.2012.0320

Murphy, B.W., Carson, P.L., Ellis, J.H., Zhang, Y.T., Hyde, R.J., Chenevert, T.L., 1993. Signal-to-noise measures for magnetic resonance imagers. Magn. Reson. Imaging 11, 425–428. https://doi.org/10.1016/0730-725X(93)90076-P

Nyquist, H., 1928. Certain Topics in Telegraph Transmission Theory. Am. Teleph. Telegr. Co. 21, 265–271. https://doi.org/10.1109/5.989875

Ogg, R.J., Kingsley, P.B., Taylor, J.S., 1994. WET, a T1-and B1-insensitive water-suppression method for in vivo localized 1H NMR spectroscopy. J. Magn. Reson. 104, 1–10.

Øren, P.E., Bakke, S., Held, R., 2007. Direct pore-scale computation of material and transport properties for North Sea reservoir rocks. Water Resour. Res. 43, 1–11. https://doi.org/10.1029/2006WR005754

Packer, K.J., 1969. The Study of Slow Coherent Molecular Motion by Pulsed Nuclear Magnetic Resonance. Mol. Phys. 17, 355–368. https://doi.org/10.1080/00268976900101131

Panfilov, M., Fourar, M., 2006. Physical Splitting of Nonlinear Effects in High-Velocity Stable Flow Through Porous Media. Adv. Water Resour. 29, 30–41. https://doi.org/10.1016/j.advwatres.2005.05.002

Pelc, N.J., Bernstein, M.A., Shimakawa, A., Glover, G.H., 1991. Encoding Strategies for Three-Direction Phase-Contrast MR Imaging of Flow. J. Magn. Reson. Imaging 1, 405–413. https://doi.org/10.1002/jmri.1880010404

Price, W.S., 2017. Diffusion NMR of Confined Systems : Fluid Transport in Porous Solids and Heterogeneous Materials, 9th ed. The Royal Society of Chemistry.

Price, W.S., 1997. Pulsed-Field Gradient Nuclear Magnetic Resonance as a Tool for Studying Translational Diffusion. Part 1. Basic Theory. Concepts Magn. Reson. 9, 299–336. https://doi.org/10.1002/chin.199750339

Ramskill, N.P., Bush, I., Sederman, A.J., Mantle, M.D., Benning, M., Anger, B.C., Appel, M., Gladden, L.F., 2016. Fast Imaging of Laboratory Core Floods using 3D Compressed Sensing RARE MRI. J. Magn. Reson. 270, 187–197. https://doi.org/10.1016/j.jmr.2016.07.017

Ramskill, N.P., Sederman, A.J., Mantle, M.D., Appel, M., de Jong, H., Gladden, L.F., 2018. In Situ Chemically-Selective Monitoring of Multiphase Displacement Processes in a Carbonate Rock Using 3D Magnetic Resonance Imaging. Transp. Porous Media. https://doi.org/10.1007/s11242-017-0945-6

Reci, A., Sederman, A.J., Gladden, L.F., 2017. Obtaining Sparse Distributions in 2D Inverse Problems. J. Magn. Reson. 281, 188–198. https://doi.org/10.1016/j.jmr.2017.05.010

Redpath, T.W., 1998. Signal-to-noise ratio in MRI. Br. J. Radiol. 71, 704–707. https://doi.org/10.1259/bjr.71.847.9771379

Rellegadla, S., Prajapat, G., Agrawal, A., 2017. Polymers for Enhanced Oil Recovery: Fundamentals and Selection Criteria. Appl. Microbiol. Biotechnol. 101, 4387–4402. https://doi.org/10.1007/s00253-017-8307-4

Reynolds, A.M., Reavell, S. V., Harral, B.B., 2000. Flow and Dispersion Through a Close-Packed Fixed Bed of Spheres. Phys. Rev. E - Stat. Physics, Plasmas, Fluids, Relat. Interdiscip. Top. 62, 3632–3639. https://doi.org/10.1103/PhysRevE.62.3632

Romanenko, K., Xiao, D., Balcom, B.J., 2012. Velocity Field Measurements in Sedimentary Rock Cores by Magnetization Prepared 3D SPRITE. J. Magn. Reson. 223, 120–128. https://doi.org/10.1016/j.jmr.2012.08.004

Roshani, S., 1990. Elucidation of Local and Global Structural Properties of Packed Bed Configurations. University of Leeds.

Sahimi, M., 2010. Flow and Transport in Porous Media and Fractured Rock. From classical to modern approaches, Zeitschrift für Physikalische Chemie.

Satter, A., Iqbal, G.M., 2016. Reservoir Rock Properties, Reservoir Engineering. https://doi.org/10.1016/b978-0-12-800219-3.00003-6

Scheenen, T.W.J., Van Dusschoten, D., De Jager, P.A., Van As, H., 2000. Quantification of Water Transport in Plants with NMR Imaging. J. Exp. Bot. 51, 1751–1759. https://doi.org/10.1093/jexbot/51.351.1751

Scheven, U.M., 2013. Pore-scale Mixing and Transverse Dispersivity of Randomly Packed Monodisperse Spheres. Phys. Rev. Lett. 110, 2–6. https://doi.org/10.1103/PhysRevLett.110.214504

Scheven, U.M., Seland, J.G., Cory, D.G., 2005a. NMR-Propagator Measurements in Porous Media in the Presence of Surface Relaxation and Internal Fields. Magn. Reson. Imaging 23, 363–365. https://doi.org/10.1016/j.mri.2004.11.054

Scheven, U.M., Seland, J.G., Cory, D.G., 2004. NMR Propagator Measurements on Flow Through a Random Pack of Porous Glass Beads and How they are Affected by Dispersion, Relaxation, and Internal Field Inhomogeneities. Phys. Rev. E - Stat. Nonlinear, Soft Matter Phys. 69, 1–9. https://doi.org/10.1103/PhysRevE.69.021201

Scheven, U.M., Sen, P.N., 2002. Spatial and Temporal Coarse Graining for Dispersion in Randomly Packed Spheres. Phys. Rev. Lett. 89, 1–4. https://doi.org/10.1103/PhysRevLett.89.254501

Scheven, U.M., Verganelakis, D., Harris, R., Johns, M.L., Gladden, L.F., 2005b. Quantitative Nuclear Magnetic Resonance Measurements of Preasymptotic Dispersion in Flow Through Porous Media. Phys. Fluids 17, 1–7. https://doi.org/10.1063/1.2131871

Schön, J.H., 2015. Physical properties of rocks: Fundamentals and principles of petrophysics, 1st ed. Elsevier B.V, Amsterdam.

Sederman, A.., Gladden, L.., 2001. Magnetic Resonance Visualisation of Single- and Two-Phase Flow in Porous Media. Magn. Reson. Imaging 19, 339–343. https://doi.org/10.1016/S0730-725X(01)00246-6

Senthilkumaran, N., Thimmiaraja, J., 2014. Histogram Equalization for Image Enhancement Using MRI brain images 2–5. https://doi.org/10.1109/WCCCT.2014.45

Seybold, H.J., Eberhard, U., Secchi, E., Cisne, R.L.C., Jiménez-Martínez, J., Andrade, R.F.S., Araújo, A.D., Holzner, M., Andrade, J.S., 2021. Localization in Flow of Non-Newtonian Fluids Through Disordered Porous Media. Front. Phys. 9, 33–37. https://doi.org/10.3389/fphy.2021.635051

Seymour, J.D., Callaghan, P.T., 1997a. Generalized Approach to NMR Analysis of Flow and Dispersion in Porous Media. AIChE J. 43, 2096–2111. https://doi.org/10.1002/aic.690430817

Seymour, J.D., Callaghan, P.T., 1997b. Transport in Ordered and Disordered Porous Media I: The Cellular Average and the Use of Weighting Functions. AIChE J. 43, 2096–2111. https://doi.org/10.1002/aic.690430817

Shende, T.S. of V.I. for N.-N.T.-P.F. in P.M., Niasar, V., Babaei, M., 2021. Pore-scale Simulation of Viscous Instability for Non-Newtonian Two-Phase Flow in Porous Media. J. Nonnewton. Fluid Mech. 296, 104628. https://doi.org/10.1016/j.jnnfm.2021.104628

Sheng, J., 2011. Modern Chemical Enhanced Oil Recovery, Journal of Chemical Information and Modeling. https://doi.org/10.1017/CBO9781107415324.004

Shikhov, I., D'Eurydice, M.N., Arns, J.-Y., Arns, C.H., 2017. An experimental and numerical study of relative permeability estimates using spatially resolved T1-z NMR. Transp. Porous Media 118, 225–250. https://doi.org/10.1007/s11242-017-0855-7

Shukla, M.N., Vallatos, A., Phoenix, V.R., Holmes, W.M., 2016. Accurate Phase-Shift Velocimetry in Rock. J. Magn. Reson. 267, 43–53. https://doi.org/10.1016/j.jmr.2016.04.006

Shutang, G., Huabin, L., Hongfu, L., 1995. Laboratory Investigation of Combination of Alkaline-Surfactant-Polymer for Daqing EOR. SPE Reserv. Eng. 10 (3), 194–197.

Singer, P.M., Mitchell, J., Fordham, E.J., 2016. Characterizing Dispersivity and Stagnation in Porous Media Using NMR Flow Propagators. J. Magn. Reson.

270, 98–107. https://doi.org/10.1016/j.jmr.2016.07.004

Singh, K., 2018. Imbibition in carbonate rocks: high-resolution time-resolved synchrotron X-ray micro-tomography [WWW Document]. URL https://figshare.com/articles/media/Imbibition_in_carbonate_rocks_high-resolution_time-resolved_synchrotron_X-ray_micro-tomography/7082900/1 (accessed 11.28.21).

Singh, K., Menke, H., Andrew, M., Lin, Q., Rau, C., Blunt, M.J., Bijeljic, B., 2017. Dynamics of Snap-off and Pore-Filling Events During Two-Phase Fluid Flow in Permeable Media. Sci. Rep. 7, 1–13. https://doi.org/10.1038/s41598-017-05204-4

Singh, K., Menke, H., Andrew, M., Rau, C., Bijeljic, B., Blunt, M.J., 2018. Data Descriptor: Time-Resolved Synchrotron X-ray Microtomography Datasets of Drainage and Imbibition in Carbonate Rocks. Sci. Data 5, 1–8. https://doi.org/10.1038/sdata.2018.265

Smallcombe, S.H., Patt, S.L., Keifer, P.A., 1995. WET Solvent Suppression and Its Applications to LC NMR and High-Resolution NMR Spectroscopy. J. Magn. Reson. 117, 295–303. https://doi.org/https://doi.org/10.1006/jmra.1995.0759

Spindler, N., Galvosas, P., Pohlmeier, A., Vereecken, H., 2011. NMR Velocimetry with 13-interval Stimulated Echo Multi-Slice Imaging in Natural Porous Media Under Low Flow Rates. J. Magn. Reson. 212, 216–223. https://doi.org/10.1016/j.jmr.2011.07.004

Spinler, E.A., Baldwin, B.A., Graue, A., 1999. Simultaneous Measurement of Multiple Capillary Pressure Curves From Wettability and Rock Property Variations Within Single Rock Plugs.

Stejskal, E.O., Tanner, J.E., 1964. Spin Diffusion Measurements : Spin Echoes in the Presence of a Time-Dependent Field Gradient. J. Chem. Phys. 42.

Stilbs, P., 1987. Fourier Pulsed-Gradient Studies of Molecular Diffusion. Prog. NMR Spectrosc. 19, 1–45.

Sullivan, S.P., Sederman, A.J., Johns, M.L., Gladden, L.F., 2007. Verification of Shear-Thinning LB Simulations in Complex Geometries. J. Nonnewton. Fluid Mech. 143, 59–63. https://doi.org/10.1016/j.jnnfm.2006.12.008

Sylta, K.E.., 2010. Primary Drainage Capillary Pressure Curves in Heterogeneous Carbonates with Ultracentrifuge and NMR. (Master's thesis Pet. Technol. Physics, Univ. Bergen). University of Bergen.

Tahmasebi, P., Sahimi, M., 2012. Reconstruction of three-dimensional porous media using a single thin section. Phys. Rev. E - Stat. Nonlinear, Soft Matter Phys. 85, 1–13. https://doi.org/10.1103/PhysRevE.85.066709

Tang, C., Blatter, D.D., Parker, D.L., 1993. Accuracy of Phase-Contrast Flow Measurements in the Presence of Partial-Volume Effects. J. Magn. Reson. Imaging 3, 377–385. https://doi.org/10.1002/jmri.1880030213

Tanner, J.E., 1970. Use of the Stimulated Echo in NMR Fiffusion Studies. J. Chem. Phys. 52, 2523–2526. https://doi.org/10.1063/1.1673336

Tapias Hernández, F.A., Moreno, R.B.Z.L., 2020. The Effectiveness of Computed Tomography for the Experimental Assessment of Surfactant-Polymer Flooding. Oil Gas Sci. Technol. 75. https://doi.org/10.2516/ogst/2019069

Terry, R.E., 2001. Enhanced Oil Recovery, in: Encyclopedia of Physical Science and Technology. pp. 503–518.

Tessier, J.J., Packer, K.J., 1998. The Characterization of Multiphase Fluid Transport in a Porous Solid by Pulsed Gradient Stimulated Echo Nuclear Magnetic Resonance. Phys. Fluids 10, 75–85. https://doi.org/10.1063/1.869551

Uhlenbeck, G.E., Ornstein, L.S., 1991. I . Brownian Motion.

Urlacher, B., Noble, O., 1997. Xanthan gum, in: Imeson, A. (Ed.), Thickening and Gelling Agents for Food. Chapman & Hall.

Vallatos, A., Al-Mubarak, H.F.I., Mullin, J.M., Holmes, W.M., 2018. Accuracy of Phase-Contrast Velocimetry in Systems with Skewed Intravoxel Velocity Distributions. J. Magn. Reson. 296, 121–129. https://doi.org/10.1016/j.jmr.2018.09.002

Van Batenburg, D.W., Berg, S., Oedai, S., Elewaut, K., 2015. Visualization of Oil Mobilization in ASP Core Floods Using X-ray CT Imaging. Soc. Pet. Eng. - SPE Kuwait Oil Gas Show Conf. https://doi.org/10.2118/175407-ms

Verganelakis, D.A., Crawshaw, J., Johns, M.L., Mantle, M.D., Scheven, U., Sederman, A.J., Gladden, L.F., 2005. Displacement Propagators of Brine Flowing within Different Types of Sedimentary Rock. Magn. Reson. Imaging 23, 349–351. https://doi.org/10.1016/j.mri.2004.11.066

Vidales, A.M., Riccardo, J.L., Zgrablich, G., 1998. Pore-level Modelling of Wetting on Correlated Porous Media. J. Phys. D. Appl. Phys. 31, 2861–2868. https://doi.org/10.1088/0022-3727/31/20/021

Vinegar, H.J., 1986. X-Ray CT and NMR imaging of rocks. J. Pet. Technol. 38, 257–259. https://doi.org/10.2118/15277-PA

Volokitin, Y., Looyestijn, W.J., Slijkerman, W.F.J., Hofman, J.P., 2001. A Practical Approach to Obtain Primary Drainage Capillary Pressure Curves from NMR Core and Log Data. Petrophysics 42, 334–343.

Waggoner, R.A., Fukushima, E., 1996. Velocity Distribution of Slow Fluid Flows in Bentheimer Sandstone: An NMRI and Propagator Study. Magn. Reson. Imaging 14, 1085–1091. https://doi.org/10.1016/S0730-725X(96)00110-5

Wang, L., Li, Y., Zhao, G., Chen, N., Xu, Y., 2019. Experimental Investigation of Flow Characteristics in Porous Media at Low Reynolds Numbers (Re → 0) under Different Constant Hydraulic Heads. Water (Switzerland) Water 2019, 1–5.

Wang, X., Sheng, J.J., 2017. Effect of Low-Velocity Non-Darcy Flow on Well Production Performance in Shale and Tight Oil Reservoirs. Fuel 190, 41–46. https://doi.org/10.1016/j.fuel.2016.11.040

Wang, X., Yin, H., Zhao, X., Li, B., Yang, Y., 2019. Microscopic Remaining Oil Distribution and Quantitative Analysis of Polymer Flooding Based on CT

Scanning. Adv. Geo-Energy Res. 3, 448–456. https://doi.org/10.26804/ager.2019.04.10

Wang, Z., Bovik, A.C., Sheikh, H.R., Simoncelli, E.P., 2004. Image Quality Assessment: From Error Visibility to Structural Similarity. IEEE Trans. Image Process. 13, 600–612. https://doi.org/10.1109/TIP.2003.819861

Wei, B., Romero-Zerón, L., Rodrigue, D., 2014. Oil Displacement Mechanisms of Viscoelastic Polymers in Enhanced Oil Recovery (EOR): A Review. J. Pet. Explor. Prod. Technol. 4, 113–121. https://doi.org/10.1007/s13202-013-0087-5

Wildenschild, D., Sheppard, A.P., 2013. X-ray imaging and analysis techniques for quantifying pore-scale structure and processes in subsurface porous medium systems. Adv. Water Resour. 51, 217–246. https://doi.org/10.1016/j.advwatres.2012.07.018

Williamson, N.H., Komlosh, M.E., Benjamini, D., Basser, P.J., 2020. Limits to Flow Detection in Phase Contrast MRI. J. Magn. Reson. Open 2–3, 100004. https://doi.org/10.1016/j.jmro.2020.100004

Willis, S.A., Stait-Gardner, T., Torres, A.M., Price, W.S., 2016. Diffusion NMR of Confined Systems. The Royal Society of Chemistry. https://doi.org/10.1039/9781782623779

Windt, C.W., Vergeldt, F.J., Adrie De Jager, P., Van As, H., 2006. MRI of Long-Distance Water Transport: a Comparison of the Phloem and Xylem Flow Characteristics and Dynamics in Poplar, Castor Bean and Tabacco. Plant, Cell Environ. 29, 1715–1719. https://doi.org/10.1111/j.1365-3040.2006.01544

Xiao, D., Balcom, B.J., 2012. Two-Dimensional T2 Distribution Mapping in Rock Core Plugs with Optimal k-space Sampling. J. Magn. Reson. 220, 70–78. https://doi.org/10.1016/j.jmr.2012.04.003

Yang, K., Li, M., Ling, N.N.A., May, E.F., Connolly, P.R.J., Esteban, L., Clennell, M.B., Mahmoud, M., El-Husseiny, A., Adebayo, A.R., Elsayed, M.M., Johns, M.L., 2019. Quantitative Tortuosity Measurements of Carbonate Rocks Using Pulsed Field Gradient NMR. Transp. Porous Media 130, 847–865. https://doi.org/10.1007/s11242-019-01341-8

Yuen, E.H.L., Sederman, A.J., Gladden, L.F., 2002. In Situ Magnetic Resonance Visualisation of the Spatial Variation of Catalytic Conversion Within a Fixed-Bed Reactor. Appl. Catal. A Gen. 232, 29–38. https://doi.org/10.1016/S0926-860X(02)00064-9

Zaeri, M.R., Hashemi, R., Shahverdi, H., Sadeghi, M., 2018. Enhanced Oil Recovery from Carbonate Reservoirs by Spontaneous Imbibition of Low Salinity Water. Pet. Sci. 15, 564–576. https://doi.org/10.1007/s12182-018-0234-1

Zaitoun, A., Makakou, P., Blin, N., Al-Maamari, R.S., Al-Hashmi, A.-A.R., Abdel-Goad, M., 2012. Shear Stability of EOR Polymers. SPE J. 17, 335–339. https://doi.org/10.2118/141113-PA

Zamani, N., Bondino, I., Kaufmann, R., Skauge, A., 2017. Computation of Polymer In-Situ Rheology Using Direct Numerical Simulation. J. Pet. Sci. Eng. 159, 92–102. https://doi.org/10.1016/j.petrol.2017.09.011

Zeng, B., Cheng, L., Li, C., 2011. Low Velocity Non-Linear Flow in Ultra-Low Permeability Reservoir. J. Pet. Sci. Eng. 80, 1–6. https://doi.org/10.1016/j.petrol.2011.10.006

Zhan, Y., Zhang, G., 2019. An Improved OTSU Algorithm Using Histogram Accumulation Moment for Ore Segmentation. Mol. Divers. Preserv. Int. Symmetry 11, 1–16. https://doi.org/10.3390/sym11030431

Zhang, Y., Blümich, B., 2014. Spatially Resolved D-T2 Correlation NMR of Porous Media. J. Magn. Reson. 242, 41–48. https://doi.org/10.1016/j.jmr.2014.01.017

Zheng, G., Price, W.S., 2010. Solvent signal suppression in NMR. Prog. Nucl. Magn. Reson. Spectrosc. 56, 267–288. https://doi.org/10.1016/j.pnmrs.2010.01.001